Exploring Sterile Neutrinos at High and Low Energy Scales

Wenna Pei

A dissertation submitted in partial fulfillment
of the requirements for the degree of
Doctor of Philosophy
of
University College London.

Department of Physics and Astronomy
University College London

January 11, 2026

I, Wenna Pei, confirm that the work presented in this thesis is my own. Where information has been derived from other sources, I confirm that this has been indicated in the work.

Abstract

The inability of the Standard Model (SM) to explain certain observations, such as neutrino masses, hints at new physics Beyond the SM (BSM). Sterile neutrinos – hypothetical right-handed neutral leptons appearing in numerous BSM theories – are compelling extensions of the SM as they can remedy several of these issues. This thesis offers a phenomenological study of light and massive sterile neutrinos in future experiments.

Without model predictions, the neutrino mass needs to be determined experimentally. Single beta-decay is the only available direct probe, thus we explore whether these experiments can search for new physics beyond the SM, such as keV-mass sterile neutrinos, which manifest as distortions in the energy and angular spectra of the emitted beta-electron. Studying these distributions, we conclude that the next generation of tritium beta-decay experiments utilising Cyclotron Radiation Emission Spectroscopy can improve existing bounds by an order of magnitude. Furthermore, we find that such experiments will also be sensitive to BSM couplings parameterising exotic interactions differing from the usual V-A structure of the weak Lagrangian.

In Effective Field Theory (EFT) frameworks, the SM can be extended with Dirac and Majorana sterile neutrino states. In the EFT formalism, the interactions are approximated by operators, and their relative coupling strength is parameterised by Wilson Coefficients (WC). Considering the Future e^+e^- Circular Collider (FCC-ee), we study monophoton final states originating from active-sterile mixing by performing and analysing computer simulations of the process using MadGraph and derive projected sensitivities to the mixing angle. Additionally, we study monophoton final states from four-fermion processes, displaced di-electron final states, and effective Z and $W^{\pm}$ mediated processes. We estimate the sensitivity of the FCC to the WCs and conclude that the FCC will place stringent limits on the operator scales of the relevant WCs associated with GeV-mass sterile states.

Impact Statement

Although the Standard Model is able to describe and predict natural phenomena to an astonishing degree of precision, it leaves several key questions unresolved. The first and so far only direct evidence of new physics is the confirmation of the massive nature of neutrinos. The neutrino sector therefore provides an exciting and natural path into the realm beyond the Standard Model. As neutrinos lie at the intersection of multiple disciplines, ranging from particle physics, through geophysics, to astrophysics and cosmology, they are ideally suited to answer some of the most fundamental questions about the Universe.

Sterile neutrinos are popular extensions of the Standard Model, appearing at various energy regimes in numerous theories. In this thesis, the prospects for sterile neutrino searches across different mass scales are investigated in the context of two classes of upcoming experiments. By studying their possible phenomenological impact in a model-independent effective field theory framework, this work highlights the potential of future facilities to probe new physics. It therefore aims to provide input valuable to both experimental strategies and theoretical interpretation.

This thesis intends to contribute to the extensive global research endeavour required to advance understanding of neutrino properties. In assessing the potential of future experiments, it is hoped that this work serves as motivation to both theorists and experimentalists to cultivate the already fertile ground of the neutrino sector, where new physics is expected to emerge. While no direct commercial or societal benefits can be derived from these results, fundamental research underpins the technological and conceptual advancements that drive cross-disciplinary innovation and broader real-world applications.

UCL Research Paper Declaration

1. **For a research manuscript that has already been published** (if not yet published, skip to section 2):

    (a) **Title of the manuscript:** Sensitivity of Future Tritium Decay Experiments to New Physics

    (b) **Provide the DOI or direct link to the published the work:** `https://link.springer.com/article/10.1007/JHEP03(2023)144`

    (c) **Publication name (e.g. journal or textbook):** JHEP

    (d) **Publisher name (e.g. Elsevier, Oxford University Press):** Springer

    (e) **Date of publication:** March 2023

    (f) **List all authors as they appear in the publication:** James A. L. Canning, Frank F. Deppisch & Wenna Pei

    (g) **Was the work peer reviewed?** Yes

    (h) **Do you retain copyright for the work?** Yes

    (i) **Was an earlier version uploaded to a preprint server (e.g., medRxiv, arXiv)?** `https://arxiv.org/abs/2212.06106v2`

    ☒ *I acknowledge permission of the publisher named under 1d to include in this thesis portions of the publication named as included in 1c.*

2. **For a manuscript prepared for publication but not yet published** (if already published, skip to section 3):

(a) **Current title of the manuscript:**

(b) **Has it been uploaded to a preprint server** (e.g., medRxiv, arXiv)? If 'Yes', provide the DOI or direct link. If not applicable, leave blank

(c) **Intended publication outlet (e.g., journal name):**

(d) **List all authors in the intended authorship order:**

(e) **Current stage of publication (e.g., in submission, under review):**

For multi-authored work, please give a statement of contribution covering all authors: The work completed in this paper was a collaborative effort between myself (sterile neutrinos), J. A. L. Canning (exotic currents) and F. F. Deppisch (tritium decay, conceptual, technical and overall guidance).

3. **In which chapter(s) of your thesis can this material be found?**
   Chapters 3 & 4

4. **e-Signatures confirming accuracy of the above information** (This form should be co-signed by the supervisor/senior author unless the work is single-authored)

   Candidate signature: Wenna Pei

   Date: 23/09/2025

   Supervisor/ Senior Author (where appropriate): Frank Deppisch

   Date: 24/09/2025

UCL Research Paper Declaration

1. **For a research manuscript that has already been published** (if not yet published, skip to section 2):
    (a) **Title of the manuscript:** Constraining the SMEFT Extended with Sterile Neutrinos at FCC-ee
    (b) **Provide the DOI or direct link to the published the work:** `https://link.springer.com/article/10.1007/JHEP10(2025)199`
    (c) **Publication name (e.g. journal or textbook):** JHEP
    (d) **Publisher name (e.g. Elsevier, Oxford University Press):** Springer
    (e) **Date of publication:** October 2025
    (f) **List all authors as they appear in the publication:** Patrick D. Bolton, Frank F. Deppisch, Suchita Kulkarni, Chayan Majumdar & Wenna Pei
    (g) **Was the work peer reviewed?** Yes
    (h) **Do you retain copyright for the work?** Yes
    (i) **Was an earlier version uploaded to a preprint server (e.g., medRxiv, arXiv)?** `https://arxiv.org/abs/2502.06972`
        ☒ *I acknowledge permission of the publisher named under 1d to include in this thesis portions of the publication named as included in 1c.*

2. **For a manuscript prepared for publication but not yet published** (if already published, skip to section 3):

   (a) **Current title of the manuscript:**
   (b) **Has it been uploaded to a preprint server** (e.g., medRxiv, arXiv)? If 'Yes', provide the DOI or direct link. If not applicable, leave blank
   (c) **Intended publication outlet (e.g., journal name):**
   (d) **List all authors in the intended authorship order:**
   (e) **Current stage of publication (e.g., in submission, under review):**

   For multi-authored work, please give a statement of contribution covering all authors: The work completed in this paper was a collaborative effort between myself (active-sterile mixing and EFT monophoton analysis), P. D. Bolton (mathematical formalism, coefficient matching), F. F. Deppisch (conceptual and overall guidance), S. Kulkarni (DV analysis) and C. Majumdar (active-sterile mixing and EFT monophoton analysis).

3. **In which chapter(s) of your thesis can this material be found?**
   Chapters 3 & 5
4. **e-Signatures confirming accuracy of the above information** (This form should be co-signed by the supervisor/senior author unless the work is single-authored)

   Candidate signature: Wenna Pei

   Date: 23/09/2025

   Supervisor/ Senior Author (where appropriate): Frank Deppisch

   Date: 24/09/2025

Acknowledgements

Firstly, I would like to thank my supervisor, Frank Deppisch, for his continuous advice, guidance and encouragement during the entire course of this PhD. I am grateful to Jonathan Butterworth for his mentorship both academically and personally. I need to thank Suchita Kulkarni and Patrick Bolton for their collaboration and many interesting conversations and especially Chayan Majumdar for the countless hours of discussions during our work together. I wish to thank all the academics and students at UCL with whom I have crossed paths, but beyond all James Canning, without whose support and friendship I could not have come this far. My sincere gratitude goes to the entire particle phenomenology group at ELTE university, in particular to Zoltán Trócsányi, for creating a welcoming environment, facilitating stimulating discussions and providing invaluable input to my research, alongside giving me opportunities to present at and attend events. I would like to express my appreciation to the organisers and participants of the lectures, events and conferences I have attended during these past few years. I owe warm thanks to my cat, Lola, for her comforting presence and reassuring cuddles during the writing of this thesis. Lastly, I am deeply indebted to my friends and family, especially my parents Ivelina and Jie, and my fiancé Bertram, for their unwavering patience, support and belief – none of this would have been possible without you.

Contents

List of Figures

List of Tables

Chapter 1

Introduction

In 1930, Wolfgang Pauli proposed the existence of an electrically neutral light particle as his solution to the problem of energy conservation in beta-decay, which he christened the *neutron* [1]. Upon the discovery of the neutron by Chadwick in 1932 [2], the particle postulated by Pauli was renamed the *neutrino* by Enrico Fermi in 1934, meaning “little neutral one” in Italian. This name encapsulated the electrically neutral charge and very light nature of the hypothesised particle. Although Pauli had his doubts about the hypothesised neutrino and even called it a “desperate remedy”, Fermi was intrigued by the proposal and formulated the theory of beta-decay, now known as Fermi theory, which describes the effective interaction between the electron, the proton, the neutron and the neutrino. Introducing the neutrino solved the problem of continuous electron kinetic energy distribution, as the emission of an additional particle alongside the electron in beta-decay results in the kinetic energy being shared between the final state particles and hence gives rise to the observed spectrum of energies. This was a rather convincing theoretical explanation and founded the branch of neutrino physics, following which the field gained popularity that lasts to this day.

In 1935, Maria Goeppert-Mayer predicted the process of double beta-decay with neutrinos in her landmark paper [3]. In 1936, Edward Teller (later one of Goeppert-Mayer’s collaborators), together with George Gamow, extended the existing theory of weak interactions by including axial-vector currents to explain spin-flipping, i.e. Gamow-Teller, transitions [4] (since vector currents only allow spin-conserving, i.e. Fermi transitions). This extension lead to the realisation that other Lorentz structures are also possible (scalar, pseudoscalar and tensor), causing much confusion (especially coupled with some erroneous experimental results at the time). An infamous review article by Emil Jan Konopinski in 1955 [5] concluded that the correct combination was scalar and tensor couplings (also biased by the results of a famous but wrong experiment at the time). In 1937, Ettore Majorana proposed [6] the possibility that neutrinos could be their own antiparticles, i.e. Majorana fermions, something that to this day remains an open question. In the same year, J. C. Street and E. C. Stevenson [7] confirmed via cloud chamber experiment the discovery of the muon, which was made a year prior by Carl D. Anderson and Seth Neddermeyer [8] through their study of the curvature of cosmic radiation in a magnetic field.

Although Fermi theory was widely accepted across the scientific community, there was a lack of experimental evidence supporting it, partly because in 1934 Hans Bethe and Rudolf Peierls predicted that the interaction strength is so low that observation may not be possible at all [9], which probably had an effect on the experimental community's enthusiasm to design any searches. Nevertheless, in the 1950s Clyde Cowan and Frederick Reines looked for ways to design an experiment that would be able to measure inverse beta-decay (antineutrino producing a positron). Ultimately, they decided to exploit the large flux of antineutrinos coming from a nuclear reactor (1400 litres of liquid scintillators), creating the first ever reactor neutrino experiment. In 1956, Cowan and Reines – after five months of data-taking with a 10 tonne detector – found the first experimental evidence of neutrinos [10] and they informed Pauli via a telegram. This discovery earned Reines the Nobel prize in 1995, 40 years after the famous experimental discovery.

At the time, parity violation was unthinkable. Yet, observations of what is known as the θ–τ puzzle of kaons posed a serious challenge: the state θ decayed into two pions, while τ decayed into three, implying opposite parities. Since both had identical spin, charge, and mass, they had to be the same particle – contradicting parity conservation in weak interactions. In 1956, Tsung-Dao Lee and Chen

Ning Yang pointed out that parity conservation in weak processes had never been experimentally established and proposed dedicated tests [11]. Chien-Shiung Wu's ^{60}Co decay experiment soon confirmed parity violation [12], earning Lee and Yang the 1957 Nobel Prize – though controversially excluding Wu's crucial role.

The discovery of parity violation initially deepened the confusion about weak interactions, as it implied that the weak Lagrangian could contain both parity-conserving and parity-violating couplings. In 1958, Feynman, Gell-Mann, Sudarshan, Marshak and Sakurai resolved this with the V–A theory, which treated the neutrino as a two-component object – where the neutrino and antineutrino are left- and right-handed, respectively. This idea was mathematically anticipated by Weyl in 1929, who introduced two-component massless spinors (now called Weyl spinors), though this was harshly rejected by Pauli in 1933 because such particles necessarily violate parity. This picture was experimentally confirmed the same year by Goldhaber, Grodzins and Sunyar at Brookhaven [13], who measured the neutrino helicity in the famous GGS experiment: electron capture in ^{152}Eu produced an electron neutrino and excited ^{152}Sm*, which then decayed emitting a photon. The photon polarisation revealed the neutrino to have negative helicity, providing strong evidence for the two-component description and solidifying the V–A theory.

Processes in which the total lepton number is not conserved are called lepton number violating (LNV), while those allowing transitions between lepton flavours are lepton flavour violating (LFV). Although lepton number conservation was introduced in 1953 to explain missing decay channels, lepton flavour conservation was only recognised later: general lepton number conservation still allowed processes like $\mu \to e + \gamma$, yet experiments showed rates far below expectations. This hinted at an additional conserved quantity, lepton flavour, leading Pontecorvo to propose a test for whether the muon and electron neutrinos are distinct [14]. The decisive experiment was carried out in 1962 at Brookhaven by Lederman, Schwartz and Steinberger, who discovered the muon neutrino [15], a result that earned them the 1988 Nobel Prize.

In 1968, the Homestake experiment, led by Raymond Davis at Brookhaven, detected solar neutrinos for the first time but found only about a third of the flux predicted by John N. Bahcall [16]. Nearly 20 years later, the Kamiokande experiment, led by Masatoshi Koshiba, confirmed the deficit in 1987 while also detecting neutrinos from a supernova [17]. Initially attributed to experimental or solar model uncertainties, this discrepancy is now understood as evidence of neutrino oscillations, confirmed only decades later.

Following the proposal of the Glashow-Weinberg-Salam model, in 1973 the Gargamelle bubble chamber neutrino experiment observed neutrino interactions mediated by the Z boson (neutral-current mediated scattering between neutrinos and electrons) [18] and this discovery was independently confirmed a year later at Fermilab [19]. These results strongly supported the SM framework and this marked the start of the myriad of particles that would be discovered in the coming decades.

The charm quark was discovered in 1974 via the J/Psi meson at Brookhaven [20] and independently at SLAC [21], followed by the bottom quark in 1977 at Fermilab [22]. The tau lepton was detected in 1975 at SLAC by Martin Perl and collaborators [23], motivating the existence of the tau neutrino. The W and Z bosons were discovered at CERN in 1983 by the UA1 [24, 25] and UA2 [26, 27] experiments, led by Carlo Rubbia and Simon van der Meer, who received the 1984 Nobel Prize. The top quark was discovered at Fermilab in 1995 [28], two decades after being proposed to explain CP violation in kaon decays. The tau neutrino, 25 years after its postulation, was discovered in 2000 by the DONUT experiment [29] using Tevatron, the world's most powerful accelerator at the time. Perl received the 1995 Nobel Prize for discovering the tau lepton (shared with Reines for the electron neutrino). By 2000, the Standard Model's full particle content – except the Higgs boson – had been discovered.

Although the tau neutrino's initial proposal was motivated by the existence of three-generations of charged leptons, its discovery prompted the question: how many generations of light neutrinos are there? This was investigated at LEP by four different collaborations. By measuring the invisible width of the Z boson, ALEPH, DELPHI, L3 and OPAL each reported the number of neutrino generations to be around 3. In 2006, these results were combined to give a value of 2.9840 ± 0.0082 [30]. It is worth noting that effective number of neutrino generations, N_{eff}, can be inferred without any colliders, simply by looking at the sky and observing the anisotropies of the CMB (which are direct consequences of the energy density of the universe). Currently, cosmological measurements give $N_{\text{eff}} = 3.044$ [31].

Kamiokande observed the atmospheric neutrino anomaly in 1988 [32], a year after Kamiokande [33] and IMB [17] registered the first supernova neutrinos. Super-Kamiokande observed the first evidence for neutrino oscillations in 1998 [34], confirmed by the SNO experiment in 2002 [35]. KamLAND detected evidence of reactor antineutrino disappearance in 2003 [36], reappearance in 2004 [37], and observed geoneutrinos in 2005 [38]. OPERA at Gran Sasso reported the first tau-neutrino candidate from CERN's beam in 2010 [39], with muon–tau oscillations discovered in 2015.

Solving the mystery of very high energy cosmic rays could by aided by the study of neutrinos. Since any object capable of producing such energetic cosmic rays is also assumed to emit similarly high energy neutrinos, the IceCube observatory is designed in part to look for such neutrinos, as they will have travelled from the production source to the Earth relatively undisturbed, given the weakly and rarely interacting nature of these particles. In 2012, IceCube detected a 2 peta-electronvolt neutrino [40], the most energetic detected at the time.

In 2015, Takaaki Kajita (Super-Kamiokande) and Arthur B. McDonald (SNO) received the Nobel Prize in Physics for confirming neutrino oscillations. Yet many questions remain about neutrinos, which the next-generation of experiments will attempt to answer. Of these, besides Hyper Kamiokande, perhaps the Deep Underground Neutrino Experiment (DUNE) [41] is the most outstanding. Its diverse program includes measuring CP violation in the leptonic sector, determining the mass hierarchy, detecting neutrinos from stellar collapse, and searching for proton decay as a test of grand unification. Groundbreaking took place in 2017, with operation planned for the 2030s.

We have thus seen that the study of neutrinos has been instrumental in the construction of the SM and therefore our understanding of the physical world. However, the discovery of oscillations confirming the massive nature of neutrinos is direct evidence of the incompleteness of the SM, as it cannot accommodate neutrino mass or explain its origin, absolute scale, mass ordering, Dirac/Majorana nature, or species count. Neutrinos therefore seem to be a natural bridge connecting the SM to new physics beyond it.

Perhaps the most straightforward way to accomplish mass generation for the SM light neutrinos is via the addition of right-handed (RH) sterile neutrinos to the SM particle content. Depending on the model in which they are embedded, they may span a wide range of masses, with distinct phenomenologies accessible to different types of experiments. As the high-energy theory in which such sterile states are embedded is unknown, it is useful to adopt model-independent approaches when searching for BSM physics, such as Effective Field Theory (EFT).

At the low-energy frontier, the only existing direct laboratory probe of light neutrino mass is single beta-decay, with the current leading constraint on the effective mass of $m_\beta < 0.45$ eV at 90% CL, coming from the KATRIN experiment [42]. However, due to the energy resolution limitations associated with the use of molecular tritium, a new generation of single beta-decay neutrino mass experiments are needed to guarantee measurement. This has led to the proposal of Cyclotron Radiation Emission Spectroscopy (CRES), which would utilise high-precision measurements of the frequency of cyclotron radiation to determine the electron energy and hence the neutrino mass. The next generation of neutrino experiments using atomic tritium and relying on the technique of CRES, besides being expected to conclusively measure the absolute mass scale of neutrinos and determine the mass hierarchy, will have the potential to probe eV and keV scale sterile neutrinos.

At the high-energy frontier, the Future Circular Collider electron-positron (FCC-ee) era will provide unprecedented statistics and a clean environment for precision studies. This will be an ideal opportunity to search for weakly interacting new physics, such as GeV scale sterile neutrinos.

This thesis investigates sterile neutrino phenomenology at two energy scales.

Chapter 2 provides a summary of the Standard Model, while Chapter 3 reviews neutrino physics and properties, and introduces the EFT formalism. Chapter 4 examines the sensitivity of future CRES-type neutrino mass experiments to keV-scale sterile neutrinos and their potential to probe exotic couplings. Chapter 5 presents a phenomenological study of GeV-scale sterile neutrinos at the FCC-ee, focusing on the collider's reach for the coefficients of EFT operators involving sterile fields. Conclusions are given in Chapter 6.

Chapter 2

Standard Model

The theoretical framework known as the Standard Model (SM), categorises all known elementary particles and describes their interactions. It is undeniably one of the greatest triumphs in the history of particle physics, and constitutes one of the two pillars on which modern physics rests, the other being the theory of general relativity. The SM is a unified theory of electromagnetic, strong and weak interactions, governing the processes of the three generations of quarks and leptons, mediated by the vector bosons, and generating masses via their interactions with the Higgs boson.

This chapter introduces the gauge theory and fundamental symmetries underpinning the SM. The particle content and interactions of the SM is presented and the masses generated upon electroweak symmetry breaking (EWSB) is discussed. Following this we consider the status of the SM, both its successes and shortcomings, and finish with a brief introduction of the EFT framework as a means for going beyond the SM.

2.1 Relativistic Theories

The two postulates of special relativity are: i) the laws of physics are the same in all inertial reference frames and ii) the speed of light is constant in all inertial reference frames, which are enforced in all relativistic theories by the Poincaré symmetry [43]. Therefore, in order to construct a model that describes the observed natural world, one must ensure that the Poincaré symmetry is respected. The Poincaré group consist of the Lorentz group plus translations. Translation symmetry dictates that physics should remain the same upon a shift in spacetime coordinates, while the Lorentz group dictates invariance with respect to boosts and rotations. Noether's theorem states that for every continuous symmetry [1] in a physical system, there exists a conserved quantity. Accordingly, translational and boost invariance imply the conservation of four-momentum, while rotational invariance results in the conservation of angular momentum.

2.2 Fundamental Fields

Field Type	Scalar	Weyl Spinor		Dirac Spinor	Vector
Notation	ϕ	ψ_L	ψ_R	ψ	A^μ
Representation	$(0,0)$	$\left(\frac{1}{2},0\right)$	$\left(0,\frac{1}{2}\right)$	$\left(\frac{1}{2},0\right)\oplus\left(0,\frac{1}{2}\right)$	$\left(\frac{1}{2},\frac{1}{2}\right)$

Table 2.1: Fundamental field types and their representations under the restricted Lorentz group $\mathrm{SO}(1,3)$.

To proceed with the construction of the model, the fundamental fields need to be introduced. These are identified based on their Lorentz structures, which determine how they transform under Lorentz transformations. A summary of the fundamental fields alongside their transformation properties can be found in Table 2.1.

The full Lorentz group $\mathrm{O}(1,3)$ is made up of connected (boost and rotations) and disconnected (parity and time reversal) components. The connected part of the full Lorentz Lie group is $\mathrm{SO}(1,3)$, with algebra $\mathfrak{so}(1,3)$, which can be expressed using two independent sub-algebras, $\mathfrak{su}(2)$. These are built from linear combinations of boosts and rotations and are labelled (i,j), with both i and j denoting a half-integer or integer, where $s=i+j$ is the spin. These quantum numbers can take integer and half integer values, resulting in the three fundamental field types $(0,0)$, $(1/2,0)$, $(0,1/2)$ and $(1/2,1/2)$. These are known as spin-0 scalar, spin-1/2 fermion and spin-1 vector fields, which give rise to the associated particles, which transform distinctly under Lorentz transformations.

---

[1] A continuous symmetry is one that is parameterised by a continuous variable, i.e. one that is not constrained to discrete values.

Conventionally integer spin particles are known as bosons, while half integer spin particles are called fermions, as the former type follows Bose-Einstein, while the latter Fermi-Dirac statistics. The key difference lies in the symmetry of their wavefunctions. In the case of bosons, the wavefunctions is symmetric, and the system is insensitive to the exchange of two particles, i.e. $\Psi(\mathbf{r_1},\mathbf{r_2}) = \Psi(\mathbf{r_2},\mathbf{r_1})$, where $\mathbf{r_1}$ and $\mathbf{r_2}$ denote the positions of the first and second particles, respectively. For fermions on the other hand, the wave function is antisymmetric, i.e. $\Psi(\mathbf{r_1},\mathbf{r_2}) = -\Psi(\mathbf{r_2},\mathbf{r_1})$, and requiring the two fermions to be in the same place via $\mathbf{r_1} = \mathbf{r_2}$ leads to $\Psi(\mathbf{r_1},\mathbf{r_2}) = -\Psi(\mathbf{r_1},\mathbf{r_2})$. These two equations can only hold true simultaneously for $\Psi(\mathbf{r_1},\mathbf{r_2}) = 0$, in other words two identical fermions cannot occupy the same quantum state simultaneously – this is known as Pauli's exclusion principle [44]. For bosons on the other hand, the symmetric nature of the wavefunctions allow two or more bosons to be in the same quantum state. Therefore, in a bosonic system at low temperatures, many bosons can be found in the lowest quantum state. This is known as Bose-Einstein condensation (BEC).

It is useful to express the general four-component fermion field, Ψ (although it was used to denote the wavefunction earlier, from now it will represent a fermion field, to stay consistent with the notational convention) in the chiral basis using Weyl spinors

$$\psi_L = P_L\Psi, \quad \psi_R = P_R\Psi \tag{2.1}$$

where

$$P_L = \frac{1}{2}(1-\gamma_5), \quad P_R = \frac{1}{2}(1+\gamma_5) \tag{2.2}$$

are the chiral projection operators and $\gamma_5 = i\gamma^0\gamma^1\gamma^2\gamma^3$. The γ^μ are the 4×4 matrices that obey the anticommutation relation $\{\gamma^\mu,\gamma^\nu\} = 2g^{\mu\nu}$, with $g_{\mu\nu} = \mathrm{diag}(+1,-1,-1,-1)$ being the flat Minkowski metric. The Dirac spinor is then composed of the left- and right-handed components

$$\Psi = \begin{pmatrix} \psi_L \\ \psi_R \end{pmatrix}. \tag{2.3}$$

The handedness, or chirality of a particle is related to its helicity, defined as

$$\hat{h} = \frac{\mathbf{S} \cdot \mathbf{p}}{p} \tag{2.4}$$

for a particle with spin vector **S**, four-momentum p and momentum **p**, i.e. the helicity is the projection of the spin along the direction of motion of the particle. Whereas chirality is a an intrinsic Lorentz invariant property dictated by the transformation of the Weyl spinors, helicity is not Lorentz invariant due to the frame dependence introduced by the momentum. In the massless case however, chirality and helicity coincide.

2.3 Free Fields

One of the most fundamental results of special relativity is the energy dispersion relation

$$E^2 = |\mathbf{p}|^2 c^2 + m^2 c^4, \tag{2.5}$$

which follows directly from the invariance of the spacetime interval between two events and where E is the particle's energy, $|\mathbf{p}|$ is the magnitude of the 3-momentum, m denotes the mass and c is the speed of light. This energy-momentum relation is the basis for the free propagating wave equations.

In the case of a spin-0 scalar field, ϕ, the replacements $E \to i\frac{\partial}{\partial t}$ and $|\mathbf{p}| \to -i\nabla$ introducing the operator forms result in the Klein-Gordon equation

$$\left(\partial_\mu \partial^\mu + m^2\right) \phi = 0, \tag{2.6}$$

where $\mu = 0, 1, 2, 3$ denotes the time-like and the three space-like components of the derivative and m is the mass of the scalar.

For spin-1/2 fermionic fields, the Klein-Gordon equation is inadequate, as it does not have the ability to treat spinors properly. Hence, to include such a mechanism, the energy-momentum relation $E = |\mathbf{p}|^2 + m^2$ needs to be cast in a linear form $E = \alpha \cdot \mathbf{p} + \beta m$, where $\alpha = (\alpha_1, \alpha_2, \alpha_3)$ is a vector of matrices corresponding to the spatial dimensions and β is a matrix, before the operators are introduced. For spin-

1/2 fermions, it will be shown later that the construction of a mass term necessarily requires the presence of both ψ_L and ψ_R. Thus, the chiral basis can only decouple in the massless limit, yielding the Weyl equations

$$i\sigma^{\mu}\partial_{\mu}\psi_L = 0, \quad i\overline{\sigma}^{\mu}\partial_{\mu}\psi_R = 0 \tag{2.7}$$

describing the dynamics of the left- and right-handed fermions, where $\sigma^{\mu} = (I, \sigma^i)$ and $\bar{\sigma^{\mu}} = (I, -\sigma^i)$ are the Pauli four-vector and its conjugate, respectively, with σ^i being the Pauli matrices and I denoting the 2×2 identity matrix. If $m \neq 0$, then the chiral Weyl spinors are coupled, resulting in the Dirac equation

$$\left(i\gamma^{\mu}\partial_{\mu} - m\right)\Psi = 0. \tag{2.8}$$

For spin-1 states, i.e. fields that transform as vectors under the Lorentz transformations, A^{μ}, the expressions describing the evolution of the field is the Proca equation

$$\partial_{\mu}\partial^{\mu}A^{\nu} - \partial^{\nu}\partial_{\mu}A^{\mu} + m^2 A^{\nu} = 0 \tag{2.9}$$

with m being the mass of the vector boson.

The Klein-Gordon (Eq. 2.6), Dirac (Eq. 2.8) and Proca (Eq. 2.9) equations above describe the evolution of spin-0, spin-1/2 and spin-1 fields, respectively, in the absence of interactions.

2.4 Gauge Theories

The SM is a relativistic quantum field theory (QFT) based on the $\mathrm{SU}(3)_c \times \mathrm{SU}(2)_L \times \mathrm{U}(1)_Y$ gauge group product. The dynamics of a field theory are dictated by its Lagrangian, which must be constructed so as to respect the symmetries of the underlying gauge group, by remaining invariant under local[2] transformations. The three symmetry groups that comprise the SM gauge group correspond to the three fundamental interaction types described by the theory. The symmetry group $\mathrm{SU}(3)_c$

---

[2] The parameters of a local transformation – as opposed to a global one – have a space-time dependence.

SM Field	$\mathrm{SU}(3)_c$	$\mathrm{SU}(2)_L$	$\mathrm{U}(1)_Y$
L_L	$\mathbf{1}$	$\mathbf{2}$	$-\frac{1}{2}$
ℓ_R	$\mathbf{1}$	$\mathbf{1}$	-1
Q_L	$\mathbf{3}$	$\mathbf{2}$	$\frac{1}{6}$
u_R	$\mathbf{3}$	$\mathbf{1}$	$\frac{2}{3}$
d_R	$\mathbf{3}$	$\mathbf{1}$	$-\frac{1}{3}$
G	$\mathbf{8}$	$\mathbf{1}$	0
W	$\mathbf{1}$	$\mathbf{3}$	0
B	$\mathbf{1}$	$\mathbf{1}$	0
H	$\mathbf{1}$	$\mathbf{2}$	$\frac{1}{2}$

Table 2.2: Transformation properties of the matter and gauge fields of the SM in their flavour basis under the gauge groups $\mathrm{SU}(3)_c$ and $\mathrm{SU}(2)_L$ and their hypercharges under $\mathrm{U}(1)_Y$.

dictates the interactions of the colour-charged quarks via gluons, known as Quantum Chromodynamics (QCD), while the combination $\mathrm{SU}(2)_L \times \mathrm{U}(1)_Y$ underpins the interactions of the electroweak (EW) force, combining the weak interaction and electromagnetism.

The complete set of fields of the UV SM are listed in Table 2.2. These include the left-handed quark doublets

$$Q_L = \begin{pmatrix} u_L \\ d_L \end{pmatrix} \tag{2.10}$$

and the left-handed lepton doublets

$$L_L = \begin{pmatrix} \nu_L \\ \ell_L \end{pmatrix} \tag{2.11}$$

where u and d denote the up- and down-type quarks, ν_L the neutrinos and ℓ_L the charged leptons. Further included are the right-handed singlet up- and down-quarks, u_R and d_R, as well as the right-handed singlet charged leptons singlets, ℓ_R. In the SM, there are no right-handed singlet neutrinos. Each of the fermion fields are repeated over three generations, i.e. carry a flavour index $u \in \{u, c, t\}$, $d \in \{d, s, b\}$, $\ell \in \{e, \mu, \tau\}$ and $\nu \in \{\nu_e, \nu_\mu, \nu_\tau\}$. In addition to the matter fields, there are the gauge fields: eight gluons, G, associated with SU(3)$_c$, three W associated with SU(2)$_L$ and B, associated with U(1)$_Y$. Finally, there is the Higgs boson, H, the only scalar particle in the SM, which gives mass to the elementary particles.

Under SU(2)$_L$, left-handed fields transform as doublets, while right-handed fields as singlets. The members of the doublet are distinguished by the third component of isospin, T^3. The quantum number associated with the U(1)$_Y$ gauge symmetry is the hypercharge, Y, which relates T^3 to the electric charge, Q, via the Gell-Mann–Nishijima relation [45,46]

$$Y = Q - T^3. \tag{2.12}$$

Having established the field content of the SM as well as the descriptions of the free fields in Sec. 2.3, it is now possible to incorporate interactions. To achieve this, we require a Lorentz invariant Lagrangian.

For massive fermions, one may construct the Lagrangian

$$\mathcal{L}_\Psi = \bar{\Psi}(i\gamma^\mu \partial_\mu - m)\Psi \tag{2.13}$$

where $\bar{\Psi} \equiv \Psi^\dagger \gamma^0$ is the Dirac adjoint, with † denoting Hermitian conjugation. From this it is easy to obtain the free-field Dirac equation in Eq. 2.8 by applying the Euler-Lagrange equations

$$\partial_\mu \frac{\partial \mathcal{L}_\Psi}{\partial(\partial_\mu \bar{\Psi})} - \frac{\partial \mathcal{L}_\Psi}{\partial \bar{\Psi}} = 0. \tag{2.14}$$

However, Eq. 2.13 does not satisfy gauge invariance. To see this, first consider the Weyl spinor content of the Dirac spinor, which allows Eq. 2.13 to be expanded into

$$\mathcal{L}_\Psi = i\,\bar{\Psi}_L \partial\!\!\!/ \Psi_L + i\,\bar{\Psi}_R \partial\!\!\!/ \Psi_R - m\bar{\Psi}_L \Psi_R - m\bar{\Psi}_R \Psi_L. \tag{2.15}$$

From this expression, it is immediately apparent that the mass terms couple both left- and right-handed Weyl spinors, which transform differently under SU(2)$_L$ × U(1)$_Y$ – as a doublet and as a singlet, respectively – and therefore these cross-terms break gauge invariance and should not appear in the Lagrangian. Under U(1)$_Y$ the fields transform as

$$\Psi \xrightarrow{\mathrm{U}(1)_Y} \Psi' = e^{i\theta(x)Y}\Psi \tag{2.16}$$

where $\theta(x)$ is a local spacetime-dependent gauge parameter and Y is the hypercharge. Applying this transformation, it is not difficult to see that the fermion bilinear, $\bar{\Psi}\Psi$ is gauge invariant.

Next, we turn our attention to the kinetic term in Eq. 2.13 to see how it transforms. Applying Eq. 2.16 yields

$$\partial_\mu\Psi \to \partial_\mu\Psi' = \partial_\mu\left(e^{i\theta(x)Y}\Psi\right) = e^{i\theta(x)Y}\partial_\mu\Psi + iY(\partial_\mu\theta(x))e^{i\theta(x)Y}\Psi. \tag{2.17}$$

Above it was already explained that $\bar{\Psi}\Psi$ is gauge invariant, so the first term is fine in the above expression. The term proportional to $\theta(x)$, however, breaks gauge invariance. It should be noted, that for global transformations, i.e. $e^{i\theta Y}$ without spacetime dependence, this term vanishes and gauge invariance is restored. To remedy the issue for local transformations, the derivative needs to be modified to

$$D_\mu = \partial_\mu - ig'YB_\mu \tag{2.18}$$

where g' will be interpreted as the gauge coupling constant and B_μ is the field associated with the vector boson of U(1)$_Y$, transforming as

$$B_\mu \to B_\mu + \frac{1}{g'}\partial_\mu\theta(x). \tag{2.19}$$

This follows from the general transformation of the field

$$B_\mu \to B'_\mu = U(x)\left(B_\mu + \frac{i}{g'}\partial_\mu\right)U^{-1}(x) \tag{2.20}$$

for the infinitesimal transformation $U(x) = e^{i\theta(x)Y}$. Eq. 2.20 can be written in the form of Eq. 2.19 using the first-order expansion of the transformation around $\theta(x) = 0$, yielding $U(x) \approx 1 + i\theta(x)Y$. The expression in Eq. 2.18 is known as the covariant derivative, since $D_\mu \Psi$ transforms in the same way as Ψ itself, thus ensuring gauge invariance.

Having removed the explicit mass terms and putting to use D_μ results in the new kinetic fermion Lagrangian,

$$\mathcal{L}_\Psi = i\bar{\Psi}\not{D}\Psi = i\bar{\Psi}\gamma^\mu \partial_\mu \Psi + g' Y \bar{\Psi}\gamma^\mu B_\mu \Psi \tag{2.21}$$

where $\not{D} = \gamma^\mu D_\mu$. Crucially, we notice from the expanded expression that interactions between fermions and the gauge fields have been introduced via the second term. While g' is a single universal constant in the SM, different particles have different values of Y, affecting their interaction strength with B_μ.

The above discussion applies to the abelian U(1) gauge symmetry. In order to similarly construct a the kinetic Lagrangian for the gauge fields B, W and G listed in Table 2.2, non-abelian gauge symmetries also need to be discussed. In general, for SU(N) the transformation will couple the N spinors, which therefore do not transform independently, but rather as an N-component column vector

$$\Psi = \begin{pmatrix} \Psi_1 \\ \Psi_2 \\ \vdots \\ \Psi_N \end{pmatrix}. \tag{2.22}$$

In the case of the non-abelian SU(2) and SU(3) groups these fields transfrom as

$$\Psi \xrightarrow{\mathrm{SU(2)}_L} \Psi' = e^{i\theta^i(x)T^i}\Psi \tag{2.23}$$

$$\Psi \xrightarrow{\mathrm{SU(3)}_c} \Psi' = e^{i\theta^a(x)t^a}\Psi \tag{2.24}$$

where $T^i = \sigma^i/2$ $(i = 1,2,3)$ and $t^a = \lambda^a/2$ $(\lambda = 1,\ldots,8)$ are the generators of the SU(2)$_L$ and SU(3)$_c$ groups, respectively, with σ^i denoting the Pauli and λ^a the Gell-Mann matrices. In general, SU(N) has $N^2 - 1$ generators, also corresponding to the number of gauge bosons. Hence, there are 3 and 8 gauge bosons associated with the SU(2)$_L$ and SU(3)$_c$ groups, respectively. While for abelian groups the generators commute, this is not the case for non-abelian groups, with the commutation relations for SU(2)$_L$ and SU(3)$_c$

$$[T^i, T^j] = i\varepsilon_{ijk}T^k, \quad [t^a, t^b] = if_{abc}t^c \tag{2.25}$$

where ε_{ijk} is the Levi-Civita symbol and f_{abc} denotes the SU(3) structure constants. Thus it is immediately apparent that due to the dimensionality of the Pauli and Gell-Mann matrices, the generators T^i and t^a have dimensions of 2×2 and 3×3, respectively and thus the transformations $e^{i\theta^i(x)T^i}$ and $e^{i\theta^a(x)t^a}$ are matrices of the same dimensions ($N \times N$ for SU(N)).

As before in the case of the fermionic Dirac Lagrangian, it makes sense to start from the free-field equation for spin-1 vector boson, A_μ ($A = B, G, W$), given by the Proca equation in Eq. 2.9.

$$\mathcal{L}_A = -\frac{1}{4}F_{\mu\nu}F^{\mu\nu} + \frac{1}{2}m^2 A_\mu A^\mu \tag{2.26}$$

where $F_{\mu\nu} = \partial_\mu A_\nu - \partial_\nu A_\mu$ is the field-strength tensor. Gauge invariance allows for the constraint $\partial_\mu A^\mu = 0$ to be imposed, removing one of the four degrees of freedom associated with the four-vector and leaving the two transverse and one longitudinal polarisations. For a massless vector of four-momentum p_μ and polarisation ε^μ, $p_\mu \varepsilon^\mu = 0$, i.e. the polarisation must be perpendicular to the direction of motion, thus eliminating the longitudinal component.

The field transforms as

$$A_\mu \rightarrow A'_\mu = U(x)A_\mu U^{-1}(x) + \frac{i}{g_A}(\partial_\mu U(x))U^{-1}(x) \tag{2.27}$$

where $U(x) = e^{i\theta(x)^a \mathcal{T}^a}$ is the gauge transformation matrix ($a = 1, \ldots, N^2 - 1$) and g_A is the gauge coupling constant, which can be rewritten via the expansion of the infinitesimal transformation $U(x) \approx 1 + i\theta^a(x)\mathcal{T}^a$

$$A^a_\mu \to A'^a_\mu = A^a_\mu - \theta^c(x) f^{abc} A^b_\mu + \frac{1}{g_A}\partial_\mu \theta^a(x) \tag{2.28}$$

Again, the mass term in Eq. 2.26 breaks gauge invariance, meaning that the gauge bosons B, W and G are massless and one can already anticipate that the term proportional to $\partial_\mu \theta(x)$ will be problematic when it comes to the field-strength tensor. To see this, the transformed vector field may be substituted into $F_{\mu\nu}$

$$F^a_{\mu\nu} \to F'^a_{\mu\nu} = \partial_\mu A'^a_\nu - \partial_\nu A'^a_\mu \tag{2.29}$$

$$\Rightarrow F'^a_{\mu\nu} = \partial_\mu A^a_\nu - \partial_\nu A^a_\mu + f^{abc}\left(\partial_\mu \theta^b(x) A^c_\nu - \partial_\nu \theta^b(x) A^c_\mu\right) \tag{2.30}$$

where it can be seen from the second equality that the term proportional to f^{abc} breaks the gauge invariance of the transformed tensor. To circumvent this, a modified $F_{\mu\nu}$ needs to be constructed of the form

$$F_{\mu\nu} = \frac{i}{g_A}[D_\mu, D_\nu] = \partial_\mu A_\nu - \partial_\nu A_\mu - i g_A [A_\mu, A_\nu] \tag{2.31}$$

$$\Rightarrow F^a_{\mu\nu} = \partial_\mu A^a_\nu - \partial_\nu A^a_\mu + g f^{abc} A^b_\mu A^c_\nu. \tag{2.32}$$

The discussion of non-abelian symmetries was thus far generalised to the spin-1 vector field, A_μ, and thus it can be used to write the covariant derivative required for a Lagrangian of the gauge bosons

$$D_\mu = D^G_\mu + D^W_\mu + D^B_\mu - 2\partial_\mu \tag{2.33}$$

$$= \partial_\mu - i g_s G^a_\mu t^a - i g W^i_\mu T^i - i g' B_\mu Y \tag{2.34}$$

with g_s and g denoting the coupling strengths of the fermionic fields to the G_μ and W_μ gauge fields, respectively. Thus, the field strength tensors for the non-abelian

SU(3)$_c$ and SU(2)$_L$ become

$$G^a_{\mu\nu} = \frac{i}{g_s}[D^G_\mu, D^G_\nu] = \partial_\mu G^a_\nu - \partial_\nu G^a_\mu + g_s f^{abc} G^b_\mu G^c_\nu \tag{2.35}$$

$$W^i_{\mu\nu} = \frac{i}{g}[D^W_\mu, D^W_\nu] = \partial_\mu W^i_\nu - \partial_\nu W^i_\mu + g\varepsilon^{ijk} W^j_\mu W^k_\nu. \tag{2.36}$$

For $W_{\mu\nu}$ the structure constant is replaced with the Levi-Civita symbol, in accordance with Eq. 2.25.

In possession of all the necessary ingredients, it is now possible to write down the kinetic part of the gauge boson Lagrangian

$$\mathcal{L}_A = -\frac{1}{4} G^a_{\mu\nu} G^{a\mu\nu} - \frac{1}{4} W^i_{\mu\nu} W^{i\mu\nu} - \frac{1}{4} B_{\mu\nu} B^{\mu\nu} \tag{2.37}$$

where the generator normalisation follows the conventional $\mathrm{Tr}(T^i T^j) = \frac{1}{2}\delta^{ij}$ and $\mathrm{Tr}(t^a t^b) = \frac{1}{2}\delta^{ab}$. This Lagrangian thus describes the free propagation of the gauge fields, but also introduces cubic and quartic terms for the G^a_μ and W^i_μ fields as a result of the field-strength tensors for non-abelian gauge symmetries. Crucially, these three- and four-point interactions are self interactions. Such self-couplings are the reason for the confinement of quarks. The tri- and quadrilinear terms are proportional to f_{abc} and therefore do not exist for abelian gauge symmetries, such as U(1)$_Y$ and thus there are no self-interactions of the B_μ field.

Analogously to how we arrived at $\mathcal{L}_A$, the kinetic part of the scalar Lagrangian may be constructed for a complex scalar field, ϕ, which transforms in the fundamental representation as the spinor Eq. 2.22 and via the introduction of the covariant derivative

$$\mathcal{L}_\phi = \left(D_\mu \phi\right)^\dagger \left(D^\mu \phi\right). \tag{2.38}$$

Due to the field content of D_μ, this Lagrangian contains terms quadratic in the gauge fields. As will be shown in Sec. 2.5.1, these terms are responsible for allowing the physical gauge bosons to acquire masses upon electroweak symmetry breaking (EWSB).

2.5 Mass in the SM

In Sec. 2.4, the gauge-invariant kinetic terms of the fermionic, vector, and scalar Lagrangians were discussed in the context of the Standard Model. However, due to this very gauge invariance, none of these fields contain explicit mass terms. Yet, in reality, most observed particles are massive, meaning that a mechanism must exist to generate their masses while preserving the underlying gauge structure.

In 1961, Sheldon Lee Glashow proposed the $SU(2) \times U(1)$ gauge model [47], which implies the existence of neutral currents in weak interactions, mediated by a yet unknown particle, the Z boson. Based on Glashow's model, a big leap in the theory of weak interactions was made in 1967 in the form of the Glashow-Weinberg-Salam model [48, 49]. In this framework, the original proposal by Glashow was extended to accommodate the mechanism suggested by Peter Higgs, François Englert and Robert Brout in 1964 [50–52]. This mechanism explains how the gauge bosons in the SM acquire a mass upon EW symmetry breaking and is therefore indispensable in creating a theory that is consistent with the real world. In 2013, upon the discovery of the Higgs boson at CERN in the previous year, Higgs and Englert were awarded the Nobel Prize some fifty years after their ground-breaking theoretical proposal.

Therefore, in the Standard Model, mass generation is achieved through electroweak symmetry breaking (EWSB) via the Brout-Englert-Higgs (BEH) mechanism [3], which will be discussed in the following subsection. This will be followed by a detailed identification of the resulting masses.

2.5.1 Higgs Mechanism

It is known from experimental observations, that most fermions are massive and therefore a mass term should include both chiral components, i.e. of the form $m_f \bar{f}_L f_R$. However, we have seen in Sec. 2.2 and Sec. 2.4 that the two chiral components are parts of different representations and hence such a mass term would violate the gauge invariance of the SM. If one was to construct such a mass term, the left-

---

[3] The most precise and formal name is the Brout–Englert–Higgs–Guralnik–Hagen–Kibble mechanism [50–52].

and right-handed chiral doublets and singlets would get mixed. This would violate gauge invariance, as the fields would not transform in consistent representations of the gauge group. To be able to construct Dirac mass terms for the fermions, it is necessary for the gauge symmetry to be broken, but only at lower energies, so that at higher energies the symmetry is preserved. This is known as the Brout-Englert-Higgs (BEH) mechanism, which describes the spontaneous symmetry breaking of the SM gauge symmetry from $SU(3)_C \times SU(2)_L \times U(1)_Y$ to $SU(3)_C \times U(1)_{em}$ through the Higgs boson acquiring a non-zero vacuum expectation value (VEV), where *em* denotes the conserved quantity, in this case the electromagnetic charge.

The Higgs field, Φ, is a complex scalar doublet under $SU(2)_L$ which can be parameterised as

$$\Phi = \begin{pmatrix} \phi^+ \\ \phi^0 \end{pmatrix}, \tag{2.39}$$

where ϕ^+ and ϕ^0 are electrically charged and neutral components, respectively. Altogether there are four degrees of freedom, since both ϕ^+ and ϕ^0 are two-component complex fields of the form $\phi^+ = \phi_A + i\phi_B$ and $\phi^0 = \phi_C + i\phi_D$. Extending the kinetic scalar Lagrangian in Eq. 2.38 with the potential, $V(\Phi)$, the part of the SM Lagrangian relevant to the Higgs sector is then

$$\mathcal{L}_{\text{Higgs}} = \left(D_\mu \Phi\right)^\dagger \left(D^\mu \Phi\right) - V(\Phi) \tag{2.40}$$

where D_μ is the covariant derivative. Denoting the $U(1)_Y$ gauge boson as B_μ and the $SU(2)_L$ gauge bosons as W^a_μ where $a = 1,2,3$ leads to the expressions

$$D_\mu \Phi = \partial_\mu \Phi - ig\frac{\sigma^a}{2} W^a_\mu \Phi + ig' Y_\Phi B_\mu \Phi. \tag{2.41}$$

The potential for the field is of the form

$$V(\Phi) = \mu^2 \Phi^\dagger \Phi + \lambda (\Phi^\dagger \Phi)^2, \tag{2.42}$$

where μ is a mass-like parameter as it appears in the term quadratic in the field and

λ is a coupling constant parameterising the the quartic term, i.e. the self-interaction. Looking at Eq. 2.42, it is noticeable that the sign of μ^2 has far reaching implications. If $\mu^2 > 0$, then $\Phi^\dagger\Phi = |\phi^+|^2 + |\phi^0|^2$ and thus $V(\Phi)$ is positive everywhere due to its upward facing parabolic shape, hence the minimum occurs at $\Phi = 0$. In this case, there is no spontaneous symmetry breaking. Knowing that it must occur, leads to the conclusion that $\mu^2 < 0$ must be realised, leading to a Mexican hat potential. Due to its shape, the ground state of the system occurs at $\Phi \neq 0$, and in fact it turns out, due to the complex nature of the Higgs field, that there is a ring of minima. Which solution the system ends up in is governed by quantum mechanical fluctuations, but due to the degeneracy of the minima, the Higgs will inevitably end up acquiring a non-zero VEV, v. To find the minimum of the potential, the first order derivative of Eq. 2.42 needs to be set equal to zero and solved for the field, yielding:

$$\Phi_0 = \sqrt{\frac{-\mu^2}{2\lambda}} \equiv \frac{v}{\sqrt{2}}. \tag{2.43}$$

So far, the treatment of Φ has been general, leaving all four of its degrees of freedom intact. The two components of Φ may be rewritten as $\phi^+ = \frac{1}{\sqrt{2}}(\phi_1 + i\phi_2)$ and $\phi^0 = \frac{1}{\sqrt{2}}(v + h(x) + i\phi_3)$, with $h(x)$ quantifying the fluctuations of the Higgs boson and x denoting the space-time dependence of this parameter, i.e. h (x-dependence dropped for convenience from here on) represents the physical Higgs boson.. From this parameterisation, it is explicit that there are still four real degrees of freedom: h, ϕ_1, ϕ_2 and ϕ_3 (v is a fixed parameter). Besides the physical Higgs, 3 degrees of freedom remain, known as the Goldstone bosons, which arise upon spontaneous symmetry breaking of a continuous global symmetry, and their number corresponds to the number of broken generators. From observation, it is known that these are not physical states and therefore one may wonder what happens to them. Earlier, in the discussion following Eq. 2.26, it was explained that a spin-1 particle has two polarisations: (two transverse modes) if massless, and three (two transverse and one longitudinal mode) if massive. As will be shown shortly, the three vector bosons of the SM are massive. This explains the fate of the Goldstones – they become the longitudinal polarisations of the physical vector bosons.

Since the Goldstone bosons are unphysical, it is convenient to gauge them away. Hence we adopt the unitary gauge, where the Higgs field is now parameterised as

$$\Phi = \frac{1}{\sqrt{2}} \begin{pmatrix} 0 \\ v+h \end{pmatrix} \tag{2.44}$$

This expression needs to be substituted into the Lagrangian of Eq. 2.40, so we start by computing $D_\mu \Phi$, the action of the covariant derivative on the field, from Eq. 2.41,

$$\begin{aligned} D_\mu \Phi &= \frac{1}{2\sqrt{2}} \begin{pmatrix} 2\partial_\mu + igW_\mu^3 + \frac{1}{2}ig'B_\mu & ig[W_\mu^1 - iW_\mu^2] \\ ig[W_\mu^1 + iW_\mu^2] & 2\partial_\mu - igW_\mu^3 + \frac{1}{2}ig'B_\mu \end{pmatrix} \begin{pmatrix} 0 \\ v+h \end{pmatrix} \\ &= \frac{1}{2\sqrt{2}} \begin{pmatrix} ig(W_\mu^1 - iW_\mu^2)(v+h) \\ (2\partial_\mu - igW_\mu^3 + \frac{1}{2}ig'B_\mu)(v+h) \end{pmatrix} \end{aligned} \tag{2.45}$$

In arriving at the above expression, we made use of the Gell-Mann–Nishijima relation given by Eq. 2.12. Knowing that the lower part of the Higgs doublet is electrically neutral, i.e. $Q = 0$ and that it has $T^3 = -\frac{1}{2}$ leads to a hypercharge of $Y = \frac{1}{2}$. The Hermitian conjugate of the expression in Eq. 2.45 needs to be taken to compute $(D_\mu \Phi)^\dagger$ and thus

$$\begin{aligned} (D_\mu \Phi)^\dagger (D^\mu \Phi) = \frac{1}{2}(\partial_\mu h)(\partial^\mu h) + \frac{1}{8}g^2 (W_\mu^1 + iW_\mu^2)(W^{1\mu} - iW^{2\mu})(v+h)^2 \\ + \frac{1}{8}(gW_\mu^3 - g'B_\mu)(gW^{3\,\mu} - g'B^\mu)(v+h)^2. \end{aligned} \tag{2.46}$$

We define the physical $W_\mu^\pm$ gauge bosons as linear combinations of W_μ^1 and W_μ^2 as

$$W_\mu^\pm = \frac{1}{\sqrt{2}}(W_\mu^1 + iW_\mu^2). \tag{2.47}$$

Using this, the terms quadratic in the fields in the kinetic term $(D_\mu \Phi)^\dagger (D^\mu \Phi)$ may be rewritten as

$$\frac{v^2}{4} g^2 W_\mu^+ W^{-\mu} + \frac{v^2}{8}(gW_\mu^3 - g'B_\mu)^2, \tag{2.48}$$

and from this it is easily read off that the mass of the W boson, m_W is given by

$$m_W = \frac{gv}{2}. \tag{2.49}$$

Now we can turn our attention to the neutral fields Z_μ and A_μ, corresponding to the Z boson and the photon, respectively. We are looking for mass terms of the form $\frac{1}{2}m_X X_\mu X^\mu$, where $X = Z, A$. Both of these are combinations of the neutral fields W^3_μ and B_μ and hence we only focus on the terms quadratic in these fields in Eq. 2.45,

$$\frac{v^2}{8}(gW^3_\mu - g'B_\mu)(gW^{3\mu} - g'B^\mu) = \frac{v^2}{8}\begin{pmatrix} W^3_\mu & B_\mu \end{pmatrix} \underbrace{\begin{pmatrix} g^2 & -gg' \\ -gg' & g'^2 \end{pmatrix}}_{\mathbf{M}} \begin{pmatrix} W^{3\mu} \\ B^\mu \end{pmatrix} \tag{2.50}$$

where $\frac{v^2}{4}\mathbf{M}$ is a squared mass matrix. As can be seen, the matrix is not diagonal, and in fact it is the off-diagonal terms, $-gg'$, that are responsible for the non-zero mixing between the two fields, thus giving rise to the physical fields. The physical fields, Z_μ and A_μ, whose masses we are interested in, are independent physical fields with well defined masses and therefore in their propagating states evolve according to the free particle Hamiltonian. As it describes independent particle fields, the mass matrix associated with this Hamiltonian is diagonal and thus in order to find the masses of the Z boson and the photon, we first need to diagonalise $\mathbf{M}$ and find its eigenvalues, ζ, by solving the characteristic equation $\det(\mathbf{M} - \zeta\mathbb{1}) = 0$, where $\mathbb{1}$ is the 2×2 identity matrix,

$$(g^2 - \zeta)(g'^2 - \zeta) - g^2 g'^2 = 0 \tag{2.51}$$

resulting in the eigenvalues

$$\zeta_1 = 0 \quad \text{and} \quad \zeta_2 = g^2 + g'^2. \tag{2.52}$$

Thus, Eq. 2.50 can be cast in the form

$$\frac{1}{8}v^2 \begin{pmatrix} A_\mu & Z_\mu \end{pmatrix} \begin{pmatrix} 0 & 0 \\ 0 & g^2+g'^2 \end{pmatrix} \begin{pmatrix} A^\mu \\ Z^\mu \end{pmatrix} \tag{2.53}$$

as we know that Z_μ and A_μ must be eigenvectors of $\mathbf{M}_{\text{diag}}$. Keeping in mind the form of the mass term respecting the normalisation convention

$$\frac{1}{2} \begin{pmatrix} A_\mu & Z_\mu \end{pmatrix} \begin{pmatrix} m_A^2 & 0 \\ 0 & M_Z^2 \end{pmatrix} \begin{pmatrix} A^\mu \\ Z^\mu \end{pmatrix} \tag{2.54}$$

and finally

$$m_A = 0 \quad \text{and} \quad m_Z = \frac{1}{2}v\sqrt{g^2+g'^2} \tag{2.55}$$

can be read off. The only thing left now is to find the two normalised eigenvectors corresponding to the two eigenvalues, which will determine the elements of the 2×2 transformation matrix, which relates the physical fields with the gauge fields as

$$\begin{aligned} A_\mu &= \frac{g'W_\mu^3 + gB_\mu}{\sqrt{g^2+g'^2}} \\ Z_\mu &= \frac{gW_\mu^3 - g'B_\mu}{\sqrt{g^2+g'^2}}. \end{aligned} \tag{2.56}$$

It is conventional to define

$$\frac{g'}{g} = \tan\theta_W \tag{2.57}$$

where we have written the couplings associated with the $SU(2)_L$ and $U(1)_Y$ gauge symmetries in terms of θ_W, the Weinberg angle [53], which parameterises the mixing of the gauge fields after symmetry breaking. Using this relation, the physical fields in Eq. 2.56 can be expressed

$$\begin{aligned} A_\mu &= \cos\theta_W B_\mu + \sin\theta_W W_\mu^3 \\ Z_\mu &= -\sin\theta_W B_\mu + \cos\theta_W W_\mu^3. \end{aligned} \tag{2.58}$$

This now allows the expression for the Z boson mass in Eq. 2.55 to be rewritten as

$$m_Z = \frac{1}{2}\frac{g}{\cos\theta_W}v \tag{2.59}$$

and with the use of the W boson mass in Eq. 2.49 yields the relation

$$m_W = m_Z \cos\theta_W. \tag{2.60}$$

This is a simple relation that can be easily tested. In fact it has been extensively verified experimentally [54], which serves as a reassuring confirmation of the realisation of the Higgs mechanism in nature.

Expanding the Higgs potential in Eq. 2.42 results in quadratic terms in the physical Higgs field

$$V(\Phi) \supset \frac{\mu^2 h^2}{2} + \frac{3\lambda v^2 h^2}{2} \tag{2.61}$$

Using the relation

$$v^2 = \frac{-\mu^2}{\lambda} \tag{2.62}$$

this can be simplified to

$$V(\Phi) \supset \lambda v^2 h^2. \tag{2.63}$$

Remembering that the mass term is of the form $\frac{1}{2}m_h^2 h^2$ means that the mass of the Higss boson must be

$$m_h = \sqrt{2\lambda}\,v. \tag{2.64}$$

Solving the expression in Eq. 2.49 of the W boson mass for v and substituting in the measured values of m_W and g yields the experimentally determined VEV

$$v = 246 \text{ GeV}. \tag{2.65}$$

We have thus seen that the original gauge group is broken from $SU(2)_L \times U(1)_Y \to U(1)_{em}$. It turns out that a subgroup of the original gauge group, $U(1)_{em}$, corresponding to QED, remains unbroken, and hence its gauge boson, the photon, does not acquire mass. Knowing that the Higgs does not have any colour charge means that $SU(3)_c$, the group corresponding to QCD also remains unbroken and therefore the mediators of the strong force, the gluons, also remain massless. Thus, the gauge group of the SM undergoes the change

$$SU(3)_c \times SU(2)_L \times U(1)_Y \to SU(3)_c \times U(1)_{em} \tag{2.66}$$

upon spontaneous symmetry breaking via the BEH mechanism.

2.5.2 Fermion Masses

In the previous section it was shown that the BEH mechanism responsible for spontaneous symmetry breaking is responsible for giving mass to the $W^{\pm}$ and Z bosons, but so far the masses of the fermions have not been discussed. The naive approach is to construct Dirac mass terms using the the bare masses of the chiral fermions of the form

$$-m\bar{\psi}\psi = -m\left(\bar{\psi}_L\psi_R + \bar{\psi}_R\psi_L\right) \tag{2.67}$$

where $\psi_{L/R}$ denotes a left/right-handed fermion. It is immediately apparent, that the bare Dirac mass term in Eq. 2.67 above does not respect the gauge symmetry $SU(2)_L \times U(1)_Y$, since the doublets and singlets transform differently under $SU(2)$. The solution to this problem is to generate mass terms for the fermions via the interaction of two chiral fermionic components with the scalar Higgs field, instead of constructing a bare mass term. This will in general result in the Yukawa part of the SM Lagrangian taking the form

$$\mathcal{L}_{\text{Yukawa}} = -\sum_{\ell=1}^{3} y_\ell \bar{L}^\ell \Phi \ell_R - \sum_{i,j=1}^{3} y^u_{ij} \bar{Q}_L{}^i \tilde{\Phi} u_R^j - \sum_{i,j}^{3} y^d_{ij} \bar{Q}_L{}^i \Phi d_R^j + \text{h.c.}. \tag{2.68}$$

The first term is associated with the leptonic sector. The scalar doublet Φ is as defined in Eq. 2.39, whose coupling to L^ℓ and ℓ is parameterised by the Yukawa couplings, y_ℓ. The second and third terms in $\mathcal{L}_{\text{Yukawa}}$ refer to the up and down quark sectors, respectively, with $\tilde{\Phi} = i\sigma_2\Phi^*$ denoting the charge-conjugate of Φ. Focusing purely on the leptonic term and $\ell = e$ i.e. considering the first generation fermions

$$\mathcal{L}^{e}_{\text{Yukawa}} = -y_e \left[\left(\begin{array}{cc} \bar{\nu}_e & \bar{e} \end{array} \right)_L \left(\begin{array}{c} \phi^+ \\ \phi^0 \end{array} \right) e_R + \bar{e_R} \left(\begin{array}{cc} \phi^{+*} & \phi^{0*} \end{array} \right) \left(\begin{array}{c} \nu_e \\ e \end{array} \right)_L \right] . \tag{2.69}$$

Let us examine whether this expression respects the $SU(2)_L \times U(1)_Y$ gauge symmetry. It is easy to see that both $\bar{L}^e \Phi e_R$ and $(\bar{L}^e \Phi e_R)^\dagger = \bar{e}_R \Phi^\dagger L^e$ form $SU(2)_L$ singlets, which are of course invariant under the group. Now it also needs to be verified whether the above expression respects the $U(1)_Y$ part of the gauge group. The hypercharge of L^e is $Y = -\frac{1}{2}$, thus for $\bar{L}^e$ it is $Y = \frac{1}{2}$, while for Φ it is $Y = \frac{1}{2}$ and $Y = -1$ for e. Hence, the combined hypercharge of the terms is zero, which means $U(1)_Y$ is respected. Thus, we have seen that the symmetry of the $SU(2)_L \times U(1)_Y$ gauge group is not violated and hence the interaction terms constructed between the fermions and the Higgs are gauge invariant, as required.

Upon spontaneous symmetry breaking, the Higgs doublet in the unitary gauge is given by Eq. 2.44 and therefore Eq. 2.69 can be rewritten as

$$\mathcal{L}^{e}_{\text{Yukawa}} = -y_e \frac{v}{\sqrt{2}} (\bar{e_L} e_R + \bar{e_R} e_L) - y_e \frac{h}{\sqrt{2}} (\bar{e_L} e_R + \bar{e_R} e_L). \tag{2.70}$$

Since $\bar{\psi}\psi = \bar{\psi_L}\psi_R + \bar{\psi_R}\psi_L$, this becomes

$$\mathcal{L}^{e}_{\text{Yukawa}} = -y_e \frac{v}{\sqrt{2}} \bar{e}e - y_e \frac{h}{\sqrt{2}} \bar{e}e. \tag{2.71}$$

It is apparent, that the first term is exactly of the desired form of Eq. 2.67, but now arises from gauge invariance as opposed to the naive approach of constructing bare fermion masses. Thus, the mass of the electron is then read off to be

$$m^e = \frac{y_e}{\sqrt{2}} v. \tag{2.72}$$

The value of the Yukawa coupling parameterising the strength of the coupling of the electron to the Higgs field is not predicted by theory, but it can be determined experimentally from the measured electron mass and the known value of the VEV

$$y_e = \sqrt{2}\frac{m^e}{v}. \tag{2.73}$$

The second term in Eq. 2.71 describes the coupling between the electron and the Higgs boson.

It is easy to see from Eq. 2.44 and Eq. 2.69 that because the upper component of the Higgs doublet has no VEV, only the lower component of the left-handed $SU(2)_L$ doublets will receive a mass and therefore the SM predicts neutrinos to be massless. From experiments it is known that neutrinos have a small but non-zero mass, and their possible mass generation mechanism will be explored in Sec. 3.5. Similarly, in the case of the upper component of the quark doublets, the left-handed up-type quarks in the upper component cannot receive a mass. To circumvent this, instead of Φ, its charge-conjugate, $\tilde{\Phi}$ is used in Eq. 2.68 to construct the gauge invariant Lagrangian term. The conjugate of the doublet in Eq. 2.39 is given by

$$\tilde{\Phi} = i\sigma_2\Phi^* = \begin{pmatrix} \phi^{0*} \\ -\phi^- \end{pmatrix} = \frac{1}{\sqrt{2}}\begin{pmatrix} \phi_3 - i\phi_4 \\ -\phi_1 + i\phi_2 \end{pmatrix}, \tag{2.74}$$

which can be shown to transform in exactly the same way as the $SU(2)_L$ doublet. Keeping in mind that the hypercharge of $\tilde{\Phi}$ is opposite that of Φ, it is straightforward to verify that the terms concerning the u-type quarks in Eq. 2.68 are gauge invariant as they should be.

It has thus been explored in this section that all fermions (apart from the neutrinos, which will be discussed separately) acquire their masses via their interactions with the Higgs field, parameterised by their respective Yukawa couplings.

Something that has not been explicitly acknowledged so far is that fact that the couplings y_ℓ, y^u and y^d, in Eq. 2.68, are 3×3 matrices, since they contain information about the couplings of three generations of fermions. A priori, the leptonic Yukawa matrix, y_ℓ, could be non-diagonal, but since lepton flavour among the charged leptons is conserved in the SM (with massless neutrinos), only the diagonal elements are non-zero. The two mass matrices, $m^u = \frac{y^u}{\sqrt{2}}v$ and $m^d = \frac{y^d}{\sqrt{2}}v$, associated with the quark terms, however, need more careful examination. Since there is nothing forbidding mixing within the quark sector, these matrices are in general non-diagonal. In fact, such mixing is indeed realised in nature, simply due to the fact that the flavour eigenstates, in which the quark states interact, are not equivalent to the mass eigenstates. Hence, the mass matrices m^u and m^d need to be diagonalised to find the mass eigenstates, which is achieved via bi-unitary transformations of the form

$$\begin{aligned} D^u &= U_L^{u\dagger} m^u U_R^u = \mathrm{diag}(m_u, m_c, m_t) \\ D^d &= U_L^{d\dagger} m^d U_R^d = \mathrm{diag}(m_d, m_s, m_b) \end{aligned} \tag{2.75}$$

and where $U_{L/R}^{d/u}$ are unitary matrices. Hence, the mass terms for the quarks

$$-\left(\sum_{i,j}^{3} \bar{u_L}^i m^u_{ij} u_R^j + \sum_{i,j}^{3} \bar{d_L}^i m^d_{ij} d_R^j\right) + \text{h.c.} \tag{2.76}$$

upon the substitution of Eq. 2.75 for the non-diagonal mass matrices becomes

$$-\sum_{i,j}^{3} \bar{u_L}^i \left(U_L^u D^u U_R^{u\dagger}\right)_{ij} u_R^j + \text{h.c.} = -\sum_{a}^{3} \bar{u_L}'^a D^u_{aa} u_R'^a \tag{2.77}$$

and

$$-\sum_{i,j}^{3} \bar{d_L}^i \left(U_L^d D^d U_R^{d\dagger}\right)_{ij} d_R^j + \text{h.c.} = -\sum_{a}^{3} \bar{d_L}' a D^d_{aa} d_R'^a \tag{2.78}$$

for up- and down-type quarks, respectively. In arriving at the latter equalities, we have made use of the fact that the up- and down-type doublets as well as the up- and down-type singlets in the flavour basis consist of a linear superposition of mass eigenstates, weighted by the unitary matrices parameterising the mixing, i.e.

$$\begin{aligned} u_L'^a &= (U_L^{u\dagger})_{ai} u_L^i, \quad d_L'^a = (U_L^{d\dagger})_{ai} d_L^i \\ u_R'^a &= (U_R^{u\dagger})_{ai} u_R^i, \quad d_R'^a = (U_R^{d\dagger})_{ai} d_R^i \end{aligned} \tag{2.79}$$

where u_L', d_L', u_R' and d_R' are the mass eigenstates for the four quark types and the unprimed fields are the unphysical fields in the interaction basis.

It is now in order to check how the field redefinitions in Eq. 2.79 affect the interactions of the quarks in the electroweak gauge bosons. To do that, one needs to compute the covariant derivatives with the correct hypercharges substituted into the expression in Eq. 2.18. Focusing on the charged-current part of the Lagrangian involving the fields W_μ^1 and W_μ^2 (and hence $W^\pm$ via the relations shown in Eq. 2.47) results in

$$\mathcal{L}_{CC} = -\frac{g}{\sqrt{2}}\sum_i(\bar{u}_{iL}\gamma^\mu W_\mu^+ d_{iL} + \bar{d}_{iL}\gamma^\mu W_\mu^- u_{iL}) \tag{2.80}$$

which can be rewritten as

$$\mathcal{L}_{CC} = -\frac{g}{\sqrt{2}}\sum_i(\bar{u}'_{iL}\gamma^\mu W_\mu^+ U_L^{u\dagger} U_L^d d'_L + \bar{d}'_{iL}\gamma^\mu W_\mu^- U_L^{d\dagger} U_L^u u'_L) \tag{2.81}$$

and from this expressions we identify

$$V_{CKM} = U_L^{u\dagger} U_L^d \tag{2.82}$$

as the Cabibbo–Kobayashi–Maskawa (CKM) matrix [55, 56]. The 3×3 unitary CKM matrix can be presented in a variety of ways, but the most common parameterisation is

$$V_{CKM} = \begin{pmatrix} c_{12}c_{13} & s_{12}c_{13} & s_{13}e^{-i\delta_{CP}} \\ -s_{12}c_{23} - c_{12}s_{23}s_{13}e^{i\delta_{CP}} & c_{12}c_{23} - s_{12}s_{23}s_{13}e^{i\delta_{CP}} & s_{23}c_{13} \\ s_{12}s_{23} - c_{12}c_{23}s_{13}e^{i\delta_{CP}} & -c_{12}s_{23} - s_{12}c_{23}s_{13}e^{i\delta_{CP}} & c_{23}c_{13} \end{pmatrix} \tag{2.83}$$

where the usual shorthand notation $c_{ij} \equiv \cos\theta_{ij}$ and $s_{ij} \equiv \sin\theta_{ij}$ has been used. There are thus four parameters parameterising V_{CKM}: three angles, $\theta_{12}, \theta_{13}, \theta_{23}$ and one phase, δ_{CP}. If $\delta_{CP} = 0$ or $\delta_{CP} = \pi$, then the $e^{i\delta_{CP}}$ is real and CP is conserved. However, for any other values $e^{i\delta_{CP}}$ will be complex and thus CP-violating effects will occur. This means that processes forwards and backwards in time do not have the same rate, which results in the particles and antiparticles, i.e. quarks and antiquarks being distinguishable from each other.

Since the charged-current interactions involve the fields W_μ^1 and W_μ^2, the relevant Pauli matrices are σ^1 and σ^2, whose only non-zero entries are found along the off-diagonal. Thus, the covariant derivative mixes the upper and lower components of the doublet field and we see that due to the nature of the charged-current which couples directly to the left-handed doublet, the up- and down-type quarks get coupled and hence quark mixing arises.

The neutral-current (NC), on the other hand, involves the fields W_μ^3 and B_μ only and hence the only relevant Pauli matrix is the diagonal σ^3. Since all of its off-diagonal entries are zero, there are no cross-flavour terms. Due to this, the mixing matrices disappear due to their unitarity $U_L^\dagger U_L = \mathbb{1}$ and $U_R^\dagger U_R = \mathbb{1}$ and the effect of the quark field redefinitions has no effect.

2.6 Low-energy SM Particle Content

The gauge symmetries underpinning the SM were discussed in Sec. 2.4 followed by an overview of the spontaneous breaking of the EW symmetry, leading to mass generation. At low energies, post-EWSB, the SM consists of 1 scalar, 12 fermions and 12 gauge bosons. The single scalar is the Higgs boson, which acquires its mass from the potential via self-interaction.

	$\mathrm{SU}(3)_c$	Q	Spin	Mass
u,c,t	**3**	$+\frac{2}{3}$	$\frac{1}{2}$	$\neq 0$
d,s,b	**3**	$-\frac{1}{3}$	$\frac{1}{2}$	$\neq 0$
e,μ,τ	**1**	-1	$\frac{1}{2}$	$\neq 0$
ν_e,ν_μ,ν_τ	**1**	0	$\frac{1}{2}$	$= 0$
G	**8**	0	1	$= 0$
$W^\pm$	**1**	± 1	1	$\neq 0$
Z	**1**	0	1	$\neq 0$
A	**1**	0	1	$= 0$
h	**1**	0	0	$\neq 0$

Table 2.3: Table summarising the low-energy SM particle content, including their representations under $\mathrm{SU}(3)_c$, their EM charges under $\mathrm{U}(1)_{em}$ (Q), their spin, and whether they are massive.

The 12 fermions comprise of 2 quarks and 2 leptons over 3 generations. The two quark types are the up- and down-quarks with an electric charge of $2/3$ and $-1/3$, respectively. The second and third generation of up-type quarks are the charm (c) and top (t), and for the down-type quarks the strange (s) and bottom (b). Each lepton generation comprises of a charged lepton and a neutrino, with electric charges of -1 and 0, respectively. The three generations of charged leptons are the electron (e), muon (μ) and tau (τ), and the electron- (ν_e), muon- (ν_μ) and tau- (ν_τ) neutrinos for the neutral leptons. Of all the fermions, only the three neutrinos are massless in the SM, with the masses of the others arising from the Yukawa interactions with the Higgs field. Quarks possess colour charge and thus interact via all fundamental forces, including the strong force. Leptons on the other hand only interact through the electromagnetic and weak forces, while neutrinos only participate in the weak interaction.

The complete particle content of the SM at low energies is summarised in Table 2.3. The SU(3)$_c$ gauge symmetry gives rise to 8 gauge bosons that mediate the strong force, and which are massless due to the unbroken nature of the gauge group. The mediator of the EM force is the photon, which similarly remains massless due to the unbroken residual symmetry U(1)$_{em}$. Finally, there are the three gauge bosons of the weak force: the Z and $W^\pm$ bosons. All three are massive as a result of EWSB. The W bosons – mediating the CC interactions – are linear combinations of the W_μ^1 and W_μ^2 fields and are therefore purely descendants of the spontaneously broken SU(2)$_L$. As such, they only act on SU(2)$_L$ doublets and thus CC interactions are maximally parity violating. The Z boson on the other hand is a combination of the SU(2)$_L$ W_μ^3 and the U(1)$_Y$ symmetries and thus couples to both left- and right-handed particles. Although not maximally parity violating, NC interactions are not completely chirally symmetric, since they couple to right-handed fields more weakly than to left-handed ones.

2.7 Discrete Symmetries

Besides the continuous symmetries of the SM dictated by the product of its gauge groups, there also exist three fundamental discrete transformations: charge-conjugation (C), parity inversion (P) and time inversion (T). The behaviour of fields under these discrete transformations has far reaching consequences both for the SM, and for BSM theories.

Charge-conjugation involves transformation of all charges by changing their signs. It should be noted that besides the electric charge, there are other charges associated with the other forces. Charge-conjugation transforms a fermionic field according to

$$\Psi^c = \eta_c C \bar{\Psi}^T \tag{2.84}$$

where $\bar{\Psi}$ is the usual Dirac adjoint, η_c is an arbitrary factor whose value depends on the representation and convention used and C is the charge-conjugation matrix satisfying

$$C\gamma^\mu C^{-1} = -(\gamma^\mu)^T. \tag{2.85}$$

Charge conjugation changes a particle into its antiparticle, but preserves chirality. [4] Therefore, since the weak interaction only couples to left-handed particles, it maximally violates charge-conjugation symmetry, due to the V-A structure of the interaction, while QED and QCD interactions are C symmetry conserving.

Parity is a spacetime symmetry and the associated transformation involves the flipping of the signs of all the spatial coordinates, while keeping the time unchanged, i.e.

$$(t,x,y,z) \xrightarrow{P} (t,-x,-y,-z). \tag{2.86}$$

This directly implies

$$P\gamma^\mu P^{-1} = \begin{cases} \gamma^0 & \text{for } \mu = 0 \\ -\gamma^i & \text{for } i = 1,2,3 \end{cases} \tag{2.87}$$

---

[4] It should be noted, that although not directly chirality flipping, charge conjugation interchanges the transformation properties of doublets and singlets under SU(2)$_L$.

and therefore

$$P\gamma^5 P^{-1} = i\gamma^0 \left(-\gamma^1\right)\left(-\gamma^2\right)\left(-\gamma^3\right) = -\gamma^5. \tag{2.88}$$

Looking at the chirality projections in Eq. 2.2 clearly means that a parity transformation necessarily flips chirality. This in turn means that similarly to C, the weak interactions are parity symmetry violating, since they treat left- and right-handed fields asymetrically, as the vector and axial-vector parts transform differently. This is not the case for QED and QCD, which both have purely vector structures, whose sign changes are compensated by the transformations of the vector boson fields (the photon and the gluons, respectively), which transform in an identical way.

The final discrete symmetry is time reversal, which is a spacetime symmetry like parity, but differs in that its associated transformation flips the sign of the temporal component, rather than the spatial ones

$$(t,x,y,z) \xrightarrow{T} (-t,x,y,z). \tag{2.89}$$

Such a transformation thus has a different effect on the time- and space-like gamma matrices

$$T\gamma^\mu T^{-1} = \begin{cases} -\gamma^0 & \text{for } \mu = 0 \\ \gamma^i & \text{for } i = 1,2,3 \end{cases} \tag{2.90}$$

and therefore the γ^5 matrix is transformed as

$$T\gamma^5 T^{-1} = i\left(-\gamma^0\right)\gamma^1\gamma^2\gamma^3 = -\gamma^5, \tag{2.91}$$

explicitly showing that time reversal, just like parity, flips chirality. Conservation of T-symmetry means that the rate of processes is the same regardless of the direction of time.

The combined CP, which is the product of C and P, is violated in the SM quark sector by the CP-phase in the CKM matrix, δ_{CP}, in Eq. 2.83 and therefore makes the weak interaction CP-violating. According to the CPT theorem, any quantum field theory that is Lorentz invariant and unitary, is invariant under simultaneous transformations of C, P and T. It follows from this, that if the combined CP symmetry is violated, then T symmetry must also not be conserved in order to ensure CPT invariance. Since the weak force violates C and P separately, and also violates the combined CP, it must also violate T symmetry. This is crucial, because non-conservation of T may partially explain the matter-antimatter asymmetry in the universe.

There also exist accidental symmetries, which rather than being fundamental, happen to emerge as a result of gauge invariance and renormalizability. These include baryon number, B, and the individual lepton flavour numbers, L_e, L_μ and L_τ (naturally lepton flavour violation is imminent for massive neutrinos.)

2.8 Status of the SM

The SM is arguably one of the most successful and complete frameworks of fundamental physics, able to accurately describe the majority of particle physics observations. It is derived from first principles and thus is based on profound mathematical foundations that ensure the fundamental properties of unitarity (probabilities adding up to 1) and Lorentz invariance. Many predictions of the SM are in remarkable agreement with experimental measurements, and it predicts its entire particle content based on the gauge theories underpinning it, with several of these particles having been anticipated before their actual discovery.

Despite the established and continued success of the SM, there are issues it is unable to address. Here we mention an incomplete list of some of the biggest challenges the theory is facing. The first of these are the 19 free parameters, whose number and precise values seem *ad hoc* and arbitrary. Moreover, this unsettlingly large number of free parameters needs to be further increased if one wishes to extend the SM to address one or more of the other problems mentioned below.

Secondly, another glaring issue is the exclusion of gravity from the theory, which is the only fundamental force of nature not described by the SM. Although there are ongoing efforts towards unification, currently the mathematical challenge of a quantised and renormalizable theory of gravity has not been surmounted.

There is also the issue known as the hierarchy problem, which is related to the Higgs boson mass. Any bare mass will get quantum corrections from interactions with virtual particles, in the form of loop corrections, which affect physical observables, such as the effective mass. These quantum loop corrections to the bare mass are quadratically divergent in the case of scalar particles [5], yet the measured mass is of the order of the EW scale, i.e. profoundly small compared to the Planck scale – a disturbingly unnatural result. This is caused by extremely precise cancellations, giving the impression of severe intentionality and fine-tuning.

Another arbitrary characteristic of the SM is the three generations of fermions, for which there seems to be no good reason or explanation. Additionally, the flavour structures observed in the quark, charged-lepton, and neutrino sectors exhibit different hierarchies and span many orders of magnitude in their masses and mixing angles, with no apparent underlying explanation offered by the SM.

Cosmology also presents the SM with challenges. Primarily, the existence of structure in the Universe, and therefore humanity, is the product of the abundance of matter over antimatter. Although the SM contains sources of CP violation, they are far too small to generate the observed asymmetry, which remains unexplained. In fact, there is nothing forbidding CP violation in QCD, yet experiments constrain such CP-violating terms to be extremely small — this is known as the strong CP problem. Furthermore, the existence of dark matter and dark energy is well established experimentally, yet the SM offers no explanations or particle candidates for these observed phenomena.

Finally, the SM predicts massless neutrinos, but this is contradicted by oscillation experiments. The absolute values of these masses, their origin, and whether there are other neutrino species – perhaps right-handed ones – remain open questions that cannot be answered by the SM.

---

[5] For fermions, in the massless limit the left- and right-handed fields connected by the mass decouple, and a new symmetry, chiral symmetry, emerges and protects the bare mass from such loop corrections.

It is clear that although the SM is a very successful theory, it is incomplete. There is general agreement about the existence of a more complete theory, of which the SM is a low-energy effective remnant. What this unified theory is, remains currently unknown.

Chapter 3

Neutrino Theory

The focus of this dissertation is BSM neutrino phenomenology and therefore this chapter is dedicated to the properties of this elusive particle. In the previous chapter we have seen that although the SM is an incredibly impressive framework, it suffers from a number of maladies, implying that the land lying beyond the SM is a rich and fertile one. Of these — in line with the topic of this thesis — we highlight the fact that neutrinos are treated as massless by the SM, but this prediction is in stark contrast with the experimental confirmation of neutrino oscillation, which implies that these particles are indeed massive. Consequently, a new and different description of neutrinos must be found, one that includes and explains their mass. There are many possible routes that one can take in search of this theory, but whichever path one takes, it will inevitably lead outside of the well-known SM and into the unfamiliar territory beyond it. In order to discuss such new physics however, it is instructive to first review the properties of the SM active neutrinos in order to establish the context and lay the basis for elevating the discussion beyond the SM.

Hence, we begin by describing and discussing the phenomenon of neutrino oscillation from a theoretical point of view in Sec. 3.1, before turning our attention to the experimental endeavors which confirmed this behaviour and the current status of oscillation experiments in Sec. 3.2. This naturally leads us to a discussion of the probes available to measure neutrino masses in Sec. 3.3. We then consider the hypothetical sterile neutrino in Sec. 3.4. In Sec. 3.5 we discuss the possible mass generation mechanisms available to the SM neutrino. We conclude the chapter with a review of the Effective Field Theory (EFT) framework in Sec. 3.6, which will serve as the foundation to our discussion of sterile neutrinos in beta-decay in Chapter 4 and in the future FCC-ee collider in Chapter 5.

3.1 Neutrino Oscillations

3.1.1 In Vacuum

Neutrino oscillations between neutrinos and antineutrinos were initially suggested by Pontecorvo in 1957 [57, 58], motivated by kaon oscillations. At the time, however, this proposal relied on the additional assumption of lepton number violation and lacked a broader theoretical framework, which limited its immediate phenomenological impact. In 1962 – in the same year as the discovery of the muon neutrino – Maki, Nakagawa and Sakata put forward the idea of neutrino flavour mixing [59], based on the misalignment of neutrino mass and flavour eigenstates. This served as the basis for Pontecorvo's proposal of neutrino flavour oscillations in his 1967 paper [60].

Oscillations are a quantum mechanical phenomenon that arises from mass mixing and leads to a macroscopic effect. Neutrino mass and flavour eigenstates do not coincide, therefore each flavour state is a different superposition of mass states. Neutrinos are produced in flavour states during interactions, but they propagate in their mass states, i.e. the solutions to the free particle Hamiltonian. Upon detection, the flavour of the neutrinos is inferred from the flavour of its associated charged lepton accompanying it. The existence of a mass splitting between the mass states leads to slightly different propagation speeds and thus gives rise to the phenomenon of oscillation [61–63].

Let us define the neutrino flavour eigenstates as

$$|\nu_\alpha\rangle = \sum_i U_{\alpha i}|\nu_i\rangle \tag{3.1}$$

where $\alpha = e, \mu, \tau$ denote the three possible neutrino flavours, $i = 1, 2, 3$ denote the mass eigenstates and $U_{\alpha j}$ are elements of the unitary lepton mixing matrix, known as the Pontecorvo–Maki–Nakagawa–Sakata (PMNS) matrix

$$U_{\text{PMNS}} = \begin{pmatrix} c_{12}c_{13} & s_{12}c_{13} & s_{13}e^{-i\delta_{CP}} \\ -s_{12}c_{23} - c_{12}s_{13}s_{23}e^{i\delta_{CP}} & c_{12}c_{23} - s_{12}s_{13}s_{23}e^{i\delta_{CP}} & c_{13}s_{23} \\ s_{12}s_{23} - c_{12}s_{13}c_{23}e^{i\delta_{CP}} & -c_{12}s_{23} - s_{12}s_{13}c_{23}e^{i\delta_{CP}} & c_{13}c_{23} \end{pmatrix}, \tag{3.2}$$

where $c_{ij} = \cos\theta_{ij}$ and $s_{ij} = \sin\theta_{ij}$. Analogously to the CKM matrix describing mixing in the quark sector, the PMNS matrix quantifies the degree of mixing between different flavours of neutrinos. However, unlike the CKM matrix which is nearly diagonal, the PMNS matrix has large off-diagonal entries, producing observable oscillations over macroscopic distances. From the expression in Eq. 3.1, it is clear that neutrino flavour states are to be treated as admixtures of the mass states, which in turn are defined as

$$|\nu_i\rangle = \sum_\alpha U^*_{\alpha i}|\nu_\alpha\rangle \tag{3.3}$$

obtained through rotation of Eq. 3.1 to the mass basis. The mass states are eigenstates of the Hamiltonian, i.e.

$$H|\nu_i\rangle = E_i|\nu_i\rangle \tag{3.4}$$

for free neutrinos in vacuum. As will be discussed in Sec. 3.1.2, this is modified in matter. In the above expression E_i is the energy eigenvalue of the neutrino state i, defined in the familiar fashion

$$E_i = \sqrt{\mathbf{p}^2 + m_i^2} = |\mathbf{p}|\sqrt{1 + \left(\frac{m_i}{|\mathbf{p}|}\right)^2} \tag{3.5}$$

Since neutrino masses are negligible compared to their typical energies in all observed processes, they are effectively highly relativistic., i.e. $E_i \gg m_i$. Therefore, Eq. 3.5 can be Taylor expanded in $m_i/|\mathbf{p}|$, yielding

$$E_i \simeq E + \frac{m_i^2}{2E} \tag{3.6}$$

to first order, where the substitution for the average neutrino energy $E = |\vec{p}|$ was used. The neutrino mass states are chosen so that they obey orthonormality, i.e.

$$\langle \nu_i | \nu_j \rangle = \delta_{ij} \tag{3.7}$$

Due to the quantum mechanical treatment of the neutrino states, the time evolution of the mass states can be written as

$$|\nu_i(t)\rangle = e^{-iE_i t} |\nu_i\rangle \tag{3.8}$$

where t is time and $|\nu_i(0)\rangle = |\nu_\alpha\rangle$ at $t = 0$, i.e. the initial state is a specific flavour. Using Eq. 3.1 and Eq. 3.8, the time evolution of the flavour eigenstates can be written as

$$|\nu_\alpha(t)\rangle = \sum_i U_{\alpha i} |\nu_i(t)\rangle \tag{3.9}$$

We have seen that each flavour eigenstate is a superposition of three different mass eigenstates m_i and thus three different energies E_i. As seen from Eq. 3.8, this superposition causes the time evolution to depend on more than just a simple exponential phase, which ultimately results in the oscillatory behaviour of neutrino flavour states.

To obtain a mathematical expression for the probability of oscillation, we start from the quantum mechanical definition of an amplitude of transition from an initial state A, to a final state B, given by

$$\mathcal{A}_{\phi_A \to \phi_B} \equiv \langle \phi_B | \phi_A \rangle. \tag{3.10}$$

The transition probability is then given by the square of the absolute value of the amplitude

$$\mathcal{P}_{\phi_A \to \phi_B} = |\mathcal{A}_{\phi_\mathcal{A} \to \phi_\mathcal{B}}|^2 = |\langle \phi_B | \phi_A \rangle|^2. \tag{3.11}$$

Analogously then, the probability of neutrino oscillation from flavour α to flavour

β is given by

$$\mathcal{P}_{\nu_\alpha \to \nu_\beta} = |\langle \nu_\beta | \nu_\alpha \rangle|^2. \tag{3.12}$$

Now we can transform the ket in Eq. 3.1 into a bra, becoming

$$|\nu_\beta\rangle = \sum_j U_{\beta j} |\nu_j\rangle \Rightarrow \langle \nu_\beta| = \sum_j U^*_{\beta j} \langle \nu_j| \tag{3.13}$$

and hence the probability can be expressed as

$$\begin{aligned} \mathcal{P}_{\nu_\alpha \to \nu_\beta} &= \left| \sum_{i,j} U_{\alpha i} U^*_{\beta j} e^{-iE_i t} \langle \nu_j | \nu_i \rangle \right|^2 = \left| \sum_i U_{\alpha i} U^*_{\beta i} e^{-iE_i t} \right|^2 \\ &= \left[\sum_i U_{\alpha i} U^*_{\beta j} \exp\left(-iE_i t\right) \right] \times \left[\sum_j U^*_{\alpha j} U_{\beta i} \exp\left(iE_j t\right) \right] \end{aligned} \tag{3.14}$$

where the second equality was obtained by using the orthonormality in Eq. 3.7. Now with the use of Eq. 3.6 and the assumption that the neutrinos are ultra-relativistic, i.e. $L = ct \simeq t$, where L is the distance traveled and $c = 1$, we obtain

$$\mathcal{P}_{\nu_\alpha \to \nu_\beta} = \sum_{i,j} U_{\alpha i} U^*_{\beta i} U^*_{\alpha j} U_{\beta j} \exp\left(-i \frac{\Delta m^2_{ij}}{2E} L \right), \tag{3.15}$$

where $\Delta m^2_{ij} \equiv m^2_{\nu_i} - m^2_{\nu_j}$, the squared mass difference, has been defined. It is understood that the summation over the indices is only performed for $i > j$, i.e. the quantity Δm_{ij} is positive. We can clearly see from this expression, that the oscillation probability depends on the mass difference squared, therefore if the neutrino masses are equal, $\Delta m^2_{ij} = 0$, thus the exponential is always equal to 1, and Eq. 3.15 reduces to $\mathcal{P}_{\nu_\alpha \to \nu_\beta} = \delta_{\alpha\beta}$ by unitarity of U [1]. For $\alpha = \beta$, this implies $\mathcal{P}_{\nu_\alpha \to \nu_\alpha} = 1$, i.e. the flavour remains unchanged and for $\alpha \neq \beta$ $\mathcal{P}_{\nu_\alpha \to \nu_\beta} = 0$, i.e. oscillation cannot occur. These results follow from the unitarity of the PMNS matrix. The case when $\alpha \neq \beta$ is usually termed *transition probability*, while $\alpha = \beta$ is called the *survival probability*.

---

[1] For $\Delta m^2_{ij} = 0$, $\exp\left(-i\frac{\Delta m^2_{ij}}{2E} L\right) = 1$, so $\mathcal{P}_{\nu_\alpha \to \nu_\beta} = \sum_{i,j} U_{\alpha i} U^*_{\beta i} U^*_{\alpha j} U_{\beta j} = |U_{\alpha i} U^*_{\beta j}|^2 = \delta_{\alpha\beta}$, where in the last equality we made use of the unitarity of U.

It can aid the discussion to express Eq. 3.15 in terms of its real and imaginary components. To do this, we make use of the trigonometric identity

$$e^{iA} = \cos A + i\sin A = 1 - 2\sin^2\frac{A}{2} + i\sin A \tag{3.16}$$

and we remember that $\Re[a] = \frac{1}{2}(a + a^*)$. Then after some algebra, we arrive at the result

$$\begin{aligned}\mathcal{P}_{\nu_\alpha \to \nu_\beta} = \delta_{\alpha\beta} &- 4\sum_{i>j}\Re[M_{\alpha\beta,ij}]\sin^2\left(\frac{\Delta m^2_{ij}L}{4E}\right) \\ &+ 2\sum_{i>j}\Im[M_{\alpha\beta,ij}]\sin\left(\frac{\Delta m^2_{ij}L}{2E}\right),\end{aligned} \tag{3.17}$$

where $M_{\alpha\beta,ij} = U_{\alpha i}U^*_{\beta i}U^*_{\alpha j}U_{\beta j}$.

Irrespective of the fraction of neutrinos that change flavour, the total number of particles is conserved, and therefore summing over the flavours at the time of production and at the time of detection equals 1, i.e.

$$\sum_{\alpha}\mathcal{P}_{\nu_\alpha \to \nu_\beta} = \sum_{\beta}\mathcal{P}_{\nu_\alpha \to \nu_\beta} = 1. \tag{3.18}$$

Using this conservation property, one can obtain an analogous expression to Eq. 3.17 for the $\alpha = \beta$ case. Since the total number of particles remains unchanged

$$\mathcal{P}_{\nu_\alpha \to \nu_\alpha} = 1 - \sum_{\alpha \neq \beta}\mathcal{P}_{\nu_\alpha \to \nu_\beta} \tag{3.19}$$

and therefore

$$\mathcal{P}_{\nu_\alpha \to \nu_\alpha} = 1 - 4\sum_{i>j}|U_{\alpha i}U^*_{\alpha j}|^2\sin^2\left(\frac{\Delta m^2_{ij}L}{4E}\right) \tag{3.20}$$

where we have used that for $\alpha = \beta$, $M_{\alpha\alpha,ij} = U_{\alpha i}U^*_{\alpha i}U^*_{\alpha j}U_{\alpha j} = |U_{\alpha i}U^*_{\alpha j}|^2$. Thus, we have now arrived at the expressions for the probability of appearance and disappearance, in the form of Eq. 3.17 and Eq. 3.20, respectively. In the context of neutrino oscillation experiments, we can differentiate between two types: appearance and disappearance experiments. In the former case, it is the transition probability that is measured and generally these set-ups allow for small mixing angles to be probed. On the other hand, experiments of the latter type tend to measure survival probability and therefore constrain larger mixing angles.

We have so far only considered the production of neutrinos. For antineutrinos, the CP phase δ_{CP} associated with neutrinos that appears in the PMNS matrix changes sign and becomes $-\delta_{CP}$ when the PMNS matrix is complex conjugated. This change can lead to an asymmetry between neutrino and antineutrino oscillation, i.e. CP violation. To quantify this, the asymmetry factor

$$\mathcal{Y} = \mathcal{P}_{\nu_\alpha \to \nu_\beta} - \mathcal{P}_{\bar{\nu}_\alpha \to \bar{\nu}_\beta} \tag{3.21}$$

may be introduced, where the bar denotes antineutrino states. We see from Eq. 3.17 that this asymmetry factor takes the form

$$\mathcal{Y} = 4 \sum_{i>j} \Im\left[M_{\alpha\beta,ij}\right] \sin\left(\frac{\Delta m_{ij}^2 L}{2E}\right). \tag{3.22}$$

As seen before, in the case of $\alpha = \beta$ the quantity $M_{\alpha\alpha,ij}$ is real and therefore $\mathcal{Y} = 0$ – in other words, there is no asymmetry between neutrino and antineutrino survival oscillation probabilities.

In order to allow for a more physical understanding of the oscillation formula, let us concentrate on mixing between two of the three known neutrino flavours, as this will result in a simpler and more easy-to-interpret result. We start by defining the matrix, U, which in this case is just a rotation matrix, only parameterised by an angle, θ.

$$U = \begin{pmatrix} \cos\theta & \sin\theta \\ -\sin\theta & \cos\theta \end{pmatrix} \tag{3.23}$$

This angle, assuming Dirac neutrinos, does not lead to physical CP violation and therefore the asymmetry factor in Eq. 3.22 vanishes. Using this mixing angle and the mass-squared difference $\Delta m^2 \equiv m_2^2 - m_1^2$, the probability for two-neutrino oscillation is obtained as

$$\mathcal{P}_{\nu_\alpha \to \nu_\beta} = \mathcal{P}_{\nu_\beta \to \nu_\alpha} = \sin^2(2\theta)\sin^2\left(\frac{\Delta m^2 L}{4E}\right) \qquad (\alpha \neq \beta) \tag{3.24}$$

$$\mathcal{P}_{\nu_\alpha \to \nu_\alpha} = \mathcal{P}_{\nu_\beta \to \nu_\beta} = 1 - \mathcal{P}_{\nu_\alpha \to \nu_\beta} \qquad (\alpha = \beta) \tag{3.25}$$

In general, the oscillation amplitude depends on the mixing angle through the $\sin^2(2\theta)$ term, while the frequency of oscillation is determined by Δm^2 and L/E. It is apparent from the *appearance* channel expression, i.e. Eq. 3.24, that although $\Delta m^2 \neq 0$ is necessary for oscillation to occur, it is not on its own sufficient, as the θ-dependant sinusodial term dictates the degree of mixing. Clearly, there is no mixing when θ is a multiple of $\pi/2$, while maximal mixing occurs when θ is a multiple of $\pi/4$. The other sinusodial term in Eq. 3.24 is dependent on L, and hence the distance over which the neutrinos propagate is also oscillatory. From the appearance probability expression, one can work out the characteristic oscillation length, which is the distance where the phase associated with the mass-squared difference is equal to π

$$L^{\text{osc}} = \frac{4\pi E}{\Delta m^2}. \tag{3.26}$$

When $L \ll L^{\text{osc}}$, the oscillations do not have sufficient time to develop and the probability is therefore very small. On the other hand, in the case $L \gg L^{\text{osc}}$, the argument of the second sinusodial term becomes large and thus the function is rapidly completing full cycles and hence it tends towards an averaged value, leaving only the θ-dependence intact.

The approach taken in deriving all of the above results assumes that the propagating neutrino states can be treated as plane waves. Although the general probability expression in Eq. 3.15 as well as the two-neutrino appearance and disappearance probabilities in the form of Eq. 3.24 and Eq. 3.25, respectively, turn out to be valid, the plane wave approach is not entirely correct to adopt. This is because treating the neutrino states as plane waves requires the assumption that they have fixed momenta. However, in line with Heisenberg's uncertainty principle

$$\Delta x \Delta p = \frac{\hbar}{2}, \tag{3.27}$$

where x denotes spatial position, p denotes spatial momentum and $\hbar = \frac{h}{2\pi}$ with h being Planck's constant. We see from this expression that definitive knowledge about the neutrino's momentum necessarily translates to an infinite uncertainty on its position, i.e. $\Delta x \to \infty$. A more rigorous quantum mechanical treatment involves the adoption of the wave-packet approach instead, where the neutrino state is described by a superposition of planes waves and it is allowed to have variable spatial momentum, which is spread out around an average value. Therefore the neutrinos are localised and the issue of infinite spatial position uncertainty is circumvented. Whereas in the case of the plane wave approach oscillations are a result of interference between the propagating waves, the wave-packet approach shows that coherence and decoherence effects – arising from the group velocities of the individual packets – between the wave-packets lead to a more intricate interference behaviour and hence oscillation patterns. In the wave-packet formalism, the one-dimensional neutrino flavour state at $t = 0$ corresponding to Eq. 3.9, up to a normalisation factor, is given by [64]

$$|\nu_\alpha(0)\rangle \simeq \sum_i U_{\alpha i} \int \exp\left(\frac{-(p-p_0)^2}{2\sigma_p^2}\right) dp |\nu_i(0,p)\rangle, \tag{3.28}$$

where p is the variable spatial momentum of the neutrino state, p_0 is the average momentum and σ_p is the variance of the Gaussian distribution of the momenta. While assuming a Gaussian shape is a specific choice, it is an appropriate one. Mathematically it is simple and convenient, while also capturing the important characteristics of a localised wave-packet, though it should be noted that the exact shape of the distribution is determined by the production mechanism of the neutrino state. Arriving at an expression for the probability of oscillation from Eq. 3.28 is rather laborious, so we just state the result [64]

$$\mathcal{P}_{\nu_\alpha \to \nu_\beta} \propto \sum_{i,j} U_{\alpha i} U^*_{\beta i} U^*_{\alpha j} U_{\beta j} \exp\left[-i \frac{\Delta m^2_{ij} L}{2E} - \left(\frac{L}{L^{\text{coh}}_{ij}} \right)^2 \right], \tag{3.29}$$

where the coherence length is given by

$$L^{\text{coh}}_{ij} = \frac{2\sqrt{2}E^2}{\sigma_p |\Delta m^2_{ij}|}. \tag{3.30}$$

This expression differs from Eq. 3.15 only in that it contains an extra term: the ratio between the propagation distance and the coherence length, suitably dubbed the *coherence* term. This ratio contains spatial information about the wave packets through their group velocities. The wave-packets associated with the different mass states which a flavour state is composed of travel at different group velocities and give rise to spatial separation and therefore overlap in certain cases. At very short distances, i.e. for $L \ll L^{\text{osc}}$ oscillations are hardly observable and thus seem to remain constant. In the case of $L \sim L^{\text{osc}}$ the sinusodial periodicity of the flavour transitions is most pronounced, while for $L \sim L^{\text{coh}}$ the spatial overlap between the individual wave-packets is reduced and hence the second term in the exponential in Eq. 3.29 starts to dominate, leading to damping of the oscillations, i.e. decoherence. For very long distances $L \gg L^{\text{coh}}$, the coherence term tends to zero, hence suppresses the oscillatory term and the oscillatory behaviour loses its distance dependence and tends to an average value.

Although the above discussion of vacuum oscillations is pivotal for understanding neutrino propagation in space, it is crucial to understand how the coherence of the wave-packets is affected by matter effects. As neutrinos propagate and, albeit weakly, interact with matter, their oscillatory behavior is altered. This will be explored in the next subsection.

3.1.2 In Matter

In 1978, it was proposed by Lincoln Wolfenstein that coherent forward scattering can alter neutrino oscillations [65]. Although continuous scattering of the neutrinos would kill oscillations altogether, coherent scattering does not and can even enhance it in some special cases. This resonance was predicted by Stanislav Mikheyev and Alexei Smirnov [66] and therefore matter effects impacting neutrino oscillations are also widely known as the Mikheyev-Smirnov-Wolfenstein (MSW) effect.

In general, the Hamiltonian, H, is given by

$$H = H_0 + V, \tag{3.31}$$

where H_0 is the Hamiltonian in free-space and V is a potential energy describing effects of matter. For neutrinos propagating in vacuum, $V = 0$ and $H = H_0$. If the neutrino propagates in a medium, the presence of a potential due to the matter particles the neutrinos scatters with alter the Hamiltonian of the system. When constructing a mathematical description of the MSW effect, it is sufficient to model matter as consisting of electrons, protons and neutrons. This is because the vast majority of matter in the universe is composed of first generation fermions, i.e. up- and down-quarks (the constituents of protons and neutrons) and electrons. Neutrinos scattering with matter is mediated by W and Z bosons, giving rise to CC and NC interactions, respectively. While all three flavours of neutrinos take part in NC scatterings, only ν_e can be involved in W-mediated CC interactions. This is precisely because, as mentioned earlier, matter is almost entirely composed of first generation fermions, and thus only ν_e is able to couple to the electrons. Hence, the potential felt by the electron neutrino will be altered, but through the admixing of the neutrinos, the mass states ν_1, ν_2 and ν_3 will also feel this effect, through the ν_e components they each contain. Since all flavours experience the potential due to NC interactions, the common phase it introduces can be neglected when trying to understand how the oscillation is modified by matter effects, and thus it is sufficient to focus only on the potential induced by CC interactions. This modifies the Hamiltonian and thus shifts the phase between the mass eigenstates. Let us assume the two flavour paradigm, let us say ν_e and ν_μ for concreteness, and find an expression for the vacuum Hamiltonian, H_0. Since the mass eigenstates propagate independently of each other, in the mass basis the vacuum Hamiltonian is

$$H_0^m = \begin{pmatrix} E_1 & 0 \\ 0 & E_2 \end{pmatrix} \tag{3.32}$$

with E_1 and E_2 denoting the energies of the mass states ν_1 and ν_2, respectively. As before, since the neutrinos are ultrarelativistic, we use Eq. 3.6 to obtain

$$H_0^m \approx \begin{pmatrix} \frac{m_1^2}{2E} & 0 \\ 0 & \frac{m_2^2}{2E} \end{pmatrix} \tag{3.33}$$

where we have dropped the terms proportional to E, as they will end up cancelling out anyway. We now transform this expression from mass to flavour basis using the relation

$$H_0^f = UH_0^mU^\dagger \tag{3.34}$$

where U is the mixing matrix in the two-flavour paradigm, as given in Eq. 3.23 matrix and H_0^f denotes the vacuum Hamiltonian in the flavour basis. Substituting in U and H_0^m into this expression and using $\Delta m^2 = m_2^2 - m_1^2$ as before yields

$$H_0^f = \frac{1}{2E}\left(m_1^2 + \frac{\Delta m^2}{2}\right)I + \frac{\Delta m^2}{4E}\begin{pmatrix} -\cos 2\theta & \sin 2\theta \\ \sin 2\theta & \cos 2\theta \end{pmatrix} \tag{3.35}$$

with I denoting the 2×2 identity matrix. All the first term is responsible for in the above expression is to introduce an overall phase, which has no effect on the oscillations. Therefore we neglect it and arrive at an expression for the effective Hamiltonian in vacuum, H_0

$$H_0 = \frac{\Delta m^2}{4E}\begin{pmatrix} -\cos 2\theta & \sin 2\theta \\ \sin 2\theta & \cos 2\theta \end{pmatrix} \tag{3.36}$$

Now using this expression, we can rewrite Eq. 3.31 as

$$\begin{aligned} H &= \frac{\Delta m^2}{4E}\begin{pmatrix} -\cos 2\theta & \sin 2\theta \\ \sin 2\theta & \cos 2\theta \end{pmatrix} + \begin{pmatrix} V & 0 \\ 0 & 0 \end{pmatrix} \\ &= \frac{\Delta m^2}{4E}\begin{pmatrix} -\cos 2\theta + \frac{2EV}{\Delta m^2} & \sin 2\theta \\ \sin 2\theta & \cos 2\theta \end{pmatrix} \end{aligned} \tag{3.37}$$

where $V = \sqrt{2} G_F n_e$ is the potential induced by CC interactions, with G_F the Fermi constant and n_e denoting the electron number density in matter [67]. Now we need to solve the Schrödinger equation

$$i\frac{d}{dt}\begin{pmatrix} \nu_1 \\ \nu_2 \end{pmatrix} = H_M \begin{pmatrix} \nu_1 \\ \nu_2 \end{pmatrix} \tag{3.38}$$

where H_M is the diagonalised Hamiltonian in the mass basis. To go from H, the Hamiltonian in the flavour base before diagonalisation, to H_M, we need to compute

$$H_M = U_M^\dagger H U_M \tag{3.39}$$

where U_M is the mixing matrix given by

$$U_M = \begin{pmatrix} \cos\theta_M & -\sin\theta_M \\ \sin\theta_M & \cos\theta_M \end{pmatrix} \tag{3.40}$$

and thus

$$H_M = \frac{1}{4E}\begin{pmatrix} -\Delta m_M^2 & 0 \\ 0 & \Delta m_M^2 \end{pmatrix} \tag{3.41}$$

The effective parameters θ_M and Δm_M^2 differ from their vacuum counterparts θ and Δm^2 and denote the effective mixing angle and mass splitting squared in matter, respectively. They are expressed as [67]

$$\sin^2 2\theta_M = \frac{\sin^2 2\theta}{\sin^2 2\theta + \left(\cos 2\theta - \frac{2EV}{\Delta m^2}\right)^2} \tag{3.42}$$

and

$$\Delta m_M^2 = \Delta m^2 \sqrt{\sin^2 2\theta + \left(\cos 2\theta - \frac{2EV}{\Delta m^2}\right)^2}. \tag{3.43}$$

Hence, the solutions to the Schrödinger equation are

$$\begin{aligned} \nu_1(t) &= \nu_1(0) e^{-i\frac{\Delta m_M^2}{4E}t} \\ \nu_2(t) &= \nu_2(0) e^{-i\frac{\Delta m_M^2}{4E}t} \end{aligned} \tag{3.44}$$

It is straightforward to compute $\nu_e(t)$ and $\nu_\mu(t)$ using the solutions above and the mixing matrix in Eq. 3.40. Since the neutrinos are ultrarelativistic, the appearance probability is

$$\mathcal{P}_{\nu_e \to \nu_\mu} = \sin^2(2\theta_M) \sin^2\left(\frac{\Delta m_M^2 L}{4E}\right). \tag{3.45}$$

When $\theta_M = \pi/4$, maximal mixing, i.e. $\sin^2(2\theta_M) = 1$ occurs, a resonance is obtained, corresponding to a maximal transition amplitude between the two neutrino flavours. The resonance condition for the potential, V_{res}, is given by

$$V_{\text{res}} = \frac{\Delta m^2}{2E} \cos(2\theta). \tag{3.46}$$

At the resonance, the mass splitting takes on its minimal value, as the second term under the square root in Eq. 3.43 is zero, thus $\Delta m_M^2 = \Delta m^2 \sin(2\theta)$, leading to rapid oscillations. When $V = 0$, clearly we recover the vacuum case with $\theta_M = \theta$ and $\Delta m_M^2 = \Delta m^2$. When $V \ll V_{res}$, corresponding to low matter density, the effective parameters are only slightly different from their vacuum counterparts and therefore the oscillation probability is similar to that in vacuum. Finally, in the case $V \gg V_{res}$, i.e. matter effects are very strong, the effective mass-splitting becomes large, while the effective mixing angle approaches zero. This results in a suppression of oscillations in the high matter density scenario.

3.2 Oscillation Experiments

The phenomenon of neutrino oscillation has been extensively studied experimentally using a wide variety of neutrino sources, including: solar, atmospheric, accelerator and reactor neutrinos.

The solar ν_e neutrino deficit was first observed by the famous Homestake experiment [16] in 1968, with final results of 2.56 ± 0.16 (stat.) ± 0.16 (syst.) solar neutrino units (SNU, with 1 SNU $= 10^{-36}$ captures per second per target atom) [68]. In comparison, the Standard Solar Model (SSM) predicts $8.46^{+0.87}_{-0.88}$ [69]. This deficit was confirmed by the Gallium Experiment (GALLEX) [70], Soviet-American Gallium Experiment (SAGE) [71] and Gallium Neutrino Observatory (GNO) [72] experiments, with proton-proton chain neutrinos. SAGE reported $65.4^{+3.1+2.6}_{-3.0-2.8}$ SNU [73], while the combined GALLEX+GNO results showed 69.3 ± 4.1 (stat.) ± 3.6 (syst.) SNU [72], compared with the SSM prediction $127.9^{+8.1}_{-8.9}$ SNU [69]. These were all radiochemical experiments, only able to provide time-averaged data. The Kamiokande experiment on the other hand, was a Cherenkov detector able to measure the neutrino capture in real time and provide directional confirmation that the neutrinos were indeed originating from the Sun (i.e. that the deficit was not resulting from some other source). Both Kamiokande [74] and its successor, Super-Kamiokande [75], confirmed the neutrino deficit as well as the origin of the neutrinos. The solar neutrino flux predicted by the SSM is $(5.46 \pm 0.66) \times 10^6$ cm^{-2} s^{-1} [76], while the most recent Super-Kamiokande results report a flux of $(2.345 \pm 0.014 \pm 0.036) \times 10^6$ cm^{-2} s^{-1} [77]. Some forty years after the solar neutrino problem, the solution came from the SN [78] and Super-Kamiokande [79] experiments, confirming the oscillatory behaviour of neutrinos. Presently, solar neutrinos are used to constrain θ_{12}, while future searches will attempt to measure the solar fluxes with more precision and study the MSW effect.

Similarly to the solar neutrino problem, a deficit of atmospheric neutrinos was observed by Kamiokande [32] and IMB [80] experiments. The evidence for atmospheric neutrino oscillations as the solution to the problem was reported by Super-Kamiokande [34]. Currently, atmospheric neutrinos are used by experiments such as Super-Kamiokande and IceCube, to study oscillations over very long baselines, constrain θ_{23} and $|\Delta m^2_{31}|$. Future experiments, including the upgraded IceCube and

Hyper-Kamiokande will aim to study CP-violating effects, alongside the mass ordering.

Accelerator neutrinos are used in long- and short-baseline oscillation experiments. The long-baseline K2K [81] alongside MINOS [82] and MINOS+ [83] confirmed ν_μ disappearance. The OPERA experiment confirmed muon to tau neutrino oscillations [84], while muon to electron neutrino oscillation was firmly established by T2K [85]. Currently, the T2K and NOvA experiments are providing constraints on δ_{CP} and the mass ordering, while the future will see Hyper-Kamiokande and DUNE studying mass ordering, δ_{CP} and the θ_{23} octant with unprecedented precision, among their rich scientific goals. The short-baseline LSND experiment [86] found an excess of events when studying electron antineutrino appearance, a result supported by the results of MiniBooNE [87], although this excess was not reported by KARMEN [88]. Similarly, the MicroBooNE collaboration did not report an excess of events [89], nor did they find any evidence of oscillations involving light sterile neutrinos [90, 91]. Recently, the JSNS^2 [92] experiment located at J-PARC has commenced operation, with the aim of looking for hints of light sterile neutrino oscillation alongside testing of the LSND anomaly.

Reactors are important sources of neutrinos, as they produce them in copious amounts. The KamLAND experiment used such rector antineutrinos to report evidence of $\bar{\nu}_e$ disappearance [36]. The three experiments Double Chooz [93], Daya Bay [94] and RENO [95] all found θ_{13} to have a non-zero value. One of the most notable next generational neutrino experiment that will utilise reactor neutrinos is JUNO. Among its rich scientific objectives, JUNO aims to determine the mass ordering of neutrinos.

3.3 Absolute Neutrino Mass Probes

Although we have seen that the existence of neutrino oscillations hinges entirely on the fact that neutrinos are not massless, oscillation experiments are unable to measure the absolute masses of neutrinos, as the transition probability relies on the mass-squared difference, rather than the absolute mass, as seen in Eq. 3.15. There are three main probes available to determine the absolute neutrino mass: cosmological measurements; neutrinoless double beta-decay and single beta-decay. In this section we review each of these. Currently, the absolute masses of the SM active neutrinos are still unknown, but experiments continue to provide more and more stringent upper bounds, with the hope of honing in on the actual mass value in the near-future. Although current experimental data shows a slight preference for normal ordering (NO) as opposed to inverted ordering (IO), the mass hierarchy of neutrinos is also unknown. While some neutrino mass experiments have the potential to probe the mass ordering, there exist a number of dedicated searches for which the question of mass hierarchy is of high priority among their outlined scientific goals. These include the Jiangmen Underground Neutrino Observatory (JUNO) [96] and Hyper-Kamiokande [97] mid- and long-baseline experiments, respectively, and the atmospheric neutrino experiments KM3NeT-ORCA [98] and IceCube-PINGU [99].

3.3.1 Cosmology

The role and nature of neutrinos in the universe has changed significantly since the Big Bang. In the early universe, ultrarelativistic neutrinos were in abundance and contributed to the radiation density of the universe through their own energy density. At a later time however, as the universe expanded and the primordial plasma – alongside neutrinos – cooled, the ultrarelativistic neutrinos gradually decoupled. Today, they contribute to the matter, rather than radiation density of the universe. It should be noted, that if neutrinos had extremely small masses, or if they were completely massless, they would have remained ultrarelativistic, still contributing to radiation density to this day. However, since they posses small but non-zero mass, by measuring the density of these relic neutrinos today, it is possible to constrain some of their properties, such as their mass, if we assume the ΛCDM [2] model [101–107]. In other words, the cosmic neutrino background contains the imprint of the primordial neutrino sea, through the influence of the transition on the large-scale structure

---

[2] Currently, the ΛCDM model shows the best fit to the cosmological observations and available data [100].

formation in the universe. It can be assumed that the relic neutrino background is homogeneously composed of the three active neutrino mass eigenstates, m_1, m_2 and m_3. Due to the resolution of the cosmological survey techniques however, such precision measurements usually constrain the sum of neutrino masses [108]

$$\Sigma \equiv \sum_i m_i \tag{3.47}$$

where the sum runs over the three neutrino mass states and thus $i = 1, 2, 3$. Eq. 3.47 can be rewritten in terms of the lightest neutrino state, m_{lightest}. This will result in two separate expressions for the two distinct mass hierarchies

$$\Sigma = m_{\text{lightest}} + \sqrt{\Delta m_{21}^2 + m_{\text{lightest}}^2} + \sqrt{\Delta m_{31}^2 + m_{\text{lightest}}^2} \qquad \text{(NO)} \tag{3.48}$$

$$\Sigma = m_{\text{lightest}} + \sqrt{-\Delta m_{32}^2 + m_{\text{lightest}}^2} + \sqrt{-\Delta m_{31}^2 + m_{\text{lightest}}^2} \qquad \text{(IO)} \tag{3.49}$$

where Δm_{ij}^2 is the mass-squared difference between the mass states m_i and m_j. It is useful to have expressions in terms of m_{lightest} since this naturally results in the appearance of mass-squared terms which facilitates straightforward comparison and combination with oscillation data. It also naturally leads to the two different hierarchical scenarios which allows for straightforward considerations of models that make mass-ordered predictions.

Constraining Σ in this manner is entirely model dependent. Although effectively all results rely on the assumption of the ΛCDM model, this is not the only choice that can influence the upper limit one obtains [108]. The resulting upper bound is also heavily dependent on the cosmological survey data it takes into consideration when performing the analysis. Estimates in [109] combine Cosmic Microwave Background (CMB) data from Planck [110], lensing [100] and baryon acoustic oscillations (BAO) [111–113] measurements. In the early universe, neutrinos suppressed structure formation due to the free-streaming effect due to their ultrarelativistic nature, as their high speed allowed them to escape the pull of matter density fluctuations to form matter. The photons of the CMB are deflected by gravitational potentials of large-scale structures, thus neutrino effects can be observed indirectly by measuring the degree of lensing. BAO are fluctuations of matter-density due to the primordial acoustic oscillations which can be used to study the expansion history of the universe, which was affected by ultrarelativistic free-streaming neutrinos through their suppression of structure-formation. The above data were combined to give current best upper bounds of $\Sigma < 0.15$ eV for NO and $\Sigma < 0.17$ eV for IO.

3.3.2 Neutrinoless Double Beta Decay

When single beta-decay is forbidden, some nuclei can undergo double beta-decay ($2\nu\beta\beta$), whereby two neutrons transform into protons accompanied by the emission of two beta-electrons and two antineutrinos in total. However, if the neutrino is a Majorana particle, then the antineutrino produced in the first decay can be absorbed by the second decay. This results in the emission of two beta-electrons, but no neutrinos and this process is hence termed neutrinoless double beta-decay ($0\nu\beta\beta$)

$$(Z,A) \to (Z+2,A) + e^- e^- \tag{3.50}$$

where Z and A are the atomic and mass numbers of the nucleus, respectively. This process can only occur, if the neutrino is able to undergo a chirality ’flip’. Given that antineutrinos are right-handed, while neutrinos are left-handed, a chirality ’flip’ is necessary for $0\nu\beta\beta$, i.e. the neutrino must be Majorana. It is important to note that constraining the neutrino mass in this fashion relies on the assumption that the dominant contribution to the neutrinoless double beta-decay is from Majorana neutrino masses, rather than some other new physics phenomenon. This, in turn, implies that if neutrinos are not in fact Majorana particles, $0\nu\beta\beta$ is a forbidden process and cannot be observed in nature.

Experiments studying $0\nu\beta\beta$ measure the decay half-life

$$(T^{0\nu}_{1/2})^{-1} = G^{0\nu}|M^{0\nu}|^2\langle m_{\beta\beta}\rangle^2 \tag{3.51}$$

where $G^{0\nu}$ denotes the so-called phase-space factor and hence determines the kinematics of the outgoing final-state particles, $|M^{0\nu}|$ is the nuclear matrix-element of the process and $\langle m_{\beta\beta}\rangle$ is the effective Majorana mass

$$\langle m_{\beta\beta}\rangle = \sum_i (U_{ei})^2 m_i = \cos^2\theta_{13}(\cos^2\theta_{12} m'_1 + \sin^2\theta_{12} m'_2) + \sin^2\theta_{13} m'_3, \quad (3.52)$$

i.e. a linear superposition of the mass states, with $m'_i = e^{i\alpha_i}$, where α_i are combinations of the CP-violating phase in the PMNS matrix and the two Majorana phases (see parametrisation in [114] for example). It is possible to express Eq. 3.52 in terms of the lightest neutrino mass, m_{lightest}. Using $m_{\text{lightest}} = m_1$ for NO and $m_{\text{lightest}} = m_3$ for IO results in two definitions for $\langle m_{\beta\beta}\rangle$ for the two mass ordering cases.

From Eq. 3.51 it is easily seen that measurements of $T^{0\nu}_{1/2}$ translate to a measurement of $\langle m_{\beta\beta}\rangle$, or to an upper bound on $\langle m_{\beta\beta}\rangle$, in the case of null signal. It should be emphasised, that there are sizable uncertainties associated with the nuclear matrix element, $|M^{0\nu}|$. Since $\langle m_{\beta\beta}\rangle$ is proportional to the half-life, these uncertainties are inevitably inherited by the limits on the effective Majorana neutrino mass. Different nuclear models result in different values of $|M^{0\nu}|$ and therefore the derived limits on $\langle m_{\beta\beta}\rangle$ also vary depending on the model used.

So far, $0\nu\beta\beta$ has not been observed. Currently, the most stringent upper bounds on the effective Majorana mass come from the KamLAND-Zen [115] and GERDA [116] experiments, which at 90% CL are

$$\langle m_{\beta\beta}\rangle < 36 - 156 \text{ meV} \quad (3.53)$$

$$\langle m_{\beta\beta}\rangle < 79 - 180 \text{ meV}, \quad (3.54)$$

respectively. The above are ranges, because the nuclear matrix elements, which are theoretically computed, vary between models and therefore impact the inferred values of $\langle m_{\beta\beta}\rangle$.

3.3.3 Single Beta Decay

In the previous subsections, two of the three probes for neutrino mass measurement – cosmology and neutrinoless double beta-decay – were introduced. It was explored that both of these are *model dependent* and *indirect* measurement techniques. The only model independent direct neutrino mass probe is single beta-decay.

During single beta-decay, one of the neutrons in the mother nucleus changes into a proton and emits two final state particles: an electron and an electron-type antineutrino

$$(Z,A) \rightarrow (Z+1,A) + e^- \ \bar{\nu}_e. \tag{3.55}$$

If the nucleus is at rest, energy-momentum conservation dictates that knowledge of the emitted electron's kinetic energy allows deductions to be made about the kinetic energy of the anti-neutrino and hence its absolute mass. In single beta-decay neutrino experiments, the parameter of interest is referred to as the effective neutrino mass [117]

$$m_\beta = \sqrt{|U_{e1}|^2 m_1^2 + |U_{e2}|^2 m_2^2 + |U_{e3}|^2 m_3^2}. \tag{3.56}$$

Eq. 3.56 can be rewritten in terms of the mass-squared differences for cases when the mass ordering needs to be explicitly emphasised. At this point it is important to note that although neutrino flavours are associated with the charged leptons they are produced along, m_β should not be referred to as 'electron-neutrino', because strictly speaking it is not a particle with a well defined mass, but it is in fact an interaction eigenstate composed of a linear superposition of mass eigenstates.

The behavior of the energy spectrum for various neutrino masses for tritium β-decay is shown in Figure 3.1. In such neutrino mass experiments, the energy spectrum of the beta particle is measured and the high energy tail can then be observed near its end-point. If neutrinos were massless, the end-point would be located at the the Q-value, the energy difference between the initial and final states of the decaying nucleus, i.e. it is the total energy available to the emitted electron and neutrino. However, knowing that neutrinos are massive, the simultaneous emission of a neutrino alongside the electron is expected to manifest itself in the form of an early round off of the energy spectrum of the electron, with the end-point located at Q$-m_\beta$ – the more massive the neutrino, the more energy it takes away from the total available and hence the earlier the spectrum is sent to zero.

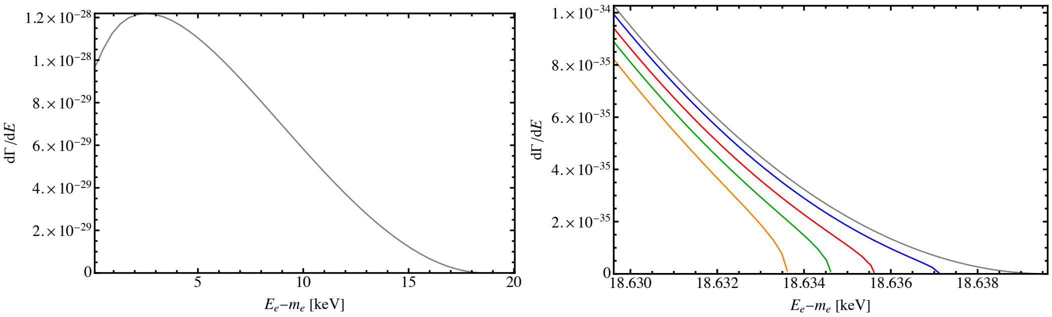

Figure 3.1: Left: electron energy spectrum in tritium beta-decay as a function of kinetic energy. Right: endpoint region of the same spectrum for a massless neutrino (gray) and various choices of neutrino mass, $m_\beta = 2.5$ eV (blue), 4 eV (red), 5 eV (green) and 6 eV (orange). As can be seen, the end-point is shifted by an amount equal to the neutrino's mass.

Choosing an appropriate isotope for a single beta-decay experiment is crucial. There are two main factors to consider: Q-value and specific activity. Since the Q-value determines the kinematics of the decay products, it needs to be large enough to accommodate the masses of both the electron and the neutrino, as well as the kinetic energy distribution of the beta-particle. On the other hand, and more importantly, the lightness of the neutrinos results only in a small distortion of the energy spectrum and therefore the lower the Q-value (and hence the larger m_β/E_K), the more noticeable the distortion and hence the higher the sensitivity. Currently, the most stringent upper bound on the effective neutrino mass is $m_\beta < 0.45$ eV at 90% CL, coming from the KATRIN collaboration [42].

3.4 Sterile Neutrinos

We will see in Sec. 3.5 that in order to generate masses for the left-handed SM neutrinos, the addition of right-handed companions is required. Although measurements of the invisible width of the Z boson constrain the number of light active neutrinos to 3 [118], one is still able to add one or more sterile states to the SM. These inert states are known as sterile neutrinos because the SM gauge group is blind to them and they do not participate in any of its interactions. Despite this, these hypothetical particles can indirectly interact with the SM sector through their mixing with the active neutrinos. In general, extending the SM with n sterile neutrinos results in the dimensions of the PMNS matrix increasing to $(3+n)\times(3+n)$. In the case of a 3+1 model, i.e. one additional neutrino state, the mixing matrix takes the form

$$\begin{pmatrix} \nu_e \\ \nu_\mu \\ \nu_\tau \\ \nu_s \end{pmatrix} = \begin{pmatrix} U_{e1} & U_{e2} & U_{e3} & U_{e4} \\ U_{\mu 1} & U_{\mu 2} & U_{\mu 3} & U_{\mu 4} \\ U_{\tau 1} & U_{\tau 2} & U_{\tau 3} & U_{\tau 4} \\ U_{s1} & U_{s2} & U_{s3} & U_{s4} \end{pmatrix} \begin{pmatrix} \nu_1 \\ \nu_2 \\ \nu_3 \\ \nu_4 \end{pmatrix} \tag{3.57}$$

where ν_s is the extra fermionic singlet interaction eigenstate and ν_4 is the fourth mass eigenstate. All neutrino-mass probes discussed in Sec. 3.3 have the ability to constrain the active-sterile mixing angle if the SM particle content is assumed to be extended by one or more sterile neutrinos, regardless of the underlying production mechanism, as long as the mixing between the active and sterile neutrinos is assumed to be non-zero.

Sterile neutrinos are well motivated both experimentally and theoretically. We will first look at the experimental hints for sterile neutrinos and then introduce the theoretical models that accommodate them.

The short-baseline Liquid Scintillator Neutrino Detector (LSND) experiment [119], which operated at Los Alamos National Laboratory, searched for neutrino oscillations between $\bar{\nu}_\mu$ and $\bar{\nu}_e$ flavour states. It found an excess of $\bar{\nu}_e$ events above the expected backgrounds [120]. Explanations involving systematic error and SM uncertainties all fail to explain the anomalous result (but nevertheless they are discussed in [121]) and therefore the LSND anomaly seems inconsistent with the three neutrino paradigm and this motivates the search for sterile neutrinos.

The short-baseline MiniBooNE experiment at Fermilab, similarly to LSND, reported an excess of electron neutrino events from a muon beam [122], but with higher statistics. MiniBooNE's task was to independently check the results of the LSND and indeed the findings of the two experiments are in agreement with each other, hinting at an anomaly that could potentially be resolved through the extension of the SM with sterile neutrinos.

An additional hint pointing to tension with the three-neutrino paradigm comes from the observed deficit of electron-neutrinos in the calibration tests of the gallium experiments GALLEX [70] and SAGE [123] and their combined results [124]. Similarly to the short-baseline experiments above, these results favour the sterile neutrino hypothesis.

On the other hand, experiments such as the Daya Bay Neutrino Experiment [125] and the Main Injector Neutrino Oscillation Search (MINOS) [126] (alongside their combined results [127]), which also searched for a deficit of SM neutrinos due to mixing with sterile states, did not observe the signal reported by LSND and MiniBooNE. Therefore, further tests are required to resolve this experiential tension.

Beyond the experimental hints, sterile neutrinos are well motivated theoretically, appearing in seesaw, left-right symmetric, various dark matter, GUT and leptogenesis models, to name a few. Through their incorporation they are able to solve some crucial issue with the SM, such as the origin of light neutrino masses, matter-antimatter asymmetry or the identity of dark matter.

3.5 Mass

In the SM, the fermions acquire Dirac masses via Yukawa Higgs couplings, whereby the left-handed $SU(2)_L$ doublets are coupled to the right-handed charged $SU(2)_L$ singlets. We have seen in Sec. 2.5.2 that the mass generation mechanism involves fermion interactions with the Higgs field, which has a non-zero VEV once the symmetry of the original gauge group has been broken spontaneously. In general, the mass matrix of a fermion, m^f is related to the Yukawa coupling, y_f and the VEV, v, through

$$y_f = \sqrt{2}\frac{m^f}{v}. \tag{3.58}$$

Thus, the experimentally measured values of v and the elements of m^f can be used to determine the size of the couplings. The largest Yukawa coupling is $\mathcal{O}(1)$ for the top quark, while the smallest $\sim 10^{-6}$ for the electron. Even if there exists a right-chiral neutrino allowing for the neutrino masses to originate from the Higgs mechanism as in the case of the other fermions, the Yukawa couplings are already heavily constrained and thus have to be very small $\sim 10^{-12}$, indicating that these masses may be generated in a different way.

Other than a Dirac mass arising from the coupling of a left- and right-chiral neutrino field, the neutrinos may have Majorana mass, in which case the neutrino and antineutrino are the same and thus there is no need for two fields of opposite chirality to be present. In fact, from an EFT perspective, neutrinos *should* have Majorana masses, since there is nothing to forbid it. In the following we review the possibility of both Dirac and Majorana neutrino masses.

3.5.1 Dirac

The most straightforward way of incorporating neutrino masses is to add right-handed neutrino $SU(2)_L$ singlets to the SM particle content, one for each generation of leptons, i.e. three in total: ν_R^i where $i = 1,2,3$. The presence of both left- and right-handed neutrino fields then allows for Dirac type masses for the neutrinos to be obtained upon spontaneous symmetry breaking, analogously to the generation of the other fermion masses, as discussed in Sec. 2.5.2.

Although there is nothing forbidding the addition of such ν_R^i states, they must transform trivially under the SM gauge group and thus may not have colour charge, hypercharge or electric charge – in other words they must be completely sterile, to be consistent with experimental observations (or non-observations, rather). Extending the SM with three right-handed neutrinos will therefore result in the extension of the Yukawa Lagrangian with the terms

$$\mathcal{L}_{\text{Yukawa}} \to \mathcal{L}_{\text{Yukawa}} - \sum_{i,j}^{3} y_{ij}^{\nu} \bar{L}^i \tilde{\Phi} \nu_R^j + \text{h.c.} \tag{3.59}$$

where L^i are the left-handed leptonic $SU(2)$ doublets, Φ is the Higgs doublet before symmetry breaking as defined is Eq. 2.39 and y_{ij}^{ν} is a general 3×3 Yukawa matrix for neutrinos. This leads to the neutrino mass term being generated upon the Higgs boson acquiring a non-zero VEV

$$\mathcal{L}_{\text{Yukawa}}^{\nu} = - \sum_{i,j=1}^{3} m_{ij}^{\nu} \bar{\nu}_L^i \nu_R^j + \text{h.c.} \tag{3.60}$$

where m^{ν}_{ij}, the neutrino mass matrix, is given by

$$m^{\nu} = \frac{v}{\sqrt{2}} y^{\nu}. \tag{3.61}$$

In exactly the same way as was done for the up-type quark case, the field appearing in Eq. 3.59 is $\tilde{\Phi}$, as defined in Eq. 2.74, rather than simply Φ, since otherwise the upper component of the left-handed doublet, i.e. the left-handed neutrino field cannot acquire mass, due to the upper component of the unbroken Higgs field being zero in Eq. 2.39.

It has already been explored in Sec. 3.1, and thereafter, that the flavour and mass eigenstates of neutrinos are not equivalent and thus the flavour fields need to be expressed in terms of the fields in the mass basis

$$\begin{aligned} \nu^i_L &= \sum_{k=1}^{3} U^{\nu L}_{ik} \nu'_L, \quad \ell^i_L = \sum_{k=1}^{3} U^{\ell L}_{ik} \ell'_L \\ \nu^i_R &= \sum_{k=1}^{3} U^{\nu R}_{ik} \nu^k_R, \quad \ell^i_R = \sum_{k=1}^{3} U^{\ell R}_{ik} \ell^k_R, \end{aligned} \tag{3.62}$$

where the primed fields denote states in the weak basis and $\ell = e, \mu, \tau$ are the charged leptons and U^X are unitary matrices. Since each flavour is a linear superposition of three mass states due to there being three generations of charged and neutral leptons, as signified by the summation in the above expressions, we know from the discussion on quark mixing in Sec. 2.5.2 that there will be two unitary matrices diagonalising the neutrino and charged lepton mass matrices. As in the case of the up- and down-type quarks, there is no reason for these diagonalising matrices to be the same, i.e. implying mixing in the lepton sector. The interactions of the left-handed neutrinos, ν_L and the left-handed charged leptons, ℓ_L with the charged current mediating W boson produce the charged-current part of the Lagrangian

$$\mathcal{L}_{CC} = -\frac{g}{\sqrt{2}} \sum_{i=1}^{3} \bar{\ell}^i_L \gamma^{\mu} W^+_{\mu} \nu^i_L + \text{h.c.}, \tag{3.63}$$

which can be rewritten using the field redefinitions in Eq. 3.62 as

$$\mathcal{L}_{CC} = -\frac{g}{\sqrt{2}} \sum_{i=1}^{3} \overline{\left(\sum_{p=1}^{3} U^{\ell L}_{ip} \ell'^{p}_{L} \right)} \gamma^{\mu} W^{+}_{\mu} \left(\sum_{q=1}^{3} U^{\nu L}_{iq} \nu'^{q}_{L} \right) + \text{h.c.} \tag{3.64}$$

leading to the identification of the PMNS matrix

$$U_{\text{PMNS}} = U^{\ell L \dagger} U^{\nu L} \tag{3.65}$$

which is analogous to the CKM matrix parameterising the flavour mixing in the quark sector. In Sec. 3.1, the PMNS matrix has already been introduced during the discussion on neutrino oscillations. Since physical observables only depend on the combination of unitary matrices as shown above, rather than on $U^{\ell L \dagger}$ or $U^{\nu L}$ individually, the leptonic unitary matrix may be assumed to be diagonal without loss of generality, i.e. $U^{\ell L \dagger} = \text{diag}(1,1,1)$. This approach is useful, because then U_{PMNS} essentially parameterises the transformation between neutrino mass and flavour eigenstates

$$\begin{pmatrix} \nu_e \\ \nu_\mu \\ \nu_\tau \end{pmatrix} = U_{\text{PMNS}} \begin{pmatrix} \nu_1 \\ \nu_2 \\ \nu_3 \end{pmatrix} = \begin{pmatrix} U_{e1} & U_{e2} & U_{e3} \\ U_{\mu 1} & U_{\mu 2} & U_{\mu 3} \\ U_{\tau 1} & U_{\tau 2} & U_{\tau 3} \end{pmatrix} \begin{pmatrix} \nu_1 \\ \nu_2 \\ \nu_3 \end{pmatrix} \tag{3.66}$$

As we have now seen that this mass generation mechanism corresponds exactly to how the fermions obtain their masses, one might wonder why right-handed neutrino fields were not included in the SM in the first place, as treating all fermions in the same way would be the most natural approach. The answer to this is that no experiment has ever found any indication of right-handed neutrinos and thus they were left out of the model, to be consistent with the observations of the real world.

3.5.2 Majorana

In the previous section it was shown that neutrinos can acquire Dirac-type masses in the same way as the other fermions with an associated Yukawa coupling, via the extension of the SM with right-handed neutrino singlets. However, this is not the only possible mass generation mechanism in the case of neutrinos.

Another way of introducing mass terms is through the construction of Majorana neutrino masses, without the addition of right-handed fields. Although this may seem impossible, since we have seen that both left- and right-chiral fields are required for a mass term, it turns out that the field content of the SM already contains the necessary right-handed fields, in the form of the right-handed antineutrinos, which are the antiparticles to the left-handed neutrino. For a four-component spinor, Ψ, which describes a free fermion has both left- and right-handed components. These can be used to write

$$\Psi = P_L\Psi + P_R\Psi = \Psi_L + \Psi_R, \tag{3.67}$$

using Eq. 2.2, which will result in the Dirac mass term

$$-m\bar{\Psi}\Psi = -m(\bar{\Psi}_L\Psi_R + \bar{\Psi}_R\Psi_L) \tag{3.68}$$

for the Dirac Lagrangian

$$\mathcal{L} = \bar{\Psi}(i\gamma^\mu\partial_\mu - m)\Psi. \tag{3.69}$$

Now if we would like to construct a mass term with only say the left-chiral field, Ψ_L, we need to ensure it is a Lorentz scalar and that it is quadratic in the field. To be able to construct a term adhering to these requirements, we introduce the charge-conjugate spinor

$$\Psi^c = C\bar{\Psi}^T \tag{3.70}$$

where $C = i\gamma_0\gamma_2$ is the 4×4 charge-conjugation. The charge-conjugate spinor, Ψ^c can be shown to transform in the same way as Ψ, which is essential to ensure Lorentz invariance. Using this it is now possible to construct a mass term using only the left-chiral field to construct a Majorana mass term

$$\begin{aligned} -\frac{m}{2}\left(\bar{\Psi}_L^c\Psi_L+\bar{\Psi}_L\Psi_L^c\right) &= -\frac{m}{2}\left(\Psi_L^T C\Psi_L+\bar{\Psi}_L C\bar{\Psi}_L^T\right) \\ &= -\frac{1}{2}\left(\Psi_L^T,(\Psi_R^c)^T\right) m\, C \begin{pmatrix}\Psi_L \\ \Psi_R^c\end{pmatrix} + \text{h.c.} \end{aligned} \tag{3.71}$$

where the mass matrix is given by

$$m = \begin{pmatrix} m & 0 \\ 0 & 0 \end{pmatrix}. \tag{3.72}$$

The result of Eq. 3.71 is the addition of a Majorana mass term to the SM

$$\mathcal{L}_{\mathcal{M}} = \frac{1}{2}\sum_{i,j=1}^{3} m_{ij}^{\nu}\nu_L^{i,T} C\nu_L^{j} + \text{h.c.} \tag{3.73}$$

where m^ν is a 3×3 neutrino mass matrix in flavour space, with $i, j = 1,2,3$ corresponding to the flavour generations ν_e, ν_μ, ν_τ. As before, in order to parameterise the neutrino mixing, the mass matrix needs to be diagonalised, which will result in an alternative U_{PMNS}^M. As opposed to U_{PMNS} which was parameterised by one CP-violating phase in the Dirac case, this new mixing matrix contains two additional CP-violating phases.

In contrast to the Majorana case above, using the charge-conjugate spinor, the Dirac mass term may be rewritten as

$$\begin{aligned} -m\left(\bar{\Psi}_L\Psi_R+\bar{\Psi}_R\Psi_L\right) &= -m\left((\Psi_L^c)^T C\Psi_R+(\Psi_R^c)^T C\Psi_L\right) \\ &= -m\left(\Psi_L^T,(\Psi_R^c)^T\right) m_D\, C \begin{pmatrix}\Psi_L \\ \Psi_R^c\end{pmatrix} \end{aligned} \tag{3.74}$$

where the Dirac mass matrix is given by

$$m_D = \begin{pmatrix} 0 & m \\ m & 0 \end{pmatrix}. \tag{3.75}$$

It is apparent from the explicit form of Eq. 3.75 above that the Dirac mass matrix only contains non-zero entries along its off-diagonal in the basis of left- and right-handed chiral components. This directly demonstrates why Dirac-type masses couple left- and right-chiral components.

On the other hand, the Majorana mass matrix in Eq. 3.72 clearly ends up killing all right-chiral components of the spinor due to the zero valued off-diagonal terms. Upon the introduction of the four-component spinor, Ψ, it was stated that it is a four-component object: describing a particle and antiparticle field, each with two possible spin configurations. It is easy to see from Eq. 3.71 that the Majorana mass term only requires Ψ_L, i.e. only half of the degrees of freedom associated with Ψ and therefore we see that there is indeed no need for the extension of the SM particle content with right-handed neutrino fields to construct Majorana mass terms. Instead, it is sufficient to have a two-component object, $\xi = \Psi_L$. Physically what this means, is that the two particles described by ξ still have two spin configurations, but the particle and antiparticle states must be one and the same, leading to the Majorana condition

$$\Psi^c = \Psi. \tag{3.76}$$

Hence, although the construction of a Majorana mass term is mathematically possible and is advantageously more economical than a Dirac mass in terms of the number of degrees of freedom involved, it has the serious real-world consequence that neutrinos and antineutrinos must be the same particles.

Additionally, it is apparent from Eq. 3.73, that such a term violates lepton number by two units, i.e. $\Delta L = +2$, since neutrinos and negatively charged leptons carry $L = +1$, while antineutrinos and positively charged leptons carry $L = -1$. Introducing lepton number violation (LNV) is a key feature of Majorana neutrinos with experimentally testable consequences. Both the particle-antiparticle equivalence and LNV can be probed in experiments, with the most notable example being the search for neutrinoless double beta-decay.

It is important to point out, that although the Majorana mass term that has been constructed for neutrinos is Lorentz invariant, it does not respect the gauge symmetry of the SM. From the perspective of EFTs, which require the inclusion of all terms permitted by the underlying symmetries, this gauge-invariance requirement leads us to consider higher-dimensional operators, including the dimension-5 Weinberg operator

$$\mathcal{L}_{\text{Weinberg}} = \frac{1}{2}\sum_{i,j=1}^{3} \frac{c_{ij}}{\Lambda_{\text{NP}}}(L^i\Phi)^T(L^j\Phi) + \text{h.c.} \tag{3.77}$$

where c_{ij} are coupling constants and Λ_{NP} is the scale of new physics. Since the Lagrangian has a mass dimension of four, the fact that the scale of new physics in the denominator is to the power of one shows that the operator is indeed dimension-5. Upon spontaneous symmetry breaking

$$\mathcal{L}_{\text{Weinberg}} \to \frac{1}{2}\sum_{i,j=1}^{3} m_{ij}^{\nu}\nu_L^{i,T}C\nu_L^{i} + \text{h.c.} \tag{3.78}$$

i.e. the symmetry breaking naturally gives rise to the Majorana neutrino masses. Since the Higgs doublet, as introduced in Eq. 2.44 contains $v+h$ and the Eq. 3.77 is quadratic in Φ, the mass matrix is given by

$$m^{\nu} = \frac{v^2}{2\Lambda_{\text{NP}}}c. \tag{3.79}$$

Although there are other terms upon expanding $(v+h)^2$, only the one quadratic in the VEV contributes to the Majorana neutrino mass term, since the cross term vh is only relevant for neutrino-Higgs coupling, while h^2 is related to the Higgs self-interaction. Assuming $c \sim 1$ and $m_\nu \sim 0.1$ eV and using $v \approx 246$ GeV means

$$\Lambda_{\text{NP}} \sim 10^{14}\ \text{GeV}. \tag{3.80}$$

This demonstrates why Majorana neutrino masses are such an attractive prospect. Although it has been discussed that Dirac mass terms may be obtained via the addition of right-handed fields, the resulting Yukawa couplings are tiny compared to those of the other fermions, and their smallness is not explained by the mass generation mechanism. Majorana mass terms on the other hand are more economical as they do not require the extension of the SM particle content (although they do upon UV completion) and the resulting small mass values are naturally explained by the high scale of new physics associated with the effective Weinberg operator.

3.5.3 Mass Models

It has been shown in the previous two sections that there are two general ways in which the active neutrinos can receive masses: the Dirac and Majorana mass mechanisms. Although the Dirac approach successfully generates neutrino masses, it suffers from several maladies: additional fields are needed even at low energies; the resulting Yukawa couplings are extremely small and unexplained; no physical consequences apart from mass, hence no testable predictions and lepton number is no longer an accidental symmetry, but one that must be imposed. Majorana mass terms on the other hand: do not require extra light fields only at UV completion; the smallness of the neutrino masses are natural consequences of the high energy theory and lead to the experimentally testable predictions of LNV and particle-antiparticle equivalence. Therefore, the Majorana option is more popular and there are in fact numerous BSM theories which generate the Weinberg operator as a low energy EFT (LEFT) operator, which in turn gives rise to the Majorana neutrino mass term, as discussed in the previous section.

The seesaw mechanism in a sense is a fusion of the Dirac and Majorana approaches, thus managing to get the best of both worlds. In the Type I seesaw model [128–132], three generations of right-handed sterile neutrino singlets are added to the SM (for a pedagogical overview of single generation Type I seesaw see Appendix A). Similarly to the Dirac approach, this will also result in the usual Dirac mass coupling the left- and right-chiral light neutrino components, however, in this case the sterile neutrinos have a Majorana mass term, which must be added since there are no symmetries forbidding it. Such extension of the SM with RH neutrino fields N_R results in the post EWSB Lagrangian

$$\mathcal{L}_{N_R} = \bar{\mathcal{N}}_{Rp} i\partial\!\!\!/ \mathcal{N}_{Rp} - \frac{1}{2}\left[[\mathcal{M}_\nu]_{pr}\bar{\mathcal{N}}^c_{Rp}\mathcal{N}_{Rr} + \text{h.c.}\right]; \quad \mathcal{N}_R \equiv \begin{pmatrix}\nu_L^c \\ N_R\end{pmatrix}, \tag{3.81}$$

where the left-handed (LH), ν_L, and RH neutrino fields are combined into the column vector $\mathcal{N}_R$, the superscript c denotes the charge-conjugate (as defined in Eq. 2.84 with $\eta_c = 1$) and where p and r are indices running over the flavour states for n_ν number of LH and n_s number of RH neutrinos. The neutrino mass matrix is

$$\mathcal{M}_\nu = \begin{pmatrix} M_L & M_D \\ M_D^T & M_R \end{pmatrix}, \tag{3.82}$$

with dimensions $(n_\nu + n_s) \times (n_\nu + n_s)$. The subblocks M_L, M_D and M_R denote the mass matrices of the LH Majorana mass, the Dirac mass coupling LH and RH neutrinos and the RH Majorana mass, respectively, with dimensions of $n_\nu \times n_\nu$, $n_\nu \times n_s$ and $n_s \times n_s$. Without any additional NP, $M_L = 0$, since ν_L is part of the $\mathrm{SU}(2)_L$ doublet L and thus a Majorana mass term of the form $M_L \nu_L^T \nu_L$ would break gauge invariance. If the SM is extended with N_R, then the Dirac mass, M_D, can be generated via the Yukawa coupling of the form $y^\nu \bar{L}^i \tilde{\Phi} \nu_R^j$ (as in Eq. 3.59 with a change in notation $\nu_R \to N_R$), resulting in the mass matrix $M_D = \frac{y^\nu v}{\sqrt{2}}$ (as in Eq. 3.61 with $m^\nu \to M_D$) once the Higgs acquires a non-zero VEV upon EWSB. For lepton number assignment, we adopt the convention $L(\nu_L) = L(N_R) = +1$. Therefore, if lepton number does not need to be conserved, then $M_R \neq 0$ is allowed.

In order to obtain the mass eigenstates, the matrix $\mathcal{M}_\nu$ needs to be diagonalised to decouple the light and heavy states, which rotates the weak states $\mathcal{N}_R$ into the mass states $\mathcal{N}_i$, with masses m_i, similarly to the procedure described in Sec. 3.5.3. This involves assuming a unitary matrix of the form $\mathcal{U} = e^\Omega \approx 1 + \Omega$ to first order in

$$\Omega = \begin{pmatrix} 0 & \Theta \\ -\Theta^\dagger & 0 \end{pmatrix} \tag{3.83}$$

which contains non-zero entries only along its off-diagonal, in order to remove the off-diagonal blocks in the mass matrix. Ω is anti-Hermitian in order to ensure a unitary transformation, i.e. $\mathcal{U}^\dagger\mathcal{U} = e^{\Omega^\dagger} e^{\Omega} = e^{-\Omega} e^{\Omega} = 1$. Θ is a small parameter which is found to be $\Theta \sim M_D/M_R$ upon computing $\mathcal{U}^T \mathcal{M}_\nu \mathcal{U}$. The diagonalisation then yields

$$\mathcal{N}_{Rr} = P_R \mathcal{U}_{ri} \mathcal{N}_i \quad \Rightarrow \quad m_i \delta_{ij} = \mathcal{U}_{pi} \mathcal{U}_{rj} [\mathcal{M}_\nu]_{pr} , \tag{3.84}$$

where $\mathcal{U}$ is an $(n_\nu + n_s) \times (n_\nu + n_s)$ unitary matrix. [3] In the SM, there are three active neutrinos, $n_\nu = 3$, and so the lighter mass states $\nu_i \equiv \mathcal{N}_i$ for $i = 1,2,3$, which to be consistent with oscillation data and constraints from direct absolute mass measurements should mostly mix with the active LH neutrino fields. The rest of the mass states $N_i = \mathcal{N}_{i+3}$ for $i = 1,\ldots,n_s$ with masses $m_{N_i} = m_{i+3}$ should then mostly mix with the RH sterile neutrino fields.

This is realised for $M_L \ll M_D \ll M_R$ and diagonalisation of the full mass matrix $\mathcal{M}_\nu$ yields the light and heavy mass matrices

$$M_\nu \approx M_L - M_D M_R^{-1} M_D^T , \quad M_N \approx M_R . \tag{3.85}$$

The above are not exact equalities because they are the result of a perturbative block-diagonalisation up to leading order in M_D/M_R. These matrices can then be used to find the mass eigenstates by rotation via the unitary matrix U

$$m_i \delta_{ij} = U^*_{pi} U^*_{rj} [M_\nu]_{pr} , \quad m_{N_i} \delta_{ij} = U_{pN_i} U_{rN_j} [M_N]_{pr} . \tag{3.86}$$

Thus, the weak and mass eigenstates are related via the mixing matrix

$$\begin{pmatrix} \nu^c_{L\alpha} \\ N_{Rs} \end{pmatrix} = P_R \begin{pmatrix} U^*_{\alpha i} & V^*_{\alpha N_i} \\ V_{si} & U_{sN_i} \end{pmatrix} \begin{pmatrix} \nu_i \\ N_i \end{pmatrix} . \tag{3.87}$$

which can be shown by assuming the charged lepton mass matrix to be diagonal

---

[3] It should be noted, that in general this should be a bi-unitary diagonalisation (such as in the case of chiral fields being coupled by a mass matrix), but since $\mathcal{M}_\nu$ is symmetric due to the Majorana condition $\Psi^c = \Psi$, only one unitary matrix is needed.

(this can be done without loss of generality, with the relative rotation between the charged lepton and SM light neutrino mass eigenstates being captured by the mixing matrix). Up to non-unitary corrections [4], the element $U_{\alpha i}$ corresponds to the PMNS mixing matrix, i.e. the overlap between the flavour and mass eigenstates of the light SM neutrinos. Similarly, U_{sN_i} quantifies the overlap between the flavour and mass eigenstates of the massive RH neutrinos. The two off-diagonal terms

$$V_{\alpha N_i} \approx \left(M_D M_R^{-1}\right)_{\alpha s} U^*_{sN_i}, \quad V_{si} \approx -\left(M_R^{-1} M_D^T\right)_{s\alpha} U^*_{\alpha i}, \tag{3.88}$$

quantify the active-sterile mixing, with the first describing the heavy mass content N_i of the flavour field ν_α and the latter the light active mass content of the heavy state N_s. As in the case of the charged leptons, it is convenient to assume that M_R is diagonal, i.e. $U_{sN_i} = \delta_{si}$. Then in the case of the Type I seesaw with $M_L = 0$ and $M_D \ll M_R$, the canonical seesaw relation $|V_{\alpha N}| \sim \sqrt{m_\nu / m_N}$ is found by substituting Eq. 3.85 into Eq. 3.88. This naturally explains the smallness of the active SM neutrino masses and sets the scale of the active-sterile mixing angle.

Although the Type I seesaw thus correctly sets the scale of the light neutrino masses originating purely from the addition of RH neutrinos fields, it should be stressed that it is not the only model that can yield the results of Eq. 3.85. In the case of the inverse seesaw [133–136], besides the RH neutrino fields an additional n_s number of LH gauge singlets, S_L (with lepton number assignment $L(S_L) = +1$) are added to the field content. Then the column vector consisting of the RH fields is modified to include S_L and the mass matrix is modified accordingly as

$$\mathcal{N}_R = \begin{pmatrix} \nu_L^c \\ N_R \\ S_L^c \end{pmatrix} \Rightarrow \mathcal{M}_\nu = \begin{pmatrix} M_L & M_D & 0 \\ M_D^T & \mu_R & M_S^T \\ 0 & M_S & \mu_S \end{pmatrix}. \tag{3.89}$$

where M_S denotes the Dirac mass coupling S_L and N_R, and μ_S and μ_R are the Majo-

---

[4] Due to the perturbative expansion being truncated at leading-order during the diagonalisation process, and the presence of non-zero active-sterile mixing resulting in a correction factor of $1 - \frac{1}{2}|V_{\alpha N}|^2$

rana mass terms of S_L and N_R, respectively. This matrix can be rewritten as

$$\mathcal{M}_\nu = \begin{pmatrix} M_L & M_D & 0 \\ M_D^T & \mu_R & M_S^T \\ 0 & M_S & \mu_S \end{pmatrix} \equiv \begin{pmatrix} M_L & \mathcal{M}_D \\ \mathcal{M}_D^T & \mathcal{M}_\mathcal{N} \end{pmatrix} \tag{3.90}$$

with $\mathcal{M}_D = (M_D, 0)$ and $\mathcal{M}_N = \begin{pmatrix} \mu_R & M_S^T \\ M_S & \mu_S \end{pmatrix}$. This form looks very similar to the mass matrix in Eq. 3.82.

For M_L, $\mu_R, \mu_S \ll M_D \ll M_S$ (which is the usual inverse seesaw limit in order to generate small SM neutrino masses without the need for large Majorana masses), after diagonalisation, the mass matrix for the light SM neutrinos is

$$M_\nu \approx M_L - M_D M_S^{-1} \mu_S M_S^{-1} M_D^T. \tag{3.91}$$

In this limit, lepton number is approximately conserved, as the Dirac masses $M_{D/S}$ dominate. Moreover, the soft breaking of the symmetry results in a small mass splitting between the heavy states, forming pseudo-Dirac pairs, consisting of Majorana states that are a linear combination of S_L and N_R, with almost degenerate masses. In contrast to the Type I seesaw, where a large sterile mass suppresses M_ν, the inverse seesaw achieves small neutrino masses via the smallness of the lepton-number-violating parameter μ_S. While $M_\nu \propto M_S^{-1}$, a small μ_S alone can yield the observed scale without requiring a very large M_S. Hence, what makes inverse seesaw more appealing compared to Type I seesaw is that the active-sterile mixing angle is proportional to $|V_{\alpha N}| \sim \sqrt{m_\nu/\mu_S}$. Thus, rather than being forced to have a very large sterile [5] mass scale, the SM neutrino data can be fitted to any mixing angle value (even large ones inaccessible by Type I seesaw given the constraints on m_ν), as the magnitude of the neutrino mass is essentially decoupled from the heavy mass scale and instead determined by μ_S.

When lepton number is conserved exactly, i.e. $M_L = \mu_R = \mu_S = 0$, the SM

---

[5] In the inverse seesaw scenario the physical sterile neutrino, i.e. the weak eigenstate, is generally a linear combination of the heavy mass states N_R and S_L.

neutrinos are left massless, while the previously pseudo-Dirac heavy states become Dirac fermions. These Dirac states, $N_i = \frac{1}{\sqrt{2}}(iN'_i + S'_i)$ are composed of the intermediate fields N'_i and S'_i, which diagonalise the sub-block $\mathcal{M}_{\mathcal{N}}$ in Eq. 3.90 for $\mu_R = \mu_S = 0$. The mixing is then

$$\begin{pmatrix} \nu^c_{L\alpha} \\ N_{Rs} \\ S^c_{Ls} \end{pmatrix} = P_R \begin{pmatrix} \delta_{\alpha i} & -\frac{i}{\sqrt{2}}V^*_{\alpha N_i} & \frac{1}{\sqrt{2}}V^*_{\alpha N_i} \\ 0 & \frac{i}{\sqrt{2}}\delta_{si} & \frac{1}{\sqrt{2}}\delta_{si} \\ V_{si} & -\frac{i}{\sqrt{2}}\delta_{si} & \frac{1}{\sqrt{2}}\delta_{si} \end{pmatrix} \begin{pmatrix} \nu^c_i \\ N'_i \\ S'_i \end{pmatrix} = P_R \begin{pmatrix} \delta_{\alpha i} & 0 & V^*_{\alpha N_i} \\ 0 & \delta_{si} & 0 \\ V_{si} & 0 & \delta_{si} \end{pmatrix} \begin{pmatrix} \nu^c_i \\ N_i \\ S^c_i \end{pmatrix}, \tag{3.92}$$

From the second equality it can be seen that all entries along the diagonal and off-diagonal are non-zero, while the rest are zero and therefore the LH and RH components transform differently and in fact independently of each other. Thus, the flavour and weak eigenstates for the RH and LH fields are expressed as

$$N_{Rs} = P_R \delta_{si} N_i\,, \qquad \begin{pmatrix} \nu_{L\alpha} \\ S_{Ls} \end{pmatrix} = P_L \begin{pmatrix} \delta_{\alpha i} & V_{\alpha N_i} \\ V^*_{si} & \delta_{si} \end{pmatrix} \begin{pmatrix} \nu_i \\ N_i \end{pmatrix}. \tag{3.93}$$

So in this limit it is not possible to generate light masses for the SM neutrinos without the addition of new degrees of freedom. Such new fields are usually RH neutrinos which allow the SM neutrinos to acquire Dirac masses [137–139].

Extending the SM with right-handed sterile states is not the only way to generate the light neutrino masses. In fact, both Type II and Type III seesaw are examples of this. Type II seesaw [132, 140–143] involves the addition of a $SU(2)_L$ scalar triplet, $\Delta = (\Delta^0, \Delta^+, \Delta^{++})^T$

$$\Delta = \begin{pmatrix} \Delta^+/\sqrt{2} & \Delta^{++} \\ \Delta^0 & -\Delta^+/\sqrt{2} \end{pmatrix} \tag{3.94}$$

where the superscripts denote the electric charges of $0, +1, +2$ of each component of the triplet due to its hypercharge. The Lagrangian is then extended with the mass terms for the triplet alongside additional interactions

$$\mathcal{L}_{\text{Seesaw II}} = \mathcal{L}_{\text{SM}} - M_\Delta^2 \text{Tr}(\Delta\,\Delta^\dagger) + \mu \Phi^T \Delta^* \Phi + \sum_{i,j} y_{ij}^\Delta L^{iT} \Delta L^j + \text{h.c.} \tag{3.95}$$

where μ is a coupling constant parameterising the interaction between the triplet and the Higgs doublet, M_Δ is the mass associated with Δ and y^Δ is the relevant Yukawa coupling. Crucially, the electrically neutral component acquires an effective VEV upon spontaneous symmetry breaking [6]

$$\langle \Delta \rangle = \begin{pmatrix} 0 & 0 \\ \langle \Delta^0 \rangle & 0 \end{pmatrix} = \begin{pmatrix} 0 & 0 \\ \frac{\mu v^2}{2M_\Delta^2} & 0 \end{pmatrix} \tag{3.96}$$

and then the neutrino mass matrix is given by $M_\nu = y^\Delta \langle \Delta^0 \rangle$. Analogously to the Type I seesaw, if the parameters are chosen such that $M_\Delta \gg v$, then the neutrino mass matrix can be expressed as

$$M_\nu = y^\Delta \frac{\mu v^2}{M_\Delta^2} \tag{3.97}$$

and thus we see that again there is an inverse relationship between M_ν and M_Δ, i.e. the more massive the scalar triplet, the lighter the active neutrinos and hence Type II seesaw is also able to naturally explain the lightness of the neutrino masses.

Finally, the third such mechanism is known as Type III seesaw [144], whereby the SM particle content is extended with three generations ($i = 1,2,3$) of fermions that transform as triplets under $SU(2)_L$, $\Omega^i = (\Omega^-, \Omega^0, \Omega^+)^{iT}$ where the superscripts on the components denote the electrical charges of -1, 0 and +1 due to the components being charged under $U(1)_Y$, i.e. they possess hypercharge. The SM Lagrangian is then modified to

$$\mathcal{L}_{\text{Seesaw III}} = \mathcal{L}_{\text{SM}} + \sum_{i,j} y_{ij}^\Omega L^{iT} \Omega^j \Phi + \sum_{i,j} M_\Omega^{ij} \Omega^{iT} \Omega^j \tag{3.98}$$

where y^Ω is the Yukawa coupling and M_Ω is the mass associated with the fermion

---

[6] Only the neutral component is allowed to acquire a VEV, otherwise U$(1)_{em}$ would be broken.

triplet. As before, the neutrino mass matrix is then given by

$$M_\nu = (y^\Omega)^T \frac{1}{M_\Omega} y^\Omega \tag{3.99}$$

in the limit where $M_\Omega \gg y^\Omega$ and once again the resulting relationship between the light neutrino masses, M_ν, and the masses of the extra fields, M_Ω is inversely proportional, thus naturally explaining the lightness of the SM active neutrino masses.

3.6 Effective Field Theories

In general there are two broad EFT approaches: top-down and bottom-up. Top-down scenarios involve a specific UV model, whose degrees of freedom and field content result in operators which can be evolved to a desirable energy scale by integrating out heavy degrees of freedom. Bottom-up EFTs on the other hand do not assume a specific UV theory and include all operators allowed by symmetry considerations.

A historical and instructive top-down EFT example is the Fermi theory of beta decay. Although in the SM the process of beta decay proceeds via a W boson, in the Fermi approximation, which is valid at low energies $E \ll m_W$, the process may be approximated as a point-like four-fermion contact interaction. This Fermi interaction is described by the Lagrangian

$$\mathcal{L}_{\text{Fermi}} = -\frac{G_F \cos\theta_C}{\sqrt{2}} [\bar{\nu}_e \gamma^\mu (1-\gamma^5) e][\bar{u}\gamma_\mu (1-\gamma^5) d] + \text{h.c.} \tag{3.100}$$

where θ_C is the Cabibbo angle. It is apparent that the heavy mediator does not appear explicitly, making this a dimension-6 effective Lagrangian and therefore a low-energy effective description of charged-current weak interactions. The Fermi constant $G_F/\sqrt{2} = g^2/8m_W^2$ encodes the information of the high-energy scale m_W and the coupling g. In this EFT, the $SU(2)_L$ gauge symmetry of the full theory is manifested in the $V-A$ structure of the currents. While this theory is non-renormalizable and its amplitudes grow with energy, it remains a highly accurate description for $E \ll m_W$. This illustrates the core EFT principle: at low energies, the details of the heavy UV physics are irrelevant and can be parameterised by effective couplings of higher-dimensional operators, which in turn may be constrained by experiments.

The SM has several shortcomings, as discussed in Sec. 2.8, necessitating extensions. This has motivated numerous BSM scenarios, which introduce additional degrees of freedom. However, without experimental validation, assessing their viability remains challenging, making parameterization choices for BSM physics uncertain and the results generally model-dependent.

The issue of model-dependency can be circumvented using the bottom-up EFT approach, which treats the SM as a low-energy limit of a more complete theory at a higher energy scale, Λ_{NP}, with $\Lambda_{EW} \ll \Lambda_{NP}$ [7]. In this framework, NP effects are incorporated in a model-independent manner through higher-dimensional operators.

In this thesis, EFTs frameworks are employed to study neutrino phenomenology at two distinct energy scales. At regimes around and above the EW scale, the standard model effective field theory (SMEFT [145–157]) extended with RH neutrinos (νSMEFT) and its low-energy descendant, low-energy EFT (LEFT [158–163]) with RH neutrinos (νLEFT) is used to study neutrino phenomenology at FCC-ee. Below the EW scale, a hadronic-level EFT is adopted to explore the sensitivity of future CRES experiments to BSM effects. In the following these two EFT frameworks will be discussed.

3.6.1 νSMEFT and νLEFT

The additional heavy degrees of freedom associated with the UV theory can be integrated out due to the large energy scale difference, but the NP effects remain encoded as corrections to the low-energy theory in the form of the series of operators, which are more suppressed the higher dimensional they are.

One of the most common and popular such frameworks is SMEFT, which treats the SM as a low-energy EFT of some UV theory. The SMEFT respects the entire gauge group of the SM and is therefore applicable to the unbroken phase and it

---

[7] Assuming the full particle content below the EW scale is known.

includes all of the SM fields. The SMEFT Lagrangian can in general be written as

$$\mathcal{L}_{\text{SMEFT}} = \mathcal{L}_{\text{SM}} + \mathcal{L}^{(5)} + \mathcal{L}^{(6)} + \mathcal{L}^{(7)} + \ldots \tag{3.101}$$

where $\mathcal{L}_{\text{SMEFT}}$ is the SM Lagrangian and

$$\mathcal{L}^{(d)} = \sum_i C_i^{(d)} Q_i^{(d)} \tag{3.102}$$

for mass-dimension d with $d \geq 5$, where $Q_i^{(d)}$ are the d-dimensional operators and $C_i^{(d)}$ are the dimensionful Wilson coefficients (WC)

$$C_i^{(d)} = \frac{c_i^{(d)}}{\Lambda^{d-4}} \tag{3.103}$$

with $c_i^{(d)}$ being dimensionless couplings and Λ denoting the scale associated with the UV theory. Since SMEFT is valid above the EW scale, $\Lambda \gg v$. SMEFT is usually considered from a bottom-up perspective, i.e. the starting point is the known low-energy limit of the theory – the SM – while its UV completion is unknown but can be constrained by putting limits on the relevant operators.[8]

In EFT analyses, interest is often focused on the operators themselves, rather than the UV completions that can give rise to them. A number of different possible mass generation mechanisms for the SM light neutrinos exist, as discussed in Sec. 3.5.3. The simplest extension of the SM to explain oscillation data involves the addition of right-handed (RH) neutrino fields, N, otherwise called HNLs, which are singlets under the SM gauge group. Due to their transformation properties, any number of them will preserve gauge invariance and they are allowed to have Majorana masses if the requirement of total lepton number conservation is relaxed [9]. The use of a bottom up EFT framework to address the issue of light neutrino masses is a desirable approach due to its model independent nature and makes a phenomenological analysis of such N fields generally applicable. If the mass of these RH

---

[8] In contrast, a top-down approach involves a specific UV theory being evolved down to lower energy scales, generally resulting in very specific predictions.

[9] Lepton number conservation is not a fundamental, but rather an accidental symmetry of the SM.

ψ^4		ψ^2H^2D	
Q_{ll}	$(\bar{L}\gamma_\mu L)(\bar{L}\gamma^\mu L)$	$Q_{Hl}^{(1)}$	$(\bar{L}\gamma_\mu L)(H^\dagger i\overleftrightarrow{D}^\mu H)$
Q_{le}	$(\bar{L}\gamma_\mu L)(\bar{e}\gamma^\mu e)$	$Q_{Hl}^{(3)}$	$(\bar{L}\gamma_\mu \tau^I L)(H^\dagger i\overleftrightarrow{D}^{I\mu} H)$
Q_{lNle}	$\varepsilon_{ij}(\bar{L}^i N)(\bar{L}^j e)$	Q_{HN}	$(\bar{N}\gamma_\mu N)(H^\dagger i\overleftrightarrow{D}^\mu H)$
Q_{lN}	$(\bar{L}\gamma_\mu L)(\bar{N}\gamma^\mu N)$	Q_{HNe}	$(\bar{N}\gamma_\mu e)(\tilde{H}^\dagger iD^\mu H)$
Q_{eN}	$(\bar{e}\gamma_\mu e)(\bar{N}\gamma^\mu N)$		

ψ^4H		ψ^2H^3D	
Q_{llleH}	$\varepsilon_{ij}\varepsilon_{mn}(\bar{e}L^i)(\bar{L}^{jc}L^m)H^n$	Q_{Nl1}	$\varepsilon_{ij}(\bar{N}^c\gamma_\mu L^i)(iD^\mu H^j)(H^\dagger H)$
Q_{lNlH}	$\varepsilon_{ij}(\bar{L}\gamma_\mu L)(\bar{N}^c\gamma^\mu L^i)H^j$	Q_{Nl2}	$\varepsilon_{ij}(\bar{N}^c\gamma_\mu L^i)H^j(H^\dagger i\overleftrightarrow{D}^\mu H)$
Q_{eNlH}	$\varepsilon_{ij}(\bar{e}\gamma_\mu e)(\bar{N}^c\gamma^\mu L^i)H^j$	Q_{leHD}	$\varepsilon_{ij}\varepsilon_{mn}(\bar{L}^{ic}\gamma_\mu e)H^jH^mD^\mu H^n$
Q_{lNeH}	$(\bar{L}N)(\bar{N}^c e)H$		
Q_{elNH}	$H^\dagger(\bar{e}L)(\bar{N}^c N)$		

Table 3.1: (ν)SMEFT operators at $d = 6$ (above) and $d = 7$ (below) which contribute to the four-fermion operators in Eq. 3.105 and effective $W^\pm$ and Z interactions in Eq. 3.106. The tree-level matching conditions are given in App. D.

neutrinos is below the TeV scale, then they cannot be integrated out and need to be part of the explicit field content of the EFT. [10] The addition of such degrees of freedom to both SMEFT (νSMEFT) and LEFT (νLEFT) has been studied extensively. For νSMEFT, the non-redundant basis of operators up to $d = 9$ has been presented [164–167].

The effective Lagrangian including RH neutrino fields is given by

$$\mathcal{L} = \mathcal{L}_{\text{SM}} + \bar{N} i\partial\!\!\!/ N - \left[\bar{L} Y_\nu N \tilde{H} + \frac{1}{2}\bar{N}^c M N + \text{h.c.}\right] + \sum_i C_i^{(d)} Q_i^{(d)} , \tag{3.104}$$

where $C_i^{(d)} = 1/\Lambda^{d-4}$ are Wilson coefficients (WCs) and $N = \mathcal{C}\bar{N}^T$, with $\mathcal{C}$ the charge conjugation matrix (note that here the coupling has been absorbed into the WC as compared to Eq. 3.103). In Chapter 5, the sensitivity of the future FCC-ee collider to HNLs will be explored within the νSMEFT and νLEFT frameworks, focusing on operators with $d \leq 7$ that contribute to the relevant processes, shown in Table 3.1, which can modify the SM process $e^+e^- \to \nu\nu$ and induce the single and

---

[10] This cut-off scale is loosely determined based on collider accessibility considerations.

pair production of HNLs, $e^+e^- \to \nu N/NN$, as well as lead to their decays. These operators can be generated at tree-level by various UV complete models as discussed in Appendix D, such as Type I and inverse seesaw. The table contains $d = 6$ (top) and $d = 7$ (bottom) operators, which generate $\Delta L = 0$ and $\Delta L = \pm 2$ operators, respectively (the LNV operators can be seen to include the charge conjugate fields ν^c and N^c).

Below the EW scale, the relevant framework is the low-energy EFT (LEFT). This is an effective theory of the SM applicable to the broken phase, i.e. respecting the residual $\mathrm{SU}(3)_c \times \mathrm{U}(1)_{\mathrm{em}}$ gauge symmetry. The field content of LEFT is identical to the SM, except for fields with masses comparable to v, such as the $W^\pm$, Z, h bosons and t, the top quark, which are integrated out. This simplifies the operators and processes involved mathematically, while still retaining the effects of the physics living at a higher scale. Any constraints derived on LEFT operators can be matched onto the SMEFT operators via matching conditions.

Similarly, νSMEFT operators induce νLEFT operators at low energies. However, at the energies applicable to the FCC, $W^\pm$, Z and Higgs are all dynamical fields, hence instead of being integrated out, the gauge fields are rotated to their mass basis and the Higgs is expanded perturbatively around v. For the sensitivity analysis, two Lagrangians are required, for the Majorana and Dirac cases, in terms of effective operators in mass basis. To this end, we start with the $\psi^4 H^n$ operators in Table 3.1, which generate the four-fermion effective interactions at the EW scale

$$\begin{aligned}\mathcal{L} \supset & \left[\frac{1}{2}C_{\nu e}^{V,LX}(\bar{\nu}\gamma_\mu \nu) + C_{\nu Ne}^{V,RX}(\bar{\nu}^c\gamma_\mu N) + \frac{1}{2}C_{Ne}^{V,RX}(\bar{N}\gamma_\mu N)\right](\bar{e}\gamma^\mu P_X e) \\ & + \left[\frac{1}{2}C_{\nu e}^{S,LX}(\bar{\nu}^c \nu) + C_{\nu Ne}^{S,RX}(\bar{\nu}N) + \frac{1}{2}C_{Ne}^{S,RX}(\bar{N}^c N)\right](\bar{e}P_X e) \\ & + \left[\frac{1}{2}C_{\nu e}^{T,LX}(\bar{\nu}^c\sigma_{\mu\nu}\nu) + C_{\nu Ne}^{T,RX}(\bar{\nu}\sigma_{\mu\nu}N) + \frac{1}{2}C_{Ne}^{T,RX}(\bar{N}^c\sigma_{\mu\nu}N)\right](\bar{e}\sigma^{\mu\nu}P_X e) + \text{h.c.},\end{aligned} \tag{3.105}$$

where $C^{Y,RX}$ are the Wilson coefficients, where $Y = V, S, T$ denotes the vector, scalar and tensor Lorentz structure of the effective operator, respectively, while $X = R, L$

ψ^4		ψ^2H^2D	
Q_{lS}	$(\bar{L}\gamma_\mu L)(\bar{S}\gamma^\mu S)$	Q_{HS}	$(\bar{S}\gamma_\mu S)(H^\dagger i\overleftrightarrow{D}^\mu H)$
Q_{eS}	$(\bar{e}\gamma_\mu e)(\bar{S}\gamma^\mu S)$		

ψ^4H		ψ^2H^3D	
Q_{lSlH}	$\varepsilon_{ij}(\bar{L}\gamma_\mu L)(\bar{S}\gamma^\mu L^i)H^j$	Q_{Sl1}	$\varepsilon_{ij}(\bar{S}\gamma_\mu L^i)(iD^\mu H^j)(H^\dagger H)$
Q_{eSlH}	$\varepsilon_{ij}(\bar{e}\gamma_\mu e)(\bar{S}\gamma^\mu L^i)H^j$	Q_{Sl2}	$\varepsilon_{ij}(\bar{S}\gamma_\mu L^i)H^j(H^\dagger i\overleftrightarrow{D}^\mu H)$
Q_{lSNeH}	$(\bar{L}S^c)(\bar{N}^c e)H$		
Q_{elSNH}	$H^\dagger(\bar{e}L)(\bar{S}N)$		

Table 3.2: Additional $\Delta L = 0$ νSMEFT operators at $d = 6$ (above) and $d = 7$ (below) when the gauge singlet field S is present.

is the chirality of the charged lepton bilinear [11] and P_X is the chirality projection operator. It should be noted that the weak eigenstate indices have been omitted for simplicity. Instead, the operators of type $\psi^2H^nD^2$ induce the effective $W^\pm$ and Z interactions at the EW scale

$$\begin{aligned}\mathcal{L} \supset &-\frac{g}{\sqrt{2}}\Big[W^L_\nu(\bar{\nu}\gamma_\mu e) + W^R_\nu(\bar{\nu}^c\gamma_\mu e) + W^L_N(\bar{N}^c\gamma_\mu e) + W^R_N(\bar{N}\gamma_\mu e)\Big]W^{+\mu} \\ &-\frac{g}{c_w}\left[\frac{1}{2}Z^L_\nu(\bar{\nu}\gamma_\mu\nu) + Z^R_{\nu N}(\bar{\nu}^c\gamma_\mu N) + \frac{1}{2}Z^R_N(\bar{N}\gamma_\mu N)\right]Z^\mu + \text{h.c.}, \qquad (3.106)\end{aligned}$$

with g denoting the $SU(2)_L$ gauge coupling and $c_w = \cos\theta_w$, where θ_w is the weak mixing angle. As the νSMEFT operators lead to LNV operators, the above expressions are valid for the Majorana HNL case.

The lepton number conserving (LNC) limit of Eq. 3.104 can be considered if beyond RH neutrinos the SM is further extended by the SM gauge singlet field S, as in the case of the inverse seesaw, with lepton number assignment $L(\nu) = L(N) = L(S) = +1$. Then the effective Lagrangian takes the form

$$\mathcal{L} = \mathcal{L}_{\text{SM}} + \bar{N}i\not{\partial}N + \bar{S}i\not{\partial}S - \left[\bar{L}Y_\nu N\tilde{H} + \bar{S}M'N + \text{h.c.}\right] + \sum_i C^{(d)}_i Q^{(d)}_i, \qquad (3.107)$$

with the sum now running over only the LNC operators. Naturally, any further

---

[11] This can be found by algebraic manipulation of the projection operators, $f_{L/R} = P_{L/R}f$, and using the properties $(\gamma^5)^\dagger = \gamma^5$, $\{\gamma^5, \gamma^\mu\} = 0$ and $P^2_{R/L} = P_{R/L}$ (and remembering that $\sigma^{\mu\nu} = \frac{i}{2}[\gamma^\mu, \gamma^\nu]$).

extensions of the field content will in general induce additional operators that will contribute to the relevant processes and would therefore need to be included.

With the addition of S and forbidding any $\Delta L = \pm 2$ operators, the additional $\Delta L = 0$ operators in Table 3.2 need to be considered. As a result, besides the LNC interactions in Eqs. 3.105 and 3.106, the additional four-fermion interactions will be induced

$$\begin{aligned}\mathcal{L} \supset & \left[C^{V,LX}_{\nu Se}(\bar{\nu}\gamma_\mu S) + \frac{1}{2}C^{V,LX}_{Se}(\bar{S}\gamma_\mu S)\right](\bar{e}\gamma^\mu P_X e) \\ & + C^{S,RX}_{SNe}(\bar{S}N)(\bar{e}P_X e) + C^{S,RX}_{SNe}(\bar{S}\sigma_{\mu\nu}N)(\bar{e}\sigma^{\mu\nu}P_X e) + \text{h.c.},\end{aligned} \tag{3.108}$$

alongside the additional effective $W^\pm$ and Z interactions and effective $W^\pm$ and Z interactions

$$\mathcal{L} \supset -\frac{g}{\sqrt{2}}W^L_S(\bar{S}\gamma_\mu e)W^{+\mu} - \frac{g}{c_w}\left[Z^L_{\nu S}(\bar{\nu}\gamma_\mu S) + \frac{1}{2}Z^L_S(\bar{S}\gamma_\mu S)\right]Z^\mu + \text{h.c.}, \tag{3.109}$$

3.6.2 Low Energy EFT for β-decay

In Chapter 4, the sensitivity of tritium beta-decay experiments to new physics will be assessed. For a model-independent analysis it is once again useful to adopt an EFT approach. At the energies involved the appropriate framework is a low-energy EFT, which considers all possible Lorentz bilinear structures, listed in Table 3.3.

Type	Form	Components
Scalar	$\bar{\psi}\psi$	1
Pseudoscalar	$\bar{\psi}\gamma^5\psi$	1
Vector	$\bar{\psi}\gamma_\mu\psi$	4
Axial vector	$\bar{\psi}\gamma_\mu\gamma^5\psi$	4
Tensor	$\bar{\psi}\sigma_{\mu\nu}\psi$	6

Table 3.3: The five possible Lorentz invariant bilinear structures.

Using these Lorentz invariant structures, chiral combinations expanded in the

$\overset{(\sim)}{\varepsilon}_j$	$\mathcal{O}_j$	$\mathcal{O}'_j$
ε_L	$\gamma_\mu(\mathbb{1}-\gamma_5)$	$\gamma^\mu(\mathbb{1}-\gamma_5)$
$\tilde{\varepsilon}_L$	$\gamma_\mu(\mathbb{1}+\gamma_5)$	$\gamma^\mu(\mathbb{1}-\gamma_5)$
ε_R	$\gamma_\mu(\mathbb{1}-\gamma_5)$	$\gamma^\mu(\mathbb{1}+\gamma_5)$
$\tilde{\varepsilon}_R$	$\gamma_\mu(\mathbb{1}+\gamma_5)$	$\gamma^\mu(\mathbb{1}+\gamma_5)$
ε_S	$\mathbb{1}-\gamma_5$	$\mathbb{1}$
$\tilde{\varepsilon}_S$	$\mathbb{1}+\gamma_5$	$\mathbb{1}$
$-\varepsilon_P$	$\mathbb{1}-\gamma_5$	γ^5
$-\tilde{\varepsilon}_P$	$\mathbb{1}+\gamma_5$	γ^5
ε_T	$\sigma_{\mu\nu}(\mathbb{1}-\gamma_5)$	$\sigma^{\mu\nu}(\mathbb{1}-\gamma_5)$
$\tilde{\varepsilon}_T$	$\sigma_{\mu\nu}(\mathbb{1}+\gamma_5)$	$\sigma^{\mu\nu}(\mathbb{1}+\gamma_5)$

Table 3.4: Coupling constants and operators encoding new physics contributions to the effective CC Lagrangian in Eq. 3.111

basis of the 4×4 gamma-matrices can be constructed

$$\begin{aligned} L \equiv \mathbb{1}-\gamma^5, \quad R \equiv \mathbb{1}+\gamma^5, \\ L_\mu \equiv \gamma_\mu L, \quad R_\mu \equiv \gamma_\mu R, \\ L_{\mu\nu} \equiv \sigma_{\mu\nu} L, \quad R_{\mu\nu} \equiv \sigma_{\mu\nu} R \end{aligned} \tag{3.110}$$

where $\mathbb{1}$ is understood to be the identity matrix of the same dimensions as the gamma-matrices and $\sigma_{\mu\nu} = \frac{i}{2}[\gamma_\mu, \gamma_\nu]$, while the L and R symbols reflect the chiral structures analogously to the projection operators in Eq. 2.2.

The process of beta-decay relevant to Chapter 4 is a CC process. Thus the relevant Lagrangian encoding both the SM contributions as well as possible new physics contributions arising from $d = 6$ operators is

$$\mathcal{L}_{CC} = -\frac{G_F V_{ud}}{\sqrt{2}} \left[(1+\delta_\beta) \left(\bar{e} L_\mu \nu_e\right) \left(\bar{u} L^\mu d\right) + \sum_j \overset{(\sim)}{\varepsilon}_j \left(\bar{e} \mathcal{O}_j \nu_e\right) \left(\bar{u} \mathcal{O}'_j d\right) \right] + \text{h.c.}, \tag{3.111}$$

where $\overset{(\sim)}{\varepsilon}_j$ are the coupling constants of the operators listed in Table 3.4, G_F is the Fermi constant, u and d are the up- and down-quarks, respectively, while V_{ud} is the CKM matrix element relating them, and δ_β quantifies the deviation from the SM (with $\delta_\beta = 0$ recovering the purely SM limit). Furthermore, e and ν_e denote the electron and electron-type SM active neutrino fields (which can in general contain a heavy RH neutrino component if the SM is extended with RH massive neutrinos). If there are no RH neutrinos, then the $\overset{(\sim)}{\varepsilon}_j$ couplings vanish.

Chapter 4

Sterile Neutrinos in Tritium Beta Decay

We have seen that the phenomenon of neutrino oscillation is confirmation of the massive nature of the SM active neutrinos. It has also been shown explicitly in Sec. 3.1, that oscillations depend on the mass difference of the states, and therefore oscillation data cannot be used to determine the absolute values of the neutrino masses. As we have seen in Sec. 3.3, the absolute mass scale of neutrinos is being constrained through indirect cosmological measurements and in neutrinoless double beta-decay searches, as well as in direct beta-decay experiments. In this section, we focus on the single beta-decay of tritium, which is a popular choice of isotope for future experiments due to its favourable properties, as outlined in Sec. 3.3.3. Thus, the process of interest is

$$^{3}\mathrm{H} \rightarrow {}^{3}\mathrm{He} + e^{-} + \bar{\nu}_{e} \tag{4.1}$$

whereby the hydrogen isotope, tritium, decays into helium, an electron and an electron-type antineutrino. Since the energy of this interaction is significantly lower than the W mass, the Lagrangian can be written without including the W boson explicitly, but instead using an effective dimension-6 operator to approximate the process as a four-fermion interaction of the form

$$\mathcal{L} = -\frac{G_F}{\sqrt{2}} V_{ud} \left[\bar{e}\gamma^{\mu}(1-\gamma^5)\nu_e \right] \left[\bar{u}\gamma_{\mu}(1-\gamma^5)d \right] + \text{h.c.}, \tag{4.2}$$

where G_F is the Fermi constant, u, d, e and ν_e are up and down quarks, electron and electron-type neutrino fields, respectively, and V_{ud} is the CKM matrix element parameterising the mixing between up and down quarks. The above Lagrangian is equivalent to that shown in Eq. 3.111 with $\delta_\beta = 0$, all $\overset{(\sim)}{\varepsilon_j} = 0$ and L_μ given in Eq. 3.110.

As has been discussed in previous sections, single beta decay is the only realistic direct probe to measure the absolute scale of neutrino masses and their orderings. The neutrino itself is relatively inert and rarely partakes in any interactions, therefore it escapes detectors without being observed. On the other hand, the beta particle, i.e., the electron, possesses EM charge and therefore interacts readily and is thus easy to detect. As a result, neutrino mass experiments relying on single beta-decay measure the outgoing electron's energy to infer the mass of the neutrino, which affects the energy available to the electron, and produces a characteristic signature, most pronounced near the endpoint energy of the spectrum. It can thus be seen that this method relies solely on the kinematics of the process and is therefore completely model independent. However, the difficulty that such experiments face are mainly two-fold. Firstly, the electron energy spectrum is only instructive when the emitted beta-particle receives maximal kinetic energy, i.e. when the neutrino is effectively left with energy sufficient only to account for its mass. However, only a very small percentage of electrons created in beta-decays will possess such high energies and thus it may be challenging for experiments to obtain the required event numbers and hence statistics. Secondly, the variation around the endpoint of the energy spectrum induced by the very light neutrino mass will will be correspondingly small, requiring high precision measurements. Obtaining the necessary energy resolution can thus pose technical challenges in an actual experiment. In addition, uncertainties in the form of spectral corrections – which will be discussed in more detail – ultimately limit the precision with which the spectral shape may be know.

The electron-type antineutrino produced in beta-decay is a linear superposition of three mass states and therefore, the final state neutrino does not have a well defined mass. With current technological limitations, it is not feasible to resolve the different mass-states that the electron-neutrino is composed of. Instead, beta-decay experiments constrain the so-called effective mass [168]

$$m_\beta^2 = \sum_{i=1}^{3} |U_{ei}|^2 m_i^2, \tag{4.3}$$

where $i = 1,2,3$ denotes the three mass eigenstates and U_{ei} are the PMNS mixing matrix elements coupling these mass states to the electron type neutrino in the flavour basis. At the time of writing, the most constraining upper bound on m_β is $m_\beta < 0.45$ eV at 90% CL, set by the KATRIN experiment [42], which is projected to constrain the effective mass at $m_\beta \sim 0.2$ eV at 90 % CL [169] by the end of its campaign. This ultimate sensitivity however, does not guarantee measurement, because in the 'worst' case scenario with a massless lightest mass state and normal ordering, the effective mass is $m_\beta \sim 9$ meV and thus below the reach of KATRIN. Therefore, in order to ensure guaranteed measurement of the effective mass, new experimental techniques need to be employed. The most promising of these is a proposal by the Project 8 collaboration [170], who intend to infer the energy of the beta-electron through a measurement of its cyclotron radiation, which is emitted in response to the presence of a constant magnetic field. The upshot of this approach is that frequency can be measured with a higher precision, resulting in improved resolution with respect to the energy of the electron. Another area of improvement could be the use of atomic tritium instead of a molecular source, as in the case of KATRIN, since the uncertainties resulting from the molecular degrees of freedom ultimately limit the precision of such neutrino mass experiments. Combining the use of cyclotron radiation measurements techniques with the use of atomic tritium, Project 8 estimate their sensitivity to the effective mass at $m_\beta \sim 40$ meV [170], which will guarantee measurement of the effective mass in the case of inversely ordered neutrinos, as in that case the minimum value is $m_\beta \sim 50$ meV. The Cyclotron Radiation Emission Spectroscopy Demonstrator Apparatus (CRESDA), in addition to the use of atomic tritium and cyclotron radiation, aims to develop quantum technologies to increase the sensitivity reach of future experiments even further [171].

Such β-decay neutrino mass experiments need high statistics to make statistically robust measurements. This translates to approximately 10^5–10^6 tritium decay electrons in the last eV of the electron energy spectrum when probing m_β at the order of $\mathcal{O}(10)$ meV. Since the end-point region is the least populated, a large event number in the tail necessarily means that high statistics are achieved across the spectrum. Such tritium decay experiments can thus be designed in a way as to be sensitive to the entirety of the spectrum and look for signatures of new physics, that produce experimental signatures towards the bulk of the distribution. In this section, which is based on [172] and largely follows the same structure, we study the sensitivity of such future tritium β-decay experiments to New Physics, focusing on the phenomenology of keV-scale sterile neutrinos and also touching upon exotic charged currents that differ from the usual $V-A$ current of the SM.

As we have seen, the SM contains fermions with Dirac masses, that are generated by Yukawa couplings between the right handed singlets and the left handed doublets under $SU(2)$. The SM neutrinos however, lack right handed singlet partners therefore motivating the extension of the SM. These additional particles need to be completely uncharged under the SM gauge group to be consistent with their lack of participation in any of the SM interactions and are thus referred to as sterile neutrinos. The simplest and most natural extension involves the introduction of a right handed sterile neutrino that can be coupled to the Higgs boson alongside the left handed SM neutrinos to give rise to a Dirac mass term for the active states, analogously to the fermionic mass generation mechanism. Being a gauge singlet, the sterile neutrino is free to have a Majorana mass. This type of extension constitutes the seesaw mechanism [173], resulting in a mass matrix that involves the Dirac mass terms as well as the Majorana mass term associated with the sterile state. Diagonalisation of this matrix results in mass states that are combinations of the sterile neutrino and the SM neutrinos, thus inducing mixing between the active and sterile sectors. As a result, the PMNS mixing matrix needs to be extended to $3+n_s$

dimensions, where n_s denotes the number of sterile states introduced. In tritium decay experiments, such an extension results in the production of keV-scale sterile neutrinos via active-sterile mixing, as long as kinematically possible, i.e. as long as the sterile mass is below the Q-value (the total energy released in the process) of tritium, $Q = 18.59$ keV.

Extending the SM with right-handed neutrinos leads to the question of whether there is a fundamental left-right symmetry in nature. This would involve a right-handed weak interaction, mirroring its left-handed counterpart within the SM, although differing in that it would need to be broken at much higher energy scales than the weak force. If it exists, such a right handed force can induce exotic interactions with phenomenological imprints on the β-decay spectrum of tritium. Even more generally, in this work we consider the full basis of Lorentz invariant hadronic operators that may couple to the left- and right-handed leptonic currents [174].

4.1 Current & Future Experiments

The quest to measure the mass of the neutrinos has seen the emergence of numerous experiments. Despite these experimental efforts, however, such a measurement has yet to be made, with experiments only being able to put upper bounds on the mass.

The strongest bounds on the absolute masses of muon- and tau-neutrinos come from precision measurements of decay processes. The most stringent constraint on m_{ν_μ} is $m_{\nu_\mu} < 0.17$ MeV at 90 % CL, which was extracted from precision measurements of pion decay, $\pi^+ \to \mu^+ \nu_\mu$ [175]. For m_{ν_τ}, the strongest upper bound is $m_{\nu_\tau} < 18.2$ MeV at 95 % CL, set by the ALEPH experiment [176], which performed precision measurements of the tau decay processes $\tau^- \to \nu_\tau \pi^- \pi^+ \pi^-$ and $\tau^- \to \nu_\tau 2\pi^- 2\pi^+ \pi^- (\pi^0)$. Both of these bounds are orders of magnitude looser than the constraints coming from oscillation experiments and the existing upper bounds on the electron-neutrino mass, m_{ν_e} and therefore β-decay experiments seem to be the most promising direct searches.

Depending on the absolute mass of the neutrino, current β-decay experimental efforts may not be sufficient to guarantee measurement, calling for a new generation of tritium β-decay neutrino mass experiments, with improved technical parameters to reach the required precision and event counts. Therefore, this section is dedicated to the discussion of current and future experiments that play and will play prominent roles in the effort of measuring the masses of the neutrinos.

4.1.1 KATRIN & TRISTAN

Currently, the most stringent upper bound on the effective neutrino mass is $m_\beta < 0.45$ eV at 90% CL set by the KATRIN collaboration [42], which presents an almost factor of two improvement upon their previous result of $m_\beta < 0.8$ eV at 90% CL [169]. The molecular gaseous tritium source emits electrons isotropically, which are then collimated using strong magnetic fields, in a way that minimises the transverse components of their momentum for transportation to the main detector. Given that KATRIN's goal is to measure the effective neutrino mass, with this mass having the biggest impact near the end point of the electron's energy spectrum, the experiment focuses on the final 300 eV region of the distribution, by employing a high-pass filter which only lets through electrons with a substantially high kinetic energy. This way, rather than measuring the energy of each electron individually, KATRIN performs an integrated count, from which the entirety of the spectrum is reconstructed. In the absence of mass measurement, the collaboration estimates the ultimate sensitivity to be $m_\beta < 0.2$ eV [177]. Once this limit is reached, a new generation of experimental efforts will be required. Increasing the energy resolution of KATRIN would require a weaker magnetic field to reduce broadening of the electron energy, but this necessitates a larger cross-sectional area, due to flux conservation, $\Phi = B \cdot A$. As the entire experimental set-up is around 70 m long, with the collimator machinery being 10 m long alone, sizing up is not a practically or financially realistic possibility [178].

TRISTAN is a proposed extension to the KATRIN experiment, with the objective of searching for sterile neutrino signatures in β-decay using the same gaseous molecular tritium source as KATRIN. As will be discussed in the coming sections, the experimental signature of sterile neutrinos (depending on their exact mass) is predominantly found along the bulk of the energy spectrum, rather than around the end-point, as is the case for the active SM neutrinos. Therefore, KATRIN's read-out system, which is designed to count the highest energy electrons of which there are very few, is not suitable for TRISTAN'S purposes, due to the increased event count resulting from studying the entire spectrum in a sterile search. TRISTAN will thus be equipped with its own read-out and event processing system that is able to handle the large number of events. The sterile neutrino search will commence upon the conclusion of KATRIN's campaign, expected around 2025 [179].

4.1.2 Project 8

The Project 8 collaboration was formed with the goal of directly measuring the electron neutrino mass in tritium β-decay, using the novel technology of Cyclotron Radiation Emissions Spectroscopy (CRES) [170].

When a charged particle, in this case the emitted electron, travels through a region of space permeated by a constant uniform magnetic field, it experiences Lorentz force, which, depending on the direction of the magnetic field and the velocity of the particle, will result in axial or helical motion. Since circular motion involves acceleration due to the constant change in the velocity direction, the electron will emit EM radiation termed cyclotron radiation, with a frequency

$$f = \frac{1}{2\pi}\frac{eB}{E_e}, \tag{4.4}$$

where B denotes the magnetic field strength, e is the charge of the electron and E_e is the electron's energy. The technology to measure this frequency to a high precision already exists and if the magnetic field strength is known well enough, yields high energy resolution, which is crucial for neutrino mass measurement.

The Project 8 collaboration estimates that the use of molecular tritium presents an irreducible limit in the energy resolution of ≈ 0.3 eV [180], due to the Final State Distribution (FSD) problem. The FSD arises due to the various rotational and vibrational degrees of freedom associated with the final state daughter molecule. The contributions from these different energy configurations available to the system are included via a probabilistic sum, which leads to a broadening of the spectrum.

To circumvent this issue, Project 8 is proposing to use an atomic rather than molecular tritium source. The collaboration estimates that this modification combined with the novel use of CRES technology will ultimately allow them to place an upper limit on the effective neutrino mass of $m_\beta \lesssim 40$ meV [170]. In addition, the set-up will be able to analyse the entirety of the spectrum, not just the end point, with an energy resolution of ~ 100 eV [181]. Since in the 'worst'-case scenario the effective mass is $m_\beta \sim 40$ meV for IO and $m_\beta \sim 9$ meV for NO, Project 8 expect to be able to decisively conclude the mass ordering of neutrinos, even if the exact value of the effective mass is not measured in the NO scenario.

Phase I of the experimental effort involved demonstration of the feasibility of the CRES concept using a gaseous source of krypton. In Phase II, the collaboration successfully performed the first measurement of the tritium energy spectrum. Currently, the project is in Phase III, with the aim of producing and trapping atomic tritium and performing CRES measurements in free space, before moving onto the final stage, Phase IV, which will see the measurement of neutrino mass with the projected sensitivity. Phase IV is expected to commence in the 2030s [182].

4.1.3 CRESDA

Although the Project 8 experiment, based on their projected sensitivities, will be able to conclusively decide the mass hierarchy of the SM neutrino sector, the experiment's sensitivity will not be enough, should the neutrino mass realised in nature be below ≈ 40 meV. Thus, for a guaranteed mass measurement, even higher energy resolution is required. This motivated the formation of the *Quantum Technologies for Neutrino Mass* (QTNM) consortium – a joint effort between several UK institutes – with the goal of making a guaranteed direct neutrino mass measurement, via the employment of quantum technologies [183].

The CRES Demonstration Apparatus, the first and current phase of the project, involves development and testing of the proposed technologies operating with hydrogen and deuterium atoms. In the following stage, the same techniques will be tested on atomic tritium. The three main challenges associated with CRES technology that the QTNM consortium in its current development stage aims to address are: i) production and trapping of tritium atoms using a magnetic trap, ii) high precision mapping of the magnetic field using quantum sensors and iii) developing quantum devices for microwave spectroscopy enabling the high precision detection of cyclotron radiation. In the initial 3-year R&D period between 2021 and 2024, the consortium will attempt to address these challenges and produce a prototype that is 'tritium-ready'. To achieve this, CRESDA aims to achieve the following strategic goals: i) produce deuterium and tritium atoms with densities of $\sim 10^{12}-10^{14}\ \mathrm{cm}^{-3}$, ii) to use the deuterium and tritium atoms in Rydberg magnetometry to map the magnetic field with a precision of $< 1\ \mu\mathrm{T}$ and iii) to develop the electronics required for the detection and processing of the microwave radiation.

The next step, estimated to take place around 2025-2029 will involve moving the CRESDA set-up to a tritium facility, most likely to the Culham Centre for Fusion Energy, where the experimental feasibility will be demonstrated on tritium with $\mathcal{O}$(eV) sensitivity. If all goes according to plan, the fully operational QTNM experiment will start data taking from 2029 onwards.

4.2 Mathematical Formalism

The typical energies involved in tritium decay experiments are around $\mathcal{O}(10\ \mathrm{keV})$ and therefore the low energy EFT approach, outlined in Sec. 3.6.2, is appropriate to use, as long as any other BSM physics states have masses $m_{\mathrm{BSM}} \gg 10$ keV. The starting point is the quark-level Lagrangian shown in Eq. 4.2, from which the analogous hadronic-level Lagrangian may be written as

$$\mathcal{L}_{\mathrm{SM}} = -\frac{G_F}{\sqrt{2}} V_{ud}(1+\delta_\beta)\left[\bar{e}\gamma^\mu(1-\gamma^5)\nu_e\right]\left[\overline{^3\mathrm{He}}\gamma_\mu\left(g_V - g_A\gamma^5\right){}^3\mathrm{H}\right] + \mathrm{h.c.} \quad (4.5)$$

This describes the effective 4-point interaction between tritium (^{3}H), helium (^{3}He), an electron (e) and an electron-type neutrino (ν_e) where G_F denotes the Fermi constant, g_V and g_A are the vector and axial-vector couplings, respectively, with values $g_V = 1$ and $g_A \approx 1.247$ [184]. V_{ud} is the CKM matrix element relating the u and d quarks, which are the constituents of the neutrons and protons and where δ_β quantifies the deviation from the SM and thus $\delta_\beta = 0$ in the SM case. As stated before, this is analogous to the quark-level Lagrangian, as the tritium and helium isotopes can be treated as approximate constituents of an $SU(2)$ isospin doublet. This is because the u and d quarks form an isospin doublet, and therefore protons and neutrons and hence the two isotopes under considerations also form an approximate doublet, since the strong force affects them in a very similar way. The term $\bar{e}\gamma^{\mu}(1-\gamma^5)\nu_e$ is the leptonic current, while $\overline{^3\mathrm{He}}\gamma_{\mu}\left(g_V - g_A\gamma^5\right){}^3\mathrm{H}$ is the hadronic current. Higher order terms $\mathcal{O}(Q/m_{\mathrm{H}})$ are neglected here, because $Q \sim 20$ keV and $m_H \sim 3$ GeV and hence $Q \ll m_H$ and thus the decay energy is much lower than the mass of the tritium isotope [174]. The process of course is influenced by the particular spin states of the fermions involved, however instead of averaging over them, we focus on specific spin configurations in order to explore correlation effects between the direction of momentum of the emitted electron and the spin orientation of the decaying tritium.

The above Lagrangian is the result of an effective operator approach, which is perfectly fine to adopt, as the typical energies of the process are much below the electroweak scale. Therefore, it is possible to integrate out any heavy particles, such as the W-boson mediating the process of interest, as its mass is much above the typical energy of the tritium decay, and hence the propagator does not appear in the Lagrangian.

In order to explore the effects of New Physics, express the full Lagrangian of interest as

$$\mathcal{L} = \mathcal{L}_{\mathrm{SM}} + \mathcal{L}_{\mathrm{exotic}} + \mathcal{L}^{N}_{\mathrm{exotic}}, \tag{4.6}$$

The term $\mathcal{L}_{\mathrm{exotic}}$ contains all possible Lorentz invariant contributions to the Fermi interaction besides the left-handed $V-A$ in the form of EFT operators. Such exotic contributions can be right-handed $V+A$ interactions, or scalar, pseudoscalar, or tensor Lorentz structures. The consideration of such interactions results in the

Current	Hadronic	Leptonic
Scalar	$H_S = g_S \, \overline{^3\mathrm{He}} \, ^3\mathrm{H}$	$j_S^{\pm} = \bar{e}(1 \pm \gamma^5)\nu_e$
Pseudoscalar	$H_P = g_P \, \overline{^3\mathrm{He}} \, \gamma^5 \, ^3\mathrm{H}$	$j_P^{\pm} = \bar{e} \, (1 \pm \gamma^5)\nu_e$
Vector/Axial	$H^{\mu}_{V\pm A} = \overline{^3\mathrm{He}}\gamma^{\mu}(g_V \pm g_A\gamma^5) \, ^3\mathrm{H}$	$j^{\mu}_{V\pm A} = \bar{e}\gamma^{\mu}(1 \pm \gamma^5)\nu_e$
Left-Tensor	$H_T^{\mu\nu} = g_T \, \overline{^3\mathrm{He}} \, \sigma^{\mu\nu}(1-\gamma^5) \, ^3\mathrm{H}$	$j_T^{\mu\nu} = \bar{e} \, \sigma^{\mu\nu}(1-\gamma^5)\nu_e$
Right-Tensor	$\tilde{H}_T^{\mu\nu} = g_T \, \overline{^3\mathrm{He}} \, \sigma^{\mu\nu}(1+\gamma^5) \, ^3\mathrm{H}$	$\tilde{j}_T^{\mu\nu} = \bar{e} \, \sigma^{\mu\nu}(1+\gamma^5)\nu_e$

Table 4.1: Hadronic and leptonic fermion bilinear currents, where $\sigma^{\mu\nu} = \frac{i}{2}[\gamma^{\mu}, \gamma^{\nu}]$.

exotic Lagrangian [174]

$$\begin{aligned}\mathcal{L}_{\text{exotic}} = -\frac{G_F}{\sqrt{2}}V_{ud}\Big(&\tilde{\varepsilon}_L H^{\mu}_{V-A} j_{\mu,V+A} + \varepsilon_R H^{\mu}_{V+A} j_{\mu,V-A} + \tilde{\varepsilon}_R H^{\mu}_{V+A} j_{\mu,V+A} \\ &+ \varepsilon_S H_S j_S^- + \tilde{\varepsilon}_S H_S j_S^+ - \varepsilon_P H_P j_P^- - \tilde{\varepsilon}_P H_P j_P^+ \\ &+ \varepsilon_T H_T^{\mu\nu} j_{T,\mu\nu} + \tilde{\varepsilon}_T \tilde{H}_T^{\mu\nu} \tilde{j}_{T,\mu\nu}\Big) + \text{h.c.},\end{aligned} \tag{4.7}$$

where H and j are the hadronic and leptonic currents respectively, with the subscripts denoting the underlying Lorentz structure, i.e. $V-A$, $V+A$, scalar (S), pseudoscalar (P) and tensor (T). The different currents are summarised in Table 4.1. The strength of the interactions is parameterised by ε_i and $\tilde{\varepsilon}_i$, where the subscript refers to the nature of the hadronic currents, $i = S, P, T, L, R$ and the tilde denotes a right-handed leptonic current.

The parameters g_X in Table 4.1, where $X = S, P, T, V, A$, are form factors, which describe the interaction of a hadron with an external probe and therefore depend on the momentum transfer, Q^2. For low values of Q^2, the hadron is only probed softly and interacts similarly to a point-like particle. This leads to the form factor being close to its value at $Q^2 = 0$, i.e. $g_X(Q^2) \approx g_x(0)$. On the other hand, for large Q^2, the probe is able to resolve the internal quark-gluon structure and the interaction is distributed over the internal dynamics and the form factor is hence smaller in value. Although in the process considered here there is no explicit probe, the weak interaction itself serves this purpose and the general behaviour of the form factors is as outlined. To assess the effect of Q^2 on g_X one needs to study the non-trivial Q^2-dependence, however a simple approximation in the dipole parameterisation form [184]

$$g_X(Q^2) = \frac{g_X(0)}{\left(1 - \frac{Q^2}{M_X^2}\right)^2} \tag{4.8}$$

models the dependence well. The characteristic mass scale, M_X, is usually taken as $M_X \sim 1$ GeV, which fits the experimental single-nucleon data well. Remembering that $Q \sim 20$ keV, we see that $M_X \gg Q$, hence $g_X(Q^2) \sim g_X(0)$ and the momentum dependence can be safely ignored [184].

The third term in Eq. 4.6 is the Lagrangian containing sterile neutrinos, expressed as

$$\begin{aligned}\mathcal{L}^N_{\text{exotic}} = -\frac{G_F}{\sqrt{2}} V_{ud} \Big(& \varepsilon^N_L H^\mu_{V-A} J_{\mu,V-A} + \tilde{\varepsilon}^N_L H^\mu_{V-A} J_{\mu,V+A} \\ & + \varepsilon^N_R H^\mu_{V+A} J_{\mu,V-A} + \tilde{\varepsilon}^N_R H^\mu_{V+A} J_{\mu,V+A} \\ & + \varepsilon^N_S H_S J^-_S + \tilde{\varepsilon}^N_S H_S J^+_S - \varepsilon^N_P H_P J^-_P - \tilde{\varepsilon}^N_P H_P J^+_P \\ & + \varepsilon^N_T H^{\mu\nu}_T J_{T,\mu\nu} + \tilde{\varepsilon}^N_T \tilde{H}^{\mu\nu}_T \tilde{J}_{T,\mu\nu} \Big) + \text{h.c.}.\end{aligned} \tag{4.9}$$

where once again ε^N_i and $\tilde{\varepsilon}^N_i$ are the coupling constants with $i = L, R, S, P, T$ denoting the nature of the hadronic current and the tilde signifying a right-handed leptonic current. The possible currents are the same as those listed in Table 4.1 but with $j \to J$ and $\nu_e \to N$ exchanged. The N superscript is used to signify that these couplings are associated with a sterile neutrino state.

In this work we assume a minimal particle content consisting of one electron neutrino, ν_e and one sterile neutrino, N, with mass $m_N \lesssim 18$ keV. Since there are only two neutrinos, the relation between the flavour and the mass eigenstates ν_1 and ν_2 is expressed as

$$\begin{pmatrix} \nu_e \\ N \end{pmatrix} = \begin{pmatrix} \cos\theta & \sin\theta \\ -\sin\theta & \cos\theta \end{pmatrix} \begin{pmatrix} \nu_1 \\ \nu_2 \end{pmatrix}. \tag{4.10}$$

Defining the active-sterile mixing angle as $V_{eN} = \sin\theta$ and using the relation

$\sin^2\theta + \cos^2\theta = 1$, the two interaction eigenstates can be expressed as

$$\begin{aligned}\nu_e &= \sqrt{1-V_{eN}^2}\,\nu_1 + V_{eN}\,\nu_2,\\ N &= -V_{eN}\,\nu_1 + \sqrt{1-V_{eN}^2}\,\nu_2.\end{aligned} \tag{4.11}$$

Since the experimental constrains on the parameter V_{eN} are quite severe [185], $0 \leq V_{eN} \ll 1$ hence $\sqrt{1-V_{eN}^2} \gg V_{eN}$ and thus it is apparent that the state ν_1 is mostly active and SM-like, while ν_2 is largely sterile. From the Lagrangian in Eq. 4.6 we thus see that the sterile neutrino may be produced by exotic currents, or through mixing with the active sector.

4.3 Spectral Corrections

Before deriving the decay rate of tritium in Sec. 4.4, there are theoretical correction factors that need to be taken into account when considering the decay of atomic tritium. Although the majority of these are not significant in most parts of the spectrum, they still affect the spectrum non-trivially when considering high energy resolutions such as in the case of neutrino mass-experiments where the very sensitive end-point is the part of the spectrum that is being investigated.

In total there are six corrections considered. The first and largest of these is the Fermi factor, $F(E_e)$, which accounts for the EM interaction of the daughter nucleus with the beta-electron emitted during the decay. Additionally, there are corrections accounting for radiative effects, $G(E_e)$; nuclear screening of the Coulomb potential, $S(Z,E_e)$; effects stemming from the finite size of the nucleus, $L(E_e)B(E_e)$ and finally the recoil effect on the Coulomb field, $Q(E_e)$. All of these effects are combined into a single overall multiplicative factor

$$C(E_e) = F(E_e) \times G(E_e) \times S(E_e) \times L(E_e) \times B(E_e) \times Q(E_e). \tag{4.12}$$

The functional form of these correction factors is given below.

Besides the corrections mentioned above, the second effect that needs to be accounted is the quantum mechanical interaction of the emitted beta-particle with

He^+ State	Energy [eV]	$\lvert T_{fi}^{(0)}\rvert^2$
$1s$	0	70.36%
$2s$	40.81	24.98%
$3s$	48.37	1.27%
$4s$	51.02	0.38%
$5s$	52.24	0.17%
continuum	$\geq$54.42	2.63%

Table 4.2: Table showing the excitation energies of the final state helium daughter atom available to the bound electron relative to the ground state energy alongside the corresponding asymptotic branching ratios.

the orbital electron of the tritium atom. The tritium is prepared such that initially its orbital electron is in the ground state, however the mathematical treatment of the process needs to take into account that this bound electron may end up in one of the bound energy states of the daughter nucleus or in the continuum, i.e. be emitted. Furthermore, it also needs to consider the possibility of the emitted and bound electrons being exchanged, as they are indistinguishable from each other once the decay takes place. It should be noted, that in principle it is possible for both electrons to end up in a bound state (i.e. forming a non-ionized daughter atom) , known as bound-state beta-decay. However, the ratio of bound to continuum decay rates for atomic tritium has been calculated to be $\Gamma_{\text{bound}}/\Gamma_{\text{continuum}} = 0.69\%$ [186] and therefore this scenario may be neglected, and it is a good approximation to assume that the daughter atom is ionized, with only one orbital electron. Depending on the energy it receives, the bound electron may end up in the ground state or in an excited state, which in turn will affect the energy available to the beta-electron and hence the end-point of the spectrum. Phenomenologically this is crucial, as besides the kinks associated with each mass state at energies where they become kinematically allowed will not be the only distortive effects, as now there will be numerous end-points depending on the excitation of the bound electron. Mathematically this leads to the decay rate being comprised of a sum over all the possible energy states that the bound electron may occupy and an integral over the energies available to the electron that escapes detection, as discussed in Appendix B. The position of these

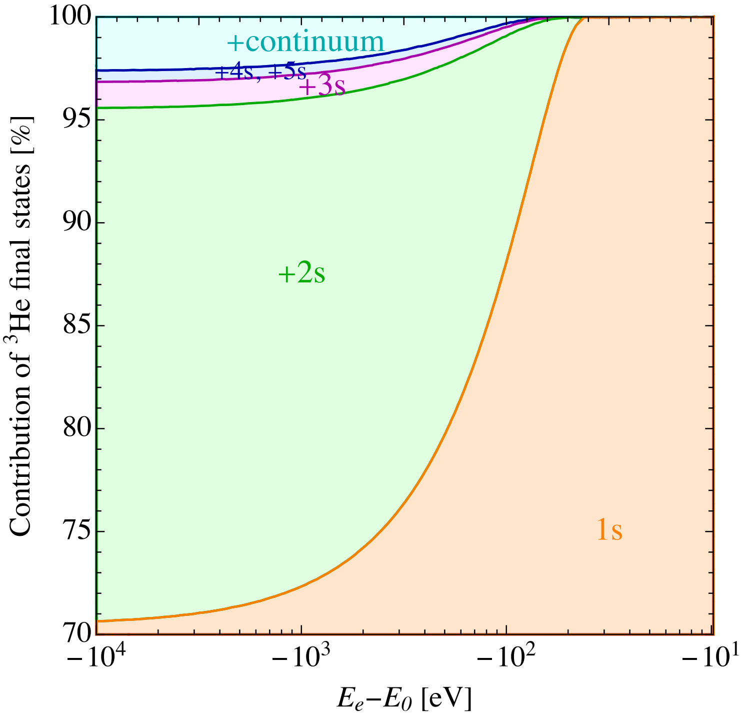

Figure 4.1: Branching probabilities of the orbital electron to helium energy levels $1s$ (orange), $2s$ (green), $3s$ (magenta), $4s + 5s$ (blue) alongside emission into continuum (cyan), as a function of the β-electron energy below the end-point.

kinks is determined by the energy separation of the helium energy levels, which are summarised in Table 4.2 based on [187], alongside the corresponding asymptotic probabilities for the electron to end up in a certain energy level of the helium atom. These transition probabilities depend on the energy available to the orbital electron, which in turn is affected by the energy taken away by the emitted β-electron. This is shown in Fig. 4.1. Unsurprisingly, it can be seen that the less energy there is available to the orbital electron, the less likely it is to occupy a higher energy level. From the table it is apparent that the separation of the energy levels is of the order of 50 eV, which is smaller than the energy resolution of 100 eV assumed in this work and therefore the effect of continuum and excited state emission could be neglected. However, future neutrino mass experiments with a higher energy resolution could benefit from the identification of the kinks associated with the excited states and could exploit them to differentiate from the massless case more efficiently, thus increasing their sensitivity.

Each of the aforementioned corrections is discussed in more detail in the following and their functional form is reproduced from [168] and [188]. The correction factors are approximately discussed in the order of the magnitude of their effect on the spectrum and natural units, i.e. $\hbar = c = 1$ are used throughout, unless otherwise stated and the electron speed is expressed in units of c as $\beta = |\mathbf{p}_e|/E_e = \sqrt{E_e^2 - m_e^2}/E_e$, where E_e denotes the electron energy. In the functions below several quantities are given in units of electron mass, m_e: the magnitude of the electron's 3-momentum, $k = |\mathbf{p}_e|/m_e = \sqrt{W^2 - 1}$; the end-point of the tritium β-decay spectrum, $W_0 = E_e^{\max} - V_f$, where V_f quantifies the change in the end-point of the spectrum for excited states; as well as the general electron energy, $W = E_e/m_e$. Furthermore, several numerical values are used: the absolute value of the ratio between the axial vector and vector nuclear coupling constants, $\lambda_t = |g_A/g_V| = 1.247$; the atomic charge of the final state helium atom, $Z = 2$; the fine structure constant, $\alpha \approx 1/137.036$; and finally the nuclear radius of the helium atom, $R_n \approx 2.88 \times 10^{-3}/m_e$ [168].

4.3.1 The Fermi Factor

The Fermi factor is a correction to the spectrum which corrects for the altering of the Coulomb interaction between the emitted electron and the daughter nucleus. The helium nucleus in the final state has a net positive charge resulting in attraction with the outgoing negatively charged β-particle which modifies the probability distribution of the electron, as the attraction decreases the electron's speed. Hence, the probability of finding the β-electron in the vicinity of the nucleus is enhanced, thus finding electrons with lower kinetic energies is increased and including the Fermi factor properly weights the distribution so that at low energies the spectrum is more populated. The functional form of the Fermi function is [168]

$$F(Z,E_e) = 4(2|\mathbf{p}_e|R_n)^{-2(1-\gamma)} e^{\pi\eta} \frac{|\Gamma(\gamma + i\eta)|^2}{\Gamma(2\gamma+1)^2} \tag{4.13}$$

$$\approx \frac{2\pi\eta(1.002037 - 0.001427|\mathbf{p}_e|/E_e)}{1 - e^{-2\pi\eta}}, \tag{4.14}$$

where $\gamma = (1-(\alpha Z)^2)^{1/2}$, $\eta = (\alpha Z E_e)/|\mathbf{p}_e|$ is the so-called Sommerfeld parameter describing the strength of the Coulomb interaction and $\Gamma(x)$ is the Gamma function.

The first line of the above expression is the fully relativistic Fermi function, which is derived under the assumption of a point-like nucleus, i.e. assuming the electric field is constant both within the nucleus and its surface [189], in order to avoid treatment of the relevant wave functions in the presence of complex nuclear structure effects. The second line of the $F(Z,E_e)$ expression corresponds to the approximate form – often referred to as the Simpson approximation [190] – which is valid for small values of the nuclear charge, Z, i.e. in the case when $\gamma \approx 1$, which is satisfied for our case with $Z = 2$.

4.3.2 Radiative Corrections

There are two kinds of radiative corrections that need to be accounted for in the β-decay process: virtual photon interactions and soft photon emission. In the context of the former, the outgoing electron can interact with the nucleus (initial neutron or final proton) or the intermediate W boson via virtual photons in loop diagrams. Such photon exchanges modify the decay rate of the process and therefore have an effect on the energy distribution of the electron. The latter type arises because accelerating or decelerating charged particles emit electromagnetic radiation in the form of real photons, which naturally affect the energy distribution of the outgoing electron and therefore the spectral shape. In order to model the spectrum more accurately, one can consider soft photon emission to some order, but doing so leads to infrared divergence, since the lower the energy of the photon, the larger the possible number of configurations, leading to a diverging result when integrating over all possible photon energies. This can be remedied by summing over photon emission to all orders, leading to a finite and well-behaved corrections factor, i.e. treating all possible photon emissions collectively, rather than individually. These effects are corrected for by including $G(E_e)$ in the decay rate expression [191]

$$G(E_e) = \left(\frac{E_e^{\max} - E_e}{m_e}\right)^{(2\alpha/\pi)t(\beta)} \left\{1 + \frac{2\alpha}{\pi}\left[t(\beta)\left(\ln 2 - \frac{3}{2} + \frac{E_e^{\max} - E_e}{E_e}\right) + \frac{1}{4}(t(\beta)+1)\left(2(1+\beta^2) - 2\ln\left(\frac{2}{1-\beta}\right) + \frac{(E_e^{\max} - E_e)^2}{6E_e^2}\right) + \frac{1}{2\beta}\left(L(\beta) - L(-\beta) + L\left(\frac{2\beta}{1+\beta}\right) + \frac{1}{2}L\left(\frac{1-\beta}{2}\right) - \frac{1}{2}L\left(\frac{1+\beta}{2}\right)\right)\right]\right\}, \tag{4.15}$$

where $L(\beta) = \int_0^\beta \frac{dt}{t}\ln(1-t)$ is known as the Spence function and $t(\beta) = \text{arctanh}(\beta)/\beta - 1$ and $E_e^{\max}$ given in Eq. 4.25. At the endpoint of the spectrum the electrons receive maximal energy from the decay, leading to a highly constrained phase-space for photon emission and the probability of soft photon emission is low, but the relative effect on the spectrum is largest. The radiative effect is most pronounced at high energies, at the endpoint of the energy distribution.

4.3.3 Screening Factor

Considering the Coulomb force without any additional considerations assumes a free β-decay process with a bare nuclear charge. However, in the context of the bound system in consideration here, the orbital electrons of the daughter atom create a screening effect, which reduces the effective charge felt by the outgoing electron and thus modifies the effective Coulomb interaction by lowering the Coulomb barrier which needs to be overcome by the electron in order to be emitted. This leads to a lower effective binding energy and therefore the total energy available for the decay is reduced, shifting the end-point of the spectrum to a slightly lower energy. The effect of the screening is encapsulated by the factor [192]

$$S(Z,W) = \frac{\overline{W}}{W}\left(\frac{\bar{k}}{k}\right)^{-1+2\gamma} \frac{|\Gamma(\gamma + i\bar{\eta})^2|}{|\Gamma(\gamma + i\eta)^2|} e^{\pi(\bar{\eta} - \eta)}, \tag{4.16}$$

where the modified electron energy, the magnitude of the electron's spatial momentum and the Sommerfeld parameter, denoted with bars, are given by $\bar{W} = W - V_0/m_e$, $\bar{k} = \sqrt{\bar{W}^2 - 1}$ and $\bar{\eta} = \alpha Z \bar{W}/\bar{k}$, respectively and the screening potential of the electron cloud associated with the daughter nucleus is $V_0 = (76 \pm 10)$ eV [193].

4.3.4 Finite Nuclear Size

In many cases it is sufficient to model the nucleus as point-like, however if one wishes to account for nuanced spectral effects, then the finite spatial extent of the nucleus needs to be acknowledged. This can be achieved via the inclusion of the correction factor $L(Z,W) \times B(Z,W)$ [194]. The first term, $L(Z,W)$ is the scaling of the Coulomb field to account for the fact that the charge distribution of the nucleus is in fact spread out over a finite volume, rather than being concentrated in a single point located at the centre of the nucleus. Its functional form is [194]

$$L(Z,W) = 1 + \frac{13}{60}(\alpha Z)^2 - \frac{W R_n \alpha Z}{15}\frac{41-26\gamma}{2\gamma-1} - \frac{\alpha Z R_n \gamma}{30W}\frac{17-2\gamma}{2\gamma-1}. \tag{4.17}$$

The acknowledgment of the finite size of the nucleus alters the wave functions of the electron and the neutrino through their interaction with the potential of the nucleus, and therefore the combined amplitude of the 3-particle interaction is described by the overlap of their individual wave functions, in other words the convolution of the electron and neutrino wave functions with the nucleonic wave function over the entire range of the finite nuclear volume,

$$B(Z,W) = 1 + B_0 + B_1 W + B_2 W^2, \tag{4.18}$$

with

$$\begin{aligned} B_0 &= -\frac{233}{630}(\alpha Z)^2 - \frac{1}{5}(W_0 R_n)^2 + \frac{2}{35}(W_0 R_n \alpha Z), \\ B_1 &= -\frac{21}{35} R_n \alpha Z + \frac{4}{9} W_0 R_n^2, \\ B_2 &= -\frac{4}{9} R_n^2. \end{aligned} \tag{4.19}$$

4.3.5 Recoiling Coulomb Field

As the initial nucleus emits the final state electron and neutrino, it experiences a recoil due to its finite mass in accordance with momentum conservation. Usually, the nucleus is assumed to be a stationary source of the Coulomb field experienced by the β-electron, however as a result of the recoil, it is in fact a moving source. This effect introduces a change in the Coulomb field which is no longer spherically isotropic, thus modifying the electron's energy spectrum. As this effect modifies the Fermi function taking into account the altered potential landscape, it will have the biggest effect at the low energy end of the spectrum, since less energetic electrons spend more time in the vicinity of the nucleus. As the energy increases, the effect of the nuclear recoil diminishes. The multiplicative correction to the spectrum accounting for this is of the form [195]

$$Q(Z,W,W_0) = 1 - \frac{\pi\alpha Z}{m_{\mathrm{He}}k}\left(1 + \frac{1-\lambda_t^2}{1+3\lambda_t^2}\frac{W_0 - W}{3W}\right). \tag{4.20}$$

4.4 Tritium Decay Rate

In the context of β-decay, both the energy and angular distributions of the outgoing electron are insightful to study and thus we start by deriving both of these. The differential decay rate is calculated as a function of the emitted electron's energy for the energy spectrum and as a function of the angle between the initial tritium spin and the direction of the electron's momentum for the angular spectrum. Thus, we start from the fully differential decay rate

$$d\Gamma = \frac{1}{2m_{\mathrm{H}}}\frac{d^3\mathbf{p}_e}{(2\pi)^3 2E_e}\frac{d^3\mathbf{p}_\nu}{(2\pi)^3 2E_\nu}\frac{d^3\mathbf{p}_{\mathrm{He}}}{(2\pi)^3 2E_{\mathrm{He}}}|M|^2(2\pi)^4\delta^4(P_{\mathrm{H}} - P_{\mathrm{He}} - P_e - P_\nu). \tag{4.21}$$

where the subscripts H, He, e and ν refer to parameters associated with the tritium, helium, final state electron and final state neutrino, respectively. $|M|^2$ denotes the matrix-elements squared of the interaction and $\mathbf{p}_X$ and P_X are the 3-momenta and 4-momenta of particle X and a four-dimensional Dirac-delta function is included to enforce energy-momentum conservation.

Since we are primarily interested in the kinematics of the outgoing electron, the decay rate can be simplified by evaluating it in the rest frame of the tritium, i.e.

where $P_{\mathrm{H}} = (m_{\mathrm{H}}, \mathbf{0})$. Expressing the electron and neutrino momenta in spherical coordinates allows one to arrive at the differential decay rate as a function of energy and angular distribution, of the form

$$\frac{d\Gamma}{dE_e d\Omega_e} = \frac{C(E_e)}{2^9 \pi^5 m_{\mathrm{H}}} \int_{\Omega} d\Omega_\nu \int_{E_\nu^-}^{E_\nu^+} dE_\nu |M|^2 \delta\left(\cos\theta_{e\nu} - \frac{\mathbf{p}_{\mathrm{He}}^2 - \mathbf{p}_e^2 - \mathbf{p}_\nu^2}{2|\mathbf{p}_e||\mathbf{p}_\nu|}\right). \tag{4.22}$$

In the above expression Ω_X is the solid angle describing the direction of emission of particle X. The frame is chosen such that the polar angle is measured relative to the direction of the tritium's spin. The angle between the spatial momenta of the electron and the neutrino is denoted by $\theta_{e\nu}$, $C(E_e)$ is the combined multiplicative factor taking into account the spectral corrections discussed in Sec. 4.3. The integral that runs over the neutrino energy has lower and upper limits E_ν^- and E_ν^+, respectively, expressed as [174]

$$E_\nu^\pm(E_e) = \frac{(m_{\mathrm{H}} - E_e)(m_{\mathrm{H}} y + m_\nu^2 + m_{\mathrm{He}} m_\nu) \pm |\mathbf{p}_e| \sqrt{(m_{\mathrm{H}} y (m_{\mathrm{H}} y + 2 m_{\mathrm{He}} m_\nu)}}{m_{12}^2}, \tag{4.23}$$

where

$$y = E_e^{\max} - E_e, \tag{4.24}$$

is the difference between the maximum kinematically allowed electron energy $E_e^{\max}$ and the electron energy, with $E_e^{\max} - m_e \approx 18.59$ keV [196, 197] being the maximal kinetic energy that the electron can receive. When the electron takes the maximal energy from the process, $E_\nu \approx m_\nu$ ($\mathbf{p}_\nu \approx 0$). Using this and the energy-momentum relations, $E_e^{\max}$ can be shown to be

$$E_e^{\max} = \frac{m_{\mathrm{H}}^2 + m_e^2 - (m_{\mathrm{He}} + m_\nu)^2}{2 m_{\mathrm{H}}}, \tag{4.25}$$

and we explicitly see that $E_e^{\max}$ and therefore y is dependent on the neutrino mass, m_ν. The m_{12}^2 parameter in the denominator of Eq. 4.23 is defined as

$$m_{12}^2 = (p_{\mathrm{H}} - p_e)^2 = m_{\mathrm{H}}^2 - 2m_{\mathrm{H}}E_e + m_e^2. \tag{4.26}$$

To proceed, the spin states and the possible correlations arising from these need to be considered. Usually, the spins of the particles are treated collectively by summing or averaging over them leading to a decay rate expression that considers up and down spin states as equally probable, useful when the source has a net spin alignment of zero, i.e. for an unpolarised ensemble. If however, one would like to retain information about the spin directions for a polarised source, the spin components of the wave functions need to be projected out using the spin projection operator [198]

$$P_S = \frac{1}{2}(1 + \gamma^5 \not{S}), \tag{4.27}$$

where $\not{S} = \gamma_\mu S^\mu$ and S^μ is the spin four-vector

$$S^\mu = \left(\frac{\mathbf{p}\cdot\hat{\mathbf{s}}}{m}, \hat{\mathbf{s}} + \frac{(\mathbf{p}\cdot\hat{\mathbf{s}})}{(m(E+m))} \right). \tag{4.28}$$

Here, $\mathbf{p}$ is the 3-momentum of the particle, $\hat{\mathbf{s}}$ is the unit vector in the direction of spin and E and m are the energy and mass, respectively. Since the process is being considered in the rest frame of the tritium, $\mathbf{p} = 0$ and hence $S^\mu = (0, \hat{\mathbf{s}})$ and the projection operator is chosen such that $P_s u_{\mathbf{p},s'} = \delta_{s,s'} u_{\mathbf{p},s'}$ and $P_s v_{\mathbf{p},s'} = \delta_{s,s'} v_{\mathbf{p},s'}$, where u and v are spinors and $s, s' = \downarrow, \uparrow$ corresponding to down and up spins. This ensures that only those spinors are preserved by the projections whose spins we are interested in. Since up and down spin states contribute oppositely to the net polarisation, the number of up and down spins, $N_\uparrow$ and $N_\downarrow$ are combined into a polarisation factor

$$f = \frac{N^\uparrow - N^\downarrow}{N^\uparrow + N^\downarrow}, \tag{4.29}$$

which helps to weight the net effect by replacing $S \to fS$. The value of f, i.e. the degree of polarisation of the ensemble of the tritium nuclei determines the angular distribution of the outgoing electrons. In the limit $|f| = 1$ corresponding to total polarisation, the resulting angular distribution is maximally affected. This is the case we consider. The other extreme case is $f = 0$, when the source is unpolarised, resulting in a completely isotropic electron distribution, without any directional dependence or preferential emission, as done in Eq. 4.37.

In the case when $f \neq 0$, i.e. the source is polarised, there exists a correlation between the spin of the source and the direction of the emitted electron's momentum. In other words, the probability of emission of the electron in a certain direction is dependent on the orientation of the tritium spin. The spin projection operator P_S from Eq. 4.27, is included at the matrix element level. The matrix element squared will then contain terms that are spin-independent from the "1", and spin-dependent terms from dot-products like $\mathbf{p_e} \cdot \hat{\mathbf{s}}$ from "$\gamma^5 \not{s}$", which can be expressed as $\cos\theta_e$. This will result in the differential decay rate taking the form

$$\frac{d\Gamma}{dE_e d\Omega_e} = a(E_e) + b(E_e)\cos\theta_e, \tag{4.30}$$

where $a(E_e)$ and $b(E_e)\cos\theta_E$ are the spin-independent and spin-dependent terms, respectively, with θ_e denoting the angle between the tritium's spin and the electron's direction of momentum.

When integrating this over the solid angle of the electron, $\Omega_e = \sin\theta_e d\theta_e d\phi_e$, the integral over the azimuthal angle contributes a factor of 2π, the integral over $\sin\theta_e$ contributes a factor of 2 and the integral over $\cos\theta_e$ vanishes, since it is an odd function with respect to θ_e and thus the contributions from the upper and lower halves of the integration range lead to a cancellation. This results in the energy distribution to take the form

$$\frac{d\Gamma}{dE_e} = 4\pi a(E_e). \tag{4.31}$$

where we see that the spin-dependent part has dropped out. Integrating over the electron energy then leads to the total tritium decay rate

$$\Gamma = 4\pi \int_{m_e}^{E_e^{\max}} a(E_e) dE_e. \tag{4.32}$$

One may also start by integrating the doubly differential decay rate expression in Eq. 4.30 over the electron energy, leaving only the angular dependence

$$\frac{d\Gamma}{d\cos\theta_e} = \frac{\Gamma}{2}(1 + k\cos\theta_e), \tag{4.33}$$

where we have defined the angular correlation factor, k,

$$k = \int_{m_e}^{E_e^{max}} b(E_e) dE_e \Bigg/ \int_{m_e}^{E_e^{max}} a(E_e) dE_e. \tag{4.34}$$

which is the ratio of spin-dependent and spin-independent contributions, quantifying the asymmetry of the angular distribution associated with the emission of the electron due to the polarised tritium source.

The emission anisotropy captured by k stems from the chirality and helicity of the particles involved in the process. The final state electron's and neutrino's combined spin can either be $S = 0$[1], (the two spins are anti-aligned and thus cancel out) or $S = 1$[2] (when both spins are aligned and add up). In the former case the emission of the electron is completely isotropic, as there is no net spin and thus no directional preference. On the other hand, in the latter case, the tritium's polarisation determines the possible emission directions of the decay products. To conserve angular momentum, the tritium's spin and the combined spin of the electron-neutrino system should be aligned. Given that the electron is a left-chiral particle (and therefore mostly left helical), its momentum is predominantly opposite to its spin direction. Therefore, in such a case the electrons are more likely to be emitted in the opposite

---

[1] The $S = 0$ combined spin corresponds to the vector current, as the vector bilinear is of the form $\bar{\psi}\gamma^\mu\psi$ for a spinor field ψ, which only affects the propagation of the particle (with γ^0 being the time components and γ^i for $i = 1,2,3$) the spatial components.

[2] The $S = 1$ state, as opposed to $S = 0$, corresponds to the axial vector bilinear of the form $\bar{\psi}\gamma^\mu\gamma_5\psi$, which can change the spin of the particle involved due to the presence of the chiral γ^5 matrix.

direction to the tritium's polarisation. Naturally, this effect is only present when considering the differential decay rate as a function of θ_e (coming from the $\mathbf{p}\cdot\hat{\mathbf{s}}$ term) and vanishes when integrating over the solid angle.

4.4.1 Standard Model

Having outlined the general approach for deriving the energy and angular distributions in tritium β-decay, we begin by exploring the SM case. Based on the Lagrangian shown in Eq. 4.5, the matrix element for the process is written in terms of the spinor bilinears

$$M_{\mathrm{SM}} = -\frac{G_F}{\sqrt{2}} V_{ud} \left[\bar{e}\gamma^{\mu}(1-\gamma^5)\nu_e\right] \left[\overline{^3\mathrm{He}}\gamma_{\mu}\left(g_V - g_A\gamma^5\right){}^3\mathrm{H}\right] \tag{4.35}$$

and thus the squared matrix element, $|M|^2 = MM^*$ is of the form

$$\begin{aligned} |M_{\mathrm{SM}}|^2 = 16G_F^2|V_{ud}|^2\,\mathrm{Tr}\left[\left(\not{P}_{\mathrm{He}}+m_{\mathrm{He}}\right)\gamma^{\lambda}\left(g_V-g_A\gamma^5\right)\left(1+\gamma^5\not{S}\right)\left(\not{P}_{\mathrm{H}}+m_{\mathrm{H}}\right)\gamma^{\rho}\left(g_V-g_A\gamma^5\right)\right] \\ \times\mathrm{Tr}\left[\left(\not{P}_e+m_e\right)\gamma_{\lambda}\left(1-\gamma^5\right)\not{P}_{\nu}\gamma_{\rho}\left(1-\gamma^5\right)\right] \end{aligned} \tag{4.36}$$

where the traces arise due to the contraction of the indices. Using trace identities and formulas allows for the matrix element squared to be expressed in terms of the dot products of the four-momenta of the particles involved

$$\begin{aligned} |M_{\mathrm{SM}}|^2 = {} & 16G_F^2|V_{ud}|^2 \\ & \times\left\{(g_A+g_V)^2(P_e\cdot P_{\mathrm{He}})(P_\nu\cdot P_{\mathrm{H}}) + (g_A-g_V)^2(P_e\cdot P_{\mathrm{H}})(P_\nu\cdot P_{\mathrm{He}})\right. \\ & \quad + (g_A^2-g_V^2)m_{\mathrm{H}}m_{\mathrm{He}}(P_e\cdot P_\nu) \\ & \quad + (g_A^2-g_V^2)m_{\mathrm{He}}\left[(P_{\mathrm{H}}\cdot P_\nu)(P_e\cdot S)-(P_{\mathrm{H}}\cdot P_e)(P_\nu\cdot S)\right] \\ & \quad \left.+(g_A-g_V)^2m_{\mathrm{H}}(P_\nu\cdot P_{\mathrm{He}})(P_e\cdot S)-(g_A+g_V)^2m_{\mathrm{H}}(P_e\cdot P_{\mathrm{He}})(P_\nu\cdot S)\right\}. \end{aligned} \tag{4.37}$$

From here, we first calculate the energy distribution assuming an unpolarised ($f = 0$) tritium source, i.e. by focusing only on the spin-independent terms of the above expressions, yielding

$$
\begin{aligned}
4\pi a_{\mathrm{SM}}(E_e) = {} & \frac{G_F^2|V_{ud}|^2}{2\pi^3} C(E_e) \sum_{i=1}^{3} |U_{ei}|^2 \frac{m_{\mathrm{H}}^2|\mathbf{p}_e|}{m_{12}^2} \widetilde{y}_i \Theta(y_i) \\
& \times \left\{ (g_V+g_A)^2 \left[\frac{m_{\mathrm{H}}(m_{\mathrm{H}}-E_e)}{m_{12}^2} \frac{m_{\mathrm{H}}E_e - m_e^2}{m_{12}^2} (y_i+\mu_i m_{\nu,i})(y_i+\mu_i m_{\mathrm{He}}) \right.\right. \\
& \left. - \frac{m_{\mathrm{H}}^2|\mathbf{p}_e|^2}{3m_{12}^4} \widetilde{y}_i^2 \right] + (g_V-g_A)^2 E_e \left(y_i + m_{\nu,i} \frac{m_{\mathrm{He}}}{m_{\mathrm{H}}} \right) \\
& \left. + (g_A^2-g_V^2) m_{\mathrm{He}} \frac{m_{\mathrm{H}}E_e - m_e^2}{m_{12}^2} (y_i + \mu_i m_{\nu,i}) \right\},
\end{aligned}
\tag{4.38}
$$

where U_{ei} and $m_{\nu,i}$ ($i = 1,2,3$) are the PMNS matrix elements coupling neutrino ν_i with the electron and the neutrino mass eigenstates which are summed over all three generations, respectively. The kinematic variable μ_i is defined as $\mu_i = (m_{\nu,i} + m_{\mathrm{He}})/m_{\mathrm{H}}$, while y_i and m_{12}^2 were given in Eq. 4.24 and Eq. 4.26, respectively and the shorthand

$$
\widetilde{y}_i = \sqrt{y_i \left(y_i + m_{\nu,i} \frac{2m_{\mathrm{He}}}{m_{\mathrm{H}}} \right)}. \tag{4.39}
$$

is introduced for a commonly occurring term. The heavy-side theta function $\Theta(y_i)$ is present in order to enforce energy conservation (effectively it returns a zero result when $E_e > E_e^{\max}$, i.e. when the electron wants to take more energy than is available). Fig. 4.2 shows the Kurie plot of this expression as a function of $\Delta E = E - E_0$, i.e. the electron energy below the endpoint for a massless lightest neutrino, $m_l = 0$, where

$$
\begin{aligned}
m_\beta &= \sqrt{|U_{e1}|^2 m_l^2 + |U_{e2}|^2(m_l^2 + \Delta m_{21}^2) + |U_{e3}|^2(m_l^2 + \Delta m_{31}^2)} \quad \text{(NO)} \\
m_\beta &= \sqrt{|U_{e1}|^2(m_l^2 + |\Delta m_{31}^2|) + |U_{e2}|^2(m_l^2 + |\Delta m_{32}^2|) + |U_{e3}|^2 m_l^2} \quad \text{(IO)}
\end{aligned}
\tag{4.40}
$$

is the effective neutrino mass expressed in terms of the lightest neutrino mass and the mass splittings, for the two mass hierarchies. The Kurie function, $d\Gamma/dE/\left(|\mathbf{p}_e|^2\, F(Z,E_e)\right)$, produces a linear energy dependence, as showcased by the gray line labeled 'massless', corresponding to $m_{\nu_e} = 0$. The exact form of the

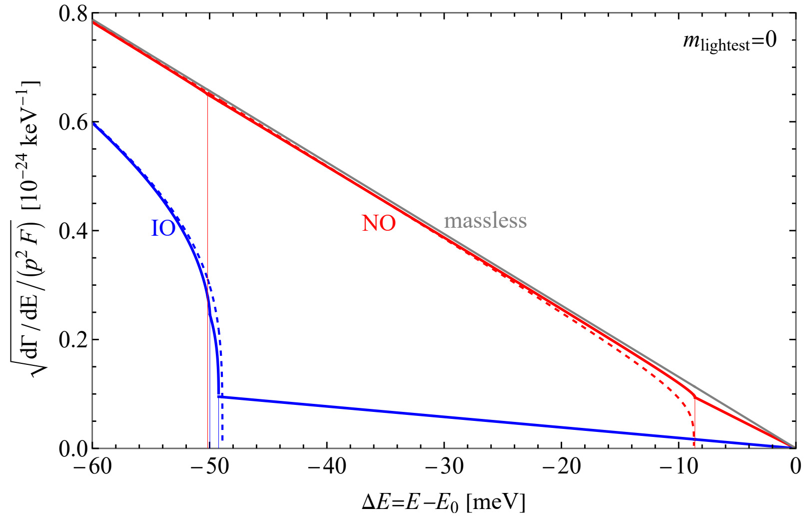

Figure 4.2: Kurie plot of the energy spectrum as a function of electron energy below the zero-mass endpoint, for a massless lightest neutrino. The single massless neutrino case (gray) is a straight line, while the exact expressions for NO (red solid) and IO (blue solid) exhibit kinks, associated with the individual mass states that contribute. Also plotted is the approximate spectrum involving the effective mass, for NO (red dashed) and IO (blue dashed).

rate in Eq. 4.38 is plotted for both mass orderings: NO (red solid) and IO (blue solid). In both cases, the three distinct endpoints, emphasised with thin vertical lines, due to the contributions of the three individual neutrino mass states are clearly visible and manifest themselves as kinks in the spectrum. The position of these kinks is at $E_e = E_0 - m_i$ for each mass state m_i. Going from right to left along the horizontal axis, each of the kinks appear when the associated mass states becomes kinematically producible. Their separation is determined by the mass splitting between the mass eigenstates, while the amplitude of the kinks is influenced by $|U_{ei}|^2$, the mixing matrix element quantifying the coupling between m_i and the electron flavour.

Since $m_H \sim \mathcal{O}(\mathrm{GeV})$ and $m_{\mathrm{He}} \sim \mathcal{O}(\mathrm{GeV})$ while $E_e \sim \mathcal{O}(\mathrm{keV})$, $m_e \sim \mathcal{O}(10^{-1}\mathrm{MeV})$ and $m_\nu \sim \mathcal{O}(10^{-1}\mathrm{eV})$, it is safe to make the approximation that

$m_{\mathrm{H}} \approx m_{\mathrm{He}} \gg E_e, m_e, m_\nu$. Then, the energy distribution simplifies to

$$4\pi a_{\mathrm{SM}}(E_e) \approx \frac{G_F^2 |V_{ud}|^2}{2\pi^3} C(E_e)(g_V^2 + 3g_A^2) m_{\mathrm{H}} m_{\mathrm{He}} \frac{m_{\mathrm{He}}|\mathbf{p}_e|}{m_{12}^2} \frac{m_{\mathrm{H}} E_e - m_e^2}{m_{12}^2} \times \sum_{i=1}^{3} |U_{ei}|^2 \Theta(y_i) \sqrt{y_i \left(y_i + m_{\nu,i} \frac{2m_{\mathrm{He}}}{m_{\mathrm{H}}} \right)} \left(y_i + m_{\nu,i} \frac{m_{\nu,i} + m_{\mathrm{He}}}{m_{\mathrm{H}}} \right). \tag{4.41}$$

This expression may be rewritten [117, 177] in a simpler form by removing the individual neutrino contributions and instead introducing the effective neutrino mass, $m_\beta^2 = \sum_{i=1}^3 |U_{ei}|^2 m_i^2$, and using $y_0 = y(m_\nu = 0)$ to ensure that there is no neutrino mass dependence outside of m_β, yielding

$$4\pi a_{\mathrm{SM}}(E_e) \approx \frac{G_F^2 |V_{ud}|^2}{2\pi^3} C(E_e)(g_V^2 + 3g_A^2) m_{\mathrm{H}} m_{\mathrm{He}} \frac{m_{\mathrm{H}}|\mathbf{p}_e|}{m_{12}^2} \frac{m_{\mathrm{H}} E_e - m_e^2}{m_{12}^2} y_0 \sqrt{y_0^2 - m_\beta^2}. \tag{4.42}$$

As opposed to the exact expressions shown with the solid lines in Fig. 4.2, this approximate form naturally results in a single endpoint located at $E_e = E_0 - m_\beta$, shown for both mass ordering: NO (red dashed) and IO (blue dashed). Since there is only one endpoint, there are no kinks in the approximate rate, but it is clearly visible that the two cases converge nicely once all mass contributions have been turned on in the exact case. Therefore, the difference between the approximate and exact forms of the energy spectrum are negligible for experiments with energy resolutions much bigger than the neutrino mass and when studying the spectrum far from the endpoint region. In this study, we focus on the bulk region of the spectrum and therefore the approximate form is safe to use.

Having discussed the energy spectrum in the SM case, we turn to the angular distribution, i.e. we calculate $b(E_e)$ in the second term of Eq. 4.30, which appears as a non-zero contribution when the tritium ensemble is polarised. To this end now the spin dependent terms of the matrix element shown in Eq. 4.37 are used, yielding the angular correlation

$$\begin{aligned} b_{\mathrm{SM}}(E_e) = &-\frac{G_F^2|V_{ud}|^2}{8\pi^4} C(E_e) \frac{m_{\mathrm{H}}}{m_{12}^2} |\mathbf{p}_e|^2 \widetilde{y}_i \\ &\times \Bigg\{ \Bigg[(g_A - g_V)^2 m_{\mathrm{H}} + (g_A^2 - g_V^2) m_{\mathrm{He}} \frac{m_{\mathrm{H}}(m_{\mathrm{H}} - E_e)}{m_{12}^2} \\ &+ (g_A^2 - g_V^2) \frac{m_{\mathrm{H}} m_{\mathrm{He}}}{m_{12}^2} E_e + (g_A + g_V)^2 \frac{m_{\mathrm{H}}}{m_{12}^2} (\alpha - m_e^2) \\ &-(g_A + g_V)^2 \frac{m_{\mathrm{H}}^2}{m_{12}^2} (y_i + \mu_i m_{\nu,i}) \frac{m_{\mathrm{H}}(m_{\mathrm{H}} - E_e)}{m_{12}^2} \Bigg] (y_i + \mu_i m_{\nu,i}) \\ &-(g_A - g_V)^2 m_{\nu,i}^2 - \frac{1}{3} (g_A + g_V)^2 \frac{m_{\mathrm{H}}^3 (m_{\mathrm{H}} - E_e)}{m_{12}^4} \widetilde{y}_i^2 \Bigg\} \end{aligned} \tag{4.43}$$

with a combination of kinematic parameters, $\alpha = m_{\mathrm{H}} E_e^{max} + m_{\nu_i}^2 + m_{\mathrm{He}} m_{\nu_i}$. This expression can be simplified dramatically if one assumes $m_{\mathrm{H}} \approx m_{\mathrm{He}} \gg E_e, m_e, m_\nu$ (as before when calculating the approximate form of the energy spectrum), yielding

$$b_{\mathrm{SM}}(E_e) \approx -\frac{2g_A^2 - 2g_A g_V}{g_V^2 + 3g_A^2} \frac{|\mathbf{p}_e|}{E_e} a_{\mathrm{SM}}(E_e) \approx -0.12 \frac{|\mathbf{p}_e|}{E_e} a_{\mathrm{SM}}(E_e). \tag{4.44}$$

The half-life

$$T_{1/2} = \frac{\ln(2)}{\Gamma} \tag{4.45}$$

can be calculated using Eq. 4.32 and Eq. 4.38, yielding $T_{1/2} = 12.6$ yr, while the angular correlation factor, k, is calculated in the SM case using Eq. 4.44 to be $k_{\mathrm{SM}} = -0.0154$.

4.5 Massive Sterile Neutrinos

In the previous sections we have discussed the spectral details and calculations relevant to tritium β-decay neutrino mass experiments. Building on this, we now turn our attention to the sensitivity of such experiments to keV-mass sterile neutrinos.

Assuming that the only production mechanism available to the sterile neutrino is via its mixing with the active sector as shown in Eq. 4.11 – parameterised by the active-sterile mixing angle, $|V_{eN}|^2$ – then the changes to the energy and angular distribution are easily modified to the extended particle content. The sum in the energy distribution expressions shown in Eq. 4.38 needs to be modified to run over the sterile neutrino states as well, i.e. $\sum_{i=1}^{3} \to \sum_{i=1}^{3+n_s}$, where n_s denotes the number of sterile neutrinos, with corresponding mass states $m_4, ..., m_{n_s+3}$ and mixing matrix elements $V_{e4}, ..., V_{e(n_s+3)}$. Considering only one active and one sterile neutrino ($n_s = 1$), N, with a corresponding mass state m_N, yields the energy spectrum

$$\frac{d\Gamma}{dE_e} = \left(1 - |V_{eN}|^2\right) \frac{d\Gamma_{\mathrm{SM}}}{dE_e} + |V_{eN}|^2 \frac{d\Gamma_N}{dE_e} \tag{4.46}$$

where the subscripts 'SM' and 'N' denote the SM and sterile contributions to the differential decay rate. Now $d\Gamma_{\mathrm{SM}}/dE_e$ corresponds to Eq. 4.31, with $\alpha(E_e)$ as given in Eq. 4.38, while

$$\frac{d\Gamma_N}{dE_e} = 4\pi\alpha_N(E_e) \tag{4.47}$$

where

$$\begin{aligned} 4\pi a_N(E_e) = {} & \frac{G_F^2|V_{ud}|^2}{2\pi^3} C(E_e) \frac{m_{\mathrm{H}}^2|\mathbf{p}_e|}{m_{12}^2} \widetilde{y_N}\Theta(y_N) \\ & \times \left\{ (g_V+g_A)^2 \left[\frac{m_{\mathrm{H}}(m_{\mathrm{H}}-E_e)}{m_{12}^2} \frac{m_{\mathrm{H}}E_e - m_e^2}{m_{12}^2} (y_N+\mu_N m_N)(y_N+\mu_N m_{\mathrm{He}}) \right.\right. \\ & \left. - \frac{m_{\mathrm{H}}^2|\mathbf{p}_e|^2}{3m_{12}^4} \widetilde{y_N}^2 \right] + (g_V-g_A)^2 E_e \left(y_N + m_N \frac{m_{\mathrm{He}}}{m_{\mathrm{H}}} \right) \\ & \left. + (g_A^2-g_V^2) m_{\mathrm{He}} \frac{m_{\mathrm{H}}E_e - m_e^2}{m_{12}^2} (y_N + \mu_N m_N) \right\}, \end{aligned} \tag{4.48}$$

where y_N is given by Eq. 4.24 with the replacement $m_\nu \to m_N$ in Eq. 4.25, $\widetilde{y_N}$ is given by Eq. 4.39 with $y_i \to y_N$ and $m_\nu \to m_N$ and $\mu_N = (m_N + m_{\mathrm{He}})/m_{\mathrm{H}}$. The phenomenological consequence of such a sterile neutrino is shown in Fig. 4.3, where $d\Gamma/dE_e$ is plotted as a function of electron kinetic energy, $E_e - m_e$, for four choices of sterile mass, $m_N = 0$ (gray), 5 (red), 10 (blue) and 15 (green) keV and $|V_{eN}|^2 = 0.25$ [3]. The massless sterile neutrino scenario corresponds to the SM case, while the presence of a massive sterile particle induces a kink in the energy spec-

---

[3] This is an unrealistically large mixing value, that is already excluded by experimental searches. It is chosen solely for visual purposes.

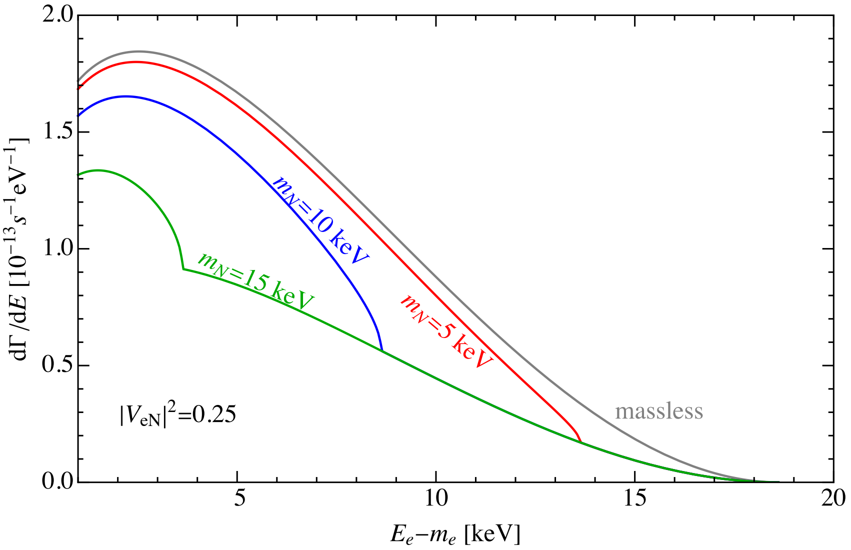

Figure 4.3: Plot showing the differential decay rate as a function of the electron kinetic energy, in the four neutrino paradigm (3 active + 1 sterile) for a mixing angle value $|V_{eN}|^2 = 0.25$. The energy spectrum is presented for four examples of the sterile mass: m_N =0 (gray), 5 (red), 10 (blue) and 15 keV (green).

trum, positioned at $E_e^{\text{max}} - m_N$, which explains why the kink is located at lower (higher) electron energies for larger (smaller) m_N. At energies higher than the kink, the spectrum is reduced by the same amount, irrespective of the sterile mass, as in this region only the SM part of the decay rate contributes (sterile neutrino production for m_N corresponding to kink location kinematically forbidden), which is why all lines with $m_N \neq 0$ converge at high energies. At energies below the kink, the spectrum is also reduced, due to the phase space suppression resulting from the presence of the massive sterile state, with a larger degree of suppression for larger values of m_N. The overall amplitude of the spectrum is suppressed by the active-sterile mixing angle, as can be understood from Eq. 4.46. The kink is a pronounced phenomenological signature, that can be searched for in experiments.

Having discussed the effect of the sterile neutrino on the energy spectrum, we now turn our attention to the angular effects, as shown in Fig. 4.4. This shows the deviation of the angular correlation factor associated with the sterile neutrino, k_N, from its SM value, k_{SM}, as a function of the sterile mass, m_N, for two choices of mixing angle values, $|V_{eN}|^2 = 0.025$ (orange) and 0.25 (blue). It can be seen that the smaller mixing angle value results in the quantity $k_N - k_{\text{SM}}$ being closer to zero, i.e.

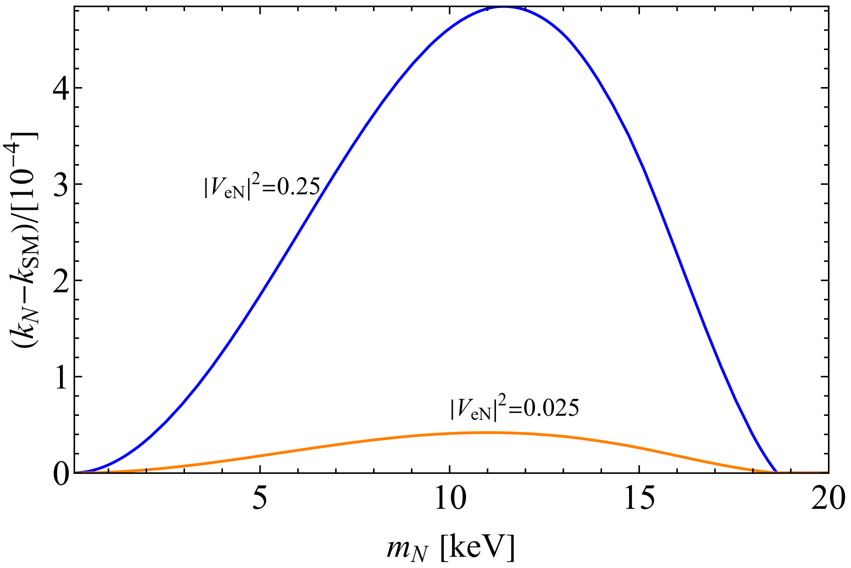

Figure 4.4: Deviation of the angular correlation factor from the SM as a function of sterile mass, for two choices of the active-sterile mixing angle: $|V_{eN}|^2 = 0.25$ (blue) and $|V_{eN}|^2 = 0.025$ (orange).

closer to the SM result. This is because when mixing with the active neutrinos is the only production mechanism available to the sterile neutrino, the smaller the mixing angle, the more the neutrino behaves like the SM active neutrino, due to the minimal sterile component. It is also apparent from the figure, that for any value of the mixing angle, the SM result is recovered as m_N approaches zero. Similarly, for the largest values of m_N, sterile neutrino production is prohibited kinematically and thus its effect on the angular correlation is diminished also. In between the two extremes, the sterile neutrino's mass acts to decouple chirality and helicity, the degree of the decoupling depending on the value of m_N. This reduction in the correlation leads to a smaller value of k and thus a more isotropic emission. Thus, at a certain value of m_N, the sterile neutrino is heavy enough to cause significant decoupling, but light enough to be producible, producing a maximal deviation, corresponding to a peak in the distribution.

Thus far it was assumed that the sterile neutrino may only be produced via active-sterile mixing. However, it is also possible for the sterile neutrino to couple directly to exotic currents in the Lagrangian of Eq. 4.9. Considering such effects will impact both the energy and angular distributions at the matrix element level.

Once the matrix element is squared, this should result in three types of terms: purely SM, purely exotic currents involving a sterile state and interference terms. Such an interference term would involve two distinct final states (active neutrino in the SM case and sterile neutrino from the exotic currents) and therefore it cannot exist. The energy and angular spectra thus take the form

$$\begin{aligned} a(E_e) &= a_{\mathrm{SM}}(E_e) + |\varepsilon_X^N|^2 a_X(E_e), \\ b(E_e) &= b_{\mathrm{SM}}(E_e) + |\varepsilon_X^N|^2 b_X(E_e). \end{aligned} \tag{4.49}$$

The functional forms of the sterile exotic contributions are given in Appendix C. If the sterile neutrino is produced solely via active-sterile mixing then $a_X(E_e)$ corresponds to $a_N(E_e)$ as in Eq. 4.48 and similarly $b_X(E_e)$ is the same as in the SM case but using the sterile mass instead of the active neutrino masses, and ε_X^N, the sterile exotic coupling is zero.

Thus we consider two production mechanisms for the sterile state. It can either be produced indirectly, with the emitted electron-neutrino possessing the heavy m_N component through active-sterile mixing, or the sterile neutrino may be produced directly by an exotic current. It is interesting to note, that for specific choices of parameter values, the two scenarios have an almost identical effect on the energy spectrum, as shown in the left panel of Fig. 4.5. Thus, it may pose a challenge to assess the origin of the sterile neutrino from the phenomenological imprints on the energy distribution for certain combinations of parameter values. This may be remedied by simultaneously studying the angular distribution as well, which for the same parameter values is shown on the right panel of the same figure. The two cases have a significantly different impact on the angular spectrum and can thus be easily differentiated.

4.6 Target Sensitivity

4.6.1 Event Count

In a β-decay experiment, the electrons observed over a given exposure make up the total number of events, N_{tot}. Experimental details, such as any acceptance cuts or

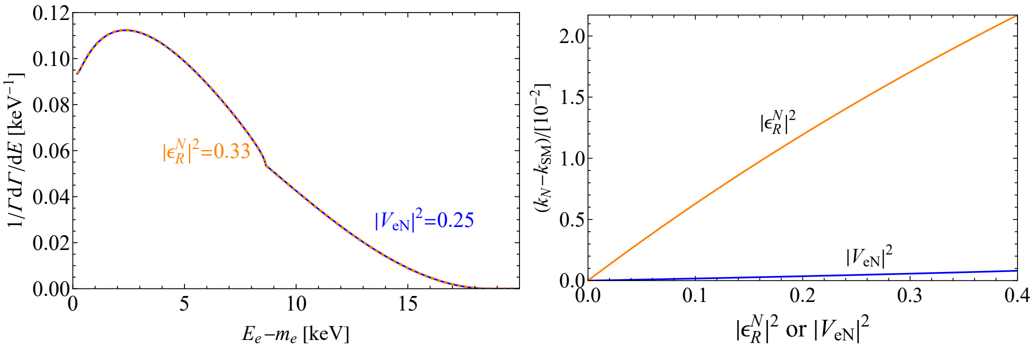

Figure 4.5: Energy and angular distributions showcasing the difference between an active-sterile mixing and an exotic right-handed leptonic current for producing a 10 keV neutrino. Left: Normalised energy distributions with active-sterile mixing, $|V_{eN}|^2 = 0.25$ (blue, dashed), overlapping with an exotic sterile $|\varepsilon_R^N|^2 = 0.33$ (orange) contribution. Right: Deviation of the angular correlation factor k from the SM value as a function of the active-sterile mixing $|V_{eN}|$ or the right-handed leptonic current parameter $|\varepsilon_R^N|$.

efficiency corrections can be combined into an overall multiplicative factor, $\eta \leq 1$, resulting in the number of collected events

$$N_{\text{events}} = \eta N_{\text{tot}}, \tag{4.50}$$

but for the purposes of this work we assume $\eta = 1$ throughout. Normally, β-decay experiments of the type considered in this work focus on a specific region – or window – of the energy spectrum, predominantly around the end point, making the quantity of interest the number of events within this window

$$N_{\text{win}} = \frac{N_{\text{events}}}{\Gamma} \int_{E_1}^{E_2} \frac{d\Gamma}{dE_e} dE_e, \tag{4.51}$$

where E_1 and E_2 are the lower and upper bounds of the energy window and the expression is normalised with respect to the total decay rate of tritium.

Since β-decay experiments for neutrino mass tend to focus on the end point region of the energy spectrum, we consider an energy window with a width of 1 eV below the end point, in order to estimate the required statistics. To assess the relative change in the number of events needed to distinguish between the two possible neutrino mass orderings, one must consider the 'worst'-case scenario of $m_{\text{lightest}} =$

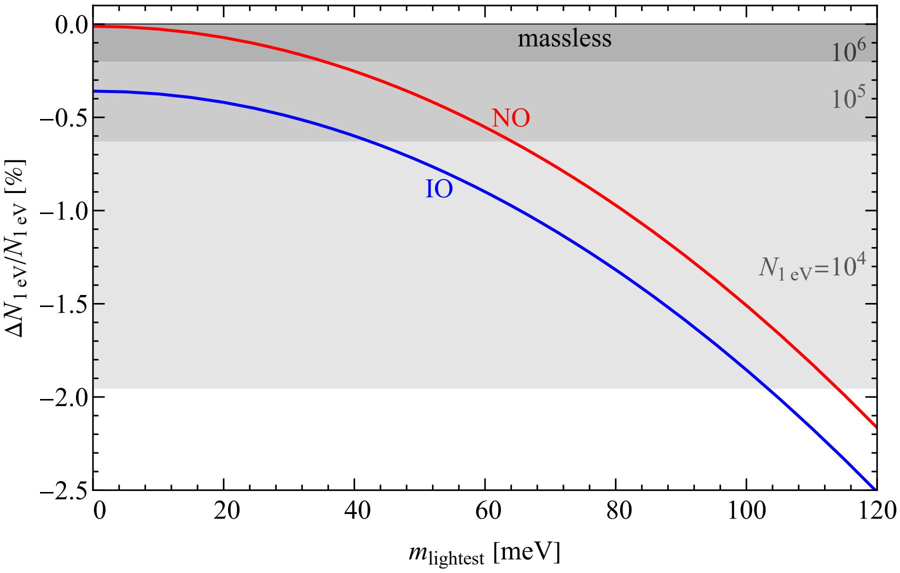

Figure 4.6: Change in percentage of the number of events in the final eV window of the energy distribution as a function of the lightest neutrino mass, for NO (red) and IO (blue) mass ordering cases. The gray shaded regions correspond to the 95% CL for a detectable change, for total number of events in the last eV of the spectrum of $N_{1\text{ eV}} = 10^4$, 10^5 and 10^6.

0. This is captured by Fig. 4.6, which shows the percentage change in the number of events in the final eV of the energy spectrum below the end point, as a function of m_{lightest}, for the two possible mass hierarchies: NO and IO.

The statistical uncertainty for $N_{1\text{ eV}}$ events in the final eV is given by [199]

$$\sigma_N = \frac{1}{\sqrt{N_{1\text{ eV}}}}. \tag{4.52}$$

From Fig. 4.6 it is visible that the percentage deviation for a massless lightest neutrino in the IO case is $\approx -0.37\%$. Inverting the above expression and using the 95% CL constraint for a one-tailed test gives a minimum number of events of $N_{1\text{ eV}} \approx 2.8 \times 10^5$. Hence, rearranging Eq. 4.51 for N_{tot}, setting $N_{\text{win}} = N_{\text{tot}} = 2.8 \times 10^5$ and accordingly setting $E_1 = E_0 - 1$ eV and $E_2 = E_0$ yields

$$N_{\text{tot}} = \Gamma \left(\int_{E_0 - 1\text{eV}}^{E_0} \frac{d\Gamma_{\text{SM}}}{dE_e} dE_d \right)^{-1} \cdot 2.8 \times 10^5 \simeq 1.3 \times 10^{18}. \tag{4.53}$$

Therefore, throughout the analysis, $N_{\text{tot}} = 10^{18}$ is used.

4.6.2 Molecular Impurities

In a realistic experiment, the atomic tritium source is not completely pure due to technical limitations – most notably recombination along the container walls – hence some level of molecular impurity is to be expected. It is therefore crucial to assess the impact of such molecular impurities to the sensitivity of future CRES-type experiments. The level of impurity present in the source is difficult to estimate without precise knowledge of the experimental set-up and techniques employed, but a good starting point is the estimate given by the Project 8 collaboration based on their proposed experiment.

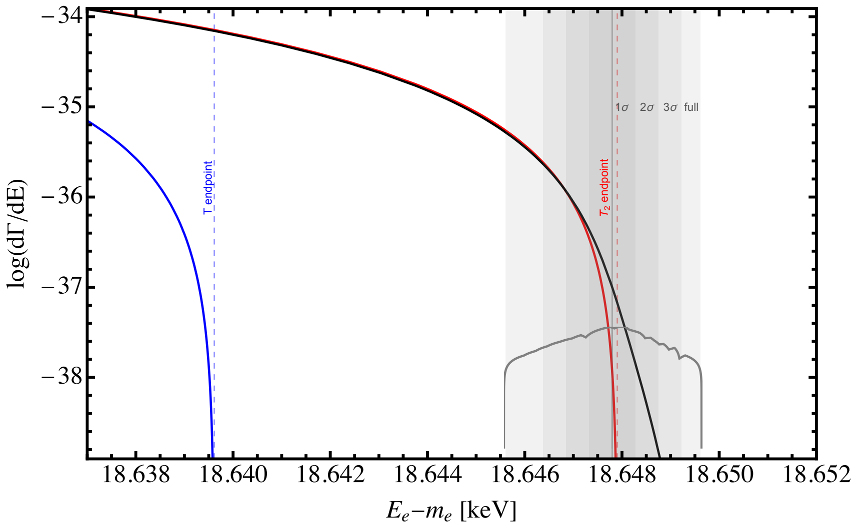

Figure 4.7: Endpoint of the differential decay rate of atomic tritium (blue), molecular tritium with fixed endpoint (black) and molecular tritium with variable endpoint (red).

For a molecular process, the daughter molecule of the beta-decay has a finite probability of ending up in excited rotational and vibrational states. The more energetic excited state the daughter occupies, the less energy there will be available to the outgoing electron and thus the endpoint will be shifted down by the corresponding amount. However, molecular tritium also has a higher binding energy than atomic tritium and therefore the total Q-value available to the process is slightly larger. This results in a smeared molecular endpoint that is roughly 10 eV higher than that of atomic tritium. A more precise modelling of the molecular endpoint requires knowledge of the final state distribution (FSD) which causes the broad-

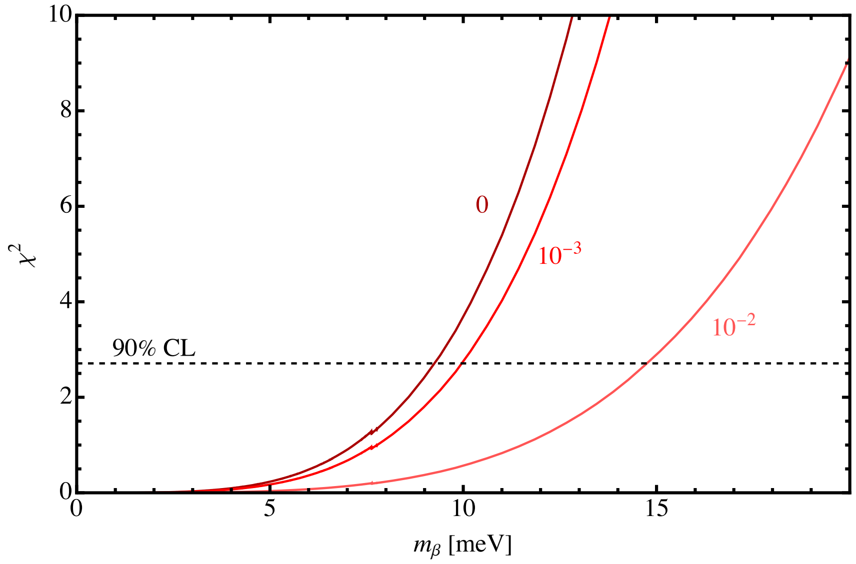

Figure 4.8: 90 % CL χ^2 variation as a function of the effective active neutrinos mass m_β, for three choices of molecular impurity levels, $n(T_2)/n(T) = 10^{-2}$ (peach), 10^{-3} (red) and 0 (burgundy).

ening. These effects are illustrated in Fig. 4.7, which shows the logarithm of the differential tritium decay rate as a function of the emitted electron's kinetic energy for atomic tritium (blue), molecular tritium with fixed endpoint shift of $\sim$ 10 eV (black) and molecular tritium with FSD taken into account (red) (this is modelled by convolving the molecular differential decay rate with the FSD from [200]).

Since the energy available to the most energetic electrons is dictated by the mass of the active neutrino – which is constrained to sub-eV level – such a change in the endpoint of the spectrum will significantly impact neutrino mass measurements. To asses the effect of the molecular contamination on the measurement of m_β in future CRES-type experiments, a minimal χ^2 analysis was performed under the assumption of different levels of molecular impurities, $n(T_2)/n(T)$, where $n(T_2)$ and $n(T)$ are the molecular and atomic tritium densities, respectively. The results of this are shown in Fig. 4.8, for three choices of impurity levels: $n(T_2)/n(T) = 10^{-2}$ (peach), 10^{-3} (red) and 0 (burgundy), motivated by the Project 8 collaborations upper limit estimate of $n(T_2)/n(T) \lesssim 10^{-4}$ [200]. The black dashed line shows 90 % CL, corresponding to $\chi^2 = 2.71$, the critical value for 1 d.o.f. The x-axis value at the intersection of this line with each of the curves gives the respective effective mass that the corresponding impurity levels allow sensitivity to. The higher the molecular contamination, the lower the sensitivity to m_β is. The highest and lowest constraining power is associated with $n(T_2)/n(T) = 0$ and $n(T_2)/n(T) = 10^{-2}$, resulting in $m_\beta \sim 9$ meV and $m_\beta \sim 15$ meV, respectively. The uncertainty in the effective mass measurement is thus of the order $\Delta m_\beta \sim 6$ meV. This is much smaller than the energy resolution of $\Delta E \sim 100$ eV assumed in this work, and therefore molecular effects can be neglected.

4.7 Projected Sensitivity

4.7.1 Statistical Analysis

Currently, sterile neutrinos have not yet been observed, which results in experimental bounds being placed on the relevant parameters associated with them, such as $|V_{eN}|^2$. To estimate the bounds that a CRES-like experiment will be able to place, a minimal-χ^2 analysis is used. This is achieved by dividing both the angular and energy distributions into bins, where the integrated event count in each bin over the entire range of the spectrum makes up the total number of events. For the angular distribution, we use two bins: the first for the 'aligned' and the second for 'anti-aligned' hemispheres. In the case of the energy distribution, the width of the bins must be larger than the expected energy resolution of the experiment, but otherwise there is no constraints on their size and thus number [177].

The test statistic, t, which quantifies the difference between the expected SM and simulated BSM results, is given by

$$t = \min_A \left[\sum_{i=1}^{N_{\text{bins}}} \frac{(N_{\text{BSM}}^{(i)} - (1+A) N_{\text{SM}}^{(i)})^2}{N_{\text{SM}}^{(i)}} + \left(\frac{A}{\sigma_A} \right)^2 \right], \tag{4.54}$$

where the the $N_X^{(i)}$ are the number of events in the i^{th} bin in the $X = \text{SM}$ or BSM cases and naturally the sum iterates over all bins, with N_{bins} denoting the total number of bins. The variable A is a nuisance parameter, which is included to account for the uncertainty in the overall normalisation of the energy distribution. The error on A is represented by σ_A, which is set to $\sigma_A = 2$ (conservatively large but with little impact). This differs from a simplistic χ^2 test, as besides the inclusion of a nuisance parameter, the summed expressions is also minimised with respect to A.

In principle, repeating the experiment many times will result in slightly different event counts in each bin for each run. To simulate this statistical fluctuation, one may perform a large number of Monte Carlo tests to find the median number of events for each bin. Since this is a computationally intensive and expensive procedure, one may use the Asimov data-set instead, which allows for the median values over a large number of runs to be replaced by their respective expectation values [201] in the asymptotic limit (i.e. when the number of events is very large). Thus, rather than being a randomly fluctuating distribution, the number of events in each bin is a fixed value, which removes the degrees of freedom associated with the bins (as each bin's event count is in general independently variable). As a result of the reduction of the degrees of freedom, the log-likelihood tends to a χ^2 distribution with one degree of freedom for each strength parameter (i.e. $|V_{eN}|^2$ or one of the ε^N). A χ^2 distribution is significant at 95% CL if it is in excess of 3.841 for one degree of freedom, or 5.99 for two degrees of freedom. If no deviations from the SM are observed, limits on the parameters of interest parameterising the BSM effect can thus be placed at 95% CL. In this work, the χ^2 analysis was performed using an integrated event count of $N_{\text{tot}} = 10^{18}$ across all bins, corresponding to $\approx 2.8 \times 10^5$ events in the last eV of the spectrum below the end point.

4.7.2 Production via Active-Sterile Mixing

In next-generational β-decay experiments, measurements of the energy and/or angular spectrum of the outgoing electron will enable the observation of sterile neutrinos, or in the absence of a positive signal, bounds will placed on the relevant parameter(s). Using the statistical analysis framework outlined in the previous section for 10^{18} total expected events and assuming an ideal experiment without any systematic uncertainties, we present upper bounds on $|V_{eN}|^2$ and ε^N, as the sterile state may either arise due to the mixing between the active and sterile sectors, or be produced directly from exotic currents. Both of these parameters in general depend on the sterile mass, m_N.

In the first case, i.e. when the sterile state arises due to the non-zero mixing between the active and sterile sectors, we consider for simplicity a one active + one sterile neutrino scenario. The estimated sensitivity to the mixing angle from the energy spectrum as a function of m_N is shown in Fig. 4.9 for 10^{16} (red solid) and 10^{18} total events (black solid) at 95% CL. The gray shaded band around the sensitivity contour for the latter case shows the 1σ variation of the sensitivity due to statistical fluctuations. It can be seen from the plot that the greatest sensitivity to the mixing angle occurs at a sterile mass around half of the maximum kinetic energy available in the process, as the greatest impact of the sterile neutrino is the presence of the 'kink', positioned at $E_e^{\max} - m_N$. As the mass approaches zero, the sterile neutrino vanishes and the energy distribution approaches the SM case, which results in the sensitivity to the mixing angle weakening and vanishing completely at $m_N = 0$. For large masses, the sensitivity is also reduced due to the limited phase space availability, and completely vanishes at the kinematic threshold where the sterile neutrino is too heavy to be produced. In this limit, all that is left behind is the SM distribution with a reduced amplitude, however this difference is obscured by the uncertainty in the overall normalisation which is the result of the minimisation over the nuisance parameter, A, in the χ^2 expression given in Eq. 4.54.

Fig. 4.9 also shows existing and projected future exclusions relevant in the region of parameter space that is of interest. These include model independent experimental results/projections as well as model dependent ones.

The model independent experimental constraints come from tritium (blue shaded) and nickel (yellow shaded) β-decay experiments. The nickel experiment – a dedicated sterile neutrino search – was performed in the mass range $4 - 30$ keV [202], while the tritium exclusion comes from regular SM neutrino mass experiments, which concentrated their efforts on the end point region of the spectrum, which is why the sensitivity to the mixing angle is constrained to a few keV in the sterile mass range.

Besides the model independent experimental constraints, there are also astrophysical bounds included in the figure, from X-ray, Cosmic Microwave Background

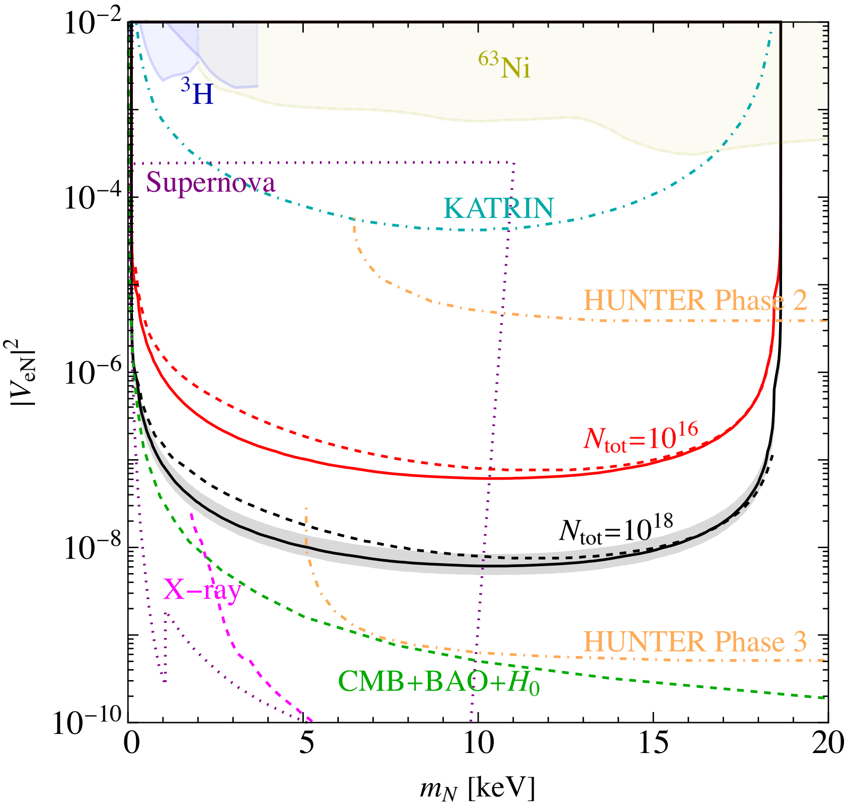

Figure 4.9: Projected sensitivities to the active-sterile mixing $|V_{eN}|^2$ as a function of sterile neutrino mass m_N at 95% CL, for a total number of events $N_{\text{tot}} = 10^{16}$ (red solid) and $N_{\text{tot}} = 10^{18}$ (black solid), alongside corresponding expected sensitivities of TRISTAN (dashed red and dashed black). The gray shaded band corresponds to the 1σ variation of the 95% CL for a large number of simulations. The shaded regions are excluded by ^{3}H (blue) and ^{63}Ni (yellow) searches together with future experimental constraints expected from KATRIN (cyan dot-dashed) and HUNTER (orange dot-dashed). The dotted lines show current astrophysical constraints from: X-ray data (pink), CMB+BAO+H_0 observations (green) and supernova data (purple).

(CMB), Baryon Acoustic Oscillation (BAO) and the Hubble parameter (H_0) measurements. These measurements can place stringent limits on the active-sterile mixing, though it should be noted that their validity is dependent on the underlying astrophysical and cosmological models employed. If keV-mass sterile neutrinos were present (produced via active-sterile mixing) in the early universe (motivated by their properties which make them viable dark matter candidates), they are expected to have undergone decays into lighter particles and mono-energetic photons with energies in the X-ray range, producing a corresponding distinct line in the spectrum when observing astrophysical sources. The data from the NuSTAR experiment does not contain any observed lines above the background and thus found no signs of sterile neutrinos, however it was able to place stringent upper bounds on the value of the mixing angle for sterile masses below around $m_N \sim 10\,\text{keV}$ [203]. If the early universe saw the production of sterile neutrinos through their mixing with the active neutrinos, they would have frozen out earlier than the active neutrinos due to the suppression of their interactions by the mixing angle, leading to a relic population of sterile states. This will have contributed to the matter and energy density of the universe, affecting the expansion history and structure formation of the universe. Observables from the recombination era can thus constrain the active-sterile mixing angle. The increased energy density of the universe due to the relic sterile neutrinos leads to faster expansion rate and a younger universe than what is observed, which in turn will affect the timing of recombination and structure formation, leaving an imprint on the CMB. Structure formation also depends on BAO, which is altered when sterile neutrinos are present in the early universe due to their free streaming, preventing small-scale structure growth. Furthermore, as the expansion is expected to be faster in such a case, the characteristic scale of BAO – called the sound horizon [4]– is shorter [204]. Lastly, the study of supernova events can also be used to probe sterile neutrinos, as neutrinos play a significant role in the general process. If there is a non-zero active-sterile mixing, part of the active neutrinos present in the core of the collapsing star may transform into sterile states and escape the collapsing star due to the lack of available interaction channels. This means part of the energy associated with the neutrinos in the core is carried away, and as as result of the insufficient pressure build up, potentially preventing the explosion. Moreover, the energy that escapes in the form of sterile neutrinos causes more rapid cooling, which can be measured. So far no deviation has been observed from the expected, producing upper bounds on the active-sterile mixing angle [205].

Additionally, Fig. 4.9 shows the projected sensitivities of future searches from

---

[4] The sound horizon is the maximum distance which the acoustic waves (due to the opposing effects of gravitational pull on matter and the 'push' from photon pressure) were able to travel before photons decoupled from the primordial plasma at recombination.

KATRIN, TRISTAN and HUNTER. KATRIN, although primarily designed to measure or constrain the electron neutrino mass, has the potential to perform sterile neutrino searches and thus constrain the active-sterile mixing angle with its current technical set-up. The estimated sensitivity that can be reached is shown to be of order $|V_{eN}|^2 \sim 10^{-4}$ [206] (cyan dot-dashed). In order to increase the search power, TRISTAN, an extension to the KATRIN experiment for a dedicated sterile neutrino search was proposed, as discussed in Sec. 4.1.1. The projected sensitivity of TRISTAN is shown for 10^{16} (red dashed) and 10^{18} (black dashed) total number of events. The first event count reflects the design sensitivity of TRISTAN that takes into account the details of the experiments, while the latter is the statistical limit [206]. These count rates translate to estimated sensitivities of order $|V_{eN}|^2 \sim 10^{-5}$ and $|V_{eN}|^2 \sim 10^{-7} - 10^{-8}$, respectively. As can be seen, these projected sensitivities are rather similar to our results, which is not unexpected given that both the physical processes and the event counts are the same in both cases, which explains the similar shape and reach of the sensitivity contours.

HUNTER is another planned experiment, which will use trapped cesium atoms undergoing electron capture. As this is a two-body process, with only a SM neutrino and the daughter nucleus in the final state, the energy-momentum and hence the nuclear recoil will be singularly dictated by the active neutrino mass. The experiment will rely on precision measurements of this recoil to measure the active neutrino mass, with the capability of searching for signs of additional decays of sterile neutrinos that the final state active neutrinos may mix into and thus constraining the active-sterile mixing parameter space. Although still under construction, Phase 1 of the experiment is expected to perform searches in the sterile mass range 50 keV–280 keV, which is beyond the region of interest for this work. As HUNTER will make nuclear recoil measurements, its resolution and sensitivity will be significantly affected by uncertainties, limiting its reach at low sterile masses of a few keV. Phase 2 and 3 on the other hand, due to the planned technological improvements to reduce uncertainties and thus increase resolution, will extend the search to lower mass regions. HUNTER's sensitivity is projected to exceed $|V_{eN}|^2 \sim 10^{-5}$ in

Phase 2 and reach as far as $|V_{eN}|^2 \sim 10^{-9}$ in Phase 3 of its operation [207]. It can be seen from the figure that the estimated sensitivity of Phase 2 will be significantly weaker than our projections for future CRES-type experiments, and although Phase 3 is expected to surpass these projections, a separate search would be required to cover the mass range $m_N < 5$ keV.

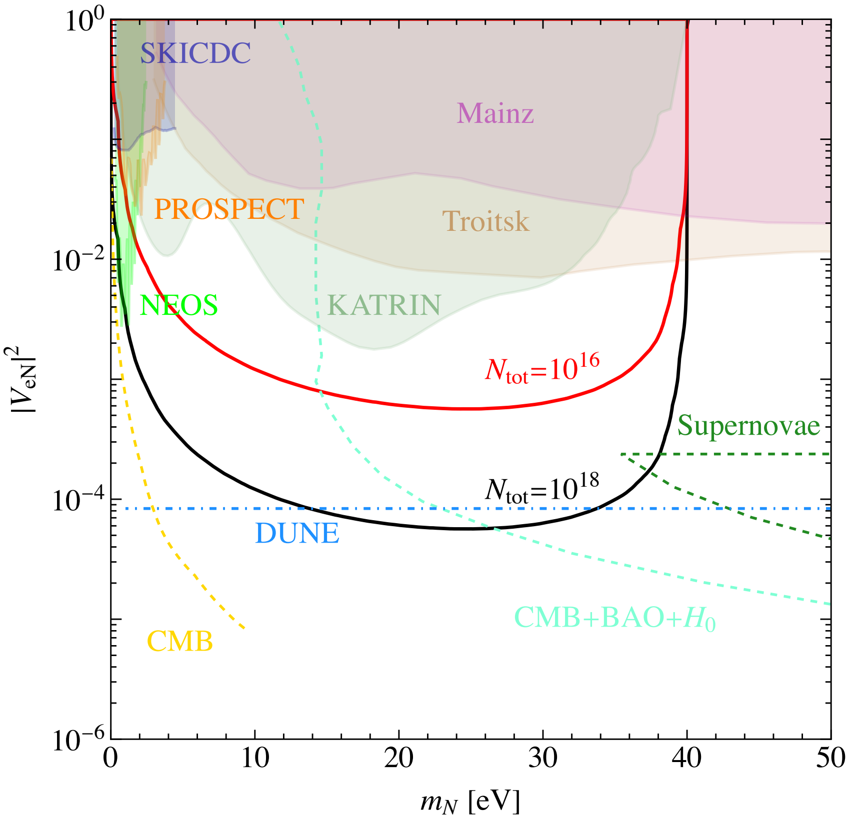

Figure 4.10: Projected sensitivities to the active-sterile mixing $|V_{eN}|^2$ as a function of light sterile neutrino mass m_N at 95% CL, for a total number of events $N_{\rm tot} = 10^{16}$ (red solid) and $N_{\rm tot} = 10^{18}$ (black solid). The shaded regions are excluded by SKICDC (blue), PROSPECT (orange), NEOS (mint green), Mainz (purple), Troitsk (light brown) and KATRIN (light green) searches. Future experimental constraints are expected from DUNE (light blue dot-dashed). The dotted lines show current astrophysical constraints from: CMB (yellow), CMB+BAO+H_0 observations (cyan) and supernova data (dark green).

Besides keV-mass sterile neutrinos, it is also possible to search for light sterile states, with a mass of around a few tens of eV. Because their effect on the energy spectrum is closer to the endpoint, modeling high-energy effects precisely is especially important. Using the same χ^2 analysis approach as in the case of keV-scale sterile neutrinos, the sensitivity of future CRES-type experiments to light sterile neutrinos was estimated. Based on the last 40 eV window of the spectrum, the projected exclusions of the active-sterile mixing angle as a function of light sterile mass are shown in Fig. 4.10 for $N_{\mathrm{tot}} = 10^{16}$ (red) and $N_{\mathrm{tot}} = 10^{18}$ (black), with maximal sensitivities is $|V_{eN}|^2 \sim 10^{-3}$ and $|V_{eN}|^2 \sim 10^{-4}$, respectively. Compared to the keV-search projections shown in Fig. 4.9, the sensitivities are a few orders of magnitude weaker. This is simply the result of the more prominent spectral impact associated with a heavier neutrino, alongside the higher event count around the bulk of the distribution, than near the endpoint. As the sterile mass tend to zero, the sensitivity is lost completely, as the spectral distortion due to the sterile neutrino vanishes and the distribution shape becomes identical to the SM one. Near $m_N = 40$ eV the sensitivity to the mixing angle is similarly reduced, due to the sterile neutrino being kinematically ’pushed’ out of the energy window under consideration.

The most substantial existing exclusion comes from the KATRIN experiment [208]. Similarly to the analysis performed here, the KATRIN results are based on the last 40 eV window of the energy spectrum, but in contrast to our analysis the endpoint is kept free and treated as a nuisance parameter. Although covering a much smaller sterile mass range, a comparably sensitive exclusion was made by NEOS [209], a reactor neutrino experiment observing inverse beta-decay using a Gadolinium liquid scintillator. A bit broader in sterile mass range and going up to ~ 5 eV is the PROSPECT [210] exclusion, similarly based on spectral measurements of reactor antineutrinos. The excluded region labeled SKICDC is attributed to Super-Kamiokande, IceCube and DeepCore (SK+IC+DC) which all provide comparable limits [211]. The excluded regions along the largest range of m_N come from the two tritium beta-decay experiments, Mainz [212] and Troitsk [213]. The DUNE experiment is expected to constrain the parameter space of interest very heavily through indirect searches studying the effects of sterile neutrinos on the production rates of active neutrinos [214]. In order to achieve the desired high sensitivities, it is essential that the DUNE flux is known very precisely.

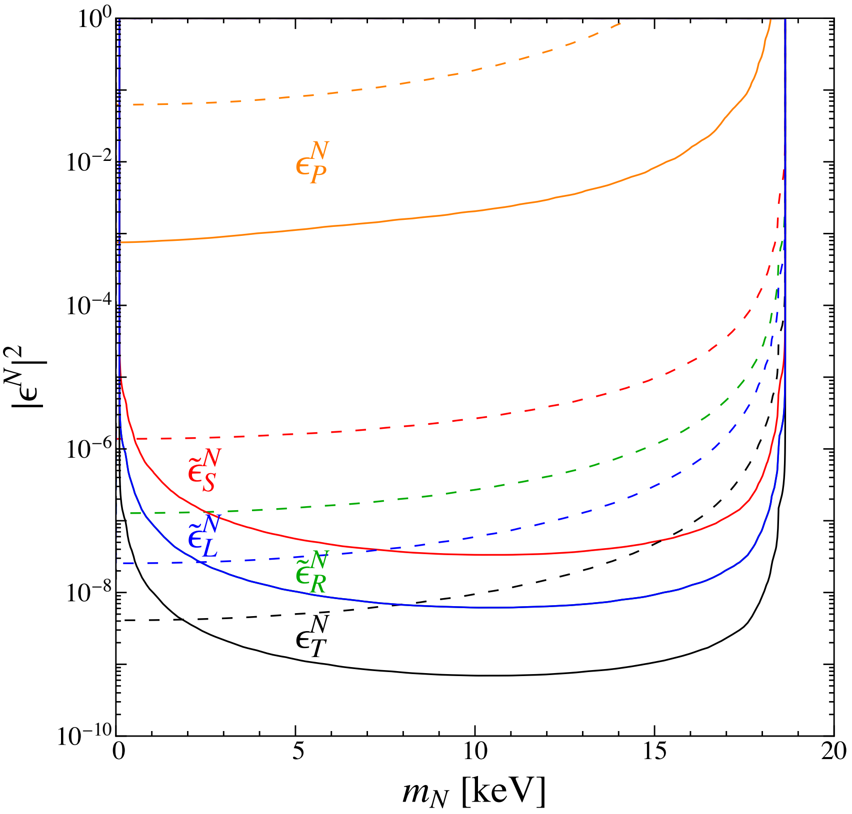

Figure 4.11: Projected sensitivities to various exotic couplings at 95 % CL, as a function of the sterile neutrino mass, based on the energy (solid) and angular (dashed) distributions. The active-sterile mixing is turned off, i.e. is set to $|V_{eN}|^2 = 0$.

4.7.3 Production via Sterile Exotic Currents

Besides mixing with the active neutrinos, sterile states might be produced via exotic currents different from the $V-A$ structure of the weak interaction, parameterised by the coupling constants ε^N. Following the same χ^2 procedure, the sensitivity to the exotic currents as a function of the sterile mass can be determined from both the energy and angular distributions.

The results are shown in Fig. 4.11 for various choices of couplings. All sensitivity contours based on the energy spectrum apart from ε_P^N have a similar shape to the admixing case above, with the sensitivity falling off as the sterile mass becomes too small to cause significant deviation from the SM case and as the mass becomes too large and sterile neutrino production is kinematically no longer possible. Maximal sensitivity is reached for a sterile mass of around $m_N \sim 10$ keV. The sensitivity contours derived using the angular distribution on the other hand exhibit

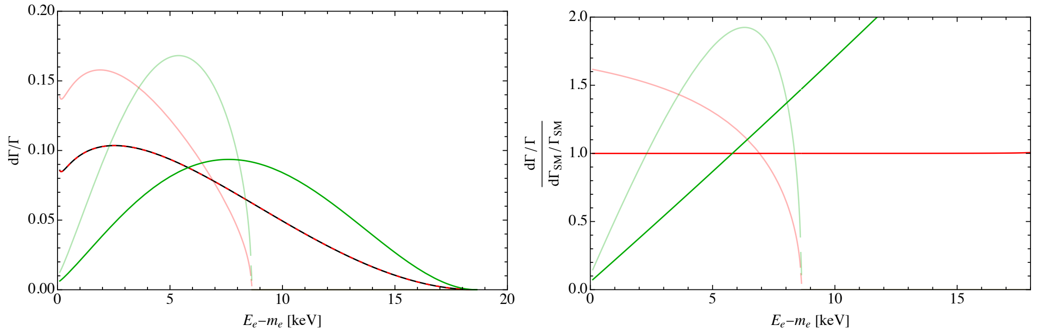

Figure 4.12: *Left:* Comparison of the spectral shapes of two exotic currents ε_S^N (red) and ε_P^N (green) and the SM (black), for $m_N = 0$ keV (opaque) and $m_N = 10$ keV (light), with the areas normalised to 1. *Right:* Normalised ratio of ε_S^N (red) and ε_P^N (green) to the SM distribution for $m_N = 0$ keV (opaque) and $m_N = 10$ keV (light).

different behaviour. In the case of ε_P^N, the sensitivity associated with the energy contour does not lose sensitivity even as $m_N \to 0$. This behaviour stems from the functional form of the pseudoscalar contribution to the decay rate. This can be seen in Fig. 4.12, which compares the shapes of three distributions: SM (black), ε_S^N (red) and ε_P^N (green) for $m_N = 0$ keV (opaque) and $m_N = 10$ keV (light), with the area under each distribution normalised to 1. In the left panel of the figure, it is clear that for $m_N = 0$ keV, the scalar and SM distributions look identical, while this is not the case for the pseudoscalar current. This explains why in Fig. 4.11 ε_S^N loses sensitivity as $m_N \to 0$ but ε_P^N does not. Conversely, for $m_N = 10$ keV both exotic currents produce distributions which are pronouncedly different from the SM and therefore translate to increased sensitivity to the mixing angle. The right hand panel of the figure shows the ratio of these exotic distributions to the SM distribution. Unsurprisingly, the scalar exotic current for a massless sterile state is a straight horizontal line of value 1, since the distribution does not deviate from the SM. In contrast, both the scalar and pseudoscalar distributions for $m_N = 10$ keV, as well as the pseudoscalar for a massless sterile neutrino deviate from the SM significantly.

In contrast to the energy distribution results, there is no loss of sensitivity at low m_N, as there is no suppression by the mixing angle. [5] Although the overall nor-

---

[5] For $m_N \to 0$, $d\Gamma_N/dE_e$ becomes almost indistinguishable from $d\Gamma_{SM}/dE_e$ in Eq. 4.46, apart from the overall normalisation difference, but this accounted for by the nuisance parameter A, in

Parameter	Energy	Angular
ε_S^N	2×10^{-4}	2×10^{-3}
$\tilde{\varepsilon}_S^N$	2×10^{-4}	2×10^{-3}
ε_P^N	5×10^{-2}	0.4
$\tilde{\varepsilon}_P^N$	5×10^{-2}	0.4
ε_T^N	3×10^{-5}	1×10^{-4}
$\tilde{\varepsilon}_T^N$	3×10^{-5}	1×10^{-4}
ε_L^N	8×10^{-5}	2×10^{-3}
$\tilde{\varepsilon}_L^N$	8×10^{-5}	2×10^{-4}
ε_R^N	8×10^{-5}	3×10^{-4}
$\tilde{\varepsilon}_R^N$	8×10^{-5}	5×10^{-4}

Table 4.3: Projected upper bounds on the sterile exotic couplings $|\varepsilon_X^N|$ at 95% CL for 10^{18} total events in the energy (left) and angular (right) distributions. The couplings are turned on one at a time, the sterile mass is fixed to $m_N = 10$ keV and the active-sterile mixing is switched off, $|V_{eN}|^2 = 0$.

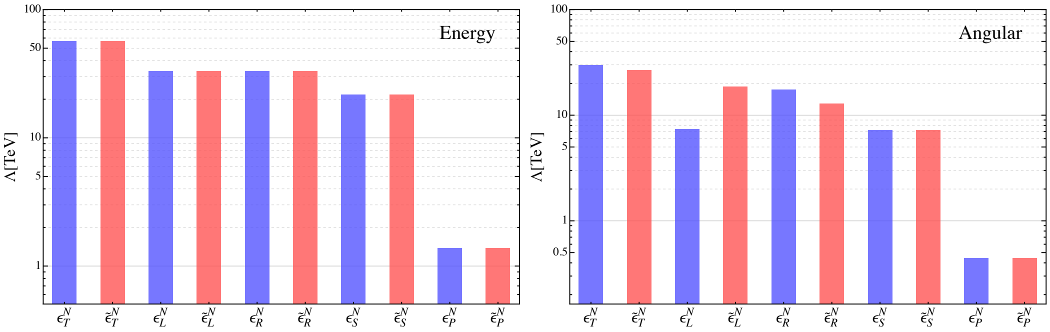

Figure 4.13: Bar charts showing the projected sensitivity of the exotic couplings to the scale of new physics at 95 % CL, using the energy (left) and angular (right) distributions. One coupling is switched on at a time, the sterile mass is fixed to $m_N = 10$ keV and the active-sterile mixing is switched off, $|V_{eN}|^2 = 0$.

malisation differences may hide some of these effects as in the energy distribution case, the contributions of the exotic currents to the angular distribution are varied and thus not all effects can be masked by the normalisation uncertainty. At high sterile masses, the drop-off in sensitivity is once again attributed to kinematic limitations. The differences in sensitivity between the couplings stems from the functional forms of their corresponding contributions to the energy and angular spectra.

Eq. 4.54. Moreover, the BSM term is suppressed by the mixing angle, which is constrained to be small.

Keeping the active-sterile mixing turned off ($|V_{eN}|^2 = 0$) it is possible to consider the sensitivity to each exotic coupling in turn (i.e. only switching on one at a time), similarly to Fig. 4.11, but with the sterile mass fixed to $m_N = 10$ keV (since this is the approximate mass at which the greatest sensitivity can be obtained). The upper bounds at 95% CL for the various exotic couplings are summarised in Table 4.3, alongside the bar charts of Fig. 4.13, which visually emphasise the variations in the projected upper bounds on the sterile exotic currents. The couplings are assumed to be real and positive. [6] As can be seen from the table, the weakest and strongest sensitivities are associated with the pseudoscalar and tensor currents, respectively, which is again a result of their functional forms. As in the case of Fig. 4.11, the table also shows that in general the angular probe is weaker than the energy distribution based approach. This is because while the kink in the energy spectrum – a rather distinctive feature – is naturally picked up in the energy distribution, the angular distribution integrates over the entire energy range and thus washes out this signature. Furthermore, the angular probe relies on the angular correlation between the tritium spin and the combined spin of the electron and neutrino final state system spin. The more massive the sterile neutrino, the weaker the helicity-chirality links becomes, making the distribution more isotropic and hence more sensitive to new physics effects. Despite this, the angular contours lose sensitivity as m_N increases, due to approaching the kinematic limit.

4.7.4 Hybrid Production

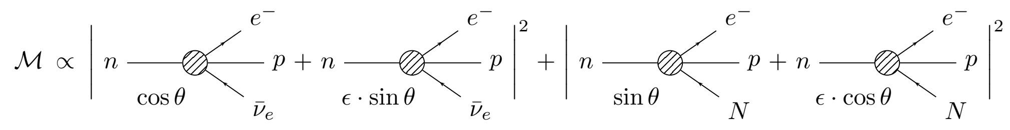

Figure 4.19: Schematic diagrams contributing showing the processes that contribute to the hybrid production matrix element.

---

[6] This is acceptable, because the lack of an interference term in Eq. 4.49 means all observables can only depend on $|\varepsilon_X^N|$, i.e. are insensitive to any complex phases. Furthermore, the assumption of positive couplings is justified, because the χ^2 procedure involves squaring the rate.

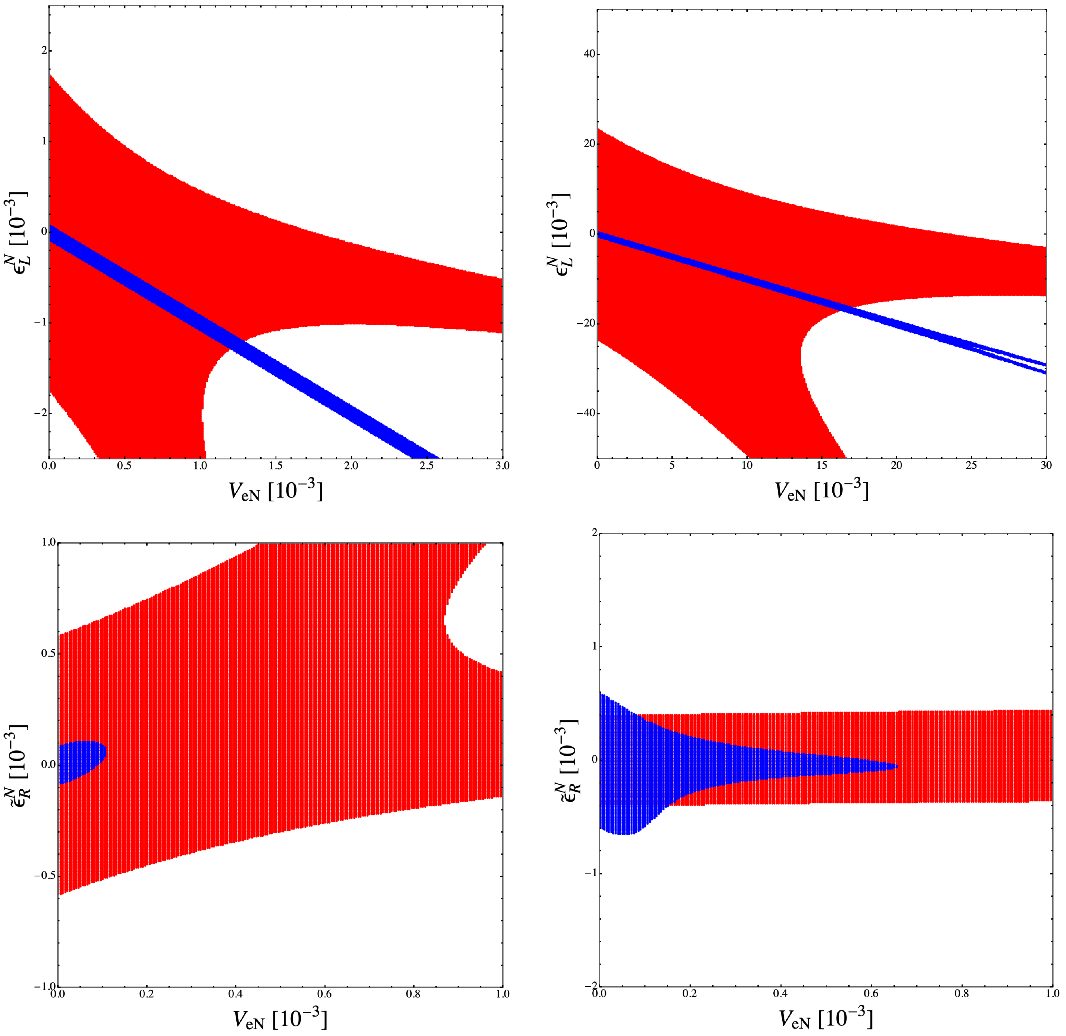

Figure 4.14: Plot showing the 95 % CL sensitivity regions for the exotic couplings ε_L^N (top) and $\tilde{\varepsilon}_R^N$ (bottom) and the active-sterile mixing angle, $|V_{eN}|^2$ for sterile masses $m_N = 10$ keV (left) and $m_N = 0.5$ keV (right). The sensitivities have been derived using the energy (blue) and angular (red) distributions, assuming 10^{18} total events.

Above, two distinct sterile neutrino production mechanisms were considered: via active-sterile mixing and directly from exotic currents. In fact, it is possible to have both $\sin\theta \neq 0$ and sterile exotic current ε turned on at the same time, resulting in the contributions to the matrix element squared shown in Fig. 4.19,

$$
\begin{aligned}
|\mathcal{M}|^2 &= |\cos\theta\ \mathcal{M}_{SM}^{\nu} + \varepsilon\sin\theta\ \mathcal{M}_{\varepsilon}^{\nu}|^2 + |\sin\theta\ \mathcal{M}_{SM}^{N} + \varepsilon\cos\theta\ \mathcal{M}_{\varepsilon}^{N}|^2 \\
&= \cos^2\theta|\mathcal{M}_{SM}^{\nu}|^2 + \varepsilon^2\sin^2\theta|\mathcal{M}_{\varepsilon}^{\nu}|^2 + 2\varepsilon\sin\theta\cos\theta\ \Re[\mathcal{M}_{SM}^{\nu}\mathcal{M}_{\varepsilon}^{\nu*}] \\
&\quad + \sin^2\theta|\mathcal{M}_{SM}^{N}|^2 + \varepsilon^2\cos^2\theta|\mathcal{M}_{\varepsilon}^{N}|^2 + 2\varepsilon\cos\theta\sin\theta\ \Re[\mathcal{M}_{SM}^{N}\mathcal{M}_{\varepsilon}^{N*}]. \qquad (4.55)
\end{aligned}
$$

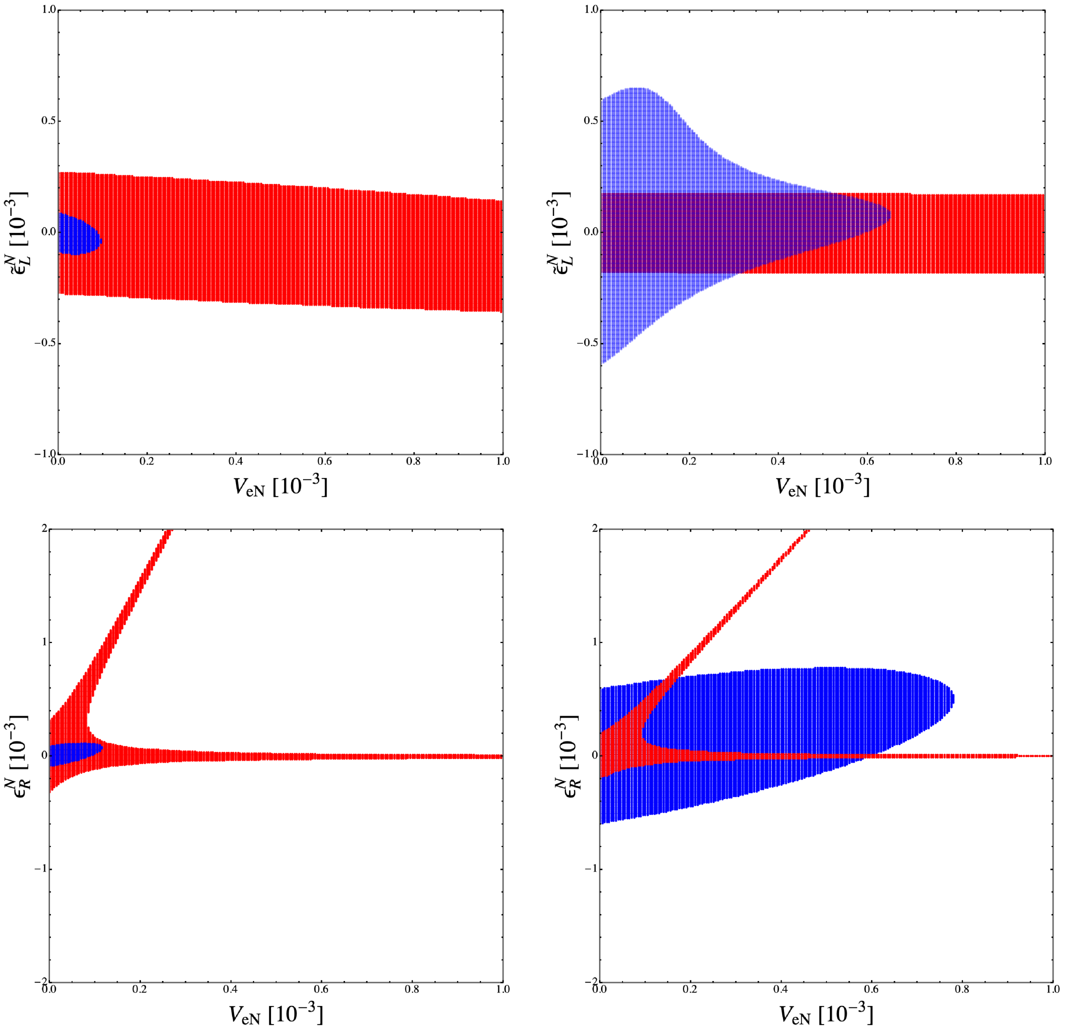

Figure 4.15: Same as Fig. 4.14 but with $\tilde{\varepsilon}_L^N$ (top) and ε_R^N (bottom).

The first two terms produce an active light neutrino in the final state, via the SM V-A and exotic interaction, respectively. The third and fourth terms instead produce a sterile neutrino in the final state, again via the V-A and exotic interaction. The gray circle denotes the effective operator, with the corresponding vertex factors shown underneath it. Since $d\Gamma/(dE_e d\Omega_e) \propto |\mathcal{M}|^2$, the contributions to the energy and

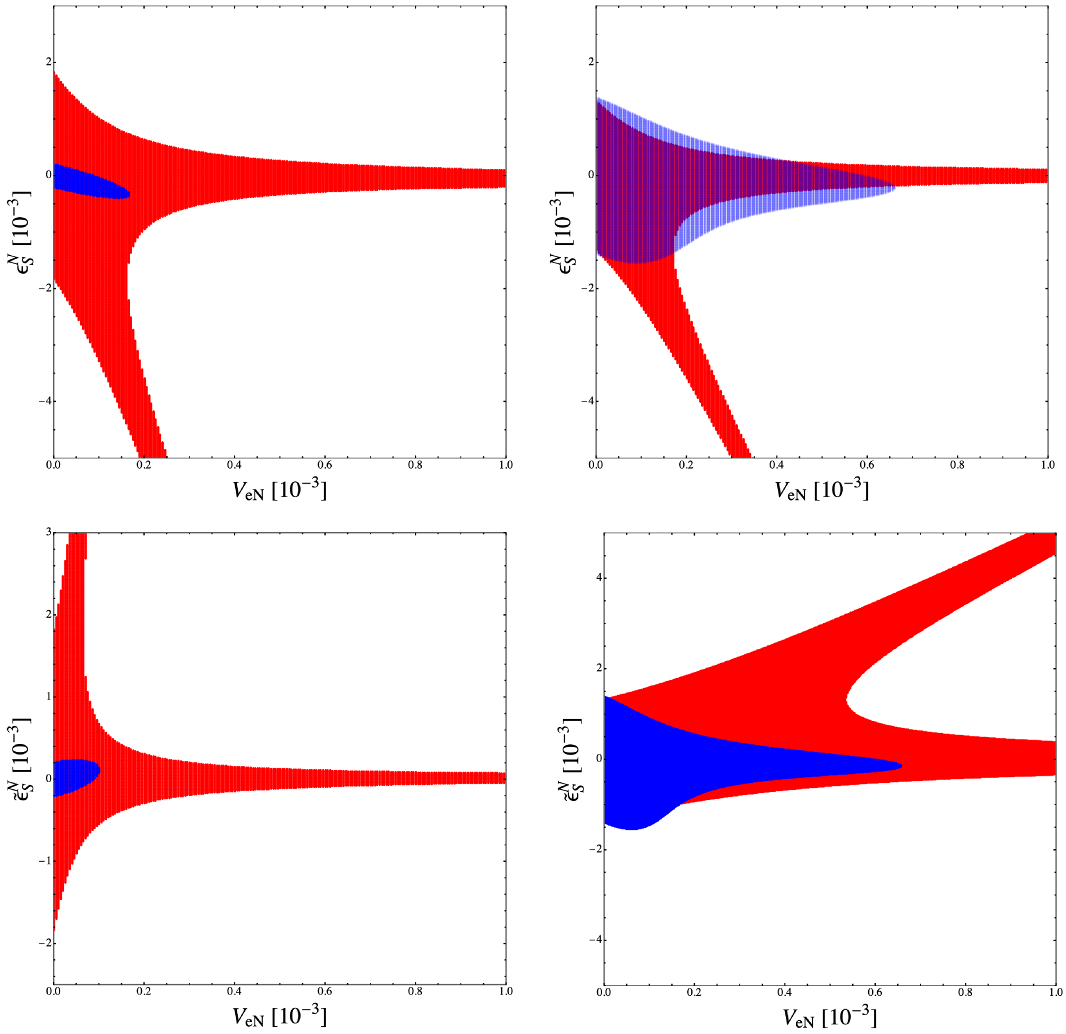

Figure 4.16: Same as Fig. 4.14 but with ε_S^N (top) and $\tilde{\varepsilon}_S^N$ (bottom).

angular spectra in Eq. 4.30 are given by

$$\begin{aligned} a(E_e) &= \cos^2\theta a_{SM}^{\nu}(E_e) + \sin^2\theta|\varepsilon|^2 a_{\varepsilon}^{\nu}(E_e) + |\varepsilon|^2\cos^2\theta a_{\varepsilon}^{N}(E_e) \\ &\qquad + \sin^2\theta a_{SM}^{N}(E_e) + 2\Re[\sin\theta\varepsilon^*]\, a_{SM,\varepsilon}^{\nu}(E_e) + 2\Re[\sin\theta\varepsilon^*]\, a_{SM,\varepsilon}^{N}(E_e), \end{aligned} \tag{4.56}$$

$$\begin{aligned} b(E_e) &= \cos^2\theta b_{SM}^{\nu}(E_e) + \sin^2\theta|\varepsilon|^2 b_{\varepsilon}^{\nu}(E_e) + |\varepsilon|^2\cos^2\theta b_{\varepsilon}^{N}(E_e) \\ &\qquad + \sin^2\theta b_{SM}^{N}(E_e) + 2\Re[\sin\theta\varepsilon^*]\, b_{SM,\varepsilon}^{\nu}(E_e) + 2\Re[\sin\theta\varepsilon^*]\, b_{SM,\varepsilon}^{N}(E_e). \end{aligned} \tag{4.57}$$

When considering one sterile exotic operator and non-zero active-sterile mixing, the parameter space of interest is the $\varepsilon - V_{eN}$ plane, which requires rewriting the above

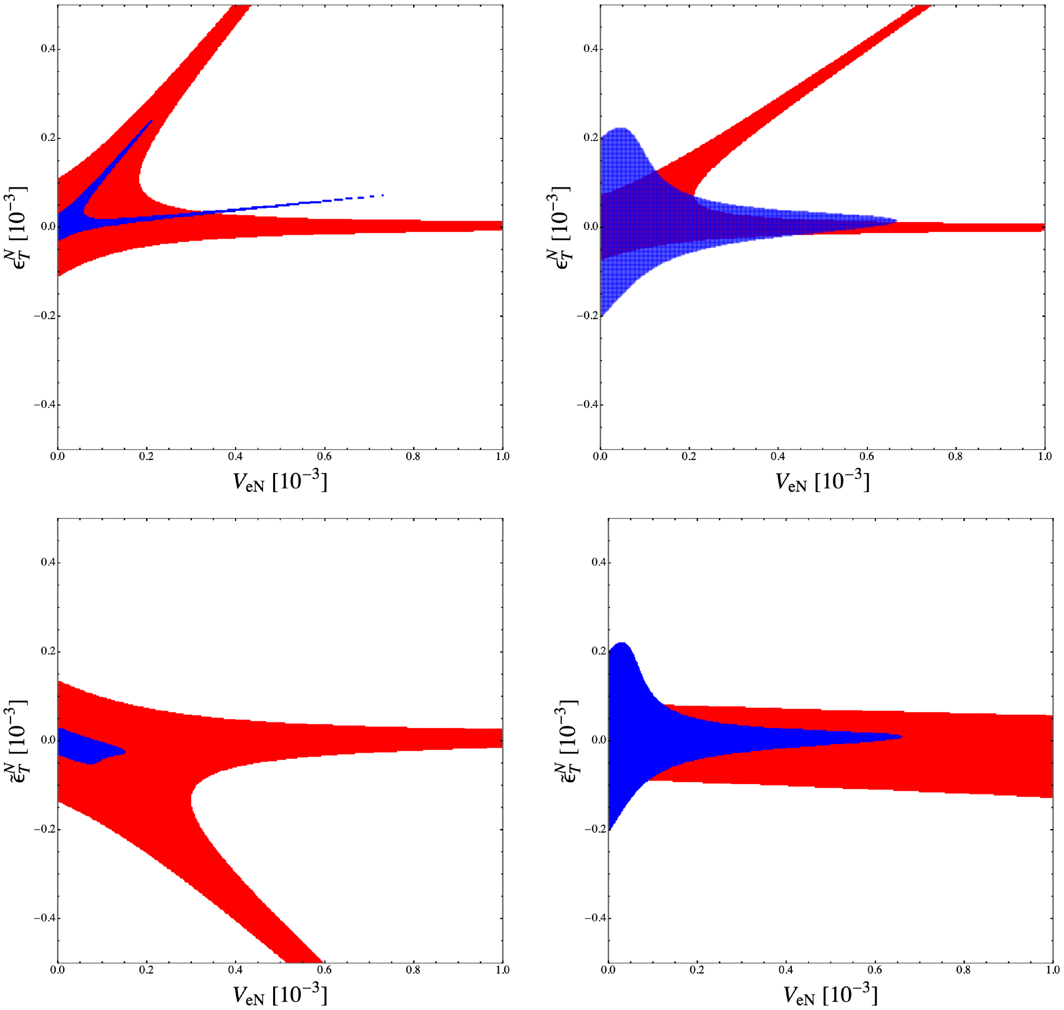

Figure 4.17: Same as Fig. 4.14 but with ε_T^N (top) and $\tilde{\varepsilon}_T^N$ (bottom).

expressions in terms of $\sin\theta \equiv V_{eN}$. Due to the existing constraints on the active-sterile mixing, it is safe to assume $\sin^2\theta = V_{eN}^2 \ll 1$ and therefore $\cos^2\theta = (1 - V_{eN}^2) \approx 1$. The sensitivity regions for the scenario with one sterile exotic operator turned on and $V_{eN} \neq 0$ are shown in Fig. 4.14, 4.15, 4.16, 4.17 and 4.18 for all sterile exotic couplings as a function of the active-sterile mixing, comparing the sensitivities of both the energy (blue) and angular (red) probes for two choices of sterile mass, $m_N = 10$ keV (left) and $m_N = 0.5$ keV (right).

The sensitivity contours based on the χ^2 analysis will in general take the form

$$\chi^2(V_{eN}, \varepsilon) = Ax^2 + By^2 + Cxy < D \tag{4.58}$$

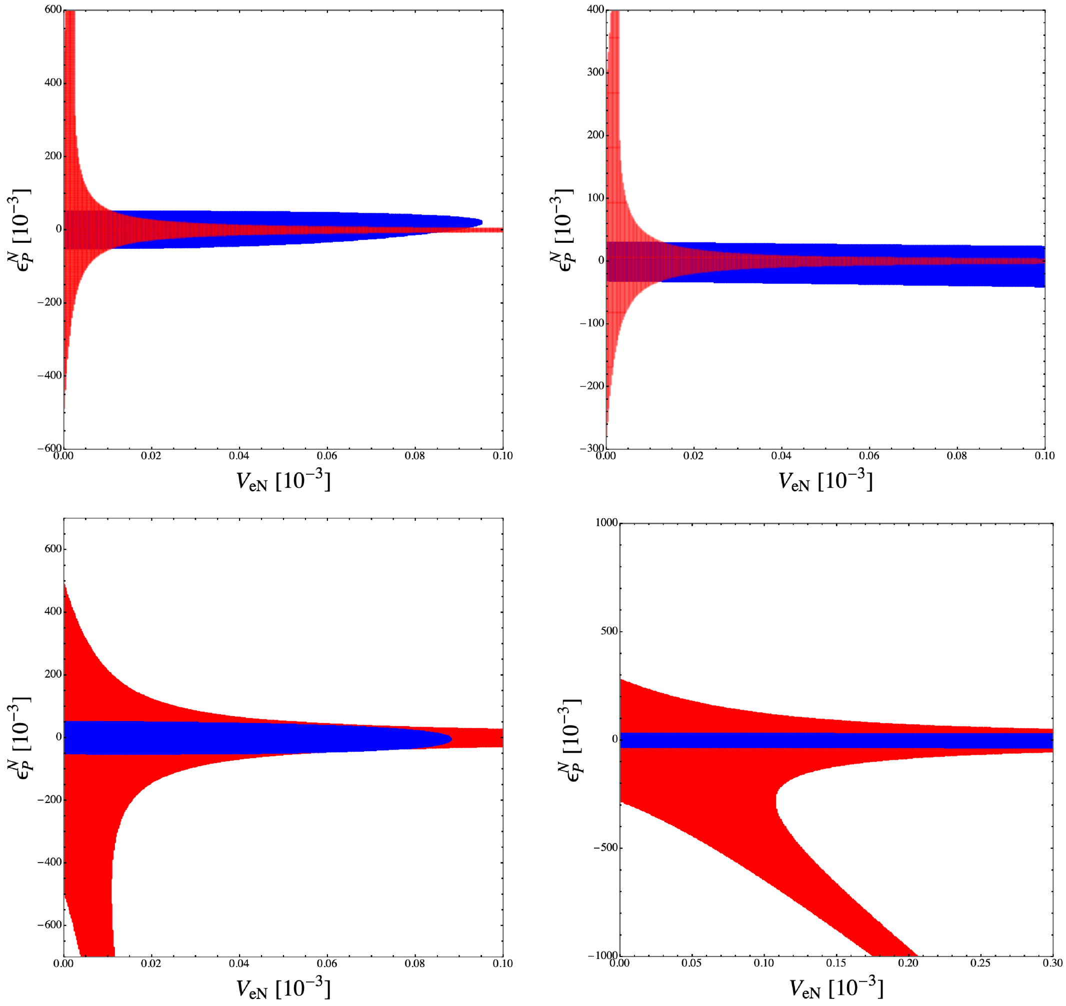

Figure 4.18: Same as Fig. 4.14 but with ε_P^N (top) and $\tilde{\varepsilon}_P^N$ (bottom).

where x and y can be identified with the parameters of interest ε and V_{eN} and D is the critical value, with $D = 5.99$ for a χ^2 confidence region at 95% CL for two degrees of freedom. The shape of the confidence region will depend on the values and signs of the coefficients. In general, the above expression describes a conic section, with its type determined by the value of the discriminant, $\Delta = C^2 - 4AB$. If $\Delta < 0$ and A, B have the same sign, the region is a closed ellipse, such as in Figs. 4.14, 4.15, 4.16 and 4.18. If $\Delta = 0$, the resulting shape is a band, as seen in Fig. 4.14, while having either $\Delta > 0$ or $AB < 0$ leads to a hyperbola of fork-like structure, as seen in Figs. 4.14, 4.15, 4.16, 4.17 and 4.18. For $\Delta < 0$ and $\Delta > 0$ the decay rate is dominated by the quadratic and interference terms, respectively, while in the case of $\Delta = 0$, they are of comparable size. In general, all geometric features of the resulting shapes depend on all three coefficients, A, B and C. The relative size of C compared to $A - B$ sets the tilt angle and the sign of C determines the tilt direction. Together, the magnitudes of A, B, C govern the thickness of the arms in the case of a hyperbola, while the orientation and openness of the arms is set by the ratio $A : B : C$.

In general, in most cases it can be seen from the plots that for all exotic couplings for $m_N = 10$ keV the constraints derived from the energy distribution are more stringent than the angular probe with respect to both the exotic couplings and the mixing angle. This is because the spectral distortion due to the sterile neutrino is a prominent kink in the energy distribution, while the sensitivity of the angular spectrum depends on the internal Lorentz structure and functional forms of the rates in a more complicated fashion. For all sterile exotic cases, the constraint based on the energy distribution is weaker for $m_N = 0.5$ keV, than for $m_N = 10$ keV. This is expected, since a lighter sterile mass leads to larger kinematic phase space overlap with the SM. The angular probe on the other hand tends to get weaker as the sterile mass becomes larger, since heavier masses break the chirality-helicity link more severely thereby reducing the angular correlation and bringing the emission closer to isotropy, at which point the angular probe gains full discriminating power, but this is killed by the phase space suppression.

For $\tilde{\varepsilon}_R^N$, $\tilde{\varepsilon}_L^N$, ε_R^N, ε_S^N, $\tilde{\varepsilon}_S^N$, ε_P^N and $\tilde{\varepsilon}_P^N$, the sensitivity regions based on the energy distribution are elliptical in shape. This is the result of the quadratic terms dominating over the interference terms. In these cases the interference terms linear in both ε and V_{eN} impact the sensitivity by tilting these elliptical regions, so as to break the symmetry around $\varepsilon = 0$. The direction and degree of the tilt depends on the sign and magnitude of the two interference terms. For all of these cases except $\tilde{\varepsilon}_L^N$, the angular confidence regions are hyperbolic forks with two arms, suggesting that the exotic-mixing interference term dominates. In the case of the angular probe for $\tilde{\varepsilon}_L^N$, the quadratic and interference terms are of comparable size, resulting in a band.

In the case of ε_L^N, the chiral structure is identical to that of the SM process and hence the interference and quadratic terms are of comparable size. Thus, the resulting sensitivity region for the energy probe is a band, along which the combination of ε and V_{eN} is constant.

In the case of ε_T^N and $\tilde{\varepsilon}_T^N$, the region based on the energy probe exhibits a hyperbolic fork shape, suggesting dominance of the interference terms over the quadratic ones. The angular results in both cases are hyperbolic. Besides ε_T^N, ε_S^N and all cases with RH leptonic current, the sensitivity region based on the energy distribution also exhibits a bulging, asymmetrical shape.

In many cases, the angular probes are narrower with respect to the exotic couplings than the mixing angle, i.e. more sensitive to them. The difference comes from the analytic forms of the $b_X(E_e)$ expressions for ε_X, compared with $b_{LL}(E_e)$, shown in Appendix C. In general, the most sizable terms in the SM case are suppressed by $(g_A - g_V)^2$ terms, while in many exotic cases either $g_A \to -g_A$ as compared to the SM, or the largest terms are unsuppressed. This leads to amplification and therefore increased sensitivity. Although in the scalar and pseudoscalar cases the pure sterile contribution to the angular spectra are zero, i.e. isotropic emission, the presence of non-zero interference terms restores the anisotropy and thus the sensitivity of the angular probe.

Chapter 5

Sterile Neutrinos at the FCC-ee

As we have seen in Sec. 3, observation of neutrino oscillations has confirmed the massive nature of the SM active neutrinos. It was also discussed that the lack of right-handed (RH) neutrino fields in the SM prevents the neutrinos from acquiring mass after EWSB through a Yukawa coupling, like the other fermions.

The most minimal extension of the SM which accommodates the observed phenomenon of oscillations is the addition of two RH neutrinos (in order to generate at least two distinct non-zero masses, in accordance with the two measured mass-splitting values) which are singlets under the SM gauge group, $SU(3)_c \otimes SU(2)_L \otimes U(1)_Y$. Since lepton number, L, is no longer an accidental global symmetry in this case, one can simply accept lepton number violation (LNV) and therefore allow the RH neutrinos to have Majorana mass terms. Extending the SM with two RH neutrinos through the minimal Type I seesaw as discussed in Sec. 3.5.3 is an attractive prospect, but it would produce sterile neutrinos with masses far beyond the reach of collider searches and are thus difficult to probe. Even if experiments had the necessary kinematic reach to accommodate such massive sterile states, the smallness of the active neutrino masses would suppress the active-sterile mixing angle to such a degree, that the number of sterile states producible would not yield high enough statistics.

Another possibility is the extension of the SM with the inverse seesaw model. In this scenario RH neutrino fields, associated with a small LNV Majorana mass, μ, are added to the SM. Since μ is very small, the mass-splitting between the sterile eigenstates is small and they form a pseudo-Dirac pair, thus suppresses the mass of the active neutrinos without themselves requiring a large mass. Phenomenologically, this is rather desirable, as it means the mass ranges of these sterile states are within the reach of collider experiments [185, 215–224]. This configuration also allows for sizable active-sterile mixing angles, and therefore such sterile neutrinos could be produced in sufficient amounts.

If the active neutrinos do not acquire their mass through the Dirac mechanism and if the SM is not extended with RH neutrinos, there still exist models that can give the active neutrinos masses. Such models include the Type II [132, 140–143] and Type III [144] seesaw mechanisms, which introduce a scalar triplet and two or more fermion triplets under $SU(2)_L$, respectively, to give rise to the light neutrino masses at tree-level. Other models have also been developed which induce the light neutrino masses at one-loop level or at higher orders.

Besides simple extensions of the SM with additional fields, as in the case of the models mentioned above, one may also extend the SM's gauge group itself to accommodate neutrino masses. The most popular of these extensions is the minimal left-right symmetric model (LRSM), which assumes the gauge group $SU(2)_L \otimes SU(2)_R \otimes U(1)_{B-L}$. This is then broken down to $SU(2)_L \otimes U(1)_Y$ and then to $U(1)_{\text{EM}}$, through two RH scalar triplets and a scalar bi-doublet acquiring VEVs, respectively. The first symmetry breaking occurs at scales much higher than the EW scale and creates the vector bosons $W_R^{\pm}$ and Z', while the latter symmetry breaking, around the EW scale, produces the $W_L^{\pm}$ and Z bosons, the SM-like mediators that couple to left-handed (LH) fields. Analogously to the three families of light neutrinos, the LRSM contains three generations of RH neutrinos, whose masses are of the order of the $SU(2)_R$ breaking scale. The existence of these RH states then allows the active neutrinos to acquire a mass through one of the seesaw mechanisms or a hybrid of them. The appeal of the LRSM, and indeed other gauge extensions, is that rather than adding individual fields which can seem arbitrary, they describe superior high-energy theories which naturally give rise to the necessary field content, through spontaneously broken symmetries, to explain phenomena such as the

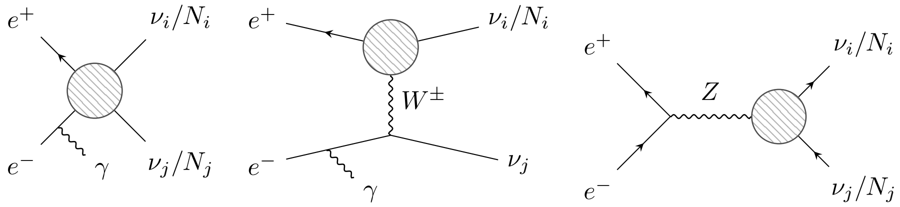

Figure 5.1: Single and pair production of HNLs at FCC-ee via the EFT operators considered in this work: four-fermion operators (left) and effective $W^\pm$ (centre) and Z (right) interactions. The active-sterile mixing V_{eN} induces the $W^\pm$ and Z diagrams, while $V_{\mu N}$ and $V_{\tau N}$ induce the Z diagram only.

mass generation of light neutrinos.

Although there exist numerous theories which employ RH neutrinos to explain the mass-generation mechanism of the SM light neutrinos, it is useful to compliment these efforts with model-independent sterile neutrino studies adopting an effective field theory (EFT) framework. In this approach, the effect of the heavy degrees of freedom at energy scales Λ are parameterised by EFT operators at low energies, containing fields that comply with the gauge group at the given low-energy regime. Therefore, the operators describing the complete unbroken phases existing in SMEFT differ from the low energy EFT (LEFT) operators parameterising the theory once symmetry breaking has taken place. Through numerous studies, the complete set of SMEFT and LEFT operators have been mapped and their renormalisation group runnings studied. In the EFT approach, it is only models that exhibit a non-zero matching to the $d = 5$ Weinberg operator and $\Delta L = \pm 2$ operators that may impart mass onto the SM light neutrinos [225–229]. In the case that the RH neutrinos have a Majorana mass that is below the TeV scale, then they are not heavy enough to integrate out and must appear explicitly in the operators. EFTs containing such fields are known as νSMEFT and νLEFT. In seesaw models the phenomenological effect of sterile neutrinos is felt through their mixing with the SM neutrinos. However, operators including N_R fields explicitly allow for various interactions with rich phenomenology beyond active-sterile mixing.

In this chapter, which is based on [230] and largely follows the same structure, we study the sensitivity of the future FCC-ee [231] to the scales of the EFT operator involving sterile neutrinos discussed in Sec 3.6 and summarised in Tables 3.1 and

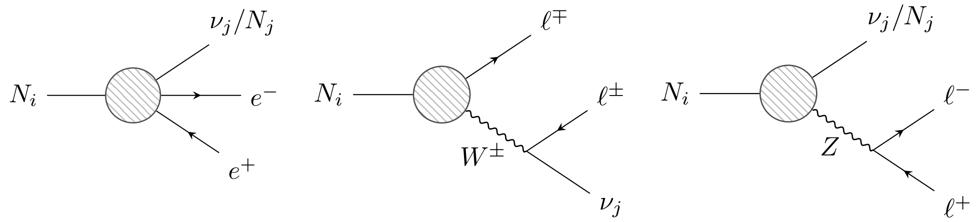

Figure 5.2: A selection of decays of HNLs via the same EFT operators in Fig. 5.1. The active-sterile mixing $V_{\alpha N}$ also induces the $W^\pm$ and Z diagrams.

3.2.

The FCC-ee is a proposed circular high-luminosity electron–positron collider at CERN, envisioned as a cornerstone of the post-LHC high-energy physics program. Designed to operate in a ~ 90 km tunnel, it would run at several centre-of-mass energies corresponding to key electroweak thresholds: the Z-pole (91 GeV), the WW threshold (161 GeV), the Higgs factory (240 GeV), and around the $t\bar{t}$ threshold (340-365 GeV). Operation at these energies would yield exceptional statistical precision and experimental accuracy. Unlike hadron colliders, the well-defined electron–positron initial state provides a clean environment, enabling precise reconstruction of final states and accurate measurements of electroweak observables. While not a discovery machine in terms of energy reach, the combination of high rates, extreme precision, and a clean environment makes FCC-ee an ideal instrument for precision tests of the Standard Model, observation of rare processes, and searches for small deviations induced by new physics. A decision on the initiative by CERN member states is expected in 2028, with construction planned for the early 2030s if approved. According to the tentative timeline, FCC-ee operations could begin in the late 2040s and continue for approximately 15 years, after which the FCC-hh hadronic collider would be installed in the same tunnel, extending the facility's high-energy program for roughly 25 years from the 2070s onward.

This phenomenological study uses two final states to constrain the $d \leq 7$ (with d being the mass dimension) νSMEFT operators: monophoton plus missing energy (mono-γ plus $\not{E}$) and displaced vertex (DV) signatures. The former is also used to constrain the active-sterile mixing angle, $V_{\alpha N}$. Such mixing can induce single HNL production via t-channel $W^\pm$ and s-channel Z exchange, as shown by the center and right diagrams of Fig. 5.1, respectively. Conversely, the νSMEFT operators are able to induce all three diagrams in Fig. 5.1, including single and pair production of HNLs. For example, in the Majorana case, the effective four-fermion and effective Z and $W^{\pm}$ interactions producing HNLs are mediated by the ΨH^n and $\Psi^2 H^n D^2$ operators, respectively.

Besides the production of HNLs, active-sterile mixing as well as the νSMEFT operators considered here allow the HNLs to decay, as shown in Figure 5.2. In order for the mono-γ plus $\not{E}$ signal to arise, the HNLs need to be long-lived enough to appear as missing energy. One way to ensure longevity along the detector length is to pair produce HNLs with a small mass splitting (such as in the pseudo-Dirac scenario). In the intermediate scenario, the HNL is long-lived enough to not decay promptly, but sufficiently short-lived to decay inside the detector to produce a DV signature.

We note briefly that there are a number of works that have studied the phenomenology of νSMEFT operators at colliders [164, 232–256]. Additionally, the set of νSMEFT operators of interest to us have been studied using mono-γ plus $\not{E}$ and DV searches at LEP [238, 244, 250] and FCC-ee [245], however these studies did not distinguish between the Majorana and Dirac HNL scenarios, nor did they consider different mass splittings between the HNLs.

5.1 Sterile Neutrinos in νSMEFT

In this chapter we use the νSMEFT framework to assess the phenomenological reach of the future FCC-ee collider. The νSMEFT contains operators constructed from the SM fields and the additional RH neutrino fields, N. The relevant set of operators which generate the processes of interest were introduced and discussed in Sec. 3.6.

5.1.1 Active-Sterile Mixing

The Lagrangian of Eq. 3.104 contains $\bar{L}Y_\nu N\tilde{H}$ and $\bar{N}^c MN$, which are the Yukawa coupling and Majorana mass terms for N. Post-symmetry breaking, these terms will lead to mixing between the active light neutrinos and the RH sterile ones, as discussed in the context of type I and inverse seesaw mechanisms in Sec. 3.5.3.

5.1.2 EFT Operators

In this chapter, we perform a phenomenological study to assess the sensitivity reach of the FCC-ee to the νSMEFT operators in Tables 3.1 and 3.2. These operators give rise to the single and pair production of HNLs, $e^+e^- \to \nu N/NN$ and also can alter the SM process $e^+e^- \to \nu\nu$. It should be noted that the list of $d \leq 7$ operators considered contributing to the production and decays of HNLs is not exhaustive. There are for example dipole operators, which are not considered here, as they have already been analysed in the context of the FCC-ee [239, 244, 245, 252], and more crucially tend to arise at loop-level and thus suffer from extra suppression.

The four-fermion and effective $W^\pm$ and Z interactions induced by these operators were given in Eqs. 3.105, 3.108, 3.106 and 3.109. These were written in the weak eigenstates, i.e. the interaction basis and therefore need to be rotated to the mass basis. Throughout the analysis of EFT operators, only one Wilson coefficient (WC) is switched on at a time, and the active-sterile mixing is assumed to vanish. This makes the rotations to the mass basis trivial, resulting in the effective four-fermion Lagrangian

$$\begin{aligned}\mathcal{L} \supset \left(\frac{1}{2}\right)\Big[&C^{i,XY}_{\nu e}(\bar{\nu}\Gamma_i P_X \nu)(\bar{e}\Gamma_i P_Y e) + C^{i,XY}_{\nu N e}(\bar{\nu}\Gamma_i P_X N)(\bar{e}\Gamma_i P_Y e) \\ &+ C^{i,XY}_{N\nu e}(\bar{N}\Gamma_i P_X \nu)(\bar{e}\Gamma_i P_Y e) + C^{i,XY}_{Ne}(\bar{N}\Gamma_i P_X N)(\bar{e}\Gamma_i P_Y e)\Big]\,, \end{aligned} \tag{5.1}$$

where $\Gamma_i \in \{\gamma_\mu, 1, \sigma_{\mu\nu}\}$ for $i \in \{V, S, T\}$ and for simplicity we rewrite the mass eigenstate fields as $\nu' \to \nu$ and $N' \to N$. The effective $W^\pm$ and Z interactions are given by

$$\begin{aligned}\mathcal{L} \supset &-\frac{g}{\sqrt{2}}\Big[W^X_\nu(\bar{\nu}\gamma_\mu P_X e) + W^X_N(\bar{N}\gamma_\mu P_X e)\Big]W^{+\mu} + \text{h.c.} \\ &-\left(\frac{1}{2}\right)\frac{g}{c_w}\Big[Z^X_\nu(\bar{\nu}\gamma_\mu P_X \nu) + Z^X_{\nu N}(\bar{\nu}\gamma_\mu P_X N) \\ &\qquad + Z^X_{N\nu}(\bar{N}\gamma_\mu P_X \nu) + Z^X_N(\bar{N}\gamma_\mu P_X N)\Big]Z^\mu\,. \end{aligned} \tag{5.2}$$

The Lagrangians above contain factors of $1/2$ in brackets. These are present, when N is Majorana. The following relations are satisfied by the WCs in both the Majorana and Dirac HNL cases

$$\begin{aligned}
&C^{V,XY}_{\underset{\alpha\beta\rho\sigma}{\nu e}} = C^{V,XY*}_{\underset{\beta\alpha\sigma\rho}{\nu e}}\,, \quad C^{V,XY}_{\underset{\alpha j\rho\sigma}{\nu Ne}} = C^{V,XY*}_{\underset{j\alpha\sigma\rho}{N\nu e}}\,, \quad C^{V,XY}_{\underset{ij\rho\sigma}{Ne}} = C^{V,XY*}_{\underset{ji\sigma\rho}{Ne}}\,,\\
&C^{S,XY}_{\underset{\alpha\beta\rho\sigma}{\nu e}} = C^{S,YX*}_{\underset{\beta\alpha\sigma\rho}{\nu e}}\,, \quad C^{S,XY}_{\underset{\alpha j\rho\sigma}{\nu Ne}} = C^{S,YX*}_{\underset{j\alpha\sigma\rho}{N\nu e}}\,, \quad C^{S,XY}_{\underset{ij\rho\sigma}{Ne}} = C^{S,YX*}_{\underset{ji\sigma\rho}{Ne}}\,,\\
&C^{T,XX}_{\underset{\alpha\beta\rho\sigma}{\nu e}} = C^{T,YY*}_{\underset{\beta\alpha\sigma\rho}{\nu e}}\,, \quad C^{T,XY}_{\underset{\alpha j\rho\sigma}{\nu Ne}} = C^{T,YX*}_{\underset{j\alpha\sigma\rho}{N\nu e}}\,, \quad C^{T,XX}_{\underset{ij\rho\sigma}{Ne}} = C^{T,YY*}_{\underset{ji\sigma\rho}{Ne}}\,,\\
&[Z^X_\nu]_{\alpha\beta} = [Z^X_\nu]^*_{\beta\alpha}\,, \quad [Z^X_{\nu N}]_{\alpha j} = [Z^X_{N\nu}]^*_{j\alpha}\,, \quad [Z^X_N]_{ij} = [Z^X_N]^*_{ji}\,,
\end{aligned} \tag{5.3}$$

while in the Majorana case the extra relations

$$\begin{aligned}
&C^{V,XY}_{\underset{\alpha\beta\rho\sigma}{\nu e}} = -C^{V,YY}_{\underset{\beta\alpha\rho\sigma}{\nu e}}\,, \quad C^{V,XY}_{\underset{\alpha j\rho\sigma}{\nu Ne}} = -C^{V,YY}_{\underset{j\alpha\rho\sigma}{N\nu e}}\,, \quad C^{V,XY}_{\underset{ij\rho\sigma}{Ne}} = -C^{V,YY}_{\underset{ji\rho\sigma}{Ne}}\,,\\
&C^{S,XY}_{\underset{\alpha\beta\rho\sigma}{\nu e}} = C^{S,XY}_{\underset{\beta\alpha\rho\sigma}{\nu e}}\,, \quad C^{S,XY}_{\underset{\alpha j\rho\sigma}{\nu Ne}} = C^{S,XY}_{\underset{j\alpha\rho\sigma}{N\nu e}}\,, \quad C^{S,XY}_{\underset{ij\rho\sigma}{Ne}} = C^{S,XY}_{\underset{ji\rho\sigma}{Ne}}\,,\\
&C^{T,XX}_{\underset{\alpha\beta\rho\sigma}{\nu e}} = -C^{T,XX}_{\underset{\beta\alpha\rho\sigma}{\nu e}}\,, \quad C^{T,XY}_{\underset{\alpha j\rho\sigma}{\nu Ne}} = -C^{T,XY}_{\underset{j\alpha\rho\sigma}{N\nu e}}\,, \quad C^{T,XX}_{\underset{ij\rho\sigma}{Ne}} = -C^{T,XX}_{\underset{ji\rho\sigma}{Ne}}\,,\\
&[Z^X_\nu]_{\alpha\beta} = -[Z^Y_\nu]_{\beta\alpha}\,, \quad [Z^X_{\nu N}]_{\alpha j} = -[Z^Y_{N\nu}]_{j\alpha}\,, \quad [Z^X_N]_{ij} = -[Z^Y_N]_{ji}\,.
\end{aligned} \tag{5.4}$$

also apply. Since the three light neutrinos are assumed to be massless Weyl fermions with LH components only, the WCs below do not exist in the Dirac case

$$C^{V,RX}_{\nu e} = C^{V,RX}_{\nu Ne} = C^{S,XY}_{\nu e} = C^{S,LX}_{\nu Ne} = C^{T,XX}_{\nu e} = C^{T,LL}_{\nu Ne} = W^R_\nu = Z^R_\nu = Z^R_{\nu N} = 0\,, \tag{5.5}$$

The SM CC and NC interactions are now contained within W^L_ν and Z^L_ν. These may be written in terms of the SM part and that originating from heavy new physics as

$$W^L_\nu = W^L_\nu\big|_{\mathrm{SM}} + \delta W^L_\nu\,, \quad Z^L_\nu = Z^L_\nu\big|_{\mathrm{SM}} + \delta Z^L_\nu\,, \tag{5.6}$$

where $W^L_\nu\big|_{\mathrm{SM}} = \mathbb{I}$ and $Z^L_\nu\big|_{\mathrm{SM}} = g^\nu_L \mathbb{I}$, with $g^\nu_L = 1/2$.

5.2 Monophoton Final State: Active-Sterile Mixing

Massive sterile neutrinos may couple to the SM through their mixing with the active neutrinos. In such a case – given that the sterile state is uncharged under the SM gauge group and the active neutrinos interact very weakly – it would be difficult to observe the sterile neutrino directly. Thus, in a realistic experiment the final state of the studied process must contain a state that interacts readily and hence indirectly supplies information about the inert sterile neutrino. Motivated by this, in this section we study the signal process $e^+e^- \to \nu N\gamma$. This can proceed via the middle and right diagrams shown in Fig. 5.1, where in this case the gray circles contain a factor of $V_{\alpha N}$. Due to the initial state particles being electron-flavour, for $W^\pm$ exchange $\alpha = e$, while for Z exchange $\alpha = e, \mu, \tau$. It should be noted, that the process $e^+e^- \to NN(\gamma)$ for non-zero active-sterile mixing is also viable via Z exchange, although it is not considered here, since the doubly inserted $V_{\alpha N}$ heavily suppresses the production cross section. Since the active and sterile neutrinos cannot be realistically detected and measured, the signal is the monophoton plus missing energy (mono-γ plus $\not{E}$). The kinematic distributions of the monophoton can be studied, as these supply indirect information about the final state HNL.

Although the presence of non-zero $V_{\alpha N}$ modifies the extended mixing matrix and thus the SM process $e^+e^- \to \nu\nu(\gamma)$, it is still completely fine to take $e^+e^- \to \nu\nu\gamma$ as the background process. This is because in the massless HNL limit (i.e. on the same kinematical footing), while the rate of the SM process is reduced, the rates of $e^+e^- \to \nu N(\gamma)/NN(\gamma)$ are increased. These two opposing effects cancel out exactly due to the unitarity of the full extended mixing matrix.

The parameter of interest is the active-sterile mixing angle, $|V_{eN}|^2$, which parameterises the strength of sterile neutrino coupling to the SM sector. It should be noted, that it is also possible to constrain $|V_{\mu N}|^2$ and $|V_{\tau N}|^2$ using the same signal process, however this will result in slightly weaker constraints due to the reduced cross section, as only Z exchange contributes to the production. Ultimately, we aim to estimate the sensitivity of the FCC-ee to $|V_{eN}|^2$ for two centre-of-mass energies $\sqrt{s} = 91.2$ GeV and $\sqrt{s} = 240$ GeV, with corresponding integrated luminosities of

$\mathcal{L} = 100$ ab^{-1} and $\mathcal{L} = 5$ ab^{-1}, respectively.

The above process was simulated using MADGRAPH5_AMC@NLO V3.4.2 – as described in Sec. 5.2.1 – with a model file from the FeynRules model database, which extends the SM with three generations of Dirac sterile neutrinos, $N_{1,2,3}$, taking $N \equiv N_1$ to be the lightest state. The resulting `.lhe` files – containing the kinematic information of the runs relating to the monophoton – were converted with the help of DELPHES to `root` format, and these were subsequently analysed to derive the sensitivity results, as explained in detail in Sec. 5.2.2.

5.2.1 Simulation Setup

The simulation process was carried out using MADGRAPH5_AMC@NLO V3.4.2 and relied on the `SM heavyN Dirac CKM Masses LO` Feyn-Rules model file, sourced from Ref. [257]. Upon performing a preliminary study of the kinematic distributions for Dirac and Majorana sterile neutrinos, it was found that the two cases produce very similar results. Therefore, we make the choice to focus on Dirac sterile neutrinos in the final state for this process, but one should bear in mind that the derived results will also similarly apply to Majorana final state sterile neutrinos. Additionally, the difference in sensitivity between Dirac and Majorana HNLs is similar in the case of EFT operators and therefore the contrasting of these two scenarios is postponed until Sec. 5.3.

Using `MadGraph5_aMC@NLO`, $N_{\text{tot}} = 5 \times 10^4$ events were generated for the signal $e^+e^- \to \nu_e \bar{N}\gamma + \bar{\nu}_e N\gamma$ and background $e^+e^- \to \sum \nu\bar{\nu}\gamma$ processes each, where the multi-particle active neutrino state is defined as $\nu \equiv \nu_e, \nu_\mu, \nu_\tau$. In other words, although the direct couplings between off-diagonal flavour states of the active and sterile states have been explicitly switched off, indirect off-diagonal couplings can still exist through the mixing amongst the active SM neutrino flavour states. For the signal process around 40 sterile mass benchmark points (BPs) were selected, spaced between 0.25 GeV and 90 GeV and between 0.25 GeV and 238 GeV for $\sqrt{s} = 91.2$ GeV and $\sqrt{s} = 240$ GeV, respectively. The BPs are not necessarily all spaced equally, their required density was determined based on the behaviour of the sensitivity contour, with more BPs being added where the structure of the curve required refinement and/or smoothing. In both the background and signal process simulation we place a cut on the transverse momentum of the outgoing photon of $p_T^\gamma > 1$ GeV at event generation level. This is done in order to avoid the presence of any soft radiation causing infrared divergence.

5.2.2 Analysis

The process of simulating events proceeded as detailed in Sec. 5.2.1. For the signal process, which has an explicit sterile mass dependence, the full set of events was simulated for each mass BP. In the case of the background process, the lack of a sterile neutrino final state means there is no sterile mass dependence, therefore it is only simulated one time.

The output of the MADGRAPH5 simulation is a file with Les Houches Event (`.lhe`) extension. This file contains general information about the simulation, such as the process itself alongside hard-coded and user settings. Its two main components are the run card and the parameter card. The run card contains information about the simulation, such as the beam energies, the number of generated events and any kinematic cuts, while the parameter card stores parameter value settings, such as the coupling and mass values. Once the `lhe` file is obtained, it is converted to `root` format using DELPHES which in turn can be analysed on an event-by-event basis. To this end, we used a PYTHON script specifically written to loop over all the events and make selections based on logical comparisons concerning PID, particle status (initial or final-state), transverse momentum, particle lifetime while also applying appropriate kinematic cuts. The resulting output of the analyser code is a two-dimensional array of monophoton energy and the corresponding number of events that survived all of the cuts imposed on them. Similarly, for the background process the same kinematic cuts were applied in order to enable comparison.

In the case of the signal process, varying m_N will naturally lead to a change in the kinematics of the phase-space. It is therefore crucial to maximise the signal-to-background ratio at each BP in order to retain as much sensitivity as possible. To this end, for each BP we examine the distributions of two kinematic variables – monophoton energy, E^γ, and the cosine of the angle between the momentum vector and the beam axis, θ^γ – and thus determine the required cuts. Fig. 5.3 shows the distributions of E^γ (top) and $\cos\theta^\gamma$ (bottom) for $\sqrt{s} = 91.2$ GeV (left) and $\sqrt{s} = 240$ GeV (right). The kinematic cuts that are derived upon the qualitative inspection of these panels are summarised in Table 5.1. The third column shows the improvement in the signal-to-background ratios upon implementing the cuts. In all four of the distributions, the background process is shown in black, while the other colours correspond to the signal process for various m_{N_1} values, as specified in the legends in units of GeV.

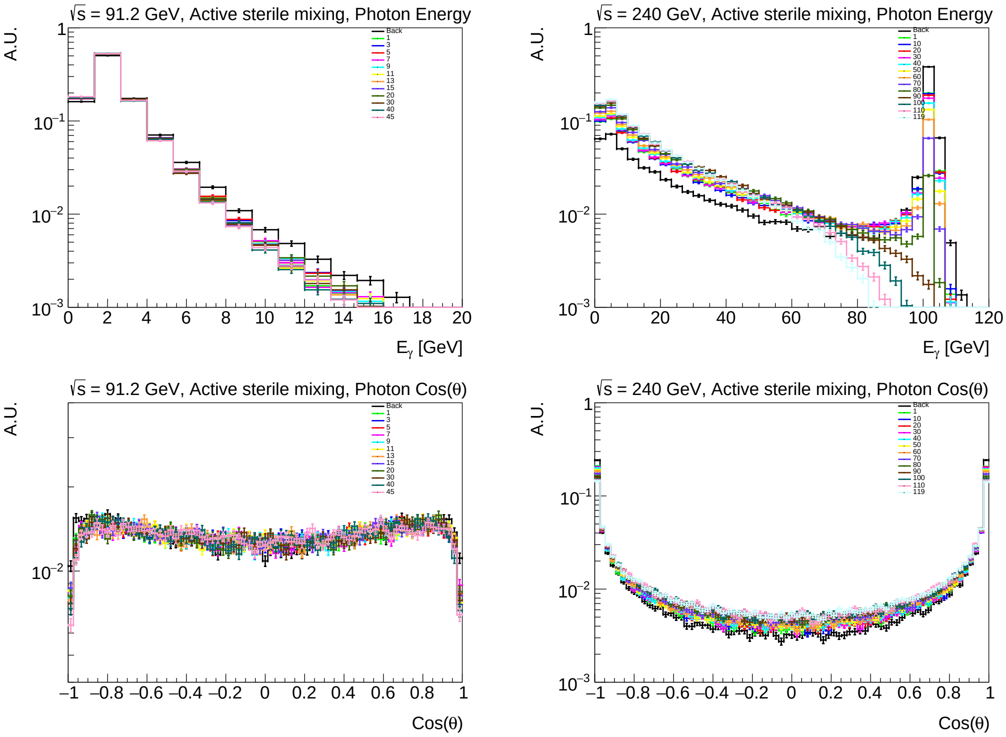

Figure 5.3: Normalised kinematic distributions showing monophoton energy (E^γ) (*top*) and cosine of the angle between the momentum vector and the beam axis (θ^γ) (*bottom*) for $e^+e^- \to \nu_e \bar{N}_1 \gamma$ signal process and $e^+e^- \to \nu\bar{\nu}\gamma$ SM background process (*black*) at $\sqrt{s} = 91.2$ GeV (*left*) and $\sqrt{s} = 240$ GeV (*right*), for various choices of sterile mass (in units of GeV).

The top-left distribution shows E^γ at $\sqrt{s} = 91.2$ GeV. As expected, the majority of the photons are of relatively low energy, due to the total available energy being shared between all final state particles. We do not observe any resonant peaks, since there is not sufficient energy available to produce any of the mediators on-shell. It can be seen that the background surpasses all signal lines for approximately

$\sqrt{s}$ [GeV]	Cuts	$\left(\frac{S}{B}\right)_{\text{cuts}} / \left(\frac{S}{B}\right)$
91.2	$\lvert\cos\theta_\gamma\rvert < 0.9$, $E_\gamma < 4$ GeV	1.03
240	$\lvert\cos\theta_\gamma\rvert < 0.95$, $E_\gamma < 90$ GeV	1.50

Table 5.1: Kinematic acceptance cuts used to maximise the signal-to-background ratio for each $\sqrt{s}$ in the active-sterile mixing sensitivity analysis. The improvement in the signal-to-background ratios after cuts is shown in the last column for the benchmark scenario $m_N = 10$ GeV and $|V_{eN}| = 10^{-3}$.

$E^\gamma > 4$ GeV. Including this region in our analysis would drastically decrease the sensitivity and therefore we discard it.

In the case of $\sqrt{s} = 240$ GeV, the E^γ distribution shown in the top-right panel exhibits a resonant peak at around $E \sim 100$ GeV, due to the on-shell Z-boson production. This peak is naturally most prominent for the background process, because the final state contains two SM light neutrinos, whose combined mass is less than the combined mass of all final state particles for the simulated signal process for all BPs considered. Therefore, a kinematic cut was applied to this distribution, accepting only events with $E^\gamma < 90$ GeV.

The bottom-left panel of Fig. 5.3 shows the cosine θ^γ distribution at $\sqrt{s} = 91.2$ GeV. Since the total available energy is not sufficient to allow the monophoton to be emitted parallel ($\theta^\gamma = 0°$, $\cos\theta^\gamma = 1$) or antiparallel ($\theta^\gamma = 180°$, $\cos\theta^\gamma = -1$) to the beam direction, the $\cos\theta^\gamma$ are distributed relatively uniformly between 1 and -1. For the background process with two SM neutrinos in the final state, the energy available to the photon is more than in the case of any of the signal BPs, thus the background distribution is shifted slightly towards the extremes. Thus, we only accept events with $|\cos\theta^\gamma| < 0.9$.

The angular distribution for $\sqrt{s} = 240$ GeV, shown in the bottom-right panel, exhibits a pronounced shift towards the extrema of the possible cosine θ^γ values. This is because the higher centre-of-mass energy now allows the monophoton to be emitted along the beam direction and thus the distribution peaks at $\cos\theta^\gamma = \pm 1$. Accordingly, the corresponding acceptance cut is relaxed to $|\cos\theta^\gamma| < 0.95$.

The production of a massive sterile neutrino via active-sterile mixing naturally leads to the possibility of it decaying through the same mechanism to SM particles.

The diagrams of such processes contributing to leptonic decays of the form $N \to \nu\ell^-\ell^+$ are shown in Fig. 5.2.

First, at event generation level we assume that the HNLs produced are stable and do not consider any decays, and thus consider only the mono-γ plus $\not{E}$ signal. Since the sterile mass range we consider corresponds to non-negligible decay lengths as compared to the FCC detector length – approximated to be spherical of radius $L = 5$ m based on the preliminary FCC-ee proposal [258] – the assumption of stable sterile neutrinos is not appropriate and the HNLs can be expected to decay inside the detector volume, producing displaced vertex (DV) signatures. An inclusive analysis can be performed if these decays are not taken into account, while the analysis is exclusive if the HNLs are assumed to decay outside of the detector (and thus without any DV signatures). Therefore, the exclusive analyses requires the decay probability to be taken into account.

To do this, the probability that the HNL decays between L_1 and L_2 needs to be computed

$$\mathcal{P}_{\text{in}}(L_1, L_2, \sqrt{s}, m_N, V_{\alpha N}) = \int db\, f(\sqrt{s}, m_N, b) \left[e^{-L_1/b\tau_N} - e^{-L_2/b\tau_N} \right], \tag{5.7}$$

where $b \equiv \beta\gamma$ is the boost factor (with $\beta = v/c$, where v stands for velocity and c denotes the speed of light), $\tau_N = 1/\Gamma_N$ is the lifetime (with Γ_N the decay width) and $f(\sqrt{s}, m_N, b)$ being the boost distribution. In the case of a 2 → 2 process, the HNL's boost is trivial, as for fixed $\sqrt{s}$ and fixed masses the final state momenta are uniquely determined, with $f(\sqrt{s}, m_N, b) = \delta(b - b')$, with $b' = (s - m_N^2)/(2m_N\sqrt{s})$ [1]. However, including the photon results in a 2 → 3 process, for which there is no simple form for the boost distribution. In general, for a 3-body process the quantity b is a distribution (rather than a single fixed value) that depends on the mass and energy of the sterile neutrino among other factors. Similarly, the decay-width also depends on the specific properties of the sterile neutrinos. Therefore, the decay-length is specific to each sterile neutrino that is produced and needs to be com-

---

[1] Since $p = \lambda(s, m_\nu, m_N)/2\sqrt{s}$, where $\lambda(x,y,z) = x^2 + y^2 + z^2 - 2xy - 2xz - 2yz$ is the Källén triangle function, $\lambda(s, 0, m_N^2) = (s - m_N^2)^2$ and so $p = (s - m_N^2)/(2\sqrt{s})$. By definition $\beta\gamma = p/m_N$ and therefore $b' = (s - m_N^2)/(2m_N\sqrt{s})$.

puted on an event-by-event basis. To this end, for each HNL event i that survived the kinematic cuts, the boost factor was extracted from the simulation one-by-one, using an analyser script to iterate over each event. Using this, the probability of each sterile neutrino decaying outside of the detector was calculated using $\mathcal{P}^i_{\text{out}} \equiv 1 - \mathcal{P}^i_{\text{in}}$, with $\mathcal{P}^i_{\text{in}}$ computed using the replacement $f(\sqrt{s}, m_N, b) = \delta(b - b_i)$ in Eq. 5.7. This then allows the approximation of the geometric acceptance as $\mathcal{P}_{\text{out}} \approx (b_{\max} - b_{\min}) \sum_i \mathcal{P}^i_{\text{out}} / (\varepsilon_k N_{\text{tot}})$, with ε_k denoting the kinematic efficiency factor and thus the product $\varepsilon_k N_{\text{tot}}$ being the number of events surviving the kinematic cuts summarised in Table 5.1. The more massive the sterile neutrino is, the larger Γ_N is and therefore the shorter its lifetime is, hence the probability of it decaying inside the detector will be larger. Thus, we expect the sensitivity of the set-up to decrease for increasing sterile neutrino mass (of course in the massless case the decay probability is zero and we recover the inclusive search limit). Once $\mathcal{P}_{\text{out}}$ has been extracted, the code performs a weighting of each event by its corresponding decay probability. This can then be used to calculate the total number of surviving mono-γ plus $\not{E}$ signal events, S,

$$S = \sigma \times \mathcal{L} \times BR \times \mathcal{P}_{\text{out}} \times \varepsilon_k, \tag{5.8}$$

where σ is the cross-section of the process, $\mathcal{L}$ is the integrated luminosity and BR denotes the branching ratio. In our analysis $BR = 1$, because communication between the sterile neutrino and the SM sector can only occur via the sterile neutrino's coupling to ν_e. In order to constrain the parameter of interest, V_{eN}, the median significance for a counting experiment of a known background is calculated using

$$\mathcal{S} = \sqrt{2\left((S+B)\ln\left(1+\frac{S}{B}\right) - S\right)} \approx \frac{S}{\sqrt{B}}, \tag{5.9}$$

where in the second equality $S \ll B$ is used, based on the assumption that the signal rate $e^+e^- \to \sum_i \nu_i \bar{N}\gamma + \bar{\nu}_i N\gamma$ is much smaller than the background rate $e^+e^- \to \sum \nu\bar{\nu}\gamma$. The expected significance, $\mathcal{S}$, measures the deviation from the expected background and quantifies the likelihood that the observed signal is not due to random fluctuations. It is computed for a range of active-sterile mixing values for each m_N point. Throughout our analysis, we strictly require $\mathcal{S} = 1.28$ in Eq. 5.9, and solve for the mixing angle value(s). This corresponds to requiring the observation of 1.28 signal events, which corresponds to a positive signal at 90% CL. Hence, for each sterile mass BP the value(s) of $|V_{eN}|^2$ that satisfy the condition imposed on the signal significance expression is calculated, which therefore outline the excluded region corresponding to $\mathcal{S} > 1.28$.

In the case of the inclusive search, the kinematic cuts summarised in Table 5.1 are similarly applied to the results of the simulation as in the exclusive search. However, contrary to the exclusive search, the decay probability is not taken into account, but simply set to $\mathcal{P}_{\text{out}} = 1$, i.e. it is assumed that the HNLs are stable within the detector length, or that they do not decay to any visible final states. However, in the inclusive case the energy of the monophoton does not determine the missing system, since in general the HNL may decay promptly to visible final states. The latter is satisfied for instance in the case of the HNL decaying to a light axion-like pseudoscalar particle, a, via the process $N \to a\nu$ [259]. This process may dominate over other channels for sterile masses of 1 GeV $\lesssim m_N \lesssim$ 100 GeV and can suppress the decays to SM particles by factors of $10^{-6}(m_N \approx 1 \text{ GeV}) - 10^{-2}(m_N \approx 100 \text{ GeV})$. It should be noted, that although an extra state a would induce extra EFT operators, those of interest here would remain present. Thus, setting the decay probability outside of the detector to unity, the sensitivity at each sterile mass BP for the inclusive search is then derived in the same way as for the exclusive search using the signal significance expression in Eq. 5.9.

It should be noted that ISR can be comprised of one or more photons. A proper treatment would thus involve simulating the process of interest perturbatively, i.e. $e^+e^- \to \nu N\gamma + \nu N2\gamma + \nu N3\gamma + ... + \nu Nn\gamma$, where n is the maximal number of photons that can be produced kinematically. At the Z-pole, i.e. for $\sqrt{s} = 91.2$ GeV, the phase-space is rather narrow and thus the emission of diphoton radiation, as opposed to monophoton, is suppressed. However, in the case of $\sqrt{s} = 240$ GeV, the available energy is well above the Z mass, which can be produced on-shell comfortably and thus the abundance of phase-space means there is a non-negligible probability of diphoton radiation. For this reason we have also simulated diphoton initial state radiation, i.e. next-to-leading order, and compared it to the monophoton case. The resulting distributions for E^γ and $\cos\theta^\gamma$ are shown in Fig. 5.4, with an acceptance cut of $p_T > 1$ GeV implemented at event generation level. For the sake of this comparison, both the mono- and diphoton process were simulated for three BP m_{N_2} values: 1 GeV (blue/dark blue), 120 GeV (green/dark green) and 230 GeV (red/brown). In terms of the general behaviour of the distributions as a function of sterile mass, the expected Z-resonant peak is observed for the 1 GeV BP and not for the others and similarly, the $\cos\theta^\gamma$ distribution is shifted towards its extrema values for the 1 GeV BP. Comparing the energy distribution for the mono- and diphoton scenarios in Fig. 5.4 (left) it is apparent that the initial overlap grows into a more considerable difference as the energy increases. This can be understood from the kinematics of the process, since a larger total energy will allow for more phase-space configurations in the diphoton scenario, whereby the two emitted photons can have very similar or very different energies. The angular distribution (right) does not exhibit any significant differences between the mono- and diphoton channels.

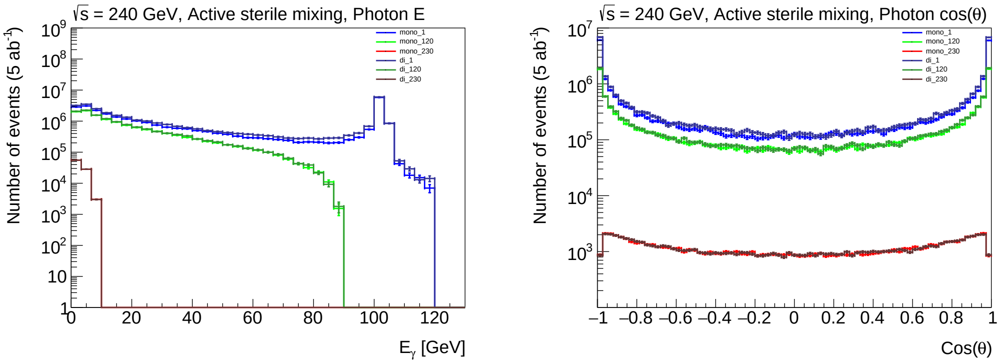

Figure 5.4: Energy (left) and outgoing angle (right) distributions for mono- and diphoton processes induced by electron-flavour mixing V_{eN}, for three choices of sterile mass, $m_{N_2} = 1, 120$ and 230 GeV.

In order to assess the importance of including the diphoton (or higher-order) corrections, we have analysed the sensitivity to the active-sterile mixing angle for a few sterile mass BPs. The results of this are summarised in Table 5.2. Here we show the derived sensitivities with and without any kinematic cuts ($E^{\gamma} > 90$ GeV, no cut on diphoton) for the monophoton and mono + diphoton scenarios for BP masses of $1, 120$ and 230 GeV. The numbers in the table correspond to the $|V_{eN}|^2$ values for the given scenario. It can be seen that the sensitivity to the mixing angle without imposing any kinematic cuts is non-negligibly increased if the diphoton channel is also included in the analysis. However, this difference is almost completely eradicated once the kinematic selection cuts are put into place, for all three mass BPs considered. Since the energy distribution for the background and signal processes at $\sqrt{s} = 240$ GeV, as shown in the top right panel of Fig. 5.3, necessarily requires a kinematic cut in order to maximise the signal to background ratio, we conclude that the inclusion of the diphoton channel and further higher-order corrections is not necessary.

M_{N_2} (GeV)	Monophoton (no cut)	Monophoton (with cut)	Mono+diphoton (no cut)	Mono+diphoton (with cut)
1	$10^{-3.163}$	$10^{-3.063}$	$10^{-3.19}$	$10^{-3.095}$
120	$10^{-2.807}$	$10^{-2.873}$	$10^{-2.822}$	$10^{-2.889}$
230	$10^{-0.638}$	$10^{-0.875}$	$10^{-0.634}$	$10^{-0.873}$

Table 5.2: Summary of the active-sterile mixing angle, $|V_{eN}|^2$, values reachable for three sterile mass BPs: 1, 120 and 230 GeV for the monophoton and mono+diphoton scenarios, with and without a kinematic cut of $E^{\gamma} > 90$ GeV on the monophoton.

With the event generation and analysis procedure outlined earlier, as well as having concluded that diphoton and higher-order corrections are negligible, we present the estimated sensitivity of the mono-γ plus $\not{E}$ search at FCC-ee electron-flavour active-sterile mixing angle as a function of the HNL mass 500 MeV$\leq m_N \leq$ 240 GeV in Fig. 5.5. The figure summarises the projected sensitivities for the two centre-of-mass energies $\sqrt{s} = 91.2$ GeV (red) and $\sqrt{s} = 240$ GeV (black), in the context of an inclusive search (dashed) and an exclusive search (solid). For $\sqrt{s} = 91.2$ GeV, maximal sensitivity is capped well above 10^{-4}, while for $\sqrt{s} = 240$ GeV it slightly surpasses 10^{-3}, for both the inclusive and exclusive searches. It might be surprising at first that the more energetic search performs worse, since intuitively one expects the provision of the extra phase-space to aid the sensitivity. However, the integrated luminosities associated with the two scenarios are vastly different, with the $\sqrt{s} = 91.2$ GeV search having almost 20 times the luminosity of the $\sqrt{s} = 240$ GeV search, thus severely constraining its reach. Furthermore, since the process is dominated by the Z-boson mediated channel, the cross-section scales as $\sigma \sim 1/(s - m_Z)^2$ due to the propagator, i.e. σ drops away from the Z-resonance. In the case of the exclusive search, the resulting exclusion contours exhibit a nose-like structure. This is due to two competing effects resulting in a double solution for the active-sterile mixing angle when solving the signal significance expression for $|V_{eN}|^2$ upon setting $\mathcal{S} = 1.28$. When the mixing-angle value is large, so is the cross-section that produces the sterile neutrino. In this case the decay-width is also large, leading to a short lifetime and thus an increased probability that the sterile neutrino decays before leaving the detector. Ultimately this results in a reduction of $\mathcal{S}$. On the other hand, for small values of $|V_{eN}|^2$, the production cross-section as well as the decay-width of the sterile state are reduced, which leads to a longer lifetime and therefore a larger probability that the sterile neutrino makes it out of the detector without undergoing decay. This corresponds to a larger $\mathcal{S}$ value. Therefore, while the horizontal reach of the contours is dictated by the cross-section, the tilted part of the contour is influenced by the decay-width and thus the decay probability. Naturally, in the case of the inclusive search there is no nose-like structure, since the sterile neutrino is allowed to decay anywhere and it's lifetime is not taken into account. The estimated sensitivity contours correspond to the observation of 1.28 signal events, but it is understood that all larger values lying above the contours are excluded. These regions have not been shaded, since the figure also shows shaded regions of various colours, which correspond to the regions of the parameter space which have been excluded by various experiments, as indicated by the colour-coded labels.

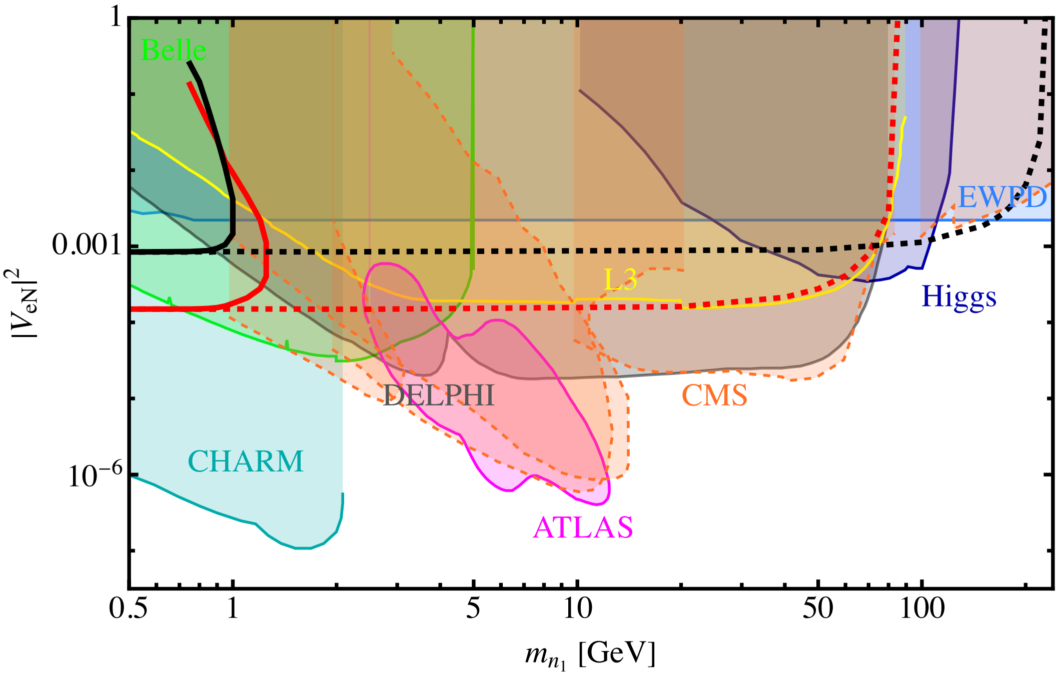

Figure 5.5: Sensitivity of mono-γ plus $\not{E}$ searches at FCC-ee to the electron-flavour mixing strength as a function of the HNL mass at 90% CL, for $\sqrt{s} = 91.2$ GeV (red) and $\sqrt{s} = 240$ GeV (black). Shown are the results of the exclusive signal analysis (solid), taking into account the probability of the HNL decaying outside the detector of length $L = 5$ m, and inclusive signal analysis (dashed), where this requirement is relaxed. The shaded regions correspond to the currently excluded regions of the parameter space.

The light green shaded region is the exclusion from the Belle collaboration [260], where a direct search for sterile neutrino decays of the form $\nu_h \to \ell^\pm \pi^\pm$ (where $\ell = e, \mu$ denotes a charged lepton, π denotes a charged pion and ν_h stands for the heavy sterile neutrino) was performed in the mass range 0.5 GeV – 5.0 GeV. The results rely on the B-mesons produced from the Υ(4S) resonance at the KEKB electron-positron collider and their subsequent decays into sterile neutrinos, of the form $B \to X \ell \nu_h$, where X denotes either a meson or 'nothing'.

The CHARM experiment [261, 262] looked for the signs of decay of heavy neutrinos, ν_h, in the mass range 0.5 GeV–2.8 GeV in two different experiments: the cooper beam dump (BD) and the wide-band neutrino beam (WBB). In BD, the experiment collided a beam of protons into a fixed copper target to produce a beam of muon-type active SM neutrinos, ν_μ and hadronic states, such as pions (π), kaons K and D-mesons D, which subsequently undergo the decay $\pi/K/D \to \ell \nu_h$. The subsequent decay of the heavy state, $N \to \ell^+\ell^-\nu_\ell$ was searched for. In the case of the WBB, the assumed heavy neutrino production mechanism was a nucleonic scattering of active neutrinos $\nu_\mu N \to X\nu_h$ (where N denotes the nucleon and X is some hadronic state) and the subsequent decay of the heavy state $\nu_h \to \mu X$ was searched for. No positive signal was found, but the parameter space was constrained as low as $|V_{eN_1}|^2 \sim 10^{-7}$ for $m_N \approx 1.5$ GeV by BD, as shown by the cyan shaded region in the figure.

At the LEP collider, both L3 [263,264] and DELPHI [265] searched for sterile neutrino production via on-shell Z production: $e^+e^- \to Z \to \nu_h\nu_\ell$, and the subsequent decays: $\nu_h \to \ell^\mp W^\pm$, $\nu_h \to \nu_\ell Z$ and $\nu_h \to \nu_\ell H$. L3 looked for the process $\nu_h \to e^\mp W^\pm$ followed by $W^\pm \to jj$ in the mass range 5 GeV–80 GeV and set a limit on the mixing angle of $|V_{eN_1}|^2 \sim 10^{-4}$, as shown by the yellow shaded region in the plot. The same search was carried out by DELPHI which with improved analysis pushed the L3 constraints down to $|V_{eN_1}|^2 \sim 10^{-5}$, indicated by the gray shaded region of the parameter space.

Constraints on the active-sterile mixing angle have been derived using LHC data around the Higgs boson mass, by searching for Higgs decay to sterile states and their subsequent decays [266]. The derived limits are of the order $|V_{eN_1}|^2 \sim 10^{-4}$ as can be seen from the dark blue shaded region in the figure.

If the SM is extended by a sterile neutrino and there exists mixing between the active and sterile neutrino sectors, the PMNS matrix needs to be extended from a 3×3 to a 4×4, to accommodate the extra neutrino state. This will result in the original mixing matrix becoming a submatrix of the new extended mixing matrix, whereby unitarity is no longer guaranteed and therefore non-unitarity effects are induced in the active neutrino sector. These effects have consequences for electroweak precision data (EWPD) observables, such as the W boson mass, the invisible decay-width of the Z boson and the Weinberg angle, among others. The Fermi constant, G_F, will also be modified as a result of the non-unitarity of the PMNS, since the extraction of G_F from muon-decay relies on the assumption that the process is purely SM-mediated. Such a modification of G_F will in turn affect the CKM matrix elements, whose values have been determined experimentally from weak processes involving G_F. As these EWPD observables have been measured to high precision, they provide a constant bound on the active-sterile mixing angle [267–270], as shown by the light blue shaded region in the plot.

The ATLAS detector at CERN searched for displaced vertices of sterile neutrinos produced in proton-proton collisions via the mechanism $W \to \nu_h \mu$ or $W \to \nu_h e$ followed by the subsequent decays into a pair of charged leptons accompanied by a neutrino [271]. The data collected spans the mass range 3 GeV–15 GeV. Although no positive signal was found, the collected data enabled the exclusion of a sizable portion of the parameter space, as shown by the magenta shaded region in the plot.

The CMS detector at CERN has performed searches of prompt as well as long lived sterile neutrinos in order to constrain the active-sterile mixing angle, in the vast mass range 1 GeV to 10 TeV. In the case of the prompt search, the semihadronic $\nu_h \to \ell^\pm q\bar{q}$ and purely leptonic $\nu_h \to \ell^\pm \ell^\mp \nu$ and $\nu_h \to \ell^\pm \ell^\pm \nu$ decays were investigated, where the predominant production involves the decay of a W boson. The produced ν_h then decays into a lepton and another W boson, with the W boson in turn decaying into a pair of leptons. In the case of long-lived sterile neutrinos, various production mechanisms were studied, such as the s-channel W boson decay, $W^\pm \to \ell^\pm N, N \to \ell^\pm \ell^\mp \nu_\ell (\ell = e, \mu)$ and displaced vertices were searched for.

As can be seen from Fig. 5.5, the estimated sensitivities based on our analysis fall entirely within regions of the parameter space that have already been excluded by various searches, for the complete mass range considered. It should be noted, that these results and the corresponding existing bounds only apply to a Dirac sterile neutrino final state. Although not shown here, the achievable sensitivity is very similar in the Majorana case (although one should keep in mind that the corresponding existing constraints are different). The only region of the parameter space where the FCC-ee is projected to be competitive is in the case of the inclusive mono-γ plus $\not{E}$ search at $\sqrt{s} = 240$ GeV, for sterile masses of $m_N \sim 80 - 130$ GeV. Additionally, for low HNL masses around $m_N \sim 10$ eV $- 2.5$ MeV, the relevant existing constraints come from β-decay experiments, which tend to place weaker bounds than those estimated in here for $\sqrt{s} = 91.2$ GeV. Since the projected bounds are not competitive for the vast majority of the parameter space, in the next section we turn our attention to processes in which the production (and decay) of the HNLs proceeds via EFT operators, which are typically constrained to a lesser extent.

5.3 Monophoton Final State: Four Fermion EFT Operators

In the previous section we estimated the sensitivity of the future FCC-ee to the active-sterile mixing angle, by investigating the monophoton process with a sterile neutrino in the final state. However, besides active-sterile mixing, sterile neutrinos may also be produced via four-fermion EFT operators. Hence, in this section we investigate the process $e^+e- \to N_iN_j(\gamma)$ (where $i, j = 1,2$ denotes the sterile neutrino family) and estimate the sensitivity of the proposed FCC-ee to the four-fermion WCs parameterising such a processes, switching one operator on at a time. Due to the possibility of two distinct sterile final states, the HNLs may be identical ($i = j$) or different ($i \neq j$). In the case of different HNLs, three different mass splittings are studied. We perform the analysis for two centre-of-mass energies $\sqrt{s} = 91.2$ GeV and $\sqrt{s} = 240$ GeV for both Dirac and Majorana HNLs. The sensitivity estimation is carried out both in the context of an inclusive and an exclusive search. The following scenarios are considered:

- Diagonal WCs of the four-fermion interactions with two HNLs:

$$C_i \in \left\{ C^{V,RR}_{\underset{iiee}{Ne}}, C^{S,RR}_{\underset{iiee}{Ne}}, C^{T,RR}_{\underset{iiee}{Ne}} \right\}, \tag{5.10}$$

  with $i = 2$, leading to the processes $e^+e^- \to N_2N_2\gamma$ (Majorana) or $e^+e^- \to N_2\bar{N}_2\gamma$ (Dirac). Due to the final state sterile neutrinos being identical, there are no decay channels open. Thus, these WCs can only be probed by the mono-γ plus $\not{E}$ signal search.

- Off-diagonal WCs of the four-fermion interactions with two HNLs:

$$C_i \in \left\{ C^{V,RR}_{\substack{Ne\\ ijee}},\, C^{S,RR}_{\substack{Ne\\ ijee}},\, C^{T,RR}_{\substack{Ne\\ ijee}} \right\}, \tag{5.11}$$

with $i = 1$ and $j = 2$, resulting in the processes $e^+e^- \to N_1 N_2 \gamma$ (Majorana) or $e^+e^- \to N_1 \bar{N}_2 \gamma + \bar{N}_1 N_2 \gamma$ (Dirac). In our analyses we consider three mass splittings, $\delta \equiv (m_{N_2} - m_{N_1})/m_{N_2}$, between the HNLs: $\delta = 0.01$, 0.1, and 1. This mass difference allows N_2 to decay to N_1 via these WCs, enabling DV searches, as discussed in Secs. 5.5 and 5.6.

- WCs of the four-fermion interactions with a light neutrino and an HNL:

$$C_i \in \left\{ C^{V,RR}_{\substack{\nu Ne\\ \alpha jee}},\, C^{S,RR}_{\substack{\nu Ne\\ \alpha jee}},\, C^{T,RR}_{\substack{\nu Ne\\ \alpha jee}} \right\}, \tag{5.12}$$

with $\alpha = e, \mu, \tau$ and $j = 2$, inducing the processes $e^+e^- \to \sum_i \nu_i N_2 \gamma$ (Majorana) and $e^+e^- \to \sum_i \nu_i \bar{N}_2 \gamma + \bar{\nu}_i N_2 \gamma$ (Dirac). It should be noted that $C^{V,RR}_{\substack{\nu Ne\\ \alpha jee}}$ does not exist for the Dirac case (as this would require ν_R as can be seen from Eq. 3.105), but for simplicity it is retained and understood to label $C^{V,LR}_{\substack{\nu Ne\\ \alpha jee}}$. The constraints from the mono-γ plus $\not{E}$ search on the above WCs can be found by considering those for the off-diagonal limits for $\delta = 1$.

- WCs for the four-fermion process with two light neutrinos

$$C_i \in \left\{ C^{V,LL}_{\substack{\nu e\\ \alpha\beta ee}},\, C^{V,LR}_{\substack{\nu e\\ \alpha\beta ee}},\, C^{S,LL}_{\substack{\nu e\\ \alpha\beta ee}},\, C^{T,LL}_{\substack{\nu e\\ \alpha\beta ee}} \right\}, \tag{5.13}$$

with $\alpha, \beta = e, \mu, \tau$, which contribute to the SM process $e^+e^- \to \sum \nu\bar{\nu}\gamma$. As for the one light neutrino and one HNL scenario, the lack of ν_R means the WCs $C^{S,LL}_{\nu e}$ and $C^{T,LL}_{\nu e}$ are not present in the Dirac case, while in the Majorana case they do not interfere with the SM. Hence, for the Majorana case the limits on these WCs can be found from the diagonal and off-diagonal constraints with $m_{N_2} \to 0$ (this is enough to give two light neutrinos even in the off-diagonal case, since $m_{N_2} > m_{N_1}$). In both the Dirac and Majorana cases, $C^{V,LL}_{\nu e}$

and $C_{\nu e}^{V,LR}$ interfere with the SM process and thus must be properly accounted for.

5.3.1 Simulation Setup

Similarly to the simulation set-up outlined in the case of active-sterile mixing, the process is simulated in MADGRAPH5 and the subsequent analysis of the event generation output is analysed with the help of DELPHES. The final state sterile neutrinos can either be Dirac or Majorana particles, and these two cases are treated separately. The model files were written in FEYNRULES, which was converted to Universal FeynRules Output (UFO) and then passed to MADGRAPH5 to perform the event generation. The model file contains information about particle content, couplings and their values, as well as the Lagrangian that determines the allowed interactions. Inside the model file, each fermion must be declared as Dirac or Majorana, by setting the self-conjugate option to “False” or “True”, respectively. In the case of Dirac particles, everything works as expected without any issues. However, in the case of Majorana sterile neutrinos MADGRAPH5 crashes. This is due to the so-called “fermion-flow violation” problem and this essentially means that the software cannot handle Majorana fermions in operators with two or more fermions. In order to compute the amplitude of a process correctly, the software requires any four-fermion operator to have a flow structure of (in, out) (in, out), in order to avoid mixing-up flows. In older versions of MADGRAPH5 a bug was found in the determination of the flows in cases where two or more Majorana fermions were present at a single four-fermion vertex. Fixing this issue would have required the developers to make fundamental changes to the code, but this being a difficult and time consuming task, they instead decided to crash the code for any ambiguous cases, with a full fix expected in the coming versions of the software. To circumvent this issue, for Majorana sterile neutrinos, we have implemented a ’trick’. This involves representing every Majorana particle with two Dirac ones. Of course this means that for a given process involving different Majorana sterile states, we need to add up the two possible Dirac processes to recover the same result. In other words: for Majorana particles N_{1M} and N_{2M} in the final state, we simulate the process $e^+e^- \to N_{1D}\bar{N}_{2D}\gamma$

Scenario	Majorana	Dirac
Diagonal	$e^+e^- \to N_2 N_2 \gamma$	$e^+e^- \to N_2 \bar{N}_2 \gamma$
Off-diagonal	$e^+e^- \to N_1 N_2 \gamma$	$e^+e^- \to N_1 \bar{N}_2 \gamma + \bar{N}_1 N_2 \gamma$

Table 5.3: Signal processes contributing in the case of identical and different Dirac and Majorana sterile neutrinos.

and $e^+e^- \to N_{2D}\bar{N}_{1D}\gamma$, where N_{1D} and N_{1D} are Dirac sterile states belonging two two distinct families. It should be noted, that the use of this remedy is only necessary in the case where the final state sterile neutrinos are different, because for identical states $\sigma(e^+e^- \to N_{1M}N_{1M}\gamma) = \frac{1}{2}\sigma(e^+e^- \to N_{1M}N_{2M}\gamma)$ [272]. Therefore, all processes are generated using Dirac fermions and hence we drop the "M/D" subscript from here onwards.

Allowing the final state sterile neutrinos to belong to either of two distinct families results in the contribution of four different signal processes, which are summarised in Table 5.3.

Again, the monophoton process has the irreducible SM background $e^+e^- \to \nu\bar{\nu}\gamma$, where $\nu \equiv \{\nu_e, \nu_\mu, \nu_\tau\}$ denotes the multiparticle state that includes all three flavours of the SM active neutrinos. As before, we simulate $N_{\text{tot}} = 5 \times 10^4$ events in MADGRAPH5, for both the background and signal processes, for which the corresponding diagram is shown on the left of Fig. 5.1. The blob in the case of the background process represents Z or W boson mediation, while in the signal process case it represents the EFT operators of the three Lorentz structures (scalar, vector and tensor) that we consider. We impose a cut of $p_T^\gamma > 1$ GeV at generation level, in order to remove any IR singularities arising in the soft limit, where diverging integrals can occur. The resulting kinematic distributions of the outgoing monophoton were extracted from the `.lhe` file, containing all information about the simulated processes. The simulation was run with only one coupling being switched on at a time and taking turns in simulating the signal process for each Lorentz structure.

5.3.2 Analysis: Diagonal WCs

As before in the active-sterile mixing scenario, we perform the sensitivity analysis using Eq. 5.9, because $\sigma(e^+e- \to \nu\bar{\nu}\gamma) \gg \sigma(e^+e^- \to N_i\bar{N}_j\gamma)$ holds true throughout. Just like in the mixing scenario, we perform the sensitivity analysis for both an inclusive and an exclusive search.

For the diagonal process where $i = j$, i.e. where the two final-state sterile neutrinos are identical, evidently no decay can occur via the operator that is involved in the production process and thus the only available search is the inclusive one. Fig. 5.6 shows the kinematic distributions of the monophoton energy, $x_\gamma \equiv 2E_\gamma/\sqrt{s}$, (bottom) and the cosine of the angle, $\cos\theta^\gamma$, (top), for the two centre-of-mass energies $\sqrt{s} = 91.2$ GeV (left) and $\sqrt{s} = 240$ GeV (right), considering Dirac sterile final states. For the energy distributions, the units are normalised to the maximum photon energy via

$$x_\gamma^{\max} \equiv \frac{2E_\gamma^{\max}}{\sqrt{s}} = 1 - \frac{m_{N_2}^2(2-\delta)^2}{s}. \tag{5.14}$$

In the case of Majorana HNLs, the resulting kinematic distributions are only mildly different and therefore we do not show them separately. The distributions shown are for a fixed sterile mass of $m_{N_1} = 10$ GeV the signal process proceeding via scalar (orange), vector (blue) and tensor (green) effective four-fermion operators, the effective Z (red) and $W^\pm$ (purple) interactions and the SM background process (gray shaded). In the case of the four-fermion and effective Z interaction, the distributions shown are for the process $e^+e^- \to N_2\bar{N}_2\gamma$, while for the effective $W^\pm$ the process is $e^+e^- \to \sum_i \nu_i\bar{N}_2\gamma + \bar{\nu}_i N_2\gamma$.

The background process, which produces two SM active neutrinos in the final state, can be a CC or an NC interaction, proceeding via $W^\pm$ (t and u channel diagrams) and Z boson (s channel diagram) mediation, respectively. In the case of the Z-mediated NC background process, the energy distribution of the monophoton exhibits a resonant feature, with the centre of this resonance occurring at [273]

$$E_{\text{res}}^\gamma = \frac{s - M_Z^2}{2\sqrt{s}}. \tag{5.15}$$

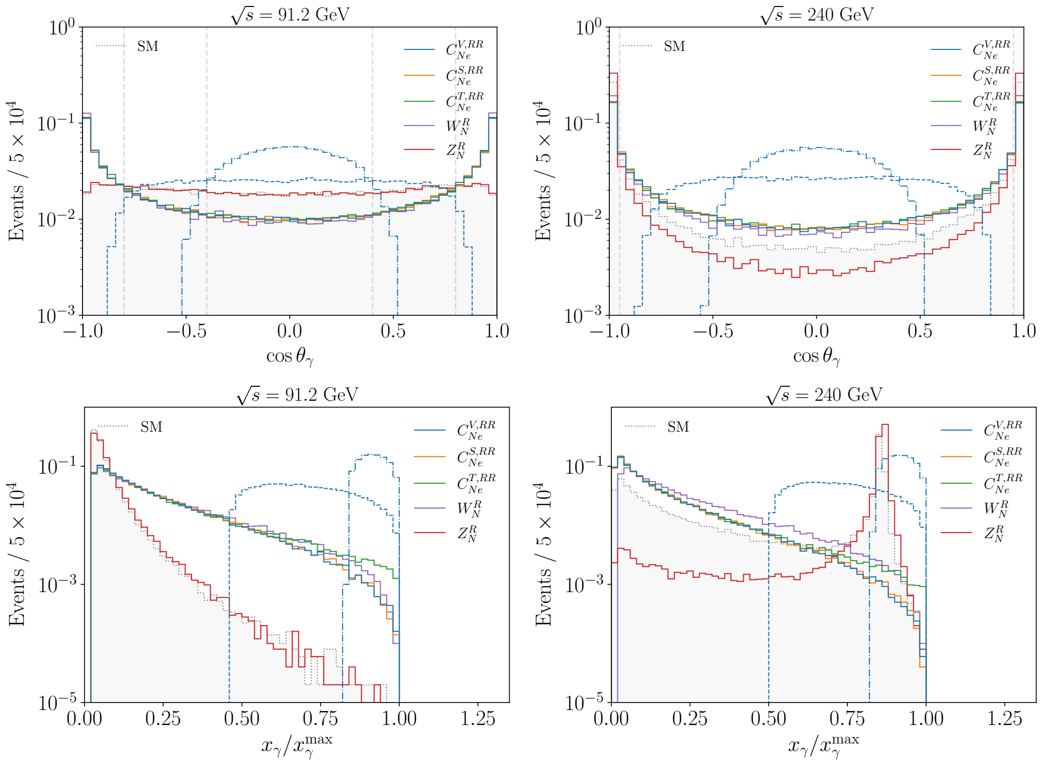

Figure 5.6: Normalised binned distributions in the cosine of the outgoing photon angle $\cos\theta_\gamma$ (above) and energy $x_\gamma = 2E_\gamma/\sqrt{s}$ (below) for mono-γ processes induced by the four-fermion, effective $W^\pm$ and Z interactions and SM background in the Dirac HNL scenario. Distributions are shown for $\sqrt{s} = 91.2$ GeV (left) and $\sqrt{s} = 240$ GeV (right). Solid lines indicate the scenario with $m_{N_2} = 10$ GeV. For the vector four-fermion operator, we also show the distributions for m_{N_2} close to the kinematic threshold, see text for details.

The full-width-at-half-maximum (FWHM) of this resonance is given by $(M_Z/\sqrt{s})\Gamma_Z$, where Γ_Z denotes the decay-width of the Z boson and M_Z is its mass. As can be seen from Eq. 5.15, the existence of a resonant peak is dependent on s, i.e. the energy of the process needs to be sufficiently large for a Z boson to be produced on-shell. Evidently, this can never occur for $\sqrt{s} = 91.2$ GeV, as all the available energy would go into producing the on-shell Z leaving no energy for the production of the monophoton. In the case of $\sqrt{s} = 240$ GeV there is ample energy for both monophoton and on-shell Z boson production and for $m_{N_1} = 10$ GeV a resonant peak at $E^\gamma_{\text{res}} \sim 102.7$ GeV occurs. Similarly, the SM process also exhibits a resonant peak, while the four-fermion and effective $W^\pm$ interactions gradually decrease as they approach $x_\gamma = x_\gamma^{\max}$. It might seem counter intuitive, that the majority of the

$\sqrt{s}$ [GeV]	Cuts	$\left(\frac{S}{B}\right)_{\text{cuts}} / \left(\frac{S}{B}\right)$				
		$C_{Ne}^{V,RR}$	$C_{Ne}^{S,RR}$	$C_{Ne}^{T,RR}$	W_N^R	Z_N^R
91.2	$\lvert\cos\theta_\gamma\rvert < 0.4$, $\lvert\cos\theta_\gamma\rvert > 0.8$	1.21	1.20	1.20	1.22	1.01
240	$\lvert\cos\theta_\gamma\rvert < 0.95$, $E_\gamma < 40$ GeV	2.30	2.30	2.23	2.00	0.05

Table 5.4: Universal kinematic cuts for maximising the signal-to-background ratio for each $\sqrt{s}$ in the EFT operator sensitivity analysis, in both the Majorana and Dirac HNL scenarios. The improvement in the signal-to-background ratios after cuts is shown in the last column, for benchmark scenarios involving a Dirac HNL with $m_{N_2} = 10$ GeV.

photons are soft in the background case while a lot more energetic for the signal processes, despite the SM active neutrinos having much lower mass than the 10 GeV sterile states.

The angular distribution is strongly forward-backward peaked for all cases, except the effective Z and SM processes, which showcase the effects of the $p_T >$ 1 GeV cut on the s-channel diagrams. As can be seen, for the vector four-fermion case two extra mass benchmarks have been shown, $m_{N_2} = 44.5$ GeV (dashed) and $m_{N_2} = 45$ GeV (dot-dashed) for $\sqrt{s} = 91.2$ GeV and $m_{N_2} = 119$ GeV and $m_{N_2} =$ 119.4 GeV for $\sqrt{s} = 240$ GeV, strongly peaked around $\cos\theta = 0$. This is to illustrate how drastically the distribution can change for different mass values and therefore to motivate the cuts.

Carefully studying the kinematic distributions for the various processes is important in ensuring that the most favourable kinematic cuts are identified that maximise the signal-to-background ratio and thus stretches the sensitivity reach to its maximum. Since both the operator type and the mass of the sterile neutrinos affects the kinematics of the process, no single cut is ideal for all scenarios. However, it is utterly unrealistic for an experiment to apply tailored kinematic cuts to its datasets and therefore we choose a universal set of acceptance cuts, which are summarised in Table 5.4.

Once the kinematic cuts have been identified, the `root` files converted from `lhe` format using DELPHES for the signal processes are passed through the analyser script, which removes any events that do not fall within the acceptance ranges. As in the case of the active-sterile mixing scenario, we compute the number of signal events using Eq. 5.8, with the difference that since the final state sterile neutrinos are identical and thus only the diagonal couplings are non-zero, sterile neutrino decay cannot take place and instead of the mixing angle, our parameter of interest is the scale of new physics. Once again $BR = 1$, since only one coupling is turned on at a time. The integrated luminosities are the same as before: $\mathcal{L} = 100$ ab^{-1} and $\mathcal{L} = 5$ ab^{-1} for $\sqrt{s} = 91.2$ GeV and $\sqrt{s} = 240$ GeV, respectively. Once the number of events have been calculated, Λ is varied, while keeping the signal significance, Eq. 5.9, fixed at 1.28.

As mentioned already, the analysis is performed in the vanishing active-sterile mixing limit of the HNL(s). The advantages of this are three-fold. Firstly, this allows for easier matching between the WCs C_i and those of νSMEFT, since the relationship between the weak and mass eigenstates of the neutrino fields are simplified to $\nu = P_L \nu'$ and $N = P_R N'$ in the Majorana case and $\nu = P_L \nu'$, $N = P_R N'$ and $S = P_L N'$ in the Dirac case for $|V_{\alpha N_i}| \ll 1$. The second advantage is that setting $|V_{\alpha N_i}|$ to be negligible assures that the HNL production channels are dominated by the EFT operators, rather than by active-sterile mixing. Thirdly, a sizable active-sterile mixing angle increases the decay width of the HNLs and thus would invalidate the assumption that N_2 is stable for the diagonal WCs considered in Eq. 5.10, and the exclusive search results derived in the case of the off-diagonal WCs in Eq. 5.11 would be altered, too.

5.3.3 Results: Diagonal WCs

The projected 90% CL sensitivities of the mono-γ plus $\not{E}$ searches at FCC-ee to the diagonal four-fermion WCs in Eq. 5.10 are shown in Fig. 5.7 as a function of m_{N_2}. The estimated sensitivities for the scalar (green), vector (red) and tensor (blue) four-fermion interactions are considered for $\sqrt{s} = 91.2$ GeV (left) and $\sqrt{s} = 240$ GeV (right) for Dirac (solid) and Majorana (dashed) HNLs. The gray shaded region bounded by the dotted line indicates the parameter space where the EFT framework's validity breaks down, assumed to be satisfied for $\Lambda < 3\sqrt{s}$, or equivalently for $C_i \equiv 1/\Lambda^2 < 1/(9s)$.

As can be seen from the figure, the sensitivity is relatively constant over the majority of the mass range and only decreases sharply at the high mass limit, due to reaching the kinematic threshold at $m_{N_2} < \sqrt{s}/2$. However, it is immediately apparent, that despite the lower luminosity, the $\sqrt{s} = 240$ GeV search is roughly 3 times more sensitive than the $\sqrt{s} = 91.2$ GeV one. This is because the signal process proceeds via a four-fermion EFT operator and therefore the cross-section scales as $\sigma \sim s/\Lambda^4$, i.e. at higher energies there is more available phase-space and hence the cross-section is larger, since it scales directly with the centre-of-mass energy. This, together with the reduced SM background (since the Z-peak is removed by the kinematic cuts) compensate for the weaker luminosity. In both energy regimes, DT is the most sensitive mode. This is simply because the tensorial production cross-sections turn out to be larger than the scalar and vector ones. In the Majorana case, the tensor four-fermion coefficient vanishes and thus there is no associated sensitivity. Lastly, it is apparent that in the case of the vector four-fermion coefficient, the Majorana constraint becomes weaker than for the other coefficients, as m_{N_2} increases. This is due to the mass suppressed negative cross-term in the Majorana cross-section (Eq. E.9), which is not present in the Dirac case. [2]

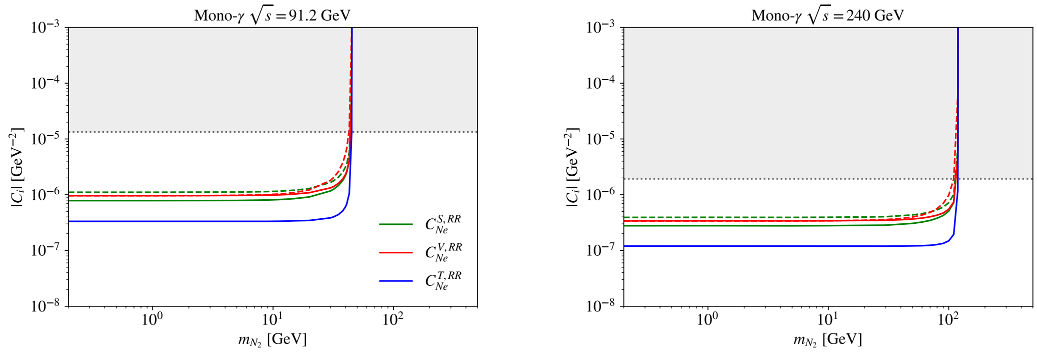

Figure 5.7: Sensitivities of mono-γ plus $\not{E}$ searches at FCC-ee to the diagonal four-fermion interaction WCs as a function of the HNL mass at 90% CL, for $\sqrt{s} = 91.2$ GeV (left) and $\sqrt{s} = 240$ GeV (right). Limits are shown for N_2 being a Dirac (solid) or Majorana (dashed) HNL. The parameter space where the EFT is not valid is indicated by the gray shaded region.

---

[2] This is due to the final state neutrinos being distinguishable in the Dirac case while they are indistinguishable in the Majorana case, leading to the amplitudes adding incoherently and coherently, respectively. Hence, there are no interference terms in the former scenario, only in the latter.

5.3.4 Analysis: Off-diagonal WCs

Besides the identical pair of sterile neutrinos in the final state explored earlier, the mono-γ plus $\not{E}$ search at FCC-ee may also be performed for off-diagonal WCs, i.e. $e^+e^- \to N_1\bar{N_2}\gamma + \bar{N_1}N_2\gamma$. In simulating this process, we only turn on the off-diagonal couplings, i.e. it is assumed that $m_{N_1} \neq m_{N_2}$. Since the labeling is arbitrary, it was assumed that $m_{N_1} < m_{N_2}$, without loss of generality. Similarly to the simulation of the identical sterile final state case, MADGRAPH was used to generate $N_{\text{tot}} = 5 \times 10^4$ signal events (the background process is the same as for the $N_2\bar{N_2}$ case and therefore did not need to be simulated again) with a cut of $p_T > 1$ GeV implemented at event generation level. As before, the analysis is performed at the two centre-of-mass energies $\sqrt{s} = 91.2$ GeV and $\sqrt{s} = 240$ GeV, as well as for three values of the mass-splitting, $\delta = 0.01, 0.1$ and 1, for each mass BP for m_{N_2}, up to the kinematic threshold $m_{N_2} \leq \sqrt{s}/(2-\delta)$. The same kinematic acceptance cuts were used as in the diagonal HNL scenario, summarised in Table 5.4.

At the analysis stage, once again the procedure mostly follows that outlined in Sec. 5.3.2. The only difference is that since the two final state neutrinos have different masses for the WCs in Eq. 5.11, it is possible for N_2 to decay via processes such as $N_2 \to \nu e^- e^+ / N_1 e^- e^+$, as shown in Figure 5.2 (with the decay rates given in Appendix C) and therefore the probability of decay needs to be accounted for. As for the case of active-sterile mixing, the geometric acceptance is obtained using Eq. 5.7, which allows for the probability that N_2 decays outside of the detector volume to be calculated for each simulated event. Based on this, the sensitivities for the exclusive mono-γ plus $\not{E}$ search are derived. We also perform the analysis for the inclusive search, taking $\mathcal{P}_{\text{out}} = 1$, as in Sec. 5.2.

The geometric acceptance together with the kinematic cuts are used in Eqs. 5.8 to calculate the number of surviving signal events, S, for each HNL mass BP. This, alongside the SM background events surviving the kinematic cuts, B, is used in Eq. 5.9 to obtain the signal sensitivity, $\mathcal{S}$. As before, the active-sterile mixing of the HNLs is assumed to be negligible.

5.3.5 Results: Off-diagonal WCs

The estimated sensitivity of the mono-γ plus $\not{E}$ search at FCC-ee at 90 % CL to the off-diagonal WCs in Eq. 5.11 is shown in Fig. 5.8 for the inclusive (light) and exclusive (opaque) scenarios. The results are shown at $\sqrt{s} = 91.2$ GeV (left) and $\sqrt{s} = 240$ GeV (right) for the scalar (top), vector (middle) and tensor (bottom) four-fermion operators, for the three mass-splitting values $\delta = 1$ (blue), 0.1 (red) and 0.01 (green), for both Dirac (solid) and Majorana (dashed) HNLs. As before, the gray shaded region shows the portion of the parameter space where the EFT approach is no longer valid.

For the inclusive search, the larger δ is, the higher m_{N_2} reach the search has, since now the mass reach extends to the kinematic threshold at $m_{N_2} < \sqrt{s}/(2-\delta)$. This is easily understood from the kinematics of the process, as for a fixed value of m_{N_2}, a larger mass-splitting means a lower value of m_{N_1} and thus there is more energy available to the photon. We see that in the case of $\delta = 0.01$, the diagonal results in Fig. 5.7 are almost recovered. This is expected, since the smaller the mass difference between the two sterile neutrinos, the closer we approach the identical HNL limit. Similarly to the diagonal search, $\sqrt{s} = 240$ GeV constrains the four-fermion WCs more heavily and in the case of the vector Majorana scenario the sensitivity falls off more rapidly as a function of m_{N_2} than it does in the case of Dirac HNLs for both centre-of-mass energies.

For the exclusive search, all contours corresponding to the various scenarios considered exhibit a nose-like structure. This is the result of the lifetime criteria that is imposed on the heavier sterile state, m_{N_2}, i.e. that it has to be long-lived enough that it does not decay within the $L = 5$ m detector volume. Generally speaking, the horizontal reach of the search is determined by the cross-section (and its dependence on the centre-of-mass energy, s), while the angle of the nose is the result of the lifetime requirement imposed. Mathematically, the nose structure can be understood as the competition between the cross-section and the decay-rate which results in a double solution when setting $\mathcal{S} = 1.28$ and solving for Λ. When Λ is larger, the cross-section has a smaller value and therefore the decay-rate is also low,

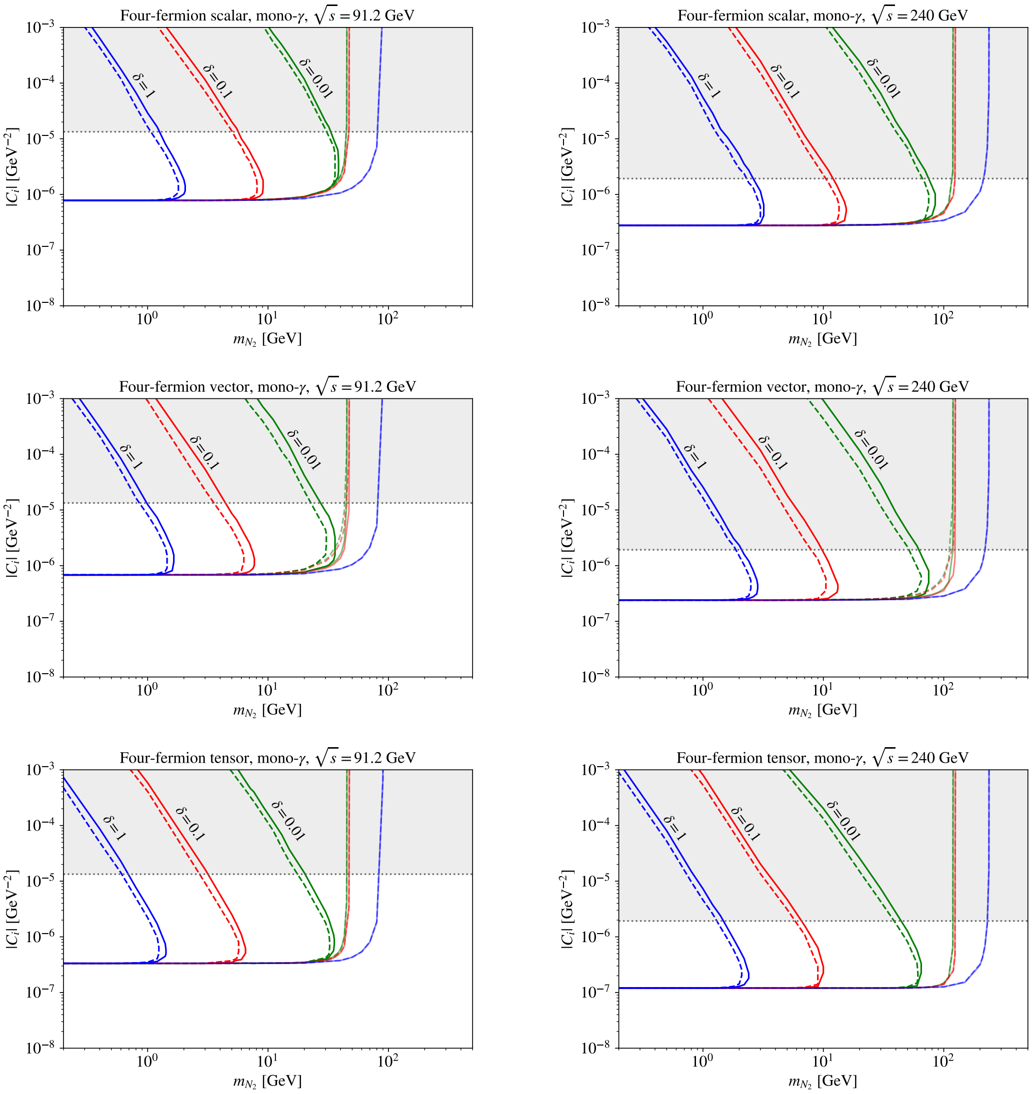

Figure 5.8: Sensitivities of the exclusive and inclusive mono-γ plus $\not{E}$ searches at FCC-ee to the off-diagonal four-fermion interaction WCs as a function of the HNL mass at 90% CL, for $\sqrt{s} = 91.2$ GeV (left) and $\sqrt{s} = 240$ GeV (right). Limits are shown for Dirac (solid) and Majorana (dashed) HNLs for three different mass splitting ratios $\delta = (m_{N_2} - m_{N_1})/m_{N_2}$. The sensitivity of the inclusive search is also shown for the Dirac (opaque) and Majorana (light) cases. The parameter space where the EFT is not valid is indicated by the gray shaded region.

hence the particle is longer lived and the probability that it will not decay within the detector is also increased. Conversely, for smaller values of Λ, the cross-section as well as the decay-rate are larger, leading to a shorter lifetime and lower probability that the sterile neutrino will travel through the detector without decaying. As in the case of the inclusive search, the $\sqrt{s} = 240$ GeV channel is more sensitive than the $\sqrt{s} = 91.2$ GeV one, since the cross-section of the process when mediated by a four-fermion EFT operator scales with the centre-of-mass energy, rather than the energy-dependence in the denominator of the intermediate propagator. In all channels considered, the mass-reach increases as the mass-splitting becomes smaller. This is simply because for $\delta \ll 1$, the mass difference between N_2 and N_1 is small, therefore the decay rate N_2 is suppressed. The horizontal constraints coming from the Dirac and Majorana HNL scenarios are identical, as can be seen from the overlap of the horizontal part of the solid and dashed lines. This is due to the normalisation of the cross-sections. On the other hand, the angled constraints are slightly different, which results from the difference in the Dirac and Majorana decay rates of N_2. In most cases, including scalar and tensor four-fermion operators, the decay rates in the Majorana case are twice as large as the Dirac case, while for vector operators they are three times as large as compared to the Dirac HNL scenario for small mass splittings. The difference in the latter case comes from the interference term in the Majorana decay rate.

5.4 Monophoton Final State: Effective Z and W Operators

Besides the four-fermion operators explored in Sec. 5.3, the mono-γ plus $\not{E}$ signal process may also proceed via effective $W^\pm/Z$ interactions, giving rise to the single and pair production of HNLs, $e^+e^- \to \nu N(\gamma)$ and $e^+e^- \to NN(\gamma)$, respectively, as shown in Fig. 5.1.

As in the previous sections, one operator is switched on at a time and the active-sterile mixing is assumed to be negligible. In this section we consider:

- Diagonal WC for the effective Z interaction with two HNLs:

$$C_i \in \left\{ \frac{2}{v^2} [Z_N^R]_{ii} \right\}, \tag{5.16}$$

  with $i = 2$ and again leading to the Majorana and Dirac processes $e^+e^- \to N_2N_2\gamma$ or $e^+e^- \to N_2\bar{N}_2\gamma$, respectively, and thus producing the mono-γ plus

$\not{E}$ signal since no decays are possible via this WC.

- Off-diagonal WC for the effective Z interaction with two HNLs:

$$C_i \in \left\{ \frac{2}{v^2}[Z_N^R]_{ij} \right\}, \tag{5.17}$$

with $i = 1$ and $j = 2$ and as in the previous section giving rise to the Majorana and Dirac HNL pair production processes $e^+e^- \to N_1N_2\gamma$ or $e^+e^- \to N_1\bar{N}_2\gamma + \bar{N}_1N_2\gamma$, respectively. Again, three mass-splitting values are considered: $\delta = 0.01, 0.1$ and 1.

- WCs of the effective Z interaction with one light neutrino and an HNL and the effective $W^\pm$ interaction with one HNL:

$$C_i \in \left\{ \frac{2}{v^2}[W_N^R]_{je}\,,\ \frac{2}{v^2}[W_N^L]_{je}\,,\ \frac{2}{v^2}[Z_{\nu N}^R]_{\alpha j} \right\}, \tag{5.18}$$

where $\alpha = e, \mu, \tau$ and $j = 2$, giving rise to the single HNL production through the processes $e^+e^- \to \sum_i \nu_i N_2\gamma$, and $e^+e^- \to \sum_i \nu_i\bar{N}_2\gamma + \bar{\nu}_i N_2\gamma$, for the Majorana and Dirac HNL scenarios, respectively. As before in the case of $C_{\nu Ne}^{V,RR}$, $Z_{\nu N}^R$ is not present in the Dirac case (as this would require ν_R as can be seen from Eq. 3.106), but the notation is kept for simplicity but understood to denote $Z_{\nu N}^L$. For the effective Z interaction, the constraint on the above WC from the mono-γ plus $\not{E}$ search may be obtained from the off-diagonal WCs in Eq. 5.17 with $\delta = 1$.

- WCs of the effective Z interaction involving two light neutrinos and the effective $W^\pm$ interaction with one light neutrino:

$$C_i \in \left\{ \frac{2}{v^2}[W_\nu^R]_{\alpha e}\,,\ \frac{2}{v^2}[\delta W_\nu^L]_{\alpha e}\,,\ \frac{2}{v^2}[\delta Z_\nu^L]_{\alpha\beta} \right\}, \tag{5.19}$$

where $\alpha, \beta = e, \mu, \tau$ contributing to the SM process $e^+e^- \to \sum \nu\bar{\nu}\gamma$. The WC W_ν^R vanishes in the Dirac case due to the lack of ν_R. The WCs δW_ν^L and δZ_ν^L can modify the SM process (depending on the flavour of the fields) and therefore need to be taken into account.

5.4.1 Simulation Setup

As in the cases of active-sterile mixing and effective four-fermion operators, the simulation is performed using `MadGraph5_aMC@NLO`. For the effective $W^\pm$ operator, the simulated signal process is $e^+e^- \to \nu_e N_2\gamma + \bar{\nu}_e N_2\gamma$ and $e^+e^- \to \nu_e \bar{N}_2\gamma + \bar{\nu}_e N_2\gamma$ for Majorana and Dirac HNL scenarios, respectively. For the effective Z operator, the simulated signal processes are $e^+e^- \to N_2N_2\gamma$ and $e^+e^- \to N_2\bar{N}_2\gamma$ for the diagonal Majorana and Dirac WCs in Eq. 5.16, respectively, and $e^+e^- \to N_1N_2\gamma$ and $e^+e^- \to N_1\bar{N}_2\gamma + \bar{N}_1N_2\gamma$ for the off-diagonal Majorana and Dirac WCs is Eq. 5.17, respectively.

As in the previous scenarios, we generate $N_{\text{tot}} = 5 \times 10^4$ events for each of the signal processes and use the same simulated SM background events as in Sec. 5.2. Once again the generator level cut in the transverse momentum is $p_T^\gamma > 1$ GeV, and the simulation is carried out for HNL masses up to the kinematic threshold. As for the active-sterile mixing and four-fermion EFT production scenarios, the simulation is performed for the two centre-of-mass energies $\sqrt{s} = 91.2$ GeV and $\sqrt{s} = 240$ GeV.

As in the case of the four-fermion EFT WCs, we consider both the diagonal and off-diagonal effective Z and $W^\pm$ WCs.

5.4.2 Analysis: Diagonal WC

The only WC relevant to the diagonal HNL scenario is that in Eq. 5.16, associated with the effective Z interaction. The effective $W^\pm$ cannot produce two HNLs in the final state at all, due to the effective operator coupling one of the incoming electrons to a light neutrino or HNL. The geometric acceptance for the diagonal effective Z interaction, as in Sec. 5.3.2, is obtained by setting $\mathcal{P}_{\text{out}} = 1$, since N_2 cannot decay. This value is then simply used in Eq. 5.8 to obtain the number of signal events surviving both the kinematic and geometric cuts, S. Subsequently, together with the number of background events surviving the kinematic cuts, B, the calculated S value is used in Eq. 5.9 to compute the median sensitivity at 90% CL, i.e. excluding the

(m_{N_2}, C_i) parameter space with $\mathcal{S} > 1.28$. As before, we assume the active-sterile mixing angle to be of negligible size.

5.4.3 Results: Diagonal WCs

The estimated sensitivity of the mono-γ plus $\not{E}$ search at FCC-ee to the diagonal WC Z_N^R in Eq. 5.16 at 90% CL is shown in Fig 5.9 for $\sqrt{s} = 91.2$ GeV (left) and $\sqrt{s} = 240$ GeV (right) for Dirac (solid) and Majorana (dashed) HNLs. It should be noted, that $C_i = \frac{2}{v^2}[Z_N^R]_{ii}$ in order to keep the units of GeV^{-2} (as to place the results on the same footing as the four-fermion ones). As before, the gray shaded region shows the portion of the parameter space where the EFT framework can no longer be assumed.

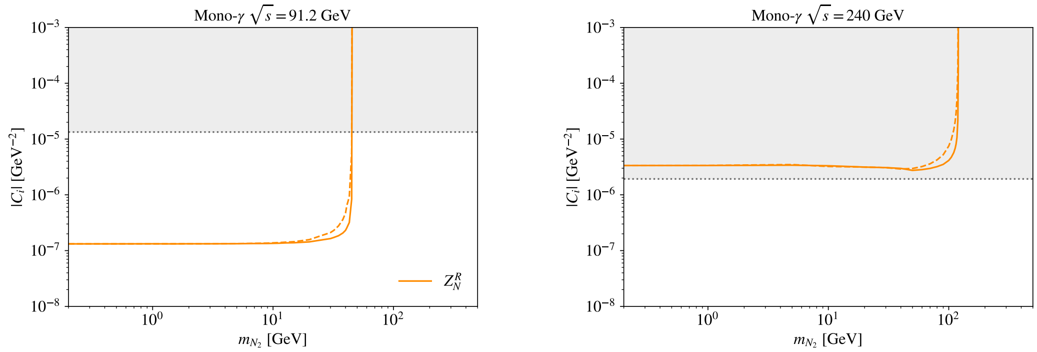

Figure 5.9: Sensitivities of mono-γ plus $\not{E}$ searches at FCC-ee to the diagonal effective Z interaction WC as a function of the HNL mass at 90% CL, for $\sqrt{s} = 91.2$ GeV (left) and $\sqrt{s} = 240$ GeV (right). Limits are shown for N_2 being a Dirac (solid) or Majorana (dashed) HNL. The parameter space where the EFT is not valid is indicated by the gray shaded region.

Similarly to the four-fermion diagonal results, the sensitivity curve is essentially constant as a function of m_{N_2} and only falls of sharply at the kinematic threshold. Unlike the four-fermion results however, for the diagonal effective Z interaction $\sqrt{s} = 240$ GeV is less sensitive than $\sqrt{s} = 91.2$ GeV. This is simply because the cross-section is inflated by the resonance at the Z-pole. For both centre-of-mass energies, the sensitivity in the Majorana case falls of more quickly for high M_{N_2}. This, just like in the vector four-fermion case, is the result of the presence of additional interference terms (which are not present in the Dirac case) contributing destructively and leading to additional suppression in the Majorana scenario.

5.4.4 Analysis: Off-diagonal WCs

The analysis of the WCs in Eqs. 5.17 and 5.18 proceed similarly to the off-diagonal four-fermion WCs in Sec. 5.3. Once again, $N_{\text{tot}} = 5 \times 10^4$ signal events were simulated and the SM background events were used as in Sec. 5.2.

As opposed to the diagonal scenario, the off-diagonal WCs allow the heavier HNL to decay via processes such as $N_2 \to \nu\nu\bar{\nu}/N_1\nu\bar{\nu}$, $N_2 \to \nu q\bar{q}/N_1 q\bar{q}$ and $N_2 \to \ell^- u\bar{d}$. To this end, we consider both an inclusive and exclusive search. For the former, we assume that the HNL is stable and does not decay within the detector, setting $\mathcal{P}_{\text{out}} = 1$. For the latter, the probability that N_2 decays outside the detector volume, therefore needs to be calculated using Eq. 5.7 on an event-by-event basis to give the total geometric acceptance, $\mathcal{P}_{\text{out}}$. As for all previous analyses, this is used to compute S, which alongside B gives the median sensitivity, $\mathcal{S}$ via Eq. 5.9. The requirement $\mathcal{S} > 1.28$ gives the excluded region of the parameter space at 90% CL.

5.4.5 Results: Off-diagonal WCs

The estimated sensitivity of the mono-γ plus $\not{E}$ search at FCC-ee to the off-diagonal WCs in Eqs. 5.17 and 5.18 are shown in Fig. 5.10 for the effective $W^\pm$ (top) and Z (bottom) interactions at $\sqrt{s} = 91.2$ GeV (left) and $\sqrt{s} = 240$ GeV (right). Once again we consider both Dirac (solid) and Majorana (dashed) HNL scenarios, for both an exclusive (opaque) and inclusive (light) search. In the case of the effective Z interaction producing two HNLs in the final state, we consider mass-splitting values of $\delta = 1$ (blue), 0.1 (red) and 0.01 (green).

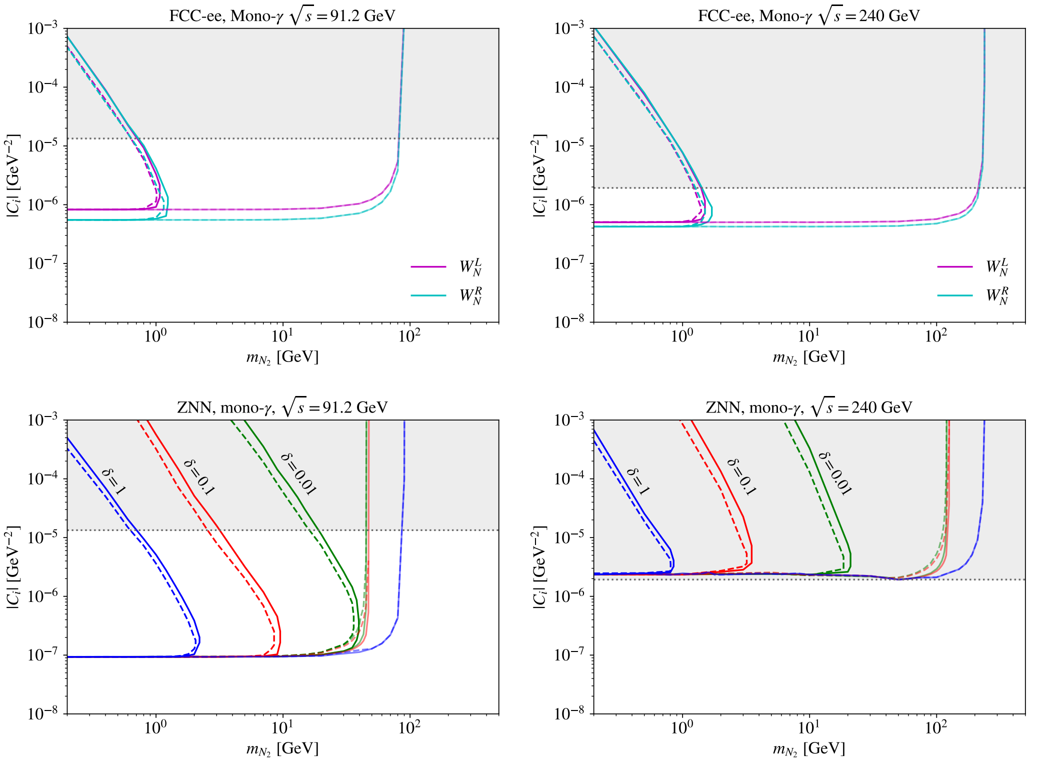

Figure 5.10: Sensitivities of the exclusive and inclusive mono-γ plus $\not{E}$ searches at FCC-ee to the effective $W^{\pm}$ and (off-diagonal) Z interactions as a function of the HNL mass, at 90% CL, for $\sqrt{s} = 91.2$ GeV (left) and $\sqrt{s} = 240$ GeV (right). The benchmark scenarios for the mass splitting ratio δ are the same as in 5.8.

For the inclusive search, the resulting constraints extend up to the kinematic threshold at $m_{N_2} < \sqrt{s} = (2 - \delta)$. In the case of the effective Z interaction, the $\sqrt{s} = 91.2$ GeV is more constraining due to the Z-resonance, while the opposite is true for the effective $W^{\pm}$ interaction, which at $\sqrt{s} = 240$ GeV benefits from the larger cross-section. The limits on $[W_N^R]_{je}$ are stronger than on $[W_N^L]_{je}$, as the cross-section of the former is larger.

For the exclusive search concerning the effective Z WCs, the impact of N_2 decaying results in the same impact as observed for the off-diagonal exclusive four-fermion WCs in Fig. 5.8: for both $|C_i|$ and m_{N_2} values above a certain size, the HNL is very unlikely to decay outside of the detector. The mass reach increases with decreasing δ, as the the decay rate of N_2 to N_1 is suppressed with increasing m_{N_1}, and thus the heavier HNL becomes longer lived.

5.5 Displaced Vertex Searches: Four-fermion EFT Operators

In this section we estimate the sensitivity of the future FCC-ee in the context of DV searches. As for the mono-γ plus $\not{E}$ EFT searches, we set $V_{\alpha N_i} = 0$ and $C_i \neq 0$, turning one WC on at a time. We consider both Dirac and Majorana HNLs and perform the study at the two centre of mass energies $\sqrt{s} = 91.2$ GeV and 240 GeV, with integrated luminosities of $\mathcal{L} = 100$ ab^{-1} and 5 ab^{-1}, respectively.

5.5.1 Simulation Setup

The diagonal four-fermion and effective Z interactions parameterised by the WCs in Eqs. 5.10 and 5.16, respectively, cannot accommodate any decays of N_2 if the active-sterile mixing is turned off. Therefore, a DV analysis is not possible for these diagonal operators. However, the off-diagonal WCs for the four-fermion EFT WCs in Eqs. 5.11 and 5.12 and the effective Z and $W^{\pm}$ interactions in 5.17 and 5.18 can induce N_2 decays and may therefore be probed by DV searches.

As for the simulations in the previous sections, we once again use `MadGraph5_aMC@NLO` to simulate $N_{\text{tot}} = 5 \times 10^4$ signal events. The signal process in the four-fermion case is $e^+e^- \to N_1\bar{N}_2 + \bar{N}_1 N_2$ for both the Dirac and Majorana scenarios (since the same issue is encountered with the Majorana fermions as in Sec. 5.3). For the effective $W^{\pm}$ and Z interactions, the fermion flow problem is not present and thus the Majorana HNLs do not pose a problem. Hence, the simulated signal processes are $e^+e^- \to \nu_e N_2 + \bar{\nu}_e N_2$ and $e^+e^- \to N_1 N_2$ for the Majorana case, respectively, and $e^+e^- \to \nu_e \bar{N}_2 + \bar{\nu}_e N_2$ and $e^+e^- \to N_1\bar{N}_2 + \bar{N}_1 N_2$ for the Dirac case, respectively.

In terms of the decay mechanism, N_2 (and additionally $\bar{N}_2$ for Dirac HNLs) is required to decay through the effective operators considered in this work, to a di-electron final state, via the decay process $N_2 \to N_1 e^- e^+$. As before, `Delphes` is used to convert to root files, however this time instead of just a simple conversion, the detector response is simulated using the Innovative Detector for Electron-positron Accelerators (IDEA) card [274].

5.5.2 Analysis

No background is considered alongside the signal process, since most SM processes that could act as backgrounds are prompt. This means the decay rates are large and hence $\tau \propto 1/\Gamma$ the lifetimes are short. Additionally, an acceptance cut of $|d_0| > 0.6$ mm [275, 276] may be imposed on the electron-track transverse impact parameter, to filter out any prompt decays. A cut is also placed on the transverse momentum of the electron, $p_T^e > 0.7$ GeV, which sets the threshold for identification. As before, Eq. 5.7 is used to compute the geometric acceptance, with the assumption of a spherical detector with $L_1 = 0.1$ mm and $L_2 = 5$ m, and $f(\sqrt{s}, m_{N_1}, m_{N_2}, b) = \delta(b - b')$ where $b' = \lambda(s, m_{N_1}^2, m_{N_2}^2)/(2m_{N_2}\sqrt{2})$ being the fixed boost factor of the heavier HNL, to give the probability of N_2 decaying inside the detector, $\mathcal{P}_{\text{in}}$. With these ingredients, the number of surviving signal events (after the kinematic cuts and the application of the geometric acceptance condition) are calculated via

$$S = \mathcal{L} \times \sigma \times \text{BR} \times \mathcal{P}_{\text{in}} \times \varepsilon_k \,. \tag{5.20}$$

where now BR denotes the branching ratio of the process $N_2 \to N_1 e^- e^+$. As before, the derived bounds on the WCs are presented at 90% CL, which in this background-free scenario is achieved by requiring $S > 2.3$.

5.5.3 Results

The estimated sensitivities of the DV searches at the FCC-ee to the WCs in Eqs. 5.11 and 5.12 at 90% CL are shown in Fig. 5.11 for $\sqrt{s} = 91.2$ GeV (left) and $\sqrt{s} = 240$ GeV (right), for vector (blue), scalar (orange) and tensor (green) four-fermion operators, considering both Dirac (solid) and Majorana (dashed) HNL scenarios. We also show the results for three mass-splitting values, $\delta = 0.1$ (light), 0.5 (medium) and 1 (dark). The gray shaded region shows the portion of the parameter space where the EFT approach is no longer valid.

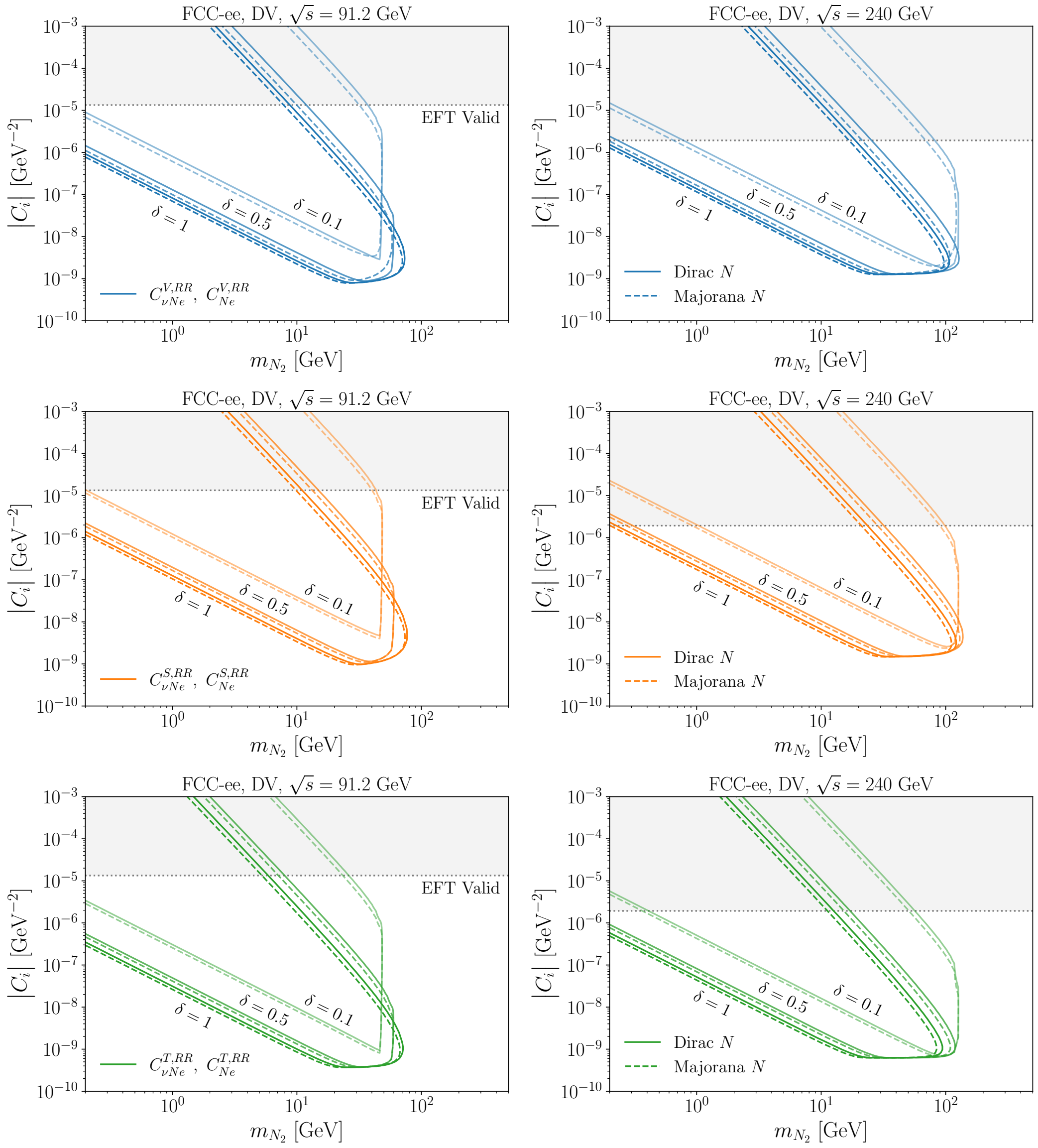

Figure 5.11: Sensitivities of the of DV search at FCC-ee to the off-diagonal four-fermion interaction WCs as a function of the HNL mass at 90% CL, for $\sqrt{s} = 91.2$ GeV (left) and $\sqrt{s} = 240$ GeV (right). Limits are shown for Majorana (dashed) and Dirac (solid) HNLs for three different mass splitting ratios $\delta = (m_{N_2} - m_{N_1})/m_{N_2}$. The parameter space where the EFT is not valid is indicated by the gray shaded region.

It can be seen that the DV search is much more sensitive to the $|C_i|$ coefficients than the mono-γ plus $\not{E}$ searches, reaching as low as $|C_i| \sim 10^{-9}$ GeV^{-2} for $\delta = 1$ in the vector four-fermion case for both $\sqrt{s} = 91.2$ GeV and 240 GeV, and even going beyond in the tensor case. Compared to the mono-γ plus $\not{E}$ searches, the DV bounds for all scenarios weaken considerably as $m_{N_2} \to 0$. At $\sqrt{s} = 91.2$ GeV, the mass reach decreases with decreasing δ, as the kinematic threshold at $m_{N_2} < \sqrt{s}/(2-\delta)$ is reached, causing the vertical bounds. Conversely, at $\sqrt{s} = 240$ GeV, decreasing δ values lead to a larger mass reach, since the lifetime of N_2 decreases with mass and smaller values of δ are required to keep the decay within the detector volume. Although the phase space is looser, the kinematic threshold is hit eventually, again resulting in the vertical bounds on the right. In essence, the curves are limited by N_2 being "too long-lived" from the left, and "too prompt" from the right.

5.6 Displaced Vertex Searches: Effective Z and W Operators

The DV searches discussed above in the context of four-fermion operators may also be investigated for the effective Z and $W^{\pm}$ operators. Again, we assume no active-sterile mixing and turn on one operator at a time. Since in the diagonal case N_2 cannot undergo decay, only the WCs in Eqs. 5.17 and 5.18 are considered. For the off-diagonal effective Z WC, the three values of mass-splitting $\delta = 0.1, 0.5$ and 1 are considered (the $\delta = 1$ scenario coincides with the effective Z interaction with N_2 and a light neutrino in the final state).

5.6.1 Simulation Setup

The events are simulated very similarly to Sec. 5.5 with only a few differences. As before, the events are generated using `MadGraph` and the detector response is simulated using the IDEA card in `Delphes`. The relevant signal processes for the effective $W^{\pm}$ and Z interactions are $e^+e^- \to \nu_e N_2 + \bar{\nu}_e N_2$ and $e^+e^- \to N_1 N_2$ in the Majorana case, respectively, and $e^+e^- \to \nu_e \bar{N}_2 + \bar{\nu}_e N_2$ and $e^+e^- \to N_1 \bar{N}_2 + \bar{N}_1 N_2$ in the Dirac case, respectively. Again, a background free approach is taken and in total $N_{\text{tot}} = 5 \times 10^4$ signal events are generated.

For the effective Z interaction we require the decay process $N_2 \to N_1 e^- e^+$, while for the effective $W^{\pm}$ $N_2 \to \nu e^- e^+$.

5.6.2 Analysis

The same kinematic cuts are implemented as in the previous section: $|d_0| > 0.6$ mm and $p_T^e > 0.7$ GeV, which determine ε_k. Then Eq. 5.20 is used in the same way as before, but now with BR for $N_2 \to \nu e^- e^+$, to compute the total number of signal events, S. Once again impose the requirement $S > 2.3$, which produces the excluded regions at 90% CL.

5.6.3 Results

The 90% CL results for the DV search at the FCC-ee in the context of effective Z and $W^\pm$ interactions is shown in Fig. 5.12 for the two centre-of-mass energies $\sqrt{s} = 91.2$ GeV (left) and $\sqrt{s} = 240$ GeV (right) for the $W^\pm$ (top) and Z (bottom) WCs, for both Dirac (solid) and Majorana (dashed) HNL scenarios. For the Z scenario, the mass-splittings $\delta = 0.1$ (light), 0.5 (medium) and 1 (dark) are considered.

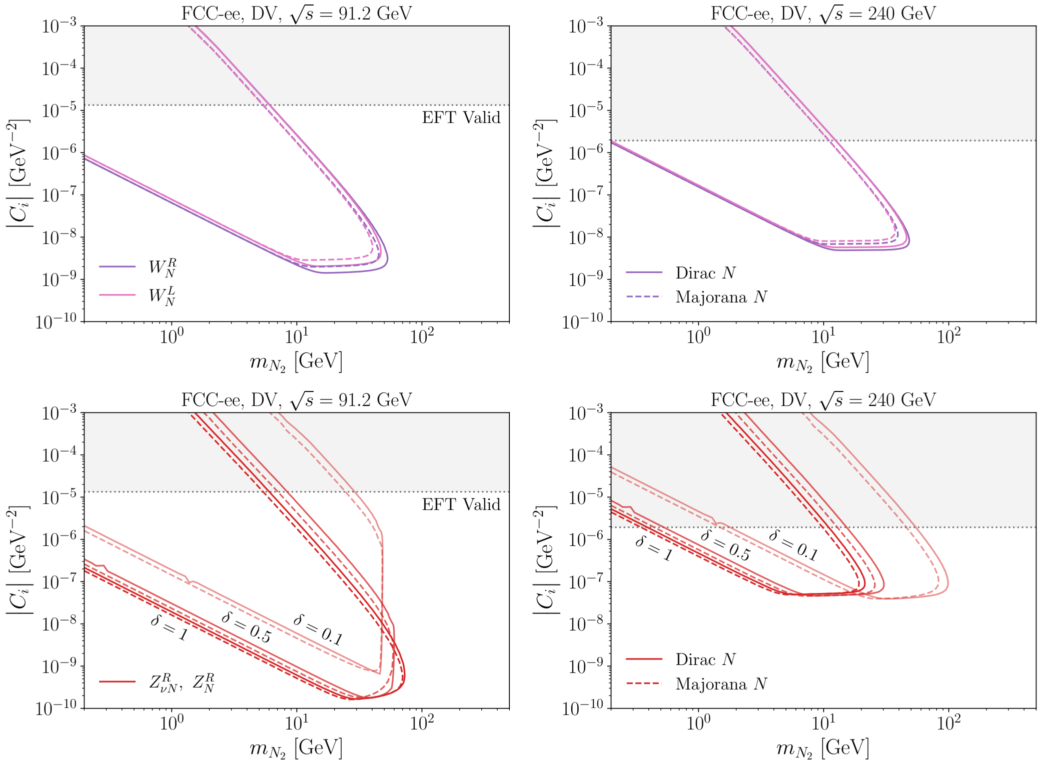

Figure 5.12: Sensitivities of the DV search at FCC-ee to the effective $W^\pm$ and (off-diagonal) Z interactions as a function of the HNL mass at 90% CL, for $\sqrt{s} = 91.2$ GeV (left) and $\sqrt{s} = 240$ GeV (right). The benchmark scenarios for the mass splitting ratio δ are the same as in Fig. 5.11.

As in the case of the four-fermion DV results, the DV search provides more stringent bounds on $|C_i|$ than the mono-γ plus $\not{E}$ search. For the effective Z interaction WCs, the mass reach is affected by the size of δ for the two centre-of-mass energies in the same fashion as seen for the four-fermion DV results. Unlike those sensitives however, the enhanced cross-section at the Z-resonance leads to significantly stricter constraints than in the $\sqrt{s} = 240$ GeV case. The $\delta = 0.1$ curve is not bounded vertically from the right, as the cross-section is not large enough to reach the kinematic threshold.

For the effective $W^{\pm}$ interaction, the $\sqrt{s} = 91.2$ GeV is able to place stronger constraints on the WCs, than $\sqrt{s} = 240$ GeV. Firstly, this is due to the lack of any backgrounds, which in the mono-γ plus $\not{E}$ search benefited higher $\sqrt{s}$. Secondly, the reduction in luminosity has a stronger negative impact on the sensitivity than the corresponding gain from the increased cross section. For both centre-of-mass energies, the search is able to constrain $[W_N^R]_{je}$ more strictly than $[W_N^L]_{je}$, simply due to the cross-section being larger in the former case. The upper parts of the exclusion bounds - dictated by the decays - are completely overlapping, because the rate of the decay process $N_2 \to \nu e^- e^+$ is independent of the operator it proceeds via.

5.7 Operator Matching & Discussion

In this section, the matching of the sensitivities to the EFT WCs obtained in the context of mono-γ plus $\not{E}$ (in Sec. 5.3 and 5.4) and DV searches (in Sec. 5.5 and 5.6) are matched onto the WCs of the νSMEFT operators in Tables 3.1 and 3.2. Additionally, the obtained limits on these WCs are converted to lower bounds on the scale of new physics, Λ. The derived constraints are then compared to existing bounds.

It should be noted, that the EFT WCs are in the mass basis, while the νSMEFT WCs are in the weak flavour basis and therefore rotations are required. The rotations and the matching itself is considerably simpler to carry out if $|V_{\alpha N_i}| = 0$ is assumed, as it prevents multiple νSMEFT operators from contributing to the low-energy operators in the broken phase.

5.7.1 $d = 6$ νSMEFT Operators

In this subsection we perform the matching of the $d = 6$ operators in Table 3.1 that contribute to the WCs in Eqs. 5.10–5.13 and 5.16–5.19. First, the relations between the mass and weak eigenstates needs to be established. These are simply $N = P_R N'$ for Majorana HNLs and $N = P_R N'$ and $S = P_L N'$ for Dirac HNLs, if the active-sterile mixing angle is assumed to be negligible, i.e. $|V_{\alpha N_i}| = 0$. Then, the indices of the νSMEFT oepraors can simply be rewritten in terms of the active neutrino flavour indices $\rho, \sigma = e, \mu, \tau$ and the HNL mass indices $i, j = 1, 2$.

Using this, the matching of the operators in Eqs. 5.10, 5.16, 5.11 and 5.17 is simply

$$\underset{ijee}{C^{V,RR}_{Ne}} = \underset{eeij}{C_{eN}}\,, \quad \frac{2}{v^2}[Z^R_N]_{ij} = \underset{ij}{C_{HN}}\,, \tag{5.21}$$

while for those in Eqs. 5.12

$$\underset{\alpha jee}{C^{S,RR}_{\nu Ne}} = \underset{\alpha jee}{C_{lNle}} + \frac{1}{2}\underset{ej\rho e}{C_{lNle}}\,, \quad \underset{\alpha jee}{C^{T,RR}_{\nu Ne}} = \frac{1}{8}\underset{ej\rho e}{C_{lNle}}\,, \quad \frac{2}{v^2}[W^R_N]_{je} = \underset{je}{C_{HNe}}\,. \tag{5.22}$$

These matching relations allow the constraints on the WCs C_i derived earlier in Figs. 5.7–5.12 to be translated to bounds on the νSMEFT operators of $d = 6$, as shown in Fig. 5.13.

The top two panels show the bounds on the coefficient C_{eN}, corresponding to the $d = 6$ operator $Q_{eN} = (\bar{e}\gamma_\mu e)(\bar{N}_{Ri}\gamma^\mu N_{Rj})$, as a function of m_{N_2}, with $i = j = 2$ (left) and $i = 1$, $j = 2$ (right) for assuming $m_{N_1} = 0$ (equivalent to maximal mass-splitting, i.e. $\delta = 1$). Similarly, the centre-left panel shows the bounds on the coefficient C_{lNle}, corresponding to the $d = 6$ νSMEFT operator $Q_{lNle} = (\bar{L}_\rho N_{Rj})\varepsilon(\bar{L}_\sigma e)$, with $\rho = \sigma = e$ and $j = 2$. The top-right panel shows the bounds on C_{HNe} for the operator νSMEFT operator $Q_{HNe} = (\bar{N}_{Rj}\gamma_\mu e)(\tilde{H}^\dagger i D^\mu H)$ with $j = 2$. Finally, the bottom panels show the constraints on C_{HN}, associated with the $d = 6$ νSMEFT operator $Q_{HN} = (\bar{N}_{Ri}\gamma_\mu N_{Rj})(H^\dagger i \overleftrightarrow{D}^\mu H)$ for $i = j = 2$ (left) and $i = 1$, $j = 2$ (right). The bounds on the various coefficients are shown for the Dirac HNL scenario, at the centre-of-mass energies $\sqrt{s} = 91.2$ GeV (red) and $\sqrt{s} = 240$ GeV (black). In the

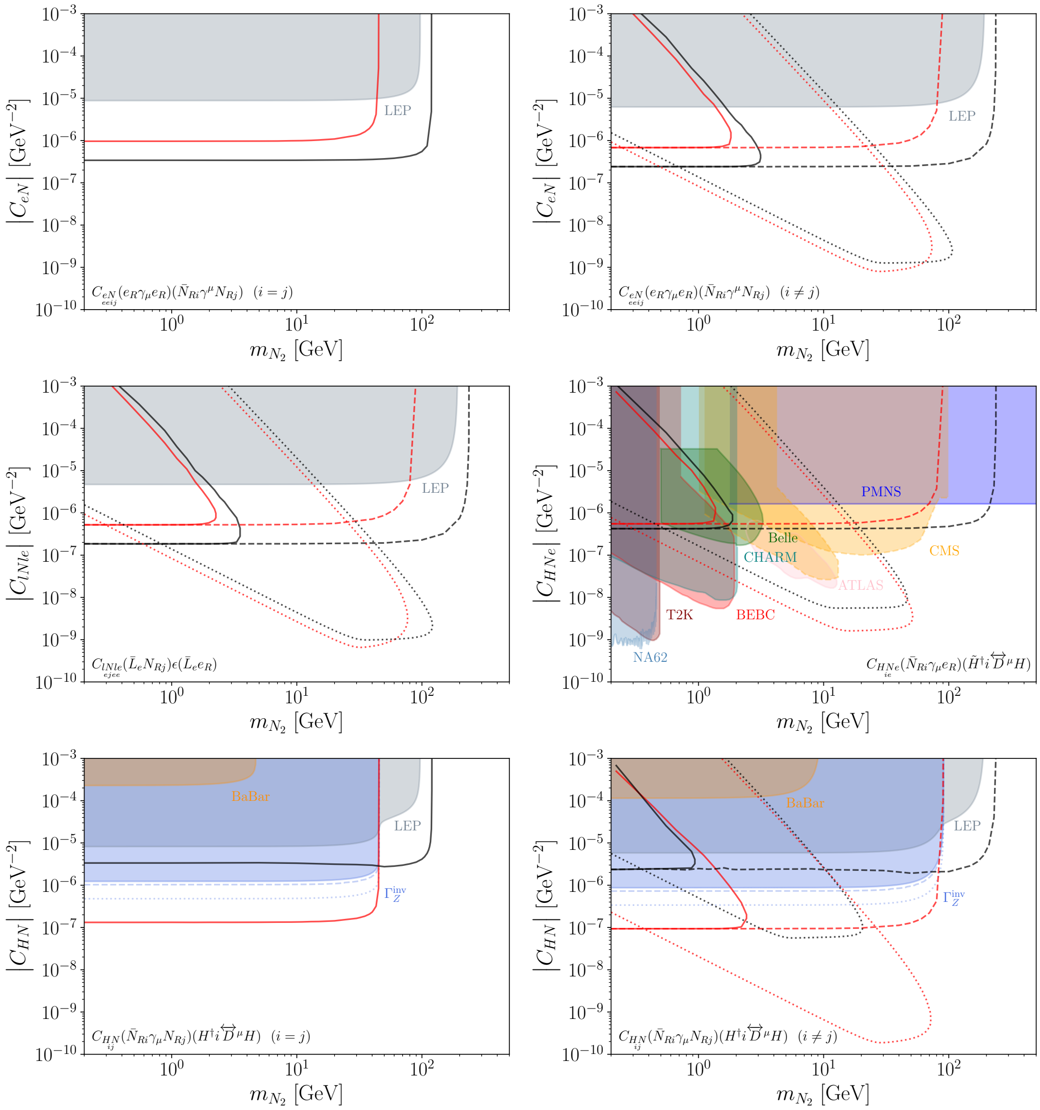

Figure 5.13: FCC-ee sensitivities to the $d=6$ νSMEFT operator WCs C_{eN} (top), C_{lNle} and C_{HNe} (centre) and C_{HN} (bottom), in the Dirac HNL scenario, compared to existing constraints. The red (black) curves correspond to $\sqrt{s}=91.2$ GeV (240 GeV), while the solid (dashed) and dot-dashed lines show the exclusive (inclusive) mono-γ plus $\not{E}$ and DV analyses, respectively. Existing bounds (shaded) are discussed in the main text.

case of $i\neq j$, the results are based on the exclusive (solid), inclusive (dashed) and DV (dotted) searches. The gray shaded regions show the existing LEP constraints from mono-γ plus $\not{E}$ searches. The original bounds were placed on a purely vector four-fermion operator of the form $(\bar{N}\gamma_\mu N)(\bar{e}\gamma^\mu e)$, but these can be rescaled to give ballpark constraints on our operator coefficients of interest, following the procedure in [250], using DELPHI data [277, 278]. This involves setting the cross-sections to be equal

$$|C_i|^2\hat{\sigma}_i = |C_j|^2\hat{\sigma}_j\,, \tag{5.23}$$

and finding the bound on the coefficient through the ratio of the two cross-sections. The hat in the above expression denotes the cross-section with the coefficient dependence removed by factoring it out.

For C_{eN}, which gives rise to the vector four-fermion EFT operator, the bounds on the νSMEFT operator WC are trivially found via the relation in Eq. 5.21. For this coefficient, the rescaled LEP bounds are the only relevant existing constraints in the parameter space and they are rescaled by setting $C_{Ne}^{V,RR} = 1/(\Lambda^2)$ in Eq. E.8. Our results suggest that the FCC-ee will be able to improve upon these bounds by over an order of magnitude for both $i = j$ and $i \neq j$, and even more significantly in the 400 MeV $\lesssim m_{N_2} \lesssim$ 110 GeV mass range with the DV search.

The operator associated with C_{lNle} contributes to both the scalar and tensor four-fermion EFT operators, with relative strengths of $C_{\nu Ne}^{S,RR} = 12C_{\nu Ne}^{T,RR} = 3C_{lNle}/2$. Since the processes were simulated with only one operator being turned on at a time, in principle it is not possible to constrain C_{lNle} from the separate results obtained for $C_{\nu Ne}^{S,RR}$ and $C_{\nu Ne}^{T,RR}$ [3] In practice however, the relationship $C_{\nu Ne}^{S,RR} = 12C_{\nu Ne}^{T,RR}$ shows that the scalar WC dominates and therefore the bounds on C_{lNle} are obtained from the scalar results via $C_{\nu Ne}^{S,RR} = 3C_{lNle}/2$. In this case, the cross-section is computed using $C_{\nu Ne}^{S,RR} = 12C_{\nu Ne}^{T,RR} = 3/(2\Lambda^2)$ in Eq. E.8. The estimated improvement with respect to the LEP bounds is very similar as in the $i \neq j$ case for the C_{eN} coefficient for all searches.

The νSMEFT operator coefficient C_{HNe} gives rise to the effective W interaction. The associated matching condition of the WCs from Eq. 5.22 means that the results of the mono-γ plus $\not{E}$ and DV searches can be directly translated onto the νSMEFT coefficient. In this case, the parameter space is heavily constrained as compared to the other coefficients. This is because processes involving the produc-

---

[3] Since situations where both coefficients are of similar size or where one dominates production and the other the decay, cannot be captured.

tion and decay of HNLs via active-sterile mixing, can also proceed via effective $W^{\pm}$ interactions, if the V_{eN} insertion is changed to $W_N^R = \frac{v^2}{2}C_{HNe}$. The more numerous constraints on the active-sterile mixing can therefore rather easily be translated onto C_{HNe}, with CC processes rescaling trivially, and NC HNL decays being rescaled using the ratio of the decay rates via active-sterile mixing and $W^{\pm}$ interactions. Such rescaled bounds on the coefficient are shown as shaded regions in the plot, coming from PMNS unitarity (blue) [279], CMS [280] (orange), ATLAS [271] (pink), Belle [281] (green), CHARM [282,283] (teal), BEBC [284] (red), T2K [285] (brown) and NA62 [286] (slate). Compared to these existing bounds, the exclusive mono-γ plus $\not{E}$ search at FCC-ee is not expected to be competitive for either centre-off-mass energy considered. Similarly, the inclusive search at $\sqrt{s} = 91.2$ GeV falls entirely within the already excluded region, but at $\sqrt{s} = 240$ GeV for masses around $m_{N_2} \sim 100$ GeV the search is sensitive to a small portion of the unconstrained parameter space. The DV search on the other hand, is able to place competitive constraints on the νSMEFT coefficient for both centre-of-mass energies for HNL masses in the range 2 GeV $\lesssim m_{N_2} \lesssim 60$ GeV.

The final coefficient considered in the figure is C_{HN}. Once again, the relations in Eq. 5.21 allow us to take the results of the mono-γ and DV searches directly and apply them as bounds on the νSMEFT coefficient. The gray shaded region is the LEP constraint for the purely vector four-fermion effective operator, rescaled via setting the relevant cross-sections equal, as before. The orange shaded exclusion comes from the BaBar experiment's upper bound on the branching ratio of $\Upsilon(1S)$ to invisible final states [287]. The blue shaded region is excluded at 90% CL, computed via a χ^2 fit to the invisible Z width measured at LEP using the decay rate for the process $Z \to NN$ in Appendix C, since C_{HN} can mediate the decay of Z to invisible states. Furthermore, similarly to LEP, the FCC-ee will be able to perform precision measurements of the invisible Z width. Assuming agreement with the SM, i.e. $\Gamma_{\text{inv}}|_{\text{SM}} = 501.48 \pm 0.04$ MeV [288], the projected bounds are shown with the blue dashed lines, while those assuming the LEP result of $\Gamma_{\text{inv}}|_{\text{exp}} = 499.0 \pm 1.5$ MeV [30] result in the blue dotted projected sensitivity.

Apart from the exclusive search for $i \neq j$ at $\sqrt{s} = 240$ GeV, all searches considered are projected to be competitive.

5.7.2 Two HNL νSMEFT Operators at $d \leq 7$

Before summarising the sensitivity of the FCC-ee to all $d \leq 7$ νSMEFT operators, we briefly discuss two operators whose matching is slightly less straightforward than the ones considered so far, as they can give rise to more than one EFT operator in the broken phase. Then we discuss the summary bar chart in Fig. 5.14.

The $d = 6$ νSMEFT operator Q_{lN} induces the low-energy operators $(\bar{N}\gamma_\mu P_R N)(\bar{e}\gamma^\mu P_L e)$ and $(\bar{N}\gamma_\mu P_R N)(\bar{\nu}_e\gamma^\mu P_L \nu_e)$. Besides the decay $N_2 \to N_1 e^- e^+$, this also opens up the decay channel $N_2 \to N_1 \nu\bar{\nu}$. While the latter was not taken into account upon computing the bounds in Fig. 5.11, for the DV search results in the bar chart for C_{eN} the extra decay mode was considered (decreasing the sensitivity slightly).

In addition, the $d = 7$ νSMEFT operator Q_{lSNeH} also induces multiple operators at the EW scale, namely the scalar and tensor four-fermion EFT operators for Dirac HNLs. The relative strength of the interactions is encoded in the relation $C_{Ne}^{S,RR} = 4C_{Ne}^{T,RR} = -vC_{lSNeH}/(2\sqrt{2})$. This poses a problem, since the signal processes were simulated with only one operator turned on at a time. However, the problem can be circumvented if the derived sensitivities are cross-section limited, because then $\Lambda^6 = \Lambda_S^6 + \Lambda_T^6$ (as being a $d = 7$ operator, $C_{lSNeH} \propto 1/\Lambda^3$ and thus $\sigma \propto C_{lSNeH}^2 \propto 1/\Lambda^6$). The scalar and tensor contribute individually, because in Eq. E.2, the interference term is proportional to $\cos\theta$, which drops out of the expression for σ upon integrating over the angle. The bar charts, to be discussed shortly, show the maximal sensitivity for each coefficient for a given search, which may occur at different values of m_{N_2}. For the mono-γ plus $\not{E}$ searches, the maximal sensitivity is always cross-section limited, since the probability of decaying outside the detector is $\mathcal{P}_{out} \approx 1$ as $m_{N_2} \to 0$. For the DV searches, the bar charts take the $\delta = 0.1$ results. In this case, although the contours are cut-off by the kinematic threshold before fully reaching the cross-section limited plateau, we have checked that the simple additive expression $\Lambda^6 \approx \Lambda_S^6 + \Lambda_T^6$ is still a good approximation. Therefore,

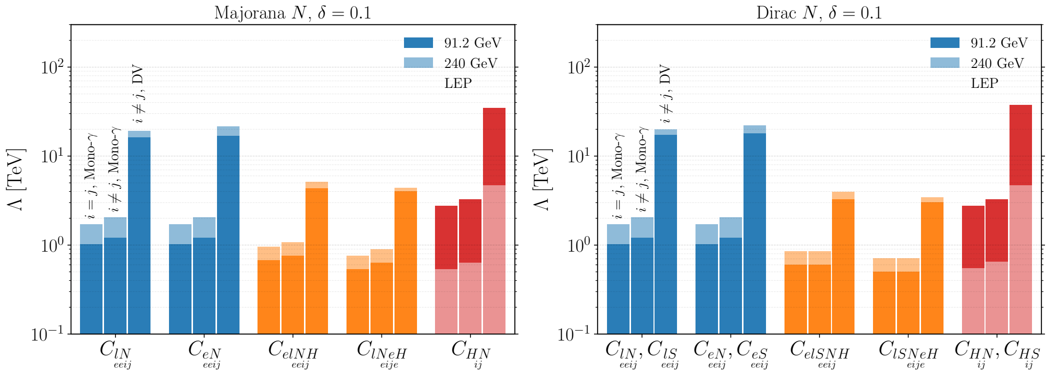

Figure 5.14: Maximum reach to the scale of new physics Λ for the $d = 6$ and $d = 7$ νSMEFT operators involving two HNLs, inducing $e^+e^- \to NN(\gamma)$, in the Majorana (left) and Dirac (right) scenarios. For each operator, the FCC-ee sensitivities from the mono-γ plus $\not{E}$ search are shown for $i = j$ (left) and $i \neq j$ (centre) and the DV search for $i \neq j$ (right). The LEP mono-γ plus $\not{E}$ constraints are shown as black striped bars.

the results are converted using $|C_{Ne}^{S,RR}| = v/(2\sqrt{2}\Lambda_S^3)$ and $|C_{Ne}^{T,RR}| = v/(8\sqrt{2}\Lambda_T^3)$ for the scalar and tensor WCs, respectively.

The summary bar chart in Fig. 5.14 shows the maximum sensitivity of the FCC-ee to the $d = 6$ and $d = 7$ νSMEFT operators giving rise to effective interactions with two HNLs at the EW scale, for both Dirac (right) and Majorana (left) HNLs, for $\delta = 0.1$ at $\sqrt{s} = 91.2$ GeV (darker) and $\sqrt{s} = 9240$ GeV (lighter). The three bars for each coefficient from left to right correspond to: mono-γ plus $\not{E}$ search for $i = j$, mono-γ plus $\not{E}$ search for $i \neq j$ and DV search for $i \neq j$. The black striped bars show the LEP constraints for the inclusive and exclusive mono-γ plus $\not{E}$ searches, excluding values up to $\Lambda \sim 300 - 500$ GeV. No LEP bounds are shown in the case of the DV search, as the LEP results are not directly comparable. The mono-γ plus $\not{E}$ searches reach sensitivities of $\Lambda \sim 1 - 2$ TeV and $\Lambda \sim 600 - 900$ GeV for $d = 6$ and $d = 7$ νSMEFT operators, respectively. This is a significant improvement over the LEP constraints. The DV searches reach $\Lambda \sim 20 - 30$ TeV and $\Lambda \sim 3 - 5$ TeV for $d = 6$ and $d = 7$ νSMEFT operators, respectively.

5.7.3 Single HNL νSMEFT Operators at $d \leq 7$

In Fig. 5.15 we summarise the sensitivity of the FCC-ee to the νSMEFT operators inducing interactions involving a single HNL in the Majorana (left) and Dirac (right)

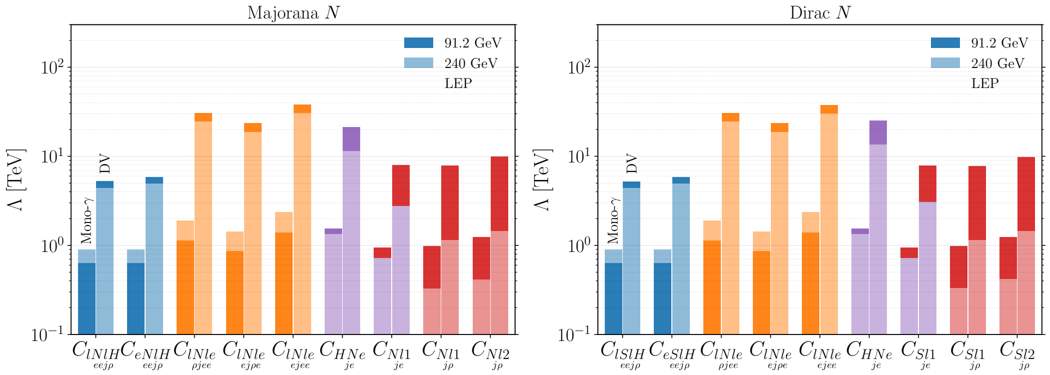

Figure 5.15: Maximum reach to the scale of new physics Λ for the $d = 6$ and $d = 7$ νSMEFT operators involving a single HNL, inducing $e^+e^- \to \nu N(\gamma)$, in the Majorana (left) and Dirac (right) scenarios. For each operator, the FCC-ee sensitivities from the mono-γ plus $\not{E}$ (left) and the DV (right) searches are shown. The LEP mono-γ plus $\not{E}$ constraints are shown as black striped bars.

case, for centre-of-mass energies $\sqrt{s} = 91.2$ GeV (darker) and $\sqrt{s} = 240$ GeV (lighter). For each operator the bounds from the mono-γ plus $\not{E}$ and DV searches are shown by the left and right bars, respectively. The existing LEP constraints are shown by the black striped bars. The mono-γ plus $\not{E}$ searches are able to reach sensitivities of $\Lambda \sim 1-2$ TeV and $\Lambda \sim 600-900$ GeV for $d = 6$ and $d = 7$ operators, respectively, while in the DV searches the lower bounds are as high as $\Lambda \sim 20-40$ TeV and $\Lambda \sim 5-10$ TeV for $d = 6$ and $d = 7$ operators, respectively. It should be noted, that due to the light neutrino in the final state, for the DV search we have used the $\delta = 1$ results from Figs. 5.11 and 5.12. In contrast, $\delta = 0.1$ was used for the summary bar chart in Fig. 5.14, which is why the reach of the search is lower in that case.

There are some νSMEFT operators, which can induce multiple effective operators after symmetry breaking. One such operator is the $d = 6$ $Q_{lNle} = (\bar{L}_\rho N_{Rj})\varepsilon(\bar{L}_\sigma e)$, which can induce both the scalar and tensor four-fermion effective low energy operators, depending on the flavours of the SU(2) doublet. For $\rho = \mu, \tau$ and $\sigma = e$, only the scalar four-fermion operator is induced, and thus the matching condition is simply $C_{\nu Ne}^{S,RR} = C_{lNle}$. Similarly, only the scalar WC is generated for $\rho = \sigma = e$, in which case the matching condition is given by $C_{\nu Ne}^{S,RR} = 3/(2\Lambda_S^2)$. The last case is $\rho = e$ and $\sigma = \mu, \tau$, which gives rise to both the scalar and tensor four-fermion interactions, with $C^{S,RR}_{\nu Ne} = 4C^{T,RR}_{\nu Ne} = C_{lNle}/2$. As before, the scalar and tensor WCs may be matched separately as $|C^{S,RR}_{\nu Ne}| = 1/(2\Lambda_S^2)$ and $|C^{T,RR}_{\nu Ne}| = 1/(8\Lambda_T^2)$ if the sensitivity is cross-section limited. Then the scale of new physics can be related to the operator coefficient as $C_{lNle} = 1/\Lambda^2$, with $\Lambda^4 = \Lambda_S^4 + \Lambda_T^4$.

Another νSMEFT operator with a more involved matching is the $d = 7$ Q_{Nl1}. This induces both effective $W^\pm$ and Z interactions in the Majorana case, with the matching condition $W_N^L = -2Z_{\nu N}^R = -v^3 C_{Nl1}/(2\sqrt{2})$. Unlike in previous cases where multiple low energy WCs were induced by a single νSMEFT operator, here the contributions are not individual and in fact the interference needs to be considered. Since for the $d = 7$ operator coefficient $C_{Nl1} = 1/\Lambda^3$ and using $|W_N^L| = v^3/(2\sqrt{2}\Lambda_W^3)$ and $|Z_{\nu N}^R| = v^3/(4\sqrt{2}\Lambda_Z^3)$, we see that the scale of new physics depends on both processes

$$\Lambda^6 = \Lambda_W^6 \left(1 - \frac{\hat{\sigma}_{WZ}}{2(\hat{\sigma}_W - \hat{\sigma}_Z)}\right) + \Lambda_Z^6 \left(1 + \frac{2\hat{\sigma}_{WZ}}{\hat{\sigma}_W - \hat{\sigma}_Z}\right). \tag{5.24}$$

where $\hat{\sigma}_W$, $\hat{\sigma}_Z$ and $\hat{\sigma}_{WZ}$ are the $W^\pm$, Z and interference mediated cross-sections for the process $e^+e^- \to \nu N(\gamma)$, respectively. Similarly, the operator Q_{Sl1} contributes to both W_N^L and $Z_{\nu N}^L$. This operator is therefore treated similarly to Q_{Nl1}.

5.7.4 SMEFT Operators at $d \leq 7$

Besides the operators inducing interactions involving one or two HNLs, SMEFT operators without any HNL content can also give rise to processes at the EW scale which generate effective operators. Depending on whether they interfere with the SM process $e^+e^- \to \nu\nu(\gamma)$, the results on the WCs $|C_i|$ need to be recast differently. Below we discuss these various operators. It should be noted, that operators involving S cannot lead to processes with $\nu\nu$ in the final state, and therefore the operators in Table 3.2 do not contribute. Since there are no HNLs, the difference between the Majorana and Dirac cases is simply the presence and lack of LNV operators, respectively. Thus, the operators Q_{llleH} and Q_{leHD} (the only operators in Table 3.1 without any N fields) vanish in the latter case and the associated results are understood to only apply in the Majorana scenario.

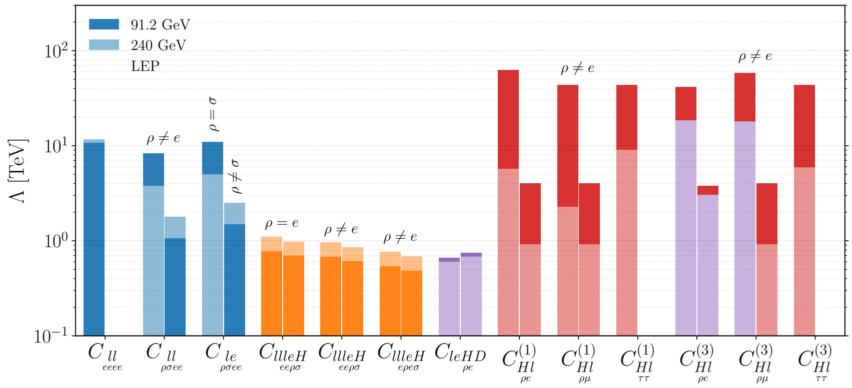

Figure 5.16: Maximum reach to the scale of new physics Λ for the $d = 6$ and $d = 7$ νSMEFT operators involving the active neutrinos, inducing $e^+e^- \to \nu\nu(\gamma)$. For each operator, the FCC-ee sensitivities from the mono-γ plus $\not{E}$ search are shown for $\rho = \sigma$ (left) and $\rho \neq \sigma$ (right). The mono-γ plus $\not{E}$ constraints from LEP are shown as black striped bars.

The maximum reach of the $d = 6$ and $d = 7$ SMEFT operators which contribute to the process $e^+e^- \to \nu\nu(\gamma)$ are shown in Fig. 5.16, again for the two centre-of-mass energies $\sqrt{s} = 91.2$ GeV (darker) and $\sqrt{s} = 240$ GeV (lighter). Since there are no HNLs that can decay to produce a DV signal, only the mono-γ plus $\not{E}$ search results are shown. As before, the existing LEP constraints are shown as black striped bars.

Starting with the $d = 6$ operators, we note that they can be separated into two groups, depending on what they induce at the EW scale: four-fermion contact operators and vertex corrections. For the former, the operators of interest are Q_{ll} and Q_{le}, which at the EW scale induce the vector four-fermion effective operators, with matching conditions of the WCs

$$C^{V,LL}_{\underset{\rho\sigma ee}{\nu e}} = C_{\underset{\rho\sigma ee}{ll}} + C_{\underset{ee\rho\sigma}{ll}} \,, \quad C^{V,LR}_{\underset{\rho\sigma ee}{\nu e}} = C_{\underset{\rho\sigma ee}{le}} \,. \tag{5.25}$$

For off-diagonal indices, i.e. $\rho \neq \sigma$, there is no interference with the SM. In the case of $\rho = \sigma$ both C_{ll} and C_{le} interfere with the SM Z exchange diagrams (due to the structure of the propagator in Eq. E.15, the interference vanishes at the Z pole). For these indices there is no interference with the SM $W^{\pm}$ exchange, as the initial and final states are not flavour matched. For the case $\rho = \sigma = e$ on the other hand, interference with the SM $W^{\pm}$ exchange occurs for C_{ll} (for C_{le} again only interference with Z exchange, since $W^{\pm}$ does not couple to RH electrons). The previous results can be recast straightforwardly using the matching relations for the cases where there is no interference with the SM. For those coefficients which do interfere, the coefficient-independent cross-sections are equated, similarly to Eq. 5.23 but now also including the interference term. Then, as before, the FCC-ee results can be recast by setting C_i to the maximum reach and solving for C_j. In the case of the LEP bounds, C_i is instead set to the maximum LEP reach.

The second class of $d = 6$ operators are those that result in vertex corrections, $Q_{Hl}^{(1)}$ and $Q_{Hl}^{(3)}$ by contributing to the Z and $W^{\pm}$ interactions with two light neutrinos. The Fermi constant is shifted by $Q_{Hl}^{(3)}$ through its contribution to the process $\mu^- \to e^- \bar{\nu}_e \nu_\mu$ which is used to determine the value of G_F, as

$$\delta G_F = \frac{1}{2\hat{G}_F}\left(C^{(3)}_{\underset{ee}{Hl}} + C^{(3)}_{\underset{\mu\mu}{Hl}}\right), \tag{5.26}$$

where $\hat{G}_F = 1.1663787 \times 10^{-5}\ \mathrm{GeV}^{-2}$ is the experimentally determined value. This in turn will also shift the deviations in Eq. 5.6 as well as the $Z - e$ couplings and the QED constant, e. The rescaling procedure therefore needs to be carried out with cross-sections that take these shifts into account. The resulting maximal sensitivities are shown in Fig. 5.16.

Finally, we discuss the $d = 7$ SMEFT operators Q_{llleH} and Q_{leHD}. These do not cause interference with the SM and therefore the matching conditions are given by

$$\begin{gathered} C^{S,LL}_{\underset{\rho\sigma ee}{\nu e}} = -\sqrt{2}v\left(C_{\underset{ee\{\rho\sigma\}}{llleH}} + \frac{1}{2}C_{\underset{e\{\rho e\sigma\}}{llleH}}\right), \quad C^{T,LL}_{\underset{\rho\sigma ee}{\nu e}} = \frac{v}{4\sqrt{2}}C_{\underset{e[\rho e\sigma]}{llleH}}, \\ \frac{2}{v^2}[W_\nu^R]_{\rho e} = -\frac{v}{\sqrt{2}}C_{\underset{\rho e}{leHD}}. \end{gathered} \tag{5.27}$$

The brackets around the indices depend on the symmetry properties. The curly brackets are around symmetric indices, while the square brackets are put around the anti-symmetric ones. As can be seen from the above matching relations, the coefficient C_{llleH} gives rise to both scalar and tensor four-fermion effective interactions after symmetry breaking. When both $C_{\nu e}^{S,LL}$ and $C_{\nu e}^{T,LL}$ are non-zero, the Λ_S and Λ_T reach of the coefficient is found individually using the above matching, and translated to the scale of new physics via $C_{llleH} = 1/\Lambda^3$, with $\Lambda^6 = \Lambda_S^6 + \Lambda_T^6$.

Chapter 6

Conclusions

Although the SM is one of the most successful theories in modern physics, it does not predict nor does it explain light neutrino masses. Sterile neutrinos – hypothetical right-handed singlets under the SM gauge group – appear in numerous extensions of the SM, as they can not only explain the origin of the light neutrino masses, but also serve as dark matter candidates or explain the baryon asymmetry of the universe. Given their ambiguity and versatility, it is essential to study sterile neutrinos in a model-independent fashion, for which the overarching framework is provided by the SM effective field theory extended with sterile neutrinos (νSMEFT). Two such approaches form the basis of this thesis. The first are single beta-decay experiments, which are the only model-independent direct probes of the absolute neutrino mass scale and potentially allow searches for keV-mass sterile neutrinos. The second is the phenomenological study of νSMEFT in the context of the FCC-ee, where the possible new interactions involving GeV-scale sterile neutrinos are parameterised by effective operators in a model-independent fashion.

In Chapter 4, the next generation of β-decay experiments employing cyclotron radiation emission spectroscopy (CRES) technology combined with the use of atomic tritium was introduced. The sensitivity of such experiments to keV-scale sterile neutrinos and sterile exotic currents was estimated. Currently, the active-sterile mixing angle in the relevant portion of the parameter space is constrained by direct β-decay searches, with upper bounds of the order $|V_{eN}|^2 \sim 10^{-2} - 10^{-3}$. Having studied the effect of the presence of a sterile neutrino on both the energy and angular spectra of the emitted electron, we conclude that CRES-type experiments have the potential to reach sensitivities of $|V_{eN}|^2 \sim 10^{-7} - 10^{-8}$ in the sterile mass range 1 keV $\lesssim m_N \lesssim$ 18 keV for a total exposure of $N_{\text{tot}} = 10^{18}$ events. Besides mixing with the SM light neutrinos, sterile states may also be produced directly via exotic charged currents with structures different from the SM $V-A$. Again, the impact of these sterile exotic currents is assessed on both the energy and angular spectra, with both sensitivities depending on the sterile mass. The constraining power is maximal for $m_N \approx 10$ keV, with maximum reach to the scale of new physics around $\Lambda \sim 50$ TeV and $\Lambda \sim 30$ TeV for the energy and angular spectra, respectively. At this mass of $m_N \approx 10$ keV, the angular spectrum is less sensitive than the energy one, as the mass of the sterile neutrino serves to wash out the angular correlations, while the distinct kink produced by the sterile neutrino in the energy spectrum results in noticeable difference compared to the SM. Therefore, future β-decay experiments have the potential to constrain such sterile exotic couplings via the electron energy spectrum, while measuring the angular correlation is still useful, as it can serve to distinguish the origin of a detected sterile neutrino.

In Chapter 5, a phenomenological analysis was performed, studying the sensitivity of the FCC-ee to the active-sterile mixing and EFT operators mediating the production and decay of GeV-scale sterile neutrinos using events simulated in `MadGraph`. The analysis of the monophoton plus missing energy (mono-γ plus $\not{E}$) and displaced vertex (DV) searches was performed for the two centre-of-mass energies of $\sqrt{s} = 91.2$ GeV ($\mathcal{L} = 100$ ab^{-1}) and $\sqrt{s} = 240$ GeV ($\mathcal{L} = 5$ ab^{-1}), considering both Dirac and Majorana sterile states. The active-sterile mixing angle was probed using the mono-γ plus $\not{E}$ search with a single Dirac HNL, in the context of both inclusive and exclusive searches. The resulting bounds for both $\sqrt{s}$ values lies almost completely within already excluded portions of the parameter space, reaching mixing values of around $|V_{eN}^2| \sim 10^{-4}$ and $|V_{eN}^2| \sim 10^{-3}$ for $\sqrt{s} = 91.2$ GeV and $\sqrt{s} = 240$ GeV, respectively. Due to the plentiful existing bounds with regards to the electron-flavour mixing, it is instructive to explore the potential sensitivity of the FCC-ee to the low-energy operators induced by νSMEFT operators with $d \leq 7$, which in general are constrained to a lesser degree. The operators of interest are those that give rise to effective four-fermion and effective Z and $W^{\pm}$ interactions. Therefore, the effective four-fermion scalar, vector and tensor and the effective Z and $W^{\pm}$ interactions were analysed in the context of double HNL production, for diagonal as well as off-diagonal couplings, also considering various mass-splittings between the two sterile states, in the limit of $V_{eN} = 0$. The resulting constraints obtained for each WC were then matched to the corresponding νSMEFT operators and the maximum reach translated to a lower bound on the scale of new physics, Λ, for the processes $e^+e^- \to NN(\gamma)$, $N\nu(\gamma)$ and $\nu\nu(\gamma)$. The results for the operators contributing to HNL pair production, i.e. the process $e^+e^- \to NN(\gamma)$, are summarised in Fig. 5.14. Of these operators, overall, sensitivity is greater to the $d = 6$ operators than the $d = 7$ ones, as the latter are suppressed by an extra power of the new physics scale in the denominator. While the mono-γ plus $\not{E}$ searches for the $d = 7$ operators Q_{elNH} and Q_{lNeH} (alongside Q_{elSNH} and Q_{lSNeH} in the Dirac case) are only around $\Lambda \sim 600 - 900$ GeV, the sensitivity of the FCC-ee to the $d = 6$ operators Q_{eN}, Q_{lN} and Q_{HN} (as well as Q_{eS}, Q_{lS} and Q_{HS} in the Dirac case) for the same search are probed with $\Lambda \sim 1 - 2$ TeV, which is a roughly 5-fold improvement over the existing LEP bounds. The difference in sensitivity is even larger for the DV results. While these searches are able to place lower bounds around $\Lambda \sim 20 - 30$ TeV for the same $d = 6$ operators, in the case of the $d = 7$ ones this range is only $\Lambda \sim 3 - 5$ TeV. The results for the operators contributing to the single production of HNLs, i.e. the process $e^+e^- \to N\nu(\gamma)$, summarised in Fig. 5.15, follow a similar pattern. While the mono-γ plus $\not{E}$ (DV) searches for the $d = 7$ operators probe $\Lambda \sim 600 - 900$ GeV ($\Lambda \sim 5 - 10$ TeV), for the $d = 6$ operators they reach $\Lambda \sim 1 - 2$ TeV ($\Lambda \sim 20 - 40$ TeV). For the former, this is again a four- or five-fold improvement over the existing LEP bounds, while for the latter it would set the first bounds in the yet unconstrained parameter space. Lastly, there are the operators contributing to the pair production of light neutrinos, i.e. $e^+e^- \to \nu\nu(\gamma)$, for which the results are summarised in Fig. 5.16. Those operators which interfere with the SM process result in enhanced sensitivities, probing operators $Q_{Hl}^{(1)}$ and

$Q_{Hl}^{(3)}$, up to $\Lambda \sim 40 - 60$ TeV. Those operators without SM interference, Q_{llleH} and Q_{leHD}, have considerably lower reaches of $\Lambda \sim 0.6 - 1$ TeV. Both the interfering and non-interfering operators have the potential to be probed at the level beyond current exclusions.

This thesis has attempted to show that the next generation of experiments will have great potential to probe new physics in the neutrino sector. CRES-type tritium beta-decay experiments being developed currently are expected not only to measure the absolute neutrino mass and determine the mass ordering, but also to push into unexplored territory by constraining keV-scale sterile neutrinos and exotic charged-current interactions. Dedicated searches such as TRISTAN [179], the planned KATRIN extension, will directly search for sterile neutrinos in the keV range, while KATRIN itself is well suited to look for light sterile states in the eV mass range [289]. At the high-energy frontier, the post-LHC era will likely be defined by the FCC, operating with unprecedented precision and energies. The potential of this future collider cannot be overstated, not only with respect to the neutrino sector, but the entirety of particle physics. The FCC will be able to perform precision measurements, constrain parameters as well as probe new physics, such as the model-independent EFT operators involving GeV-mass sterile neutrinos discussed here.

Despite its remarkable success, the SM leaves fundamental questions unanswered, many of which are rooted in the elusive nature of neutrinos. With a broad, multi-front experimental program — from oscillation and reactor experiments to colliders, direct kinematic searches, and cosmological and astrophysical observations — neutrino physics now stands at the threshold of a new era, one that could both complete our understanding of the known neutrino sector and perhaps reveal the first clear glimpses of new physics through its study. Exactly what exotic physics lurks beyond the SM is unknown, but it is certain that neutrinos will play an exciting and instrumental role in propelling particle physics into the realm of new physics.

Appendix A

Pedagogical Single Generation Type I Seesaw

In the Type I seesaw model, three generations of right-handed 'sterile' neutrino singlets are added to the SM. These states are completely uncharged under the SM gauge group and therefore do not participate directly in any interactions, hence their name. Similarly to the simple Dirac approach, this will also result in the usual Dirac mass coupling the left- and right-chiral light neutrino components, however, in this case the sterile neutrinos are given a Majorana mass term. Doing so results in the Lagrangian

$$\mathcal{L}_{\text{Seesaw I}} = \mathcal{L}_{\text{SM}} - \sum_{ij} y^{\nu}_{ij} \bar{L}^i \tilde{\Phi} \nu^j_R + \frac{1}{2} \sum_{ij} M_{ij} \nu^{i,T}_R C \nu^j_R + \text{h.c.} \tag{A.1}$$

where $i, j = 1, 2, 3$ are the indices iterating over the three generations of SM lepton doublets and right-handed sterile neutrinos and M_{ij} is a 3×3 Majorana mass matrix for the sterile neutrinos. After symmetry breaking occurs, the seesaw contribution to the Lagrangian becomes

$$\mathcal{L}_{\text{Seesaw I}} = -\sum_{ij} m^{ij}_D \bar{\nu}^i_L \nu^j_R + \frac{1}{2} \sum_{ij} M_{ij} \nu^{i,T}_R C \nu^j_R + \text{h.c.}, \tag{A.2}$$

which can be expressed as

$$\mathcal{L}_{\text{Seesaw I}} = n^T_L \; \mathcal{M} \; C \;\; n_L \tag{A.3}$$

where we have defined the vector

$$n_L = \begin{pmatrix} \nu_L^i \\ \nu_R^{j,c} \end{pmatrix} \tag{A.4}$$

and the 6×6 mass matrix, $\mathcal{M}$, in block form is

$$\mathcal{M} = \begin{pmatrix} 0 & m_D \\ (m_D)^T & M \end{pmatrix} \tag{A.5}$$

i.e. m_D and M are 3×3 Dirac and Majorana mass matrices, respectively and the zero entry is in fact a 3×3 matrix containing only zeroes. As before, the next point of business is to find the mass eigenstates by diagonalising the mass matrix. Since the dimensions of $\mathcal{M}$ means that there will be six mass states in total, it is more instructive to focus on the two neutrino scenario where the particle content solely consists of ν_L and ν_R, i.e. one active SM neutrino and one sterile neutrino. Then the diagonalisation requirement is

$$U^T \, \mathcal{M} \, U = \mathcal{M}' \tag{A.6}$$

where $\mathcal{M}'$ is the diagonalised matrix containing the masses

$$\mathcal{M}' = \begin{pmatrix} m_\nu & 0 \\ 0 & m_N \end{pmatrix}. \tag{A.7}$$

The elements of this matrix have been labelled in anticipation of the neutrino content for each mass, with ν denoting the active light SM neutrino and N the sterile state. To this end, we consider U to be a two-dimensional rotation matrix

$$U = \begin{pmatrix} \cos\theta & -\sin\theta \\ \sin\theta & \cos\theta \end{pmatrix} \tag{A.8}$$

which can be used together with its transpose, as shown in Eq. A.6 and the method of block diagonalisation to find the matrix $\mathcal{M}'$, which is approximately diagonal in the limit $M \gg m_D$, known as the seesaw limit. Solving the characteristic equation leads to the general mass eigenvalues

$$m_\nu = \frac{1}{2}\left(M - \sqrt{M^2 + 4m_D^2}\right), \quad m_N = \frac{1}{2}\left(M + \sqrt{M^2 + 4m_D^2}\right) \tag{A.9}$$

which in the seesaw limit after a perturbative expansion in $\frac{m_D}{M}$ becomes

$$m_\nu \approx -\frac{m_D^2}{M}, \quad m_N \approx M + \frac{m_D^2}{M} \tag{A.10}$$

to first order in the expansion. Thus we see the appeal of this mass generation mechanism: since m_ν and m_N are inversely proportional, the light neutrino masses are naturally explained by a heavy Majorana mass for the right-handed neutrino. If the Yukawa couplings are of order one and $M \sim 10^{14}$ GeV, the resulting light masses are $m_\nu \sim 0.1$ eV, consistent with experimental constraints.

In the one neutrino generation case and working in the small-angle approximation ($\cos\theta \approx 1$ and $\sin\theta \approx \theta$) the flavour eigenstates appearing in the Lagrangian can be related to the mass eigenstates, ν and N for the light SM and sterile neutrinos respectively, via the matrix U, yielding the relations

$$\begin{aligned} \nu_L &= \cos\theta\nu - \sin\theta N \approx \nu - \theta N \\ \nu_R &= \sin\theta\nu + \cos\theta N \approx N + \theta\nu. \end{aligned} \tag{A.11}$$

It is very interesting to note that the interaction eigenstate ν_L in fact contains a small sterile components, while ν_R is in fact not completely sterile, as it can couple to the SM via its small ν content. Although the admixtures are present, it should be noted that they are suppressed by the mixing angle θ, which in the seesaw limit assuming the same values as before is around $\theta \approx 10^{-12}$. Furthermore, a major consequence of this mechanism is that while the left- and right-chiral components are coupled by the Dirac mass, m_D, the resulting mostly active SM-like mass state, ν in fact acquires a small but non-zero Majorana mass, m_ν, as can be seen in Eq. A.10.

Appendix B

Continuum and Excited State Emission in Tritium β-Decay

Beta-decay neutrino mass measurements rely on precise knowledge about the endpoint of the β particle distribution and therefore its energy. It is thus crucial to take into account the fact that the orbital electron of the tritium is in principle indistinguishable from the outgoing β electron, meaning that quantum mechanical exchange between the two electrons may cause the originally emitted β particle to become orbitally bound, while the daughter electron ends up in the continuum. Table 4.2 shows the energy gaps separating the different excited states available to the atomic electron alongside the associated branching ratios (transition probabilities). Also shown are the population probabilities for each energy level in the zeroth order sudden approximation [1]

Therefore, the full decay rate needs to be a sum over the decay rates to each excited state and the continuum, where each of the constituent rates has its own shifted endpoint. This is done by shifting the effective masses for the tritium and

---

[1] For a rapidly changing Hamiltonian, i.e. $t_2 - t_1 \sim 0$, $\langle b|U(t_2,t_1)|a\rangle \approx \langle b|a\rangle$, where $U(t_2,t_1)$ is some transition function depending on time t_1 and a later time t_2. Hence, the transition probability is $|\langle b|U(t_2,t_1)|a\rangle|^2 \sim |\langle b||a\rangle|^2$.

helium by including the electron and its binding or kinetic energy,

$$E_e^{\max} \to \begin{cases} E_e^{\max}(n),\ m_{\mathrm{H}} \to m_{\mathrm{H}} - R_h,\ m_{\mathrm{He}} \to m_{\mathrm{He}} + m_e - 4R_h/n^2, & n = 1,2,3,\ldots, \\ E_e^{\max}(\tau),\ m_{\mathrm{H}} \to m_{\mathrm{H}} - R_h,\ m_{\mathrm{He}} \to m_{\mathrm{He}} + m_e + 4R_h/\tau^2, & \tau = -2\alpha/k, \end{cases} \tag{B.1}$$

where $R_h = 13.61$ eV is the Rydberg energy [290] and with the top case being to a helium bound state and the bottom being to the continuum. Combining these terms with the appropriate weightings gives the full decay rate over all possible bound and continuum helium final states [291],

$$\begin{aligned} \frac{d\Gamma_{\text{full}}}{dE_e} = & \sum_{n=1}^{\infty} 2\frac{d\Gamma}{dE_e}(E_e^{\max}(n)) \left[256n^5 \frac{(n-2)^{2n-4}}{(n+2)^{2n+4}} + \frac{\alpha^2(\tau)}{n^3} - 16n\frac{(n-2)^{n-2}}{(n+2)^{n+2}}\alpha(\tau)\right] \\ & + \frac{1}{\pi}\int_{-\infty}^{\tau} \frac{d\tau'}{\tau'^4} \frac{d\Gamma}{dE_e}(E_e^{\max}(\tau')) \frac{2\pi\tau'}{e^{2\pi\tau'}-1} \left[\alpha^2(\tau) - \alpha(\tau)\alpha(\tau') + \alpha^2(\tau')\right], \end{aligned} \tag{B.2}$$

where

$$a(\tau) = \exp\left[2\tau \arctan\left(-\frac{2}{\tau}\right)\right]\left(\frac{\tau^2}{1+\frac{1}{4}\tau^2}\right)^2, \tag{B.3}$$

and $\tau = -2\alpha/k$. In the first line of the expression above a sum is performed over the bound energy levels available to the electron, while the second line is responsible for integrating over the continuum energies for an electron that escapes.

Appendix C

Full Analytic Expressions for Tritium Differential Decay Rate

Below the individual sterile exotic contributions $a_X(E_e)$ and $b_X(E_e)$ to $a(E_e)$ and $b(E_e)$ are presented alongside the interference terms. In the expressions, y_N is given by Eq. 4.24 with the replacement $m_\nu \to m_N$ in Eq. 4.25, $\widetilde{y_N}$ is given by Eq. 4.39 with $y_i \to y_N$ and $m_\nu \to m_N$ and $\mu_N = (m_N + m_{\mathrm{He}})/m_{\mathrm{H}}$.

C.1 Individual SM and Exotic Contributions

Vector Currents *LL*, *RR*, *RL*, *LR* The SM contribution (LL) is related to that of $\tilde{\varepsilon}_R^N$ (RR) by using $\gamma_5 \to -\gamma_5$ (and $S \to -S$). This has the same energy distribution and reverse angular correlation,

$$\begin{aligned}
a_{LL}(E_e) &= a_{RR}(E_e) \\
&= \widetilde{C}(E_e)\frac{m_{\mathrm{H}}^2|\vec{p}_e|}{m_{12}^2}\widetilde{y_N} \\
&\times\Bigg\{(g_V+g_A)^2\left[\frac{m_{\mathrm{H}}(m_{\mathrm{H}}-E_e)}{m_{12}^2}\frac{m_{\mathrm{H}}E_e-m_e^2}{m_{12}^2}(y_N+\mu_N m_N)(y_N+\mu_N m_{\mathrm{He}})-\frac{m_{\mathrm{H}}^2|\vec{p}_e|^2}{3m_{12}^4}\widetilde{y_N}^2\right] \\
&\quad+(g_V-g_A)^2E_e\left(y_N+m_N\frac{m_{\mathrm{He}}}{m_{\mathrm{H}}}\right)+(g_A^2-g_V^2)m_{\mathrm{He}}\frac{m_{\mathrm{H}}E_e-m_e^2}{m_{12}^2}(y_N+\mu_N m_N)\Bigg\},
\end{aligned} \tag{C.1}$$

$$\begin{aligned}
b_{LL}(E_e) &= -b_{RR}(E_e) \\
&= -\widetilde{C}(E_e)\frac{m_{\mathrm{H}}}{m_{12}^2}|\vec{p}_e|^2\widetilde{y_N} \\
&\times\Bigg\{\Bigg[(g_A-g_V)^2m_{\mathrm{H}}+(g_A^2-g_V^2)m_{\mathrm{He}}\frac{m_{\mathrm{H}}(m_{\mathrm{H}}-E_e)}{m_{12}^2} \\
&\quad+(g_A^2-g_V^2)\frac{m_{\mathrm{H}}m_{\mathrm{He}}}{m_{12}^2}E_e+(g_A+g_V)^2\frac{m_{\mathrm{H}}}{m_{12}^2}(\alpha-m_e^2) \\
&\quad-(g_A+g_V)^2\frac{m_{\mathrm{H}}^2}{m_{12}^2}(y_N+\mu_N m_N)\frac{m_{\mathrm{H}}(m_{\mathrm{H}}-E_e)}{m_{12}^2}\Bigg](y_N+\mu_N m_N) \\
&\quad-(g_A-g_V)^2m_N^2-\frac{1}{3}(g_A+g_V)^2\frac{m_{\mathrm{H}}^3(m_{\mathrm{H}}-E_e)}{m_{12}^4}\widetilde{y_N}^2\Bigg\}.
\end{aligned} \tag{C.2}$$

The contributions related to $\tilde{\varepsilon}_L^N$ (LR) and ε_R^N (RL) can be obtained from the SM (LL) terms by applying $g_A \to -g_A$ with an additional $S \to -S$ for the right-handed lepton term,

$$a_{LR}(E_e) = a_{RL}(E_e) = a_{LL}(E_e)(g_A \to -g_A), \tag{C.3}$$

$$b_{LR}(E_e) = -b_{RL}(E_e) = -b_{LL}(E_e)(g_A \to -g_A). \tag{C.4}$$

Scalar Currents

$$\begin{aligned} a_S(E_e) = a_{\tilde{S}}(E_e) &= \frac{1}{2} g_S^2 \widetilde{C}(E_e) \frac{m_{\mathrm{H}}^2 |\vec{p}_e|}{m_{12}^2} \widetilde{y_N} \\ &\times \left\{ (m_{\mathrm{He}} + m_{\mathrm{H}} - E_e) \frac{m_{\mathrm{H}} E_e - m_e^2}{m_{12}^2} (y_N + \mu_N m_N) - \frac{1}{3} \frac{m_{\mathrm{H}}^2 |\vec{p}_e|^2}{m_{12}^4} \widetilde{y_N}^2 \right. \\ &\left. - \frac{m_{\mathrm{H}}(m_{\mathrm{H}} - E_e)}{m_{12}^2} \frac{m_{\mathrm{H}} E_e - m_e^2}{m_{12}^2} (y_N + \mu_N m_N)^2 \right\}, \end{aligned} \tag{C.5}$$

$$b_S(E_e) = b_{\tilde{S}}(E_e) = 0. \tag{C.6}$$

Pseudoscalar Currents

$$\begin{aligned} a_P(E_e) = a_{\tilde{P}}(E_e) &= \frac{1}{2} g_P^2 \widetilde{C}(E_e) \frac{m_{\mathrm{H}}^2 |\vec{p}_e|}{m_{12}^2} \widetilde{y_N} \\ &\times \left\{ -(m_{\mathrm{He}} - m_{\mathrm{H}} + E_e) \frac{m_{\mathrm{H}} E_e - m_e^2}{m_{12}^2} (y_N + \mu_N m_N) - \frac{1}{3} \frac{m_{\mathrm{H}}^2 |\vec{p}_e|^2}{m_{12}^4} \widetilde{y_N}^2 \right. \\ &\left. - \frac{m_{\mathrm{H}}(m_{\mathrm{H}} - E_e)}{m_{12}^2} \frac{m_{\mathrm{H}} E_e - m_e^2}{m_{12}^2} (y_N + \mu_N m_N)^2 \right\}, \end{aligned} \tag{C.7}$$

$$b_P(E_e) = b_{\tilde{P}}(E_e) = 0. \tag{C.8}$$

Tensor Currents

$$\begin{aligned} a_T(E_e) &= a_{\tilde{T}}(E_e) = \\ &= 16 \widetilde{C}(E_e) g_T^2 \frac{m_{\mathrm{H}}^2 |\vec{p}_e|}{m_{12}^2} \widetilde{y_N} \left[\frac{m_{\mathrm{H}}(m_{\mathrm{H}} - E_e)}{m_{12}^2} \frac{m_{\mathrm{H}} E_e - m_e^2}{m_{12}^2} (y_N + \mu_N m_N)(3 y_N + 2 \mu_N m_{\mathrm{He}} + \mu_N m_N) \right. \\ &\left. - \frac{1}{3} \frac{m_{\mathrm{H}}^2 |\vec{p}_e|^2}{m_{12}^4} \widetilde{y_N}^2 + 2 E_e \left(y_N + m_N \frac{m_{\mathrm{He}}}{m_{\mathrm{H}}} \right) - 2 (m_{\mathrm{H}} - E_e)(y_N + \mu_N m_N) \frac{m_{\mathrm{H}} E_e - m_e^2}{m_{12}^2} \right], \end{aligned} \tag{C.9}$$

$$\begin{aligned} b_T(E_e) &= -b_{\tilde{T}}(E_e) \\ &= 16 \widetilde{C}(E_e) g_T^2 \frac{m_{\mathrm{H}}^2}{m_{12}^2} |\vec{p}_e|^2 \widetilde{y_N} \left[\frac{1}{3} \frac{m_{\mathrm{H}}(m_{\mathrm{H}} - E_e)}{m_{12}^2} \frac{m_{\mathrm{H}} |\vec{p}_e|}{m_{12}^2} \widetilde{y_N} \right. \\ &\left. + \left(2 + \frac{m_{\mathrm{H}} E_e - m_e^2}{m_{12}^4} m_{\mathrm{H}} (y_N + \mu_N m_N) - \frac{m_{\mathrm{H}} E_e}{m_{12}^2} - \frac{2 m_N^2}{m_{\mathrm{H}} |\vec{p}_e|} \right) (y_N + \mu_N m_N) \right]. \end{aligned} \tag{C.10}$$

C.2 Interference Terms

Vector Currents: (LL) **with** (LR)

$$\begin{aligned} a_{LL,LR}(E_e) = \widetilde{C}(E_e) m_e m_\nu \frac{m_{\mathrm{H}}|\vec{p}_e|}{m_{12}^2}\widetilde{y}\bigg[& 2(g_A^2 - g_V^2)m_{\mathrm{He}} + (g_A^2+g_V^2)(m_{\mathrm{H}} - E_e) \\ & -(g_A^2+g_V^2)\frac{m_{\mathrm{H}}(m_{\mathrm{H}}-E_e)}{m_{12}^2}(y+\mu m_\nu)\bigg], \end{aligned} \tag{C.11}$$

$$b_{LL,LR}(E_e) = -\widetilde{C}(E_e) g_A g_V m_e m_\nu |\vec{p}_e|^2 \frac{m_{\mathrm{H}}}{m_{12}^2}\widetilde{y}\left[1 - \frac{m_{\mathrm{H}}}{m_{12}^2}(y+\mu m_\nu)\right]. \tag{C.12}$$

Vector Currents: (LL) **with** (RL)

$$\begin{aligned} a_{LL,RL}(E_e) = & -\widetilde{C}(E_e)\frac{m_{\mathrm{H}}|\vec{p}_e|}{m_{12}^2}\widetilde{y} \\ & \times\Bigg\{(g_A^2-g_V^2)\left[\frac{m_{\mathrm{H}}(m_{\mathrm{H}}-E_e)}{m_{12}^2}\frac{m_{\mathrm{H}}E_e-m_e^2}{m_{12}^2}(y+\mu m_\nu)(y+\mu m_{\mathrm{He}}) - \frac{m_{\mathrm{H}}^2|\vec{p}_e|^2}{3m_{12}^4}\widetilde{y}^2\right] \\ & +(g_A^2-g_V^2)E_e\left(y m_\nu \frac{m_{\mathrm{He}}}{m_{\mathrm{H}}}\right) + (g_A^2+g_V^2)m_{\mathrm{He}}\left(\frac{m_{\mathrm{H}}E_e-m_e^2}{m_{12}^2}(y+\mu m_\nu)\right)\Bigg\}, \end{aligned} \tag{C.13}$$

$$\begin{aligned} b_{LL,RL}(E_e) = & -\widetilde{C}(E_e)\frac{m_{\mathrm{H}}}{m_{12}^2}|\vec{p}_e|^2\widetilde{y} \\ & \times\Bigg\{\bigg[(g_A^2-g_V^2)m_{\mathrm{H}} + (g_A^2+g_V^2)m_{\mathrm{He}}\frac{m_{\mathrm{H}}(m_{\mathrm{H}}-E_e)}{m_{12}^2} + (g_A^2+g_V^2)\frac{m_{\mathrm{H}}m_{\mathrm{He}}}{m_{12}^2}E_e \\ & +(g_A^2-g_V^2)\frac{m_{\mathrm{H}}}{m_{12}^2}(\alpha-m_e^2) - (g_A^2-g_V^2)\frac{m_{\mathrm{H}}^2}{m_{12}^2}(y+\mu m_\nu)\frac{m_{\mathrm{H}}(m_{\mathrm{H}}-E_e)}{m_{12}^2}\bigg](y+\mu m_\nu) \\ & -(g_A^2-g_V^2)m_\nu^2 - \frac{1}{3}(g_A^2-g_V^2)\frac{m_{\mathrm{H}}^3(m_{\mathrm{H}}-E_e)}{m_{12}^4}\widetilde{y}^2\Bigg\}. \end{aligned} \tag{C.14}$$

Vector Currents: (LL) **with** (RR)

$$\begin{aligned} a_{LL,RR}(E_e) = -\widetilde{C}(E_e) m_e m_\nu \frac{m_{\mathrm{H}}^2|\vec{p}_e|}{m_{12}^2}\widetilde{y}\bigg[& (2(g_A^2+g_V^2)m_{\mathrm{He}} + (g_A^2-g_V^2)(m_{\mathrm{H}}-E_e) \\ & -(g_A^2-g_V^2)\frac{m_{\mathrm{H}}(m_{\mathrm{H}}-E_e)}{m_{12}^2}(y+\mu m_\nu)\bigg], \end{aligned} \tag{C.15}$$

$$b_{LL,RR}(E_e) = 0. \tag{C.16}$$

LL with Left-handed Scalar Current

$$\begin{aligned} a_{LL,S}(E_e) &= \widetilde{C}(E_e) g_S g_V m_e \frac{m_{\mathrm{H}}|\vec{p}_e|}{m_{12}^2}\widetilde{y} \\ &\quad \times \left[m_{\mathrm{H}} \left(1 + \frac{m_{\mathrm{He}}(m_{\mathrm{H}} - E_e)}{m_{12}^2} \right) (y + \mu m_\nu) - m_\nu^2 \right], \end{aligned} \tag{C.17}$$

$$b_{LL,S}(E_e) = -\widetilde{C}(E_e) g_S g_A m_e m_{\mathrm{He}} \frac{m_{\mathrm{H}}^2}{m_{12}^2} \frac{|\vec{p}_e|^2}{m_{12}^2} \widetilde{y}(y + \mu m_\nu). \tag{C.18}$$

LL with Right-handed Scalar Current

$$\begin{aligned} a_{LL,\tilde{S}}(E_e) &= -\widetilde{C}(E_e) g_S g_V m_\nu \frac{m_{\mathrm{H}}|\vec{p}_e|}{m_{12}^2}\widetilde{y} \\ &\quad \times \left[(m_{\mathrm{H}} + m_{\mathrm{He}}) E_e - m_e^2 - m_{\mathrm{H}} \frac{m_{\mathrm{H}} E_e - m_e^2}{m_{12}^2} (y + \mu m_\nu) \right], \end{aligned} \tag{C.19}$$

$$b_{LL,\tilde{S}}(E_e) = -\widetilde{C}(E_e) g_S g_A m_\nu M \frac{|\vec{p}_e|^2}{m_{12}^2} \widetilde{y} \left[\frac{m_{\mathrm{H}}^2}{m_{12}^2} (y + \mu m_\nu) - (m_{\mathrm{H}} + m_{\mathrm{He}}) \right]. \tag{C.20}$$

LL with Left-handed Pseudoscalar Current

$$\begin{aligned} a_{LL,P}(E_e) &= \widetilde{C}(E_e) g_P g_A m_e \frac{m_{\mathrm{H}}|\vec{p}_e|}{m_{12}^2}\widetilde{y} \\ &\quad \times \left[m_{\mathrm{H}} \left(\frac{m_{\mathrm{He}}(m_{\mathrm{H}} - E_e)}{m_{12}^2} - 1 \right) (y + \mu m_\nu) + m_\nu^2 \right], \end{aligned} \tag{C.21}$$

$$b_{LL,P}(E_e) = -\widetilde{C}(E_e) g_P g_V m_e m_{\mathrm{He}} \frac{m_{\mathrm{H}}^2}{m_{12}^2} \frac{|\vec{p}_e|^2}{m_{12}^2} \widetilde{y}(y + \mu m_\nu). \tag{C.22}$$

LL with Right-handed Pseudoscalar Current

$$\begin{aligned} a_{LL,\tilde{P}}(E_e) &= \widetilde{C}(E_e) g_P g_A m_\nu \frac{m_{\mathrm{H}}|\vec{p}_e|}{m_{12}^2}\widetilde{y} \\ &\quad \times \left[(m_{\mathrm{H}} - m_{\mathrm{He}}) E_e - m_e^2 - m_{\mathrm{H}} \frac{m_{\mathrm{He}} E_e - m_e^2}{m_{12}^2} (y + \mu m_\nu) \right], \end{aligned} \tag{C.23}$$

$$b_{LL,\tilde{P}}(E_e) = \widetilde{C}(E_e) g_P g_V m_\nu m_{\mathrm{H}} \frac{|\vec{p}_e|^2}{m_{12}^2} \widetilde{y} \left[\frac{m_{\mathrm{H}}^2}{m_{12}^2} (y + \mu m_\nu) - (m_{\mathrm{H}} - m_{\mathrm{He}}) \right]. \tag{C.24}$$

LL with Left-handed Tensor Current

$$
\begin{aligned}
a_{LL,T}(E_e) = {} & -12\widetilde{C}(E_e) g_T m_e \frac{m_{\mathrm{H}}|\vec{p}_e|}{m_{12}^2}\widetilde{y} \\
& \times \left[m_{\mathrm{H}} \left((g_A + g_V) \frac{m_{\mathrm{He}}(m_{\mathrm{H}} - E_e)}{m_{12}^2} + (g_A - g_V) \right) (y + \mu m_\nu) - (g_A - g_V) m_\nu^2 \right],
\end{aligned} \tag{C.25}
$$

$$
b_{LL,T}(E_e) = 12\widetilde{C}(E_e) g_T (g_A + g_V) m_e m_{\mathrm{He}} \frac{m_{\mathrm{H}}^2}{m_{12}^2} \frac{|\vec{p}_e|^2}{m_{12}^2} \widetilde{y}(y + \mu m_\nu). \tag{C.26}
$$

LL with Right-handed Tensor Current

$$
\begin{aligned}
a_{LL,\tilde{T}}(E_e) = {} & 12\widetilde{C}(E_e) g_T m_\nu \frac{m_{\mathrm{H}}|\vec{\vec{p}}_e|}{m_{12}^2}\widetilde{y} \\
& \times \left[(g_A + g_V) \left(m_{\mathrm{H}} E_e - m_e^2 - m_{\mathrm{H}} \frac{m_{\mathrm{H}} E_e - m_e^2}{m_{12}^2} (y + \mu m_\nu) \right) + (g_A - g_V) m_{\mathrm{He}} E_e \right],
\end{aligned} \tag{C.27}
$$

$$
\begin{aligned}
b_{LL,\tilde{T}}(E_e) = {} & 4\widetilde{C}(E_e) g_T m_\nu m_{\mathrm{H}} \frac{|\vec{p}_e|^2}{m_{12}^2}\widetilde{y} \\
& \times \left[3(g_A - g_V) m_{\mathrm{He}} + (g_A + g_V) m_{\mathrm{H}} - (g_A + g_V) \frac{m_{\mathrm{H}}^2}{m_{12}^2} (y + \mu m_\nu) \right].
\end{aligned} \tag{C.28}
$$

Appendix D

Operator Matching

In the analysis, the WCs of the EFT operators at the EW scale, $\mathcal{O}_i$ were constrained. These need to matched onto the νSMEFT operators Q_i in Tables 3.1 and 3.2. The relevant matching conditions for the four-fermion effective operators in Eqs. 3.105 and 3.108 are given in Table D.1. The matching conditions for the effective $W^{\pm}$ and Z interactions in Eqs. 3.106 and 3.109 are given in Table D.2.

Vector Four-Fermion Operators

Operator	Coefficient	Parameters		Matching ($X=R,L$)
		Total	CP-even	
$\mathcal{O}^{V,LX}_{\nu e}$	$\underset{prst}{C^{V,LX}_{\nu e}}$	$n_\nu^2 n_e^2$	$\frac{1}{2}n_\nu n_e(n_\nu n_e+1)$	$\underset{prst}{C_{le}}\ ,\ \underset{prst}{C_{ll}}+\underset{stpr}{C_{ll}}$
$\mathcal{O}^{V,RX}_{\nu Ne}+\text{h.c.}$	$\underset{prst}{C^{V,RX}_{\nu Ne}}$	$2n_\nu n_s n_e^2$	$n_\nu n_s n_e^2$	$-\frac{v}{\sqrt{2}}\underset{strp}{C_{eNlH}}\ ,\ -\frac{v}{\sqrt{2}}\underset{strp}{C_{lNlH}}$
$\mathcal{O}^{V,RX}_{Ne}$	$\underset{prst}{C^{V,RX}_{Ne}}$	$n_s^2 n_e^2$	$\frac{1}{2}n_s n_e(n_s n_e+1)$	$\underset{stpr}{C_{eN}}\ ,\ \underset{stpr}{C_{lN}}$
$\mathcal{O}^{V,LX}_{\nu Se}+\text{h.c.}$	$\underset{prst}{C^{V,LX}_{\nu Se}}$	$2n_\nu n_s n_e^2$	$n_\nu n_s n_e^2$	$\frac{v}{\sqrt{2}}\underset{tsrp}{C^{*}_{eSlH}}\ ,\ \frac{v}{\sqrt{2}}\underset{tsrp}{C^{*}_{lSlH}}$
$\mathcal{O}^{V,LX}_{Se}$	$\underset{prst}{C^{V,LX}_{Se}}$	$n_s^2 n_e^2$	$\frac{1}{2}n_s n_e\big(n_s n_e+1\big)$	$\underset{stpr}{C_{eS}}\ ,\ \underset{stpr}{C_{lS}}$

Scalar Four-Fermion Operators (+ h.c.)

Operator	Coefficient	Parameters		Matching ($X=R,L$)
		Total	CP-even	
$\mathcal{O}^{S,LX}_{\nu e}$	$\frac{1}{2}\underset{prst}{C^{S,LX}_{\nu e}}$	$n_\nu(n_\nu+1)n_e^2$	$\frac{1}{2}n_\nu(n_\nu+1)n_e^2$	$0\ ,\ -\frac{v}{\sqrt{2}}\big(\underset{st\{pr\}}{C_{llleH}}+\frac{1}{2}\underset{s\{ptr\}}{C_{llleH}}\big)$
$\mathcal{O}^{S,RX}_{\nu Ne}$	$\underset{prst}{C^{S,RX}_{\nu Ne}}$	$2n_\nu n_s n_e^2$	$n_\nu n_s n_e^2$	$\underset{prst}{C_{lNle}}+\frac{1}{2}\underset{srpt}{C_{lNle}}\ ,\ 0$
$\mathcal{O}^{S,RX}_{Ne}$	$\frac{1}{2}\underset{prst}{C^{S,RX}_{Ne}}$	$n_s(n_s+1)n_e^2$	$\frac{1}{2}n_s(n_s+1)n_e^2$	$-\frac{v}{2\sqrt{2}}\underset{s\{pr\}t}{C_{lNeH}}\ ,\ \frac{v}{\sqrt{2}}\underset{stpr}{C_{elNH}}$
$\mathcal{O}^{S,RX}_{SNe}$	$\underset{prst}{C^{S,RX}_{SNe}}$	$2n_\nu n_s n_e^2$	$n_\nu n_s n_e^2$	$-\frac{v}{2\sqrt{2}}\underset{sprt}{C_{lSNeH}}\ ,\ \frac{v}{\sqrt{2}}\underset{stpr}{C_{elSNH}}$

Tensor Four-Fermion Operators (+ h.c.)

Operator	Coefficient	Parameters		Matching
		Total	CP-even	
$\mathcal{O}^{T,LL}_{\nu e}$	$\frac{1}{2}\underset{prst}{C^{T,LL}_{\nu e}}$	$n_\nu(n_\nu-1)n_e^2$	$\frac{1}{2}n_\nu(n_\nu-1)n_e^2$	$\frac{v}{8\sqrt{2}}\underset{s[ptr]}{C_{llleH}}$
$\mathcal{O}^{T,RR}_{\nu Ne}$	$\underset{prst}{C^{T,RR}_{\nu Ne}}$	$2n_\nu n_s n_e^2$	$n_\nu n_s n_e^2$	$\frac{1}{8}\underset{srpt}{C_{lNle}}$
$\mathcal{O}^{T,RR}_{Ne}$	$\frac{1}{2}\underset{prst}{C^{T,RR}_{Ne}}$	$n_s(n_s-1)n_e^2$	$\frac{1}{2}n_s(n_s-1)n_e^2$	$\frac{v}{8\sqrt{2}}\underset{s[pr]t}{C_{lNeH}}$
$\mathcal{O}^{T,RR}_{SNe}$	$\underset{prst}{C^{T,RR}_{SNe}}$	$2n_\nu n_s n_e^2$	$n_\nu n_s n_e^2$	$-\frac{v}{8\sqrt{2}}\underset{sprt}{C_{lSNeH}}$

Table D.1: Matching between the vector (top), scalar (centre) and tensor (bottom) four-fermion interactions and the $d \leq 7$ νSMEFT operators.

Effective $W^{\pm}$ Interactions (+ h.c.)

Operator	Coefficient	Parameters		Matching
		Total	CP-even	
$\mathcal{O}^L_{\nu eW}$, $\mathcal{O}^R_{\nu eW}$	$[W^L_\nu]_{pr}$, $[W^R_\nu]_{pr}$	$2n_\nu n_e$	$n_\nu n_e$	$\delta_{pr} + v^2 C^{(3)}_{\underset{pr}{Hl}}$, $-\frac{v^3}{2\sqrt{2}} C_{\underset{pr}{leHD}}$
$\mathcal{O}^R_{NeW}$, $\mathcal{O}^L_{NeW}$	$[W^R_N]_{pr}$, $[W^L_N]_{pr}$	$2n_s n_e$	$n_s n_e$	$\frac{v^2}{2} C_{\underset{pr}{HNe}}$, $-\frac{v^3}{2\sqrt{2}} C_{\underset{pr}{Nl1}}$
$\mathcal{O}^L_{SeW}$	$[W^L_S]_{pr}$	$2n_s n_e$	$n_s n_e$	$-\frac{v^3}{2\sqrt{2}} C_{\underset{pr}{Sl1}}$

Effective Z Interactions

Operator	Coefficient	Parameters		Matching
		Total	CP-even	
$\mathcal{O}^L_{\nu Z}$	$[Z^L_\nu]_{pr}$	n_ν^2	$\frac{1}{2} n_\nu (n_\nu + 1)$	$g^\nu_L \delta_{pr} - \frac{v^2}{2} \big(C^{(1)}_{\underset{pr}{Hl}} - C^{(3)}_{\underset{pr}{Hl}} \big)$
$\mathcal{O}^R_{\nu NZ} + \text{h.c.}$	$[Z^R_{\nu N}]_{pr}$	$2n_\nu n_s$	$n_\nu n_s$	$\frac{v^3}{4\sqrt{2}} \big(C_{\underset{rp}{Nl1}} + 2C_{\underset{rp}{Nl2}} \big)$
$\mathcal{O}^R_{NZ}$	$[Z^R_N]_{pr}$	n_s^2	$\frac{1}{2} n_s (n_s + 1)$	$-\frac{v^2}{2} C_{\underset{pr}{HN}}$
$\mathcal{O}^L_{\nu SZ}$	$[Z^L_{\nu S}]_{pr}$	$2n_\nu n_s$	$n_\nu n_s$	$-\frac{v^3}{4\sqrt{2}} \big(C^*_{\underset{rp}{Sl1}} + 2C^*_{\underset{rp}{Sl2}} \big)$
$\mathcal{O}^L_{SZ}$	$[Z^L_S]_{pr}$	n_s^2	$\frac{1}{2} n_s \big(n_s + 1 \big)$	$-\frac{v^2}{2} C_{\underset{pr}{HS}}$

Table D.2: Matching between the effective $W^{\pm}$ (top) and Z (bottom) interactions and the $d \leq 7$ νSMEFT operators.

Appendix E

HNL Production Cross-sections

Here we give the analytical cross-sections for the processes $e^+e^- \to \nu\nu(\gamma)$, $e^+e^- \to \nu N(\gamma)$ and $e^+e^- \to NN(\gamma)$, which can generated at the EW scale by the νSMEFT operators listed in Tables 3.1 and 3.2. We work in the Feynman gauge and use the Feynman rules from Ref. [292] to treat the Majorana fermions. The starting point is the general process

$$\ell^+_\alpha \ell^-_\beta \to \sum_{i\leq j} \mathcal{N}_i \mathcal{N}_j(\gamma) \quad (\text{Majorana}), \quad \ell^+_\alpha \ell^-_\beta \to \sum_{i,j} \mathcal{N}_i \bar{\mathcal{N}}_j(\gamma) \quad (\text{Dirac}), \tag{E.1}$$

where the four-momenta are given by $p_\alpha + p_\beta = p_i + p_j$. The fields label $\mathcal{N}_i = \nu_i$ for $i = 1,2,3$ and $\mathcal{N}_{i+3} = N_i$ for $i = 1,\ldots n_s$. In the Dirac case, ν_i are massless Weyl fermions and N_i are Dirac fermions. In the Majorana case, both ν_i and N_i are Majorana fermions.

The differential cross-section for the $2 \to 2$ scattering (without the photon) at leading order (LO) is given by

$$\begin{aligned}
\frac{d\sigma}{dc_\theta} = &\left(\frac{1}{2}\right)\frac{1}{128\pi}\sum_{i,j}^{3+n_s}\lambda^{\frac{1}{2}}(s,m_i^2,m_j^2) \\
&\times\Bigg[\left(1-\frac{(m_i^2-m_j^2)^2}{s^2}+\frac{\lambda(s,m_i^2,m_j^2)}{s^2}c_\theta^2\right)\left(|L^{V,RR}_{\underset{ij\alpha\beta}{\mathcal{N}e}}|^2+|L^{V,RL}_{\underset{ij\alpha\beta}{\mathcal{N}e}}|^2\right) \\
&+\left(1-\frac{m_i^2+m_j^2}{s}\right)\left(|L^{S,RR}_{\underset{ij\alpha\beta}{\mathcal{N}e}}|^2+|L^{S,RL}_{\underset{ij\alpha\beta}{\mathcal{N}e}}|^2\right) \\
&+16\left(\frac{m_i^2+m_j^2}{s}-\frac{(m_i^2-m_j^2)^2}{s^2}+\frac{\lambda(s,m_i^2,m_j^2)}{s^2}c_\theta^2\right)|L^{T,RR}_{\underset{ij\alpha\beta}{\mathcal{N}e}}|^2 \\
&+\frac{4m_im_j}{s}\mathrm{Re}\left[2L^{V,LR}_{\underset{ij\alpha\beta}{\mathcal{N}e}}L^{V,RR*}_{\underset{ij\alpha\beta}{\mathcal{N}e}}-L^{S,LR}_{\underset{ij\alpha\beta}{\mathcal{N}e}}L^{S,RR*}_{\underset{ij\alpha\beta}{\mathcal{N}e}}\right] \\
&+\frac{2\lambda^{\frac{1}{2}}(s,m_i^2,m_j^2)}{s}c_\theta\left(|L^{V,RR}_{\underset{ij\alpha\beta}{\mathcal{N}e}}|^2-|L^{V,RL}_{\underset{ij\alpha\beta}{\mathcal{N}e}}|^2-4\,\mathrm{Re}\left[L^{S,RR}_{\underset{ij\alpha\beta}{\mathcal{N}e}}L^{T,RR*}_{\underset{ij\alpha\beta}{\mathcal{N}e}}\right]\right)\Bigg] \\
&+(L\leftrightarrow R)\,, \qquad \text{(E.2)}
\end{aligned}$$

with $c_\theta = \cos\theta$, where θ denotes the angle between the ℓ_β^- and $\mathcal{N}_i$, $\lambda(x,y,z)$ is the Källen function and $s = (p_\alpha + p_\beta)^2 = (p_i + p_j)^2$ the centre-off-mass energy. For each of the terms, another term with L and R swapped needs to be added, as indicated by $(L \leftrightarrow R)$ at the end of the expression. The factor of $1/2$ in brackets is applicable in the Majorana case, to compensate for the double counting inside the sum.

For the Dirac case, the coefficients appearing in the above expression are given by

$$\begin{aligned}
L^{V,XX}_{\underset{ij\alpha\beta}{\mathcal{N}e}}\Big|_{\mathrm{Dirac}} &\equiv C^{V,XX}_{\underset{ij\alpha\beta}{\mathcal{N}e}}+\chi_Z[Z^X_\mathcal{N}]_{ij}[Z^X_e]_{\alpha\beta}+\chi^\alpha_W[W^{XX}_\mathcal{N}]_{ij\alpha\beta}\,, \\
L^{V,XY}_{\underset{ij\alpha\beta}{\mathcal{N}e}}\Big|_{\mathrm{Dirac}} &\equiv C^{V,XY}_{\underset{ij\alpha\beta}{\mathcal{N}e}}+\chi_Z[Z^X_\mathcal{N}]_{ij}[Z^Y_e]_{\alpha\beta}+\chi^\alpha_W\frac{m_im_j}{2M_W^2}[W^{YY}_\mathcal{N}]_{ij\alpha\beta}\,, \\
L^{S,XX}_{\underset{ij\alpha\beta}{\mathcal{N}e}}\Big|_{\mathrm{Dirac}} &\equiv C^{S,XX}_{\underset{ij\alpha\beta}{\mathcal{N}e}}+\chi^\alpha_W\frac{m_im_j}{2M_W^2}[W^{XY}_\mathcal{N}]_{ij\alpha\beta}\,, \\
L^{S,XY}_{\underset{ij\alpha\beta}{\mathcal{N}e}}\Big|_{\mathrm{Dirac}} &\equiv C^{S,XY}_{\underset{ij\alpha\beta}{\mathcal{N}e}}-2\chi^\alpha_W[W^{YX}_\mathcal{N}]_{ij\alpha\beta}\,, \\
L^{T,XX}_{\underset{ij\alpha\beta}{\mathcal{N}e}}\Big|_{\mathrm{Dirac}} &\equiv C^{T,XX}_{\underset{ij\alpha\beta}{\mathcal{N}e}}+\chi^\alpha_W\frac{m_im_j}{8M_W^2}[W^{XY}_\mathcal{N}]_{ij\alpha\beta}\,, \qquad \text{(E.3)}
\end{aligned}$$

for $X \neq Y = R, L$, and using

$$[W_{\mathcal{N}}^{XY}]_{ij\alpha\beta} \equiv [W_{\mathcal{N}}^{X}]_{i\beta}[W_{\mathcal{N}}^{Y}]^{*}_{j\alpha}\,, \tag{E.4}$$

and

$$[Z_e^R]_{\alpha\beta} = g_R^e \delta_{\alpha\beta}\,, \quad [Z_e^L]_{\alpha\beta} = g_L^e \delta_{\alpha\beta} - \frac{v^2}{2}\big(C^{(1)}_{\substack{Hl\\ \alpha\beta}} + C^{(3)}_{\substack{Hl\\ \alpha\beta}}\big)\,, \tag{E.5}$$

where $g_R^e = s_w^2$ and $g_L^e = -1/2 + s_w^2$, with $s_w = \sin\theta_w$. The coefficients in Eq. E.3 also make use of the propagator factors for the t-channel $W^{\pm}$ and s-channel Z exchange

$$\chi_W^{\alpha} = \frac{g^2}{2}\frac{1}{t_\alpha^2 - M_W^2 + i\Gamma_W M_W}\,, \quad \chi_Z = \frac{g^2}{c_w^2}\frac{1}{s - M_Z^2 + i\Gamma_Z M_Z}\,, \tag{E.6}$$

respectively, with $t_\alpha = (p_j - p_\alpha)^2$.

In the Majorana case, the coefficients are given by

$$\begin{aligned}
L^{V,XX}_{\substack{\mathcal{N}e\\ ij\alpha\beta}}\Big|_{\text{Maj}} &\equiv L^{V,XX}_{\substack{\mathcal{N}e\\ ij\alpha\beta}}\Big|_{\text{Dirac}} - \chi_W^{\beta}\frac{m_i m_j}{2M_W^2}[W_{\mathcal{N}}^{XX}]_{ji\alpha\beta}\,,\\
L^{V,XY}_{\substack{\mathcal{N}e\\ ij\alpha\beta}}\Big|_{\text{Maj}} &\equiv L^{V,XY}_{\substack{\mathcal{N}e\\ ij\alpha\beta}}\Big|_{\text{Dirac}} - \chi_W^{\beta}[W_{\mathcal{N}}^{YY}]_{ji\alpha\beta}\,,\\
L^{S,XX}_{\substack{\mathcal{N}e\\ ij\alpha\beta}}\Big|_{\text{Maj}} &\equiv L^{S,XX}_{\substack{\mathcal{N}e\\ ij\alpha\beta}}\Big|_{\text{Dirac}} + \chi_W^{\beta}\frac{m_i m_j}{2M_W^2}[W_{\mathcal{N}}^{XY}]_{ji\alpha\beta}\,,\\
L^{S,XY}_{\substack{\mathcal{N}e\\ ij\alpha\beta}}\Big|_{\text{Maj}} &\equiv L^{S,XY}_{\substack{\mathcal{N}e\\ ij\alpha\beta}}\Big|_{\text{Dirac}} - 2\chi_W^{\beta}[W_{\mathcal{N}}^{YX}]_{ji\alpha\beta}\,,\\
L^{T,XX}_{\substack{\mathcal{N}e\\ ij\alpha\beta}}\Big|_{\text{Maj}} &\equiv L^{T,XX}_{\substack{\mathcal{N}e\\ ij\alpha\beta}}\Big|_{\text{Dirac}} - \chi_W^{\beta}\frac{m_i m_j}{8M_W^2}[W_{\mathcal{N}}^{XY}]_{ji\alpha\beta}\,,
\end{aligned} \tag{E.7}$$

for $X \neq Y = R, L$.

In order to compute the total cross-section, we note first that we take the $\Gamma_W \ll M_W$ limit, so that the complex part of the t-channel $W^{\pm}$ exchange is neglected and the propagator simplifies to $1/(t - M_W^2)$. Then, the differential cross-section in Eq. E.2 is integrated over the range [-1,1] for c_θ. Thus, the total cross-section at LO in the Dirac case is

$$
\begin{aligned}
\sigma(s)\big|_{\text{Dirac}} = \frac{1}{192\pi}\sum_{i,j}\lambda^{\frac{1}{2}}(s,m_i^2,m_j^2)& \\
\times\Bigg[\frac{192G_F^2M_W^4}{s^2}&\left(F_W^{ij}\big|[W_{\mathcal{N}}^{RR}]_{ij\alpha\beta}\big|^2+G_W^{ij}\big|[W_{\mathcal{N}}^{RL}]_{ij\alpha\beta}\big|^2\right) \\
&+4\left(1-\frac{m_i^2+m_j^2}{2s}-\frac{(m_i^2-m_j^2)^2}{2s^2}\right)\left(\big|L^{V,RR}_{\substack{\mathcal{N}e\\ ij\alpha\beta}}\big|^2+\big|L^{V,RL}_{\substack{\mathcal{N}e\\ ij\alpha\beta}}\big|^2\right) \\
&+3\left(1-\frac{m_i^2+m_j^2}{s}\right)\left(\big|L^{S,RR}_{\substack{\mathcal{N}e\\ ij\alpha\beta}}\big|^2+\big|L^{S,RL}_{\substack{\mathcal{N}e\\ ij\alpha\beta}}\big|^2\right) \\
&+16\left(1+\frac{m_i^2+m_j^2}{s}-\frac{2(m_i^2-m_j^2)^2}{s^2}\right)\big|L^{T,RR}_{\substack{\mathcal{N}e\\ ij\alpha\beta}}\big|^2 \\
&+\frac{12m_im_j}{s}\mathrm{Re}\Big[2L^{V,LR}_{\substack{\mathcal{N}e\\ ij\alpha\beta}}L^{V,RR*}_{\substack{\mathcal{N}e\\ ij\alpha\beta}}-L^{S,LR}_{\substack{\mathcal{N}e\\ ij\alpha\beta}}L^{S,RR*}_{\substack{\mathcal{N}e\\ ij\alpha\beta}}\Big] \\
&+\frac{48G_FM_W^2}{\sqrt{2}s}\mathrm{Re}\Bigg[\left(F_{VW}^{ij}L^{V,RR}_{\substack{\mathcal{N}e\\ ij\alpha\beta}}+G_{VW}^{ij}L^{V,LR}_{\substack{\mathcal{N}e\\ ij\alpha\beta}}\right)[W_{\mathcal{N}}^{RR}]^*_{ij\alpha\beta} \\
&\qquad+\left(F_{SW}^{ij}L^{S,RR}_{\substack{\mathcal{N}e\\ ij\alpha\beta}}+G_{SW}^{ij}L^{S,LR}_{\substack{\mathcal{N}e\\ ij\alpha\beta}}+F_{TW}^{ij}L^{T,RR}_{\substack{\mathcal{N}e\\ ij\alpha\beta}}\right)[W_{\mathcal{N}}^{RL}]^*_{ij\alpha\beta}\Bigg]\Bigg] \\
&+(L\leftrightarrow R)\,,
\end{aligned}
\tag{E.8}
$$

where $G_F = 1/(\sqrt{2}v^2)$ is the Fermi constant. Conversely, in the Majorana case, the total cross-section at LO is given by

$$\begin{aligned}
\sigma(s)\big|_{\text{Maj}} = \frac{1}{192\pi}\sum_{i\leq j}\left(1-\frac{\delta_{ij}}{2}\right)\lambda^{\frac{1}{2}}(s,m_i^2,m_j^2) \\
\times\Bigg[\frac{192G_F^2M_W^4}{s^2}\bigg(& F_W^{ij}\Big(\big|[W_{\mathcal{N}}^{RR}]_{ij\alpha\beta}\big|^2+\big|[W_{\mathcal{N}}^{LL}]_{ij\alpha\beta}\big|^2\Big) \\
&+G_W^{ij}\Big(\big|[W_{\mathcal{N}}^{RL}]_{ij\alpha\beta}\big|^2+\big|[W_{\mathcal{N}}^{LR}]_{ij\alpha\beta}\big|^2\Big) \\
&+F_{WW}^{ij}\,\mathrm{Re}\Big[[W_{\mathcal{N}}^{RR}]_{ij\alpha\beta}[W_{\mathcal{N}}^{RR}]_{ij\beta\alpha}+[W_{\mathcal{N}}^{LL}]_{ij\alpha\beta}[W_{\mathcal{N}}^{LL}]_{ij\beta\alpha}\Big] \\
&+G_{WW}^{ij}\,\mathrm{Re}\Big[[W_{\mathcal{N}}^{LR}]_{ij\alpha\beta}[W_{\mathcal{N}}^{RL}]_{ij\beta\alpha}\Big]\bigg) \\
+4\left(1-\frac{m_i^2+m_j^2}{2s}-\frac{(m_i^2-m_j^2)^2}{2s^2}\right)&\Big(\big|L^{V,RR}_{\substack{\mathcal{N}e\\ ij\alpha\beta}}\big|^2+\big|L^{V,RL}_{\substack{\mathcal{N}e\\ ij\alpha\beta}}\big|^2\Big) \\
+3\left(1-\frac{m_i^2+m_j^2}{s}\right)&\Big(\big|L^{S,RR}_{\substack{\mathcal{N}e\\ ij\alpha\beta}}\big|^2+\big|L^{S,RL}_{\substack{\mathcal{N}e\\ ij\alpha\beta}}\big|^2\Big) \\
+16\left(1+\frac{m_i^2+m_j^2}{s}-\frac{2(m_i^2-m_j^2)^2}{s^2}\right)&\big|L^{T,RR}_{\substack{\mathcal{N}e\\ ij\alpha\beta}}\big|^2 \\
-\frac{12m_im_j}{s}\mathrm{Re}\Big[L^{V,RR}_{\substack{\mathcal{N}e\\ ij\alpha\beta}}L^{V,RR}_{\substack{\mathcal{N}e\\ ij\beta\alpha}}&+L^{V,RL}_{\substack{\mathcal{N}e\\ ij\alpha\beta}}L^{V,RL}_{\substack{\mathcal{N}e\\ ij\beta\alpha}}+L^{S,RL}_{\substack{\mathcal{N}e\\ ij\alpha\beta}}L^{S,RR}_{\substack{\mathcal{N}e\\ ij\beta\alpha}}\Big] \\
+\frac{48G_FM_W^2}{\sqrt{2}s}\mathrm{Re}\bigg[L^{V,RR}_{\substack{\mathcal{N}e\\ ij\alpha\beta}}\Big(&F_{VW}^{ij}[W_{\mathcal{N}}^{RR}]^*_{ij\alpha\beta}-G_{VW}^{ij}[W_{\mathcal{N}}^{RR}]^*_{ji\alpha\beta}\Big) \\
&+L^{V,RL}_{\substack{\mathcal{N}e\\ ij\alpha\beta}}\Big(G_{VW}^{ij}[W_{\mathcal{N}}^{LL}]^*_{ij\alpha\beta}-F_{VW}^{ij}[W_{\mathcal{N}}^{LL}]^*_{ji\alpha\beta}\Big) \\
&+F_{SW}^{ij}L^{S,RR}_{\substack{\mathcal{N}e\\ ij\alpha\beta}}[W_{\mathcal{N}}^{RL}]^*_{\{ij\}\alpha\beta}+G_{SW}^{ij}L^{S,RL}_{\substack{\mathcal{N}e\\ ij\alpha\beta}}[W_{\mathcal{N}}^{LR}]^*_{\{ij\}\alpha\beta} \\
&+F_{TW}^{ij}L^{T,RR}_{\substack{\mathcal{N}e\\ ij\alpha\beta}}[W_{\mathcal{N}}^{RL}]^*_{[ij]\alpha\beta}\bigg]\Bigg] \\
+(\alpha\leftrightarrow\beta,\ \chi\leftrightarrow\chi^*)&, \qquad\qquad \text{(E.9)}
\end{aligned}$$

where $[W_{\mathcal{N}}^{XY}]_{\{ij\}\alpha\beta} \equiv [W_{\mathcal{N}}^{XY}]_{ij\alpha\beta} + [W_{\mathcal{N}}^{XY}]_{ji\alpha\beta}$ and $[W_{\mathcal{N}}^{XY}]_{[ij]\alpha\beta} \equiv [W_{\mathcal{N}}^{XY}]_{ij\alpha\beta} -$

$[W_{\mathcal{N}}^{XY}]_{ji\alpha\beta}$. In both Eqs. E.8 and E.9, the coefficients are given by

$$\begin{aligned}
L^{V,XY}_{\substack{\mathcal{N}e\\ ij\alpha\beta}} &\equiv C^{V,XY}_{\substack{\mathcal{N}e\\ ij\alpha\beta}} + \chi_Z [Z_{\mathcal{N}}^{X}]_{ij}[Z_e^{Y}]_{\alpha\beta}\,, \\
L^{S,XY}_{\substack{\mathcal{N}e\\ ij\alpha\beta}} &\equiv C^{S,XY}_{\substack{\mathcal{N}e\\ ij\alpha\beta}}\,, \\
L^{T,XX}_{\substack{\mathcal{N}e\\ ij\alpha\beta}} &\equiv C^{T,XX}_{\substack{\mathcal{N}e\\ ij\alpha\beta}}\,.
\end{aligned} \tag{E.10}$$

The final line in Eq. E.9 indicates that for each term, an additional term must be included with $\alpha \leftrightarrow \beta$ and $\chi \leftrightarrow \chi^*$ in the coefficients in Eq. E.10. The factors F_X^{ij} and G_X^{ij} are given by,

$$\begin{aligned}
F_W^{ij} &= 1 + \frac{1}{2\omega} - (1+\omega_{ij})L_{ij} + A_{ij}^2\left(1 - \frac{2\omega}{(1+2\omega_{ij})^2 - \lambda_{ij}} - \omega_{ij}L_{ij}\right), \\
G_W^{ij} &= \frac{1}{2\omega} - \frac{2\omega}{(1+2\omega_{ij})^2 - \lambda_{ij}} + A_{ij}^2\left(1 - \frac{2\omega}{(1+2\omega_{ij})^2 - \lambda_{ij}} - \omega_{ij}L_{ij}\right), \\
F_{WW}^{ij} &= A_{ij}\left(1 - \frac{2\omega}{1+2\omega_{ij}}\left(\frac{1}{2\omega} + \frac{\omega_{ij}}{\omega} + \frac{(1+2\omega_{ij})^2 - \lambda_{ij}}{4\omega} - A_{ij}^2\right)L_{ij}\right), \\
G_{WW}^{ij} &= 2\left(1 - \frac{2\omega}{1+2\omega_{ij}}\right)L_{ij} + A_{ij}^2\left(1 + \frac{\omega}{1+2\omega_{ij}}\left(8 - \frac{(1+2\omega_{ij})^2 - \lambda_{ij}}{2\omega}\right)L_{ij}\right), \\
F_{VW}^{ij} &= 3 + 2\omega_{ij} - 2\Big((1+\omega)(1+2\omega_{ij}-\omega) + 2\omega(1+2\omega)A_{ij}^2\Big)L_{ij}\,, \\
G_{VW}^{ij} &= -A_{ij}\left(1 - 2\omega_{ij} + 2\omega\left(1 + \frac{(1+2\omega_{ij})^2 - \lambda_{ij}}{4\omega}\right)L_{ij}\right), \\
F_{SW}^{ij} &= -A_{ij}\big(1 + 3\omega L_{ij}\big)\,, \\
G_{SW}^{ij} &= \Big(1 + 2\omega_{ij} - 2\omega\big(1 - A_{ij}^2\big)\Big)L_{ij}\,, \\
F_{TW}^{ij} &= 8A_{ij}\left(\omega_{ij} + \frac{\omega}{2}\left(1 - \frac{(1+2\omega_{ij})^2 - \lambda_{ij}}{2\omega}\right)L_{ij}\right),
\end{aligned} \tag{E.11}$$

where we define,

$$\lambda_{ij} \equiv \lambda\left(1, \frac{m_i^2}{s}, \frac{m_j^2}{s}\right), \quad \omega_{ij} \equiv \omega - \frac{m_i^2 + m_j^2}{2s}\,, \quad A_{ij} \equiv \frac{m_i m_j}{2M_W^2}\,, \tag{E.12}$$

and,

$$L_{ij} \equiv \frac{1}{\sqrt{\lambda_{ij}}} \log\left(\frac{1+2\omega_{ij}+\sqrt{\lambda_{ij}}}{1+2\omega_{ij}-\sqrt{\lambda_{ij}}}\right), \tag{E.13}$$

for convenience.

Using Eq. E.8, we can calculate the cross section for the SM process $\ell_\alpha^+\ell_\beta^- \to \sum \nu\bar{\nu}$, where the neutrinos are massless Weyl fermions with $\nu_{Lp} = P_L\delta_{pi}\nu_i$. The SM charged- and neutral-current couplings in Eq. 5.6 are inserted into Eq. E.8 and the limit $m_i, m_j \to 0$ taken. This yields

$$\begin{aligned}\sigma(s)\big|_{\mathrm{SM}} = \frac{G_F^2 M_Z^4}{6\pi s}\Bigg[&\chi_1 N_\nu\left((g_R^e)^2+(g_L^e)^2\right)\delta_{\alpha\beta} + 6c_w^4\left(1+\frac{1}{2\omega}-(1+\omega)\log\left(\frac{1+\omega}{\omega}\right)\right)\\ &+3\chi_2 g_L^e c_w^2\delta_{\alpha\beta}\left(3+2\omega-2(1+\omega)^2\log\left(\frac{1+\omega}{\omega}\right)\right)\Bigg],\end{aligned} \tag{E.14}$$

with $\omega \equiv M_W^2/s$ and

$$\chi_1 \equiv \frac{s^2}{(s-M_Z^2)^2+(\Gamma_Z M_Z)^2}, \quad \chi_2 \equiv \frac{s(s-M_Z^2)}{(s-M_Z^2)^2+(\Gamma_Z M_Z)^2}. \tag{E.15}$$

The first term in Eq. E.14 corresponds to s-channel Z exchange, the second to t-channel $W^\pm$ exchange, and the last to the interference between the two contributions. The cross section in Eq. E.14 is also applicable for light Majorana or Dirac neutrinos with non-zero active-sterile mixing, as long as the PMNS mixing matrix is approximately unitary. For non-zero EFT interactions, Eqs. E.8 and E.9 provide the leading interference effects between the SM and heavy new physics contributions to the process $\ell_\alpha^+\ell_\beta^- \to \sum \nu\bar{\nu}$, which we make use of in Sec. 5.7.

The expressions in Eqs. E.8 and E.9 can also be used to compute the cross section for the processes $\ell_\alpha^+\ell_\beta^- \to \sum_{ij}\nu_i N_j$ (Majorana) and $\ell_\alpha^+\ell_\beta^- \to \sum_{ij}\nu_i\bar{N}_j + \bar{\nu}_i N_j$ (Dirac) induced by the active-sterile mixing $V_{\alpha N_j}$. In both cases, the total cross section is

$$\begin{aligned}\sigma(s)\big|_{\text{mix}} = \frac{G_F^2 M_Z^4}{6\pi s} \sum_{\rho,j} |V_{\rho N_j}|^2 (1-y_j) \\ \times \Bigg[(1-y_j)(2+y_j)\chi_1 \left((g_R^e)^2 + (g_L^e)^2\right) \delta_{\alpha\beta} \\ + 6c_w^4 (\delta_{\alpha\rho} + \delta_{\beta\rho}) \left(1 + \frac{1}{2\omega} - \left(1 + \omega - \frac{y_j}{2}\right) L_{ij}\right) \\ + 6\chi_2 g_L^e c_w^2 \delta_{\alpha\beta} \delta_{\alpha\rho} \Big(3 + 2\omega - y_j - 2(1+\omega)(1+\omega-y_j) L_{ij}\Big)\Bigg] ,\end{aligned} \tag{E.16}$$

where $L_{ij} \equiv \log[(1+\omega-y_j)/\omega]/(1-y_j)$, and χ_1, χ_2 are given in Eq. E.15. As in Eq. E.14, the first and second terms in parenthesis in Eq. E.16 correspond to Z and $W^\pm$ exchange, respectively, and the last term to $Z - W^\pm$ interference.

Finally, although the $2 \to 2$ cross-sections above are used for the DV searches, the photon in the final state needs to be accounted for in the cross-section expression used for the mono-γ plus $\not{E}$. These $2 \to 3$ cross-sections can be computed from the total cross-sections $\sigma(s)$ in Eqs. E.8 and E.9 as

$$\frac{d^2\sigma}{dx_\gamma dc_\gamma} = \sigma(s(1-x_\gamma)) \frac{\alpha}{\pi} \frac{1+(1-x_\gamma)^2}{x_\gamma} \frac{1}{1-\beta_e^2 c_\gamma^2} , \tag{E.17}$$

where $\alpha = e^2/(4\pi)$ is the QED fine-structure constant, $x_\gamma = 2E_\gamma/\sqrt{s}$ is the fraction of the beam energy carried away by the photon and $c_\gamma = \cos\theta_\gamma$, with θ_γ the angle of the photon with respect to the beam axis.

$\mathcal{N}_j$ Decays

Operator	$(q^2)^{\rm max} \lesssim 1$ GeV^2	$(q^2)^{\rm max} \gtrsim 1$ GeV^2	$(q^2)^{\rm max} \gtrsim M_W^2, M_Z^2, M_h^2$
$C_{\mathcal{N}\mathcal{N}}^{V,XY}$	$\mathcal{N}_i\mathcal{N}_k\mathcal{N}_l$	$\mathcal{N}_i\mathcal{N}_k\mathcal{N}_l$	$\mathcal{N}_i\mathcal{N}_k\mathcal{N}_l$
$C_{\mathcal{N}e}^{V,XY}, C_{\mathcal{N}e}^{S,XY}, C_{\mathcal{N}e}^{T,XX}$	$\mathcal{N}_i\ell_\alpha^-\ell_\beta^+$	$\mathcal{N}_i\ell_\alpha^-\ell_\beta^+$	$\mathcal{N}_i\ell_\alpha^-\ell_\beta^+$
$[W_\mathcal{N}^X]_{j\alpha}$	$\mathcal{N}_i\ell_\alpha^-\ell_\beta^+$ $\ell_\alpha^\mp P^\pm/V^\pm$	$\mathcal{N}_i\ell_\alpha^-\ell_\beta^+$ $\ell_\alpha^- u\bar{d}$ $(\ell_\alpha^+\bar{u}d)$	$\ell_\alpha^\mp W^\pm$
$[Z_\mathcal{N}^X]_{ij}$	$\mathcal{N}_i\mathcal{N}_k\mathcal{N}_l$ $\mathcal{N}_i\ell_\alpha^-\ell_\alpha^+$ $\mathcal{N}_iP^0/V^0$	$\mathcal{N}_i\mathcal{N}_k\mathcal{N}_l$ $\mathcal{N}_i\ell_\alpha^-\ell_\alpha^+$ $\mathcal{N}_iq\bar{q}$	$\mathcal{N}_iZ$

Table F.1: Majorana HNL decays induced by the νSMEFT operators in Tables 3.1, for three different $(q^2)^{\rm max}$ regimes.

Appendix F

HNL Decay Rates

Having considered the production mechanisms available to the HNLs, we now consider their decay modes. The νSMEFT operators in Tables 3.1 and 3.2 that produce the HNLs, may also mediate their decays. These decay modes are summarised in Table F.1. In the case of the four-fermion effective operators, we assume that only the $\alpha = \beta = e$ WCs are present and therefore the only available decay channel is $\mathcal{N}_j \to \mathcal{N}_i e^- e^+$. Additionally, the effective Z and $W^\pm$ interactions can lead to the decay modes $\mathcal{N}_j \to \mathcal{N}_i\ell_\alpha^-\ell_\alpha^+$ for $\alpha = \mu, \tau$ and $\mathcal{N}_j \to \mathcal{N}_i\ell_\alpha^-\ell_\beta^+$ with $\alpha = e$ and $\beta = \mu, \tau$, respectively. Furthermore, in the case of Majorana HNLs, the channel $\mathcal{N}_j \to \mathcal{N}_i\ell_\alpha^-\ell_\beta^+$ with $\alpha = \mu, \tau$ and $\beta = e$ is also available. Neglecting threshold effects, the decay rates for the above mentioned processes can be expressed as

$$\begin{aligned}\Gamma(\mathcal{N}_j \to \mathcal{N}_i f_\alpha \bar{f}_\beta) = \frac{N_c m_j^5}{1536\pi^3} \Bigg[I_1^{i\alpha\beta} \Bigg(&|L^{V,RR}_{\substack{\mathcal{N}f\\ ij\alpha\beta}}|^2 + |L^{V,RL}_{\substack{\mathcal{N}f\\ ij\alpha\beta}}|^2 \\ &+ \frac{1}{4}\Big(|L^{S,RR}_{\substack{\mathcal{N}f\\ ij\alpha\beta}}|^2 + |L^{S,RL}_{\substack{\mathcal{N}f\\ ij\alpha\beta}}|^2\Big) + 12|L^{T,RR}_{\substack{\mathcal{N}f\\ ij\alpha\beta}}|^2 \Bigg) \\ &- I_3^{\alpha\beta i} \mathrm{Re}\Big[L^{V,LR}_{\substack{\mathcal{N}f\\ ij\alpha\beta}} L^{V,RR*}_{\substack{\mathcal{N}f\\ ij\alpha\beta}} - \frac{1}{2} L^{S,LR}_{\substack{\mathcal{N}f\\ ij\alpha\beta}} L^{S,RR*}_{\substack{\mathcal{N}f\\ ij\alpha\beta}} \Big] \Bigg] \\ + (L \leftrightarrow R)\,, \end{aligned} \tag{F.1}$$

for $f = e = \ell$ and the number of colors $N_c = 1$. The above assumes that the HNL mass much below the EW scale. In the above, $I_1^{i\alpha\beta} = I_1(y_i, y_\alpha, y_\beta)$ and $I_3^{\alpha\beta i} = I_3(y_\alpha, y_\beta, y_i)$, where $y_X \equiv m_X/m_j$ and the functions $I_1(x,y,z)$ and $I_3(x,y,z)$ are given by,

$$\begin{aligned} I_1(x,y,z) &= 12 \int_{(x+y)^2}^{(1-z)^2} \frac{ds}{s} (1 + z^2 - s)(s - x^2 - y^2) \lambda^{\frac{1}{2}}(1, s, z^2) \lambda^{\frac{1}{2}}(s, x^2, y^2)\,, \\ I_3(x,y,z) &= 24z \int_{(x+y)^2}^{(1-z)^2} \frac{ds}{s} (s - x^2 - y^2) \lambda^{\frac{1}{2}}(1, s, z^2) \lambda^{\frac{1}{2}}(s, x^2, y^2)\,. \end{aligned} \tag{F.2}$$

Furthermore, the coefficients in the decay rate expression are those in Eqs. E.3 and E.7 for the Dirac and Majorana HNL scenario, respectively. Instead of using the propagator factor of Eq. E.6, the limit

$$\chi_W^\alpha \to -\frac{g^2}{2M_W^2}\,, \quad \chi_Z \to -\frac{g^2}{c_w^2 M_Z^2}\,. \tag{F.3}$$

is taken, as we are assuming to be in the post EW-breaking regime with the heavy mediators integrated out. This and therefore Eq. F.1 is valid for HNLs with masses in the GeV range, i.e. the middle column of Table F.1.

In the same $(q^2)^{\max}$ regime, the effective $W^\pm$ and Z interactions can also lead to HNL decays to quarks. For the effective $W^\pm$ interactions the induced process is

$\mathcal{N}_j \to \ell_\alpha^- u_\rho \bar{d}_\sigma$, with the decay rate

$$\Gamma(\mathcal{N}_j \to \ell_\alpha^- u_\rho \bar{d}_\sigma) = \frac{N_c m_j^5}{1536\pi^3}\left[I_1^{\alpha\rho\sigma}\left(|L^{V,RL}_{\substack{e\mathcal{N}ud\\ \alpha j\rho\sigma}}|^2 + |L^{V,LL}_{\substack{e\mathcal{N}ud\\ \alpha j\rho\sigma}}|^2\right) - I_3^{\rho\sigma\alpha}\,\mathrm{Re}\left[L^{V,RL}_{\substack{e\mathcal{N}ud\\ \alpha j\rho\sigma}} L^{V,LL*}_{\substack{e\mathcal{N}ud\\ \alpha j\rho\sigma}}\right]\right], \tag{F.4}$$

with $N_c = 3$ and

$$L^{V,XL}_{\substack{e\mathcal{N}ud\\ \alpha j\rho\sigma}} \equiv -\frac{g^2}{2M_W^2}[W^X_{\mathcal{N}}]^*_{j\alpha} V_{\rho\sigma}\,, \tag{F.5}$$

where V denotes the CKM matrix. The above decay rate is also applicable to the process $\mathcal{N}_j \to \ell_\alpha^+ \bar{u}_\rho d_\sigma$ in the Majorana HNL case. For the effective Z this will lead to processes $\mathcal{N}_j \to \mathcal{N}_i q_\alpha \bar{q}_\beta$, with the corresponding decay rate as given in Eq. F.1 with $N_c = 3$ and $f = q$, where $\alpha, \beta = u, c$ for $q = u$ and $\alpha, \beta = d, s, b$ for $q = d$. In the Dirac HNL case the coefficients are given by

$$L^{V,XY}_{\substack{\mathcal{N}q\\ ij\alpha\beta}} \equiv -\frac{g^2}{c_w^2 M_Z^2}[Z^X_{\mathcal{N}}]_{ij}[Z^Y_q]_{\alpha\beta}\,, \quad L^{S,XY}_{\substack{\mathcal{N}q\\ ij\alpha\beta}} \equiv 0\,, \quad L^{T,RR}_{\substack{\mathcal{N}q\\ ij\alpha\beta}} \equiv 0\,, \tag{F.6}$$

where $[Z^R_q]_{\alpha\beta} = g^q_R \delta_{\alpha\beta}$ and $[Z^L_q]_{\alpha\beta} = g^q_L \delta_{\alpha\beta}$ with $g^u_R = -2s_w^2/3$, $g^u_L = 1/2 - 2s_w^2/3$, $g^u_R = s_w^2/3$ and $g^u_L = -1/2 + s_w^2/3$. Conversely, in the Majorana HNL scenario, the same coefficients are used but with the replacement $[Z^L_{\mathcal{N}}]_{ij} \to -[Z^R_{\mathcal{N}}]^*_{ij}$. In order to account for large QCD corrections to the decays involving final state quarks, the decay rates in Eqs. F.1 and F.4 are multiplied by the factor [293]

$$1 + \Delta_{\mathrm{QCD}} \equiv \frac{\Gamma(\tau \to \nu_\tau + \mathrm{hadr.})}{\sum_q \Gamma(\tau \to \nu_\tau + \bar{u}q)\big|_{\mathrm{tree}}} = 1 + \frac{\alpha_s}{\pi} + 5.2\frac{\alpha_s^2}{\pi^2} + 26.4\frac{\alpha_s^3}{\pi^3}\,. \tag{F.7}$$

following the prescription of [221], with α_s evaluated at maximum momentum transfer.

Below the QCD scale, i.e. in the $(q^2)^{\max} \lesssim 1$ GeV^2 regime corresponding to the first column of Table F.1, instead of producing jets, the outgoing quarks hadronise. In the case of the effective $W^\pm$ this induces the decays $\mathcal{N}_j \to \ell_\alpha^- P^+$ and $\mathcal{N}_j \to \ell_\alpha^- V^+$, producing charged pseudoscalar and vector mesons, respectively, with decay rates

$$\Gamma(\mathcal{N}_j \to \ell_\alpha^- P^+) = \frac{G_F^2 f_P^2 m_j^3 |V_{q\bar{q}}|^2}{16\pi} \lambda^{\frac{1}{2}}(1, y_\alpha^2, y_P^2) \Big[F(y_\alpha, y_P) \Big(\big|[W_\mathcal{N}^R]_{j\alpha}\big|^2 + \big|[W_\mathcal{N}^L]_{j\alpha}\big|^2 \Big) \\ + 4 y_\alpha y_P^2 \mathrm{Re}\Big[[W_\mathcal{N}^R]_{j\alpha} [W_\mathcal{N}^L]_{j\alpha}^* \Big] \Big] , \tag{F.8}$$

$$\Gamma(\mathcal{N}_j \to \ell_\alpha^- V^+) = \frac{G_F^2 f_V^2 m_j^3 |V_{q\bar{q}}|^2}{16\pi} \lambda^{\frac{1}{2}}(1, y_\alpha^2, y_V^2) \Big[G(y_\alpha, y_V) \Big(\big|[W_\mathcal{N}^R]_{j\alpha}\big|^2 + [W_\mathcal{N}^L]_{j\alpha}\big|^2 \Big) \\ - 12 y_\alpha y_V^2 \mathrm{Re}\Big[[W_\mathcal{N}^R]_{j\alpha} [W_\mathcal{N}^L]_{j\alpha}^* \Big] \Big] , \tag{F.9}$$

where $F(x,y) = 1 - y^2 - x^2(2 - x^2 + y^2)$, $G(x,y) = (1 - y^2)(1 + 2y^2) + x^2(x^2 + y^2 - 2)$, and the pseudoscalar and vector form factors are defined via $\langle 0 | \bar{q} \gamma_\mu \gamma_5 q | P \rangle = i f_P p_\mu$ and $\langle 0 | \bar{q} \gamma_\mu q | V \rangle = i f_V m_V \varepsilon_\mu$, respectively. The values taken for these form factors are given in Table IV of [294]. The lightest states are $P^\pm = \{\pi^\pm, K^\pm, D^\pm, D_s^\pm\}$ and $V^\pm = \{\rho^\pm, K^{*\pm}\}$ and thus in the Majorana HNL case the decay processes $\mathcal{N}_j \to \ell_\alpha^+ P^-$ and $\mathcal{N}_j \to \ell_\alpha^+ V^-$ are also allowed for the effective $W^\pm$ interaction, with the decay rates also given by the 2-body decay expression in Eq. F.8. In the same regime, the effective Z instead induces the decays $\mathcal{N}_j \to \mathcal{N}_i P^0$ and $\mathcal{N}_j \to \mathcal{N}_i V^0$ to neutral pseudoscalar and vector mesons, respectively. Here, the states are $P^0 = \{\pi^0, \eta, \eta'\}$ and $V^0 = \{\rho, \omega, \phi\}$. The decay rates for these processes are given by

$$\Gamma(\mathcal{N}_j \to \mathcal{N}_i P^0) = \frac{G_F^2 f_P^2 m_j^3}{8\pi} \lambda^{\frac{1}{2}}(1, y_i^2, y_P^2) \Big[F(y_i, y_P) \Big(\big|[Z_\mathcal{N}^R]_{ij}\big|^2 + \big|[Z_\mathcal{N}^L]_{ij}\big|^2 \Big) \\ + 4 y_i y_P^2 \mathrm{Re}\Big[[Z_\mathcal{N}^R]_{ij} [Z_\mathcal{N}^L]_{ij}^* \Big] \Big] , \tag{F.10}$$

$$\Gamma(\mathcal{N}_j \to \mathcal{N}_i V^0) = \frac{G_F^2 f_V^2 \kappa_V^2 m_j^3}{8\pi} \lambda^{\frac{1}{2}}(1, y_i^2, y_V^2) \Big[G(y_i, y_V) \Big(\big|[Z_\mathcal{N}^R]_{ij}\big|^2 + [Z_\mathcal{N}^L]_{ij}\big|^2 \Big) \\ - 12 y_i y_V^2 \mathrm{Re}\Big[[Z_\mathcal{N}^R]_{ij} [Z_\mathcal{N}^L]_{ij}^* \Big] \Big] , \tag{F.11}$$

where $\kappa_\rho = 1 - 2s_w^2$, $\kappa_\omega = -2s_w^2/3$ and $\kappa_\phi = -\sqrt{2}(1/2 - 2s_w^2/3)$ [223].

The final regime is $(q^2)^{\max} \gtrsim M_W^2, M_Z^2, M_h^2$, i.e. when the vector bosons can be produced on-shell, corresponding to the third column of Table F.1. In such cases the effective $W^\pm$ and Z interactions can induce the decays $\mathcal{N}_j \to \ell_\alpha^- W^+$, $\mathcal{N}_j \to \mathcal{N}_i Z$ and $\mathcal{N}_j \to \mathcal{N}_i h$, with decay rates

$$\begin{aligned}
\Gamma(\mathcal{N}_j \to \ell_\alpha^- W^+) &= \frac{G_F m_j^3}{8\sqrt{2}\pi}\lambda^{\frac{1}{2}}(1, y_\alpha^2, y_W^2)\Big[G(y_\alpha, y_W)\Big(\big|[W_\mathcal{N}^R]_{j\alpha}\big|^2 + \big|[W_\mathcal{N}^L]_{j\alpha}\big|^2\Big) \\
&\qquad - 12 y_\alpha y_W^2 \mathrm{Re}\Big[[W_\mathcal{N}^R]_{j\alpha}[W_\mathcal{N}^L]^*_{j\alpha}\Big]\Big], \\
\Gamma(\mathcal{N}_j \to \mathcal{N}_i Z) &= \frac{G_F m_j^3}{4\sqrt{2}\pi}\lambda^{\frac{1}{2}}(1, y_i^2, y_Z^2)\Big[G(y_\alpha, y_Z)\Big(\big|[Z_\mathcal{N}^R]_{ij}\big|^2 + [Z_\mathcal{N}^L]_{ij}\big|^2\Big) \\
&\qquad - 12 y_i y_Z^2 \mathrm{Re}\Big[[Z_\mathcal{N}^R]_{ij}[Z_\mathcal{N}^L]^*_{ij}\Big]\Big],
\end{aligned} \tag{F.12}$$

For $(q^2)^{\max} < M_W^2, M_Z^2$, the total HNL width in the Dirac case is

$$\begin{aligned}
\Gamma_{\mathcal{N}_j}\big|_{\mathrm{Dirac}} = &\sum_{i \le k, l} \Gamma_{\mathcal{N}_i \mathcal{N}_k \bar{\mathcal{N}}_l} + \sum_{i,\alpha,\beta} \Gamma_{\mathcal{N}_i \ell_\alpha^- \ell_\beta^+} \\
&+ \sum_i \Big[\Theta_{ij} \sum_{P^0} \Gamma_{\mathcal{N}_i P^0} + \Theta_{ij} \sum_{V^0} \Gamma_{\mathcal{N}_i V^0} + (1 - \Theta_{ij}) \sum_{\alpha,\beta} \Gamma_{\mathcal{N}_i q_\alpha \bar{q}_\beta}\Big] \\
&+ \sum_\alpha \Big[\Theta_{\alpha j} \sum_{P^+} \Gamma_{\ell_\alpha^- P^+} + \Theta_{\alpha j} \sum_{V^+} \Gamma_{\ell_\alpha^- V^+} + (1 - \Theta_{\alpha j}) \sum_{\rho,\sigma} \Gamma_{\ell_\alpha^- u_\rho \bar{d}_\sigma}\Big],
\end{aligned} \tag{F.13}$$

while in the Majorana case

$$\begin{aligned}
\Gamma_{\mathcal{N}_j}\big|_{\mathrm{Maj}} = &\sum_{i \le k \le l} \Gamma_{\mathcal{N}_i \mathcal{N}_k \mathcal{N}_l} + \sum_{i,\alpha,\beta} \Gamma_{\mathcal{N}_i \ell_\alpha^- \ell_\beta^+} \\
&+ \sum_i \Big[\Theta_{ij} \sum_{P^0} \Gamma_{\mathcal{N}_i P^0} + \Theta_{ij} \sum_{V^0} \Gamma_{\mathcal{N}_i V^0} + (1 - \Theta_{ij}) \sum_{\alpha,\beta} \Gamma_{\mathcal{N}_i q_\alpha \bar{q}_\beta}\Big] \\
&+ 2\sum_\alpha \Big[\Theta_{\alpha j} \sum_{P^+} \Gamma_{\ell_\alpha^- P^+} + \Theta_{\alpha j} \sum_{V^+} \Gamma_{\ell_\alpha^- V^+} + (1 - \Theta_{\alpha j}) \sum_{\rho,\sigma} \Gamma_{\ell_\alpha^- u_\rho \bar{d}_\sigma}\Big],
\end{aligned} \tag{F.14}$$

where we have used $\Gamma_X \equiv \Gamma(\mathcal{N}_j \to X)$ and the shorthand

$$\Theta_{ab} \equiv \Theta\bigg(1 - \frac{(m_b - m_a)^2}{1\ \mathrm{GeV}^2}\bigg). \tag{F.15}$$

Bibliography

[1] W. Pauli. Dear radioactive ladies and gentlemen. *Phys. Today*, 31N9:27, 1978.

[2] J. Chadwick. Possible Existence of a Neutron. *Nature*, 129:312, 1932.

[3] M. Goeppert-Mayer. Double beta-disintegration. *Physical Review*, 48(6):512, 1935.

[4] G. Gamow and E. Teller. Selection rules for the beta-disintegration. *Phys. Rev.*, 49:895–899, 1936.

[5] E. J. Konopinski. Fermi's theory of beta-decay. *Rev. Mod. Phys.*, 27:254–257, Jul 1955.

[6] E. Majorana. Teoria simmetrica dell'elettrone e del positrone. *Il Nuovo Cimento (1924-1942)*, 14(4):171–184, 1937.

[7] J. C. Street and E. Stevenson. New evidence for the existence of a particle of mass intermediate between the proton and electron. *Physical Review*, 52(9):1003, 1937.

[8] C. D. Anderson and S. H. Neddermeyer. Note on the nature of cosmic-ray particles. *Phys. Rev*, 51(884):51, 1937.

[9] H. Bethe and R. Peierls. The 'neutrino'. *Nature*, 133:532, 1934.

[10] C. L. Cowan Jr et al. Detection of the free neutrino: a confirmation. *Science*, 124(3212):103–104, 1956.

[11] T.-D. Lee and C. N. Yang. Question of parity conservation in weak interactions. *Physical Review*, 104(1):254, 1956.

[12] C.-S. Wu et al. Experimental test of parity conservation in beta decay. *Physical review*, 105(4):1413, 1957.

[13] M. Goldhaber et al. Helicity of neutrinos. *Physical review*, 109(3):1015, 1958.

[14] B. Pontecorvo. Electron and muon neutrinos. *Zhur. Eksptl'. i Teoret. Fiz.*, 37, 1959.

[15] G. Danby et al. Observation of high-energy neutrino reactions and the existence of two kinds of neutrinos. *Physical Review Letters*, 9(1):36, 1962.

[16] R. Davis, Jr. et al. Search for neutrinos from the sun. *Phys. Rev. Lett.*, 20:1205–1209, 1968.

[17] K. Hirata et al. Observation of a Neutrino Burst from the Supernova SN 1987a. *Phys. Rev. Lett.*, 58:1490–1493, 1987.

[18] F. J. Hasert et al. Observation of Neutrino Like Interactions Without Muon Or Electron in the Gargamelle Neutrino Experiment. *Phys. Lett. B*, 46:138–140, 1973.

[19] A. Benvenuti et al. Observation of Muonless Neutrino Induced Inelastic Interactions. *Phys. Rev. Lett.*, 32:800–803, 1974.

[20] J. J. Aubert et al. Experimental Observation of a Heavy Particle J. *Phys. Rev. Lett.*, 33:1404–1406, 1974.

[21] J. E. Augustin et al. Discovery of a Narrow Resonance in e^+e^- Annihilation. *Phys. Rev. Lett.*, 33:1406–1408, 1974.

[22] S. W. Herb et al. Observation of a Dimuon Resonance at 9.5 GeV in 400 GeV Proton-Nucleus Collisions. *Phys. Rev. Lett.*, 39:252–255, 1977.

[23] M. L. Perl et al. Evidence for Anomalous Lepton Production in e+ - e- Annihilation. *Phys. Rev. Lett.*, 35:1489–1492, 1975.

[24] G. Arnison et al. Experimental Observation of Isolated Large Transverse Energy Electrons with Associated Missing Energy at $\sqrt{s} = 540$ GeV. *Phys. Lett. B*, 122:103–116, 1983.

[25] G. Arnison et al. Experimental Observation of Lepton Pairs of Invariant Mass Around 95-GeV/c**2 at the CERN SPS Collider. *Phys. Lett. B*, 126:398–410, 1983.

[26] M. Banner et al. Observation of Single Isolated Electrons of High Transverse Momentum in Events with Missing Transverse Energy at the CERN anti-p p Collider. *Phys. Lett. B*, 122:476–485, 1983.

[27] P. Bagnaia et al. Evidence for $Z^0 \to e^+e^-$ at the CERN $\bar{p}p$ Collider. *Phys. Lett. B*, 129:130–140, 1983.

[28] F. Abe et al. Observation of top quark production in $\bar{p}p$ collisions. *Phys. Rev. Lett.*, 74:2626–2631, 1995.

[29] K. Kodama et al. Observation of tau neutrino interactions. *Phys. Lett. B*, 504:218–224, 2001.

[30] S. Schael et al. Precision electroweak measurements on the Z resonance. *Phys. Rept.*, 427:257–454, 2006.

[31] M. Cielo et al. Neff in the Standard Model at NLO is 3.043. *Phys. Rev. D*, 108(12):L121301, 2023.

[32] K. S. Hirata et al. Experimental Study of the Atmospheric Neutrino Flux. *Phys. Lett. B*, 205:416, 1988.

[33] R. M. Bionta et al. Observation of a Neutrino Burst in Coincidence with Supernova SN 1987a in the Large Magellanic Cloud. *Phys. Rev. Lett.*, 58:1494, 1987.

[34] Y. Fukuda et al. Evidence for oscillation of atmospheric neutrinos. *Phys. Rev. Lett.*, 81:1562–1567, 1998.

[35] Q. R. Ahmad et al. Direct evidence for neutrino flavor transformation from neutral current interactions in the Sudbury Neutrino Observatory. *Phys. Rev. Lett.*, 89:011301, 2002.

[36] K. Eguchi et al. First results from KamLAND: Evidence for reactor antineutrino disappearance. *Phys. Rev. Lett.*, 90:021802, 2003.

[37] T. Araki et al. Measurement of neutrino oscillation with KamLAND: Evidence of spectral distortion. *Phys. Rev. Lett.*, 94:081801, 2005.

[38] T. Araki et al. Experimental investigation of geologically produced antineutrinos with KamLAND. *Nature*, 436:499–503, 2005.

[39] N. Agafonova et al. Observation of a first ν_τ candidate in the OPERA experiment in the CNGS beam. *Phys. Lett. B*, 691:138–145, 2010.

[40] M. G. Aartsen et al. Observation of High-Energy Astrophysical Neutrinos in Three Years of IceCube Data. *Phys. Rev. Lett.*, 113:101101, 2014.

[41] R. Acciarri et al. Long-Baseline Neutrino Facility (LBNF) and Deep Underground Neutrino Experiment (DUNE): Conceptual Design Report, Volume 2: The Physics Program for DUNE at LBNF. 12 2015.

[42] M. Aker et al. Direct neutrino-mass measurement based on 259 days of KATRIN data. *Science*, 388(6743):adq9592, 2025.

[43] E. P. Wigner. On Unitary Representations of the Inhomogeneous Lorentz Group. *Annals Math.*, 40:149–204, 1939.

[44] W. Pauli. Über den zusammenhang des abschlusses der elektronengruppen im atom mit der komplexstruktur der spektren. *Zeitschrift für Physik*, 31(1):765–783, 1925.

[45] M. Gell-Mann. Isotopic spin and new unstable particles. *Physical Review*, 92(3):833, 1953.

[46] T. Nakano and K. Nishijima. Charge independence for v-particles. *Progress of Theoretical Physics*, 10(5):581–582, 1953.

[47] S. L. Glashow. Partial Symmetries of Weak Interactions. *Nucl. Phys.*, 22:579–588, 1961.

[48] S. Weinberg. A Model of Leptons. *Phys. Rev. Lett.*, 19:1264–1266, 1967.

[49] A. Salam. Weak and Electromagnetic Interactions. *Conf. Proc. C*, 680519:367–377, 1968.

[50] F. Englert and R. Brout. Broken symmetry and the mass of gauge vector mesons. *Physical review letters*, 13(9):321, 1964.

[51] P. W. Higgs. Broken symmetries, massless particles and gauge fields. *Phys. Lett.*, 12:132–133, 1964.

[52] G. S. Guralnik et al. Global conservation laws and massless particles. *Physical Review Letters*, 13(20):585, 1964.

[53] S. Weinberg. A model of leptons. *Physical review letters*, 19(21):1264, 1967.

[54] S. Navas et al. Review of particle physics. *Phys. Rev. D*, 110(3):030001, 2024.

[55] N. Cabibbo. Unitary symmetry and leptonic decays. *Physical Review Letters*, 10(12):531, 1963.

[56] M. Kobayashi and T. Maskawa. Cp-violation in the renormalizable theory of weak interaction. *Progress of theoretical physics*, 49(2):652–657, 1973.

[57] B. Pontecorvo. Mesonium and Antimesonium. *Sov. Phys. JETP*, 6:429–431, 1958.

[58] B. Pontecorvo. Inverse Beta Processes and Nonconservation of Lepton Charge. *Sov. Phys. JETP*, 7:172–173, 1958.

[59] Z. Maki et al. Remarks on the unified model of elementary particles. *Prog. Theor. Phys.*, 28:870–880, 1962.

[60] B. Pontecorvo. Neutrino Experiments and the Problem of Conservation of Leptonic Charge. *Sov. Phys. JETP*, 26:984–988, 1968.

[61] S. Eliezer and A. R. Swift. Experimental Consequences of electron Neutrino-Muon-neutrino Mixing in Neutrino Beams. *Nucl. Phys. B*, 105:45–51, 1976.

[62] H. Fritzsch and P. Minkowski. Vector-Like Weak Currents, Massive Neutrinos, and Neutrino Beam Oscillations. *Phys. Lett. B*, 62:72–76, 1976.

[63] S. M. Bilenky and B. Pontecorvo. Again on Neutrino Oscillations. *Lett. Nuovo Cim.*, 17:569, 1976.

[64] F. F. Deppisch. *A modern introduction to neutrino physics*. Morgan & Claypool Publishers, 2019.

[65] L. Wolfenstein. Neutrino Oscillations in Matter. *Phys. Rev. D*, 17:2369–2374, 1978.

[66] S. P. Mikheyev and A. Y. Smirnov. Resonance Amplification of Oscillations in Matter and Spectroscopy of Solar Neutrinos. *Sov. J. Nucl. Phys.*, 42:913–917, 1985.

[67] C. Giunti and C. W. Kim. *Fundamentals of neutrino physics and astrophysics*. Oxford university press, 2007.

[68] B. T. Cleveland et al. Measurement of the solar electron neutrino flux with the Homestake chlorine detector. *Astrophys. J.*, 496:505–526, 1998.

[69] C. Pena-Garay and A. Serenelli. Solar neutrinos and the solar composition problem. 11 2008.

[70] W. Hampel et al. GALLEX solar neutrino observations: Results for GALLEX IV. *Phys. Lett. B*, 447:127–133, 1999.

[71] J. N. Abdurashitov et al. Solar neutrino flux measurements by the Soviet-American Gallium Experiment (SAGE) for half the 22 year solar cycle. *J. Exp. Theor. Phys.*, 95:181–193, 2002.

[72] M. Altmann et al. Complete results for five years of GNO solar neutrino observations. *Phys. Lett. B*, 616:174–190, 2005.

[73] J. N. Abdurashitov et al. Measurement of the solar neutrino capture rate with gallium metal. III: Results for the 2002–2007 data-taking period. *Phys. Rev. C*, 80:015807, 2009.

[74] Y. Fukuda et al. Solar neutrino data covering solar cycle 22. *Phys. Rev. Lett.*, 77:1683–1686, 1996.

[75] Y. Fukuda et al. Measurements of the solar neutrino flux from Super-Kamiokande's first 300 days. *Phys. Rev. Lett.*, 81:1158–1162, 1998. [Erratum: Phys.Rev.Lett. 81, 4279 (1998)].

[76] N. Vinyoles et al. A new Generation of Standard Solar Models. *Astrophys. J.*, 835(2):202, 2017.

[77] K. Abe et al. Solar Neutrino Measurements in Super-Kamiokande-IV. *Phys. Rev. D*, 94(5):052010, 2016.

[78] Q. R. Ahmad et al. Measurement of the rate of $\nu_e + d \to p + p + e^-$ interactions produced by ^{8}B solar neutrinos at the Sudbury Neutrino Observatory. *Phys. Rev. Lett.*, 87:071301, 2001.

[79] S. Fukuda et al. Solar B-8 and hep neutrino measurements from 1258 days of Super-Kamiokande data. *Phys. Rev. Lett.*, 86:5651–5655, 2001.

[80] D. Casper et al. Measurement of atmospheric neutrino composition with IMB-3. *Phys. Rev. Lett.*, 66:2561–2564, 1991.

[81] M. H. Ahn et al. Measurement of Neutrino Oscillation by the K2K Experiment. *Phys. Rev. D*, 74:072003, 2006.

[82] P. Adamson et al. Combined Analysis of ν_μ Disappearance and $\nu_\mu \to \nu_e$ Appearance in MINOS Using Accelerator and Atmospheric Neutrinos. *Phys. Rev. Lett.*, 112:191801, 2014.

[83] P. Adamson et al. Precision Constraints for Three-Flavor Neutrino Oscillations from the Full MINOS+ and MINOS Dataset. *Phys. Rev. Lett.*, 125(13):131802, 2020.

[84] M. Cacciari et al. Fully Differential Vector-Boson-Fusion Higgs Production at Next-to-Next-to-Leading Order. *Phys. Rev. Lett.*, 115(8):082002, 2015. [Erratum: Phys.Rev.Lett. 120, 139901 (2018)].

[85] K. Abe et al. Observation of Electron Neutrino Appearance in a Muon Neutrino Beam. *Phys. Rev. Lett.*, 112:061802, 2014.

[86] A. Aguilar et al. Evidence for neutrino oscillations from the observation of $\bar{\nu}_e$ appearance in a $\bar{\nu}_\mu$ beam. *Phys. Rev. D*, 64:112007, 2001.

[87] A. A. Aguilar-Arevalo et al. Updated MiniBooNE neutrino oscillation results with increased data and new background studies. *Phys. Rev. D*, 103(5):052002, 2021.

[88] B. Armbruster et al. Upper limits for neutrino oscillations muon-anti-neutrino —> electron-anti-neutrino from muon decay at rest. *Phys. Rev. D*, 65:112001, 2002.

[89] P. Abratenko et al. Search for an Excess of Electron Neutrino Interactions in MicroBooNE Using Multiple Final-State Topologies. *Phys. Rev. Lett.*, 128(24):241801, 2022.

[90] P. Abratenko et al. First Constraints on Light Sterile Neutrino Oscillations from Combined Appearance and Disappearance Searches with the MicroBooNE Detector. *Phys. Rev. Lett.*, 130(1):011801, 2023.

[91] P. Abratenko et al. Search for light sterile neutrinos with two neutrino beams at MicroBooNE. *Nature*, 648(8092):64–69, 2025.

[92] S. Ajimura et al. The JSNS2 detector. *Nucl. Instrum. Meth. A*, 1014:165742, 2021.

[93] Y. Abe et al. Indication of Reactor $\bar{\nu}_e$ Disappearance in the Double Chooz Experiment. *Phys. Rev. Lett.*, 108:131801, 2012.

[94] F. P. An et al. Observation of electron-antineutrino disappearance at Daya Bay. *Phys. Rev. Lett.*, 108:171803, 2012.

[95] J. K. Ahn et al. Observation of Reactor Electron Antineutrino Disappearance in the RENO Experiment. *Phys. Rev. Lett.*, 108:191802, 2012.

[96] F. An et al. Neutrino Physics with JUNO. *J. Phys. G*, 43(3):030401, 2016.

[97] K. Abe et al. Hyper-Kamiokande Design Report. 5 2018.

[98] S. Adrian-Martinez et al. Letter of intent for KM3NeT 2.0. *J. Phys. G*, 43(8):084001, 2016.

[99] M. G. Aartsen et al. PINGU: A Vision for Neutrino and Particle Physics at the South Pole. *J. Phys. G*, 44(5):054006, 2017.

[100] N. Aghanim et al. Planck 2018 results. VI. Cosmological parameters. *Astron. Astrophys.*, 641:A6, 2020. [Erratum: Astron.Astrophys. 652, C4 (2021)].

[101] J. Lesgourgues and S. Pastor. Massive neutrinos and cosmology. *Physics Reports*, 429(6):307–379, 2006.

[102] Y. Y. Wong. Neutrino mass in cosmology: status and prospects. *Annual Review of Nuclear and Particle Science*, 61(1):69–98, 2011.

[103] J. Lesgourgues and S. Pastor. Neutrino mass from cosmology. *Advances in High Energy Physics*, 2012(1):608515, 2012.

[104] K. N. Abazajian et al. Neutrino physics from the cosmic microwave background and large scale structure. *Astroparticle Physics*, 63:66–80, 2015.

[105] J. Lesgourgues and S. Pastor. Neutrino cosmology and planck. *New Journal of Physics*, 16(6):065002, 2014.

[106] M. Archidiacono et al. Physical effects involved in the measurements of neutrino masses with future cosmological data. *Journal of Cosmology and Astroparticle Physics*, 2017(02):052, 2017.

[107] M. Gerbino and M. Lattanzi. Status of neutrino properties and future prospects—cosmological and astrophysical constraints. *Frontiers in Physics*, 5:70, 2018.

[108] J. A. Formaggio et al. Direct measurements of neutrino mass. *Physics Reports*, 914:1–54, 2021.

[109] S. R. Choudhury and S. Hannestad. Updated results on neutrino mass and mass hierarchy from cosmology with planck 2018 likelihoods. *Journal of Cosmology and Astroparticle Physics*, 2020(07):037, 2020.

[110] N. Aghanim et al. Planck 2018 results-v. cmb power spectra and likelihoods. *Astronomy & Astrophysics*, 641:A5, 2020.

[111] S. Alam et al. The clustering of galaxies in the completed SDSS-III Baryon Oscillation Spectroscopic Survey: cosmological analysis of the DR12 galaxy sample. *Mon. Not. Roy. Astron. Soc.*, 470(3):2617–2652, 2017.

[112] A. J. Ross et al. The clustering of the SDSS DR7 main Galaxy sample – I. A 4 per cent distance measure at $z = 0.15$. *Mon. Not. Roy. Astron. Soc.*, 449(1):835–847, 2015.

[113] F. Beutler et al. The 6df galaxy survey: baryon acoustic oscillations and the local hubble constant. *Monthly Notices of the Royal Astronomical Society*, 416(4):3017–3032, 2011.

[114] R. L. Workman and Others. Review of Particle Physics. *PTEP*, 2022:083C01, 2022.

[115] S. Abe et al. Search for the majorana nature of neutrinos in the inverted mass ordering region with kamland-zen. *Physical Review Letters*, 130(5):051801, 2023.

[116] M. Agostini et al. Final results of gerda on the search for neutrinoless double-β decay. *Physical review letters*, 125(25):252502, 2020.

[117] R. E. Shrock. New tests for and bounds on neutrino masses and lepton mixing. *Physics Letters B*, 96(1-2):159–164, 1980.

[118] L. Collaboration et al. Precision electroweak measurements and constraints on the standard model. *arXiv preprint arXiv:0712.0929*, 2007.

[119] C. Athanassopoulos et al. The liquid scintillator neutrino detector and lampf neutrino source. *Nuclear Instruments and Methods in Physics Research Section A: Accelerators, Spectrometers, Detectors and Associated Equipment*, 388(1-2):149–172, 1997.

[120] A. Aguilar et al. Evidence for neutrino oscillations from the observation of electron anti-neutrinos in a muon anti-neutrino beam. *arXiv preprint hep-ex/0104049*, 2001.

[121] B. Dasgupta and J. Kopp. Sterile neutrinos. *Physics Reports*, 928:1–63, 2021.

[122] A. A. Aguilar-Arevalo et al. Updated miniboone neutrino oscillation results with increased data and new background studies. *Physical Review D*, 103(5):052002, 2021.

[123] J. N. Abdurashitov et al. The SAGE and LNGS experiment: Measurement of solar neutrinos at LNGS using gallium from SAGE. *Astropart. Phys.*, 25:349–354, 2006.

[124] M. A. Acero et al. Limits on nu(e) and anti-nu(e) disappearance from Gallium and reactor experiments. *Phys. Rev. D*, 78:073009, 2008.

[125] C. Giganti et al. Neutrino oscillations: The rise of the PMNS paradigm. *Prog. Part. Nucl. Phys.*, 98:1–54, 2018.

[126] P. Adamson et al. Search for Sterile Neutrinos Mixing with Muon Neutrinos in MINOS. *Phys. Rev. Lett.*, 117(15):151803, 2016.

[127] P. Adamson et al. Limits on Active to Sterile Neutrino Oscillations from Disappearance Searches in the MINOS, Daya Bay, and Bugey-3 Experiments. *Phys. Rev. Lett.*, 117(15):151801, 2016. [Addendum: Phys.Rev.Lett. 117, 209901 (2016)].

[128] P. Minkowski. $\mu \to e\gamma$ at a Rate of One Out of 10^9 Muon Decays? *Phys. Lett. B*, 67:421–428, 1977.

[129] R. N. Mohapatra and G. Senjanovic. Neutrino Mass and Spontaneous Parity Nonconservation. *Phys. Rev. Lett.*, 44:912, 1980.

[130] T. Yanagida. Horizontal gauge symmetry and masses of neutrinos. *Conf. Proc. C*, 7902131:95–99, 1979.

[131] M. Gell-Mann et al. Complex Spinors and Unified Theories. *Conf. Proc. C*, 790927:315–321, 1979.

[132] J. Schechter and J. W. F. Valle. Neutrino Masses in SU(2) x U(1) Theories. *Phys. Rev. D*, 22:2227, 1980.

[133] R. N. Mohapatra. Mechanism for Understanding Small Neutrino Mass in Superstring Theories. *Phys. Rev. Lett.*, 56:561–563, 1986.

[134] S. Nandi and U. Sarkar. A Solution to the Neutrino Mass Problem in Superstring E6 Theory. *Phys. Rev. Lett.*, 56:564, 1986.

[135] R. N. Mohapatra and J. W. F. Valle. Neutrino Mass and Baryon Number Nonconservation in Superstring Models. *Phys. Rev. D*, 34:1642, 1986.

[136] M. C. Gonzalez-Garcia and J. W. F. Valle. Fast Decaying Neutrinos and Observable Flavor Violation in a New Class of Majoron Models. *Phys. Lett. B*, 216:360–366, 1989.

[137] E. Ma and R. Srivastava. Dirac or inverse seesaw neutrino masses with $B-L$ gauge symmetry and S_3 flavor symmetry. *Phys. Lett. B*, 741:217–222, 2015.

[138] J. W. F. Valle and C. A. Vaquera-Araujo. Dynamical seesaw mechanism for Dirac neutrinos. *Phys. Lett. B*, 755:363–366, 2016.

[139] S. Centelles Chuliá et al. Dirac Neutrinos and Dark Matter Stability from Lepton Quarticity. *Phys. Lett. B*, 767:209–213, 2017.

[140] M. Magg and C. Wetterich. Neutrino Mass Problem and Gauge Hierarchy. *Phys. Lett. B*, 94:61–64, 1980.

[141] T. P. Cheng and L.-F. Li. Neutrino Masses, Mixings and Oscillations in SU(2) x U(1) Models of Electroweak Interactions. *Phys. Rev. D*, 22:2860, 1980.

[142] G. Lazarides et al. Proton Lifetime and Fermion Masses in an SO(10) Model. *Nucl. Phys. B*, 181:287–300, 1981.

[143] R. N. Mohapatra and G. Senjanovic. Neutrino Masses and Mixings in Gauge Models with Spontaneous Parity Violation. *Phys. Rev. D*, 23:165, 1981.

[144] R. Foot et al. Seesaw Neutrino Masses Induced by a Triplet of Leptons. *Z. Phys. C*, 44:441, 1989.

[145] W. Buchmuller and D. Wyler. Effective Lagrangian Analysis of New Interactions and Flavor Conservation. *Nucl. Phys. B*, 268:621–653, 1986.

[146] B. Grzadkowski et al. Dimension-Six Terms in the Standard Model Lagrangian. *JHEP*, 10:085, 2010.

[147] E. E. Jenkins et al. Renormalization Group Evolution of the Standard Model Dimension Six Operators I: Formalism and lambda Dependence. *JHEP*, 10:087, 2013.

[148] E. E. Jenkins et al. Renormalization Group Evolution of the Standard Model Dimension Six Operators II: Yukawa Dependence. *JHEP*, 01:035, 2014.

[149] R. Alonso et al. Renormalization Group Evolution of the Standard Model Dimension Six Operators III: Gauge Coupling Dependence and Phenomenology. *JHEP*, 04:159, 2014.

[150] L. Lehman. Extending the Standard Model Effective Field Theory with the Complete Set of Dimension-7 Operators. *Phys. Rev. D*, 90(12):125023, 2014.

[151] Y. Liao and X.-D. Ma. Renormalization Group Evolution of Dimension-seven Baryon- and Lepton-number-violating Operators. *JHEP*, 11:043, 2016.

[152] I. Brivio and M. Trott. The Standard Model as an Effective Field Theory. *Phys. Rept.*, 793:1–98, 2019.

[153] C. W. Murphy. Dimension-8 operators in the Standard Model Effective Field Theory. *JHEP*, 10:174, 2020.

[154] Y. Liao and X.-D. Ma. An explicit construction of the dimension-9 operator basis in the standard model effective field theory. *JHEP*, 11:152, 2020.

[155] H.-L. Li et al. Complete set of dimension-eight operators in the standard model effective field theory. *Phys. Rev. D*, 104(1):015026, 2021.

[156] R. V. Harlander et al. Standard model effective field theory up to mass dimension 12. *Phys. Rev. D*, 108(5):055020, 2023.

[157] D. Zhang. Renormalization group equations for the SMEFT operators up to dimension seven. *JHEP*, 10:148, 2023.

[158] E. E. Jenkins et al. Low-Energy Effective Field Theory below the Electroweak Scale: Operators and Matching. *JHEP*, 03:016, 2018. [Erratum: JHEP 12, 043 (2023)].

[159] E. E. Jenkins et al. Low-Energy Effective Field Theory below the Electroweak Scale: Anomalous Dimensions. *JHEP*, 01:084, 2018. [Erratum: JHEP 12, 042 (2023)].

[160] Y. Liao et al. Extending low energy effective field theory with a complete set of dimension-7 operators. *JHEP*, 08:162, 2020.

[161] C. W. Murphy. Low-Energy Effective Field Theory below the Electroweak Scale: Dimension-8 Operators. *JHEP*, 04:101, 2021.

[162] H.-L. Li et al. Low energy effective field theory operator basis at d $\leq$ 9. *JHEP*, 06:138, 2021.

[163] S. Hamoudou et al. Dimension-8 SMEFT matching conditions for the low-energy effective field theory. *JHEP*, 03:157, 2023.

[164] A. Aparici et al. Right-handed neutrino magnetic moments. *Phys. Rev. D*, 80:013010, 2009.

[165] S. Bhattacharya and J. Wudka. Dimension-seven operators in the standard model with right handed neutrinos. *Phys. Rev. D*, 94(5):055022, 2016. [Erratum: Phys.Rev.D 95, 039904 (2017)].

[166] Y. Liao and X.-D. Ma. Operators up to Dimension Seven in Standard Model Effective Field Theory Extended with Sterile Neutrinos. *Phys. Rev. D*, 96(1):015012, 2017.

[167] H.-L. Li et al. Operator bases in effective field theories with sterile neutrinos: d $\leq$ 9. *JHEP*, 11:003, 2021.

[168] M. Kleesiek et al. β-decay spectrum, response function and statistical model for neutrino mass measurements with the katrin experiment. *The European Physical Journal C*, 79(3):204, 2019.

[169] Direct neutrino-mass measurement with sub-electronvolt sensitivity. *Nature Physics*, 18(2):160–166, 2022.

[170] W. C. Pettus et al. Overview of project 8 and progress towards tritium operation. In *Journal of Physics: Conference Series*, volume 1342, pp. 012040. IOP Publishing, 2020.

[171] R. Saakyan et al. Determination of neutrino mass with quantum technologies. In *UK HEP Forum*, 2020.

[172] J. A. Canning et al. Sensitivity of future tritium decay experiments to new physics. *Journal of High Energy Physics*, 2023(3):1–44, 2023.

[173] E. K. Akhmedov et al. Seesaw mechanism and structure of neutrino mass matrix. *Physics Letters B*, 478(1-3):215–223, 2000.

[174] P. O. Ludl and W. Rodejohann. Direct neutrino mass experiments and exotic charged current interactions. *Journal of High Energy Physics*, 2016(6):1–38, 2016.

[175] K. Assamagan et al. Upper limit of the muon-neutrino mass and charged pion mass from momentum analysis of a surface muon beam. *Phys. Rev. D*, 53:6065–6077, 1996.

[176] R. Barate et al. An Upper limit on the tau-neutrino mass from three-prong and five-prong tau decays. *Eur. Phys. J. C*, 2:395–406, 1998.

[177] G.-Y. Huang et al. Effective neutrino masses in KATRIN and future tritium beta-decay experiments. *Phys. Rev. D*, 101(1):016003, 2020.

[178] K. Collaboration. Katrin design report 2004. *FZKA report*, 7090, 2005.

[179] T. Houdy et al. Hunting kev sterile neutrinos with katrin: building the first tristan module. In *Journal of Physics: Conference Series*, volume 1468, pp. 012177. IOP Publishing, 2020.

[180] B. Monreal and P. . Collaboration. Project 8: Update on a radiofrequency tritium spectrometer. In *AIP Conference Proceedings*, volume 1441, pp. 441–443. American Institute of Physics, 2012.

[181] R. Adhikari et al. A white paper on kev sterile neutrino dark matter. *Journal of cosmology and astroparticle physics*, 2017(01):025, 2017.

[182] P. . Collaboration. Input to the european strategy for particle physics – 2026 update: The project 8 neutrino mass experiment. CERN Indico contribution, March 31, 2025.

[183] A. A. S. Amad et al. Determining Absolute Neutrino Mass using Quantum Technologies. 12 2024.

[184] F. Šimkovic et al. Exact relativistic tritium β-decay endpoint spectrum in a hadron model. *Physical Review C—Nuclear Physics*, 77(5):055502, 2008.

[185] P. D. Bolton et al. Neutrinoless double beta decay versus other probes of heavy sterile neutrinos. *JHEP*, 03:170, 2020.

[186] J. N. Bahcall. Theory of Bound-State Beta Decay. *Phys. Rev.*, 124:495–499, 1961.

[187] R. Williams and S. Koonin. Atomic final-state interactions in tritium decay. *Physical Review C*, 27(4):1815, 1983.

[188] S. Mertens et al. Sensitivity of next-generation tritium beta-decay experiments for kev-scale sterile neutrinos. *Journal of Cosmology and Astroparticle Physics*, 2015(02):020, 2015.

[189] E. Fermi. An attempt of a theory of beta radiation. 1. *Z. Phys.*, 88:161–177, 1934.

[190] J. Simpson. Measurement of the β-energy spectrum of h 3 to determine the antineutrino mass. *Physical Review D*, 23(3):649, 1981.

[191] W. W. Repko and C.-E. Wu. RADIATIVE CORRECTIONS TO THE END-POINT OF THE TRITIUM BETA DECAY SPECTRUM. *Phys. Rev. C*, 28:2433–2436, 1983.

[192] H. Behrens and W. Buhring. *Electron radial wave functions and nuclear beta-decay*. Monographs on Physics. Oxford University Press, London, England, October 1982.

[193] C. Hargrove et al. Measurement of the screening potential in 3 h β decay. *Physical Review C*, 60(3):034608, 1999.

[194] D. Wilkinson. Evaluation of beta-decay: Ii. finite mass and size effects. *Nuclear Instruments and Methods in Physics Research Section A: Accelerators, Spectrometers, Detectors and Associated Equipment*, 290(2-3):509–515, 1990.

[195] D. H. Wilkinson. Analysis of neutron β-decay. *Nuclear Physics A*, 377(2-3):474–504, 1982.

[196] G. Audi et al. The ame2003 atomic mass evaluation:(ii). tables, graphs and references. *Nuclear physics A*, 729(1):337–676, 2003.

[197] S. S. Masood et al. Exact relativistic β decay endpoint spectrum. *Physical Review C—Nuclear Physics*, 76(4):045501, 2007.

[198] P. B. Pal. *An introductory course of particle physics*. Taylor & Francis, 2014.

[199] G. Cowan. *Statistical data analysis*. 1998.

[200] A. A. Esfahani et al. The Project 8 Neutrino Mass Experiment. In *Snowmass 2021*, 3 2022.

[201] G. Cowan et al. Asymptotic formulae for likelihood-based tests of new physics. *The European Physical Journal C*, 71:1–19, 2011.

[202] E. Holzschuh et al. Search for heavy neutrinos in the β-spectrum of 63ni. *Physics Letters B*, 451(1):247–255, 1999.

[203] K. C. Ng et al. New constraints on sterile neutrino dark matter from nustar m31 observations. *Physical Review D*, 99(8):083005, 2019.

[204] I. Mocioiu et al. Low-energy limits on the antisymmetric tensor field background on the brane and on the non-commutative scale. *Physics Letters B*, 489(3):390–396, 2000.

[205] X. Shi and G. Sigl. A Type II supernovae constraint on electron-neutrino - sterile-neutrino mixing. *Phys. Lett. B*, 323:360–366, 1994. [Erratum: Phys.Lett.B 324, 516–516 (1994)].

[206] S. Mertens et al. A novel detector system for katrin to search for kev-scale sterile neutrinos. *Journal of Physics G: Nuclear and Particle Physics*, 46(6):065203, 2019.

[207] C. Martoff et al. Hunter: precision massive-neutrino search based on a laser cooled atomic source. *Quantum Science and Technology*, 6(2):024008, 2021.

[208] H. Acharya et al. Sterile-neutrino search based on 259 days of KATRIN data. *arXiv:2503.18667*, 3 2025.

[209] Y. Ko et al. Sterile neutrino search at the neos experiment. *Physical review letters*, 118(12):121802, 2017.

[210] J. Ashenfelter et al. First search for short-baseline neutrino oscillations at hfir with prospect. *Physical review letters*, 121(25):251802, 2018.

[211] M. Dentler et al. Updated global analysis of neutrino oscillations in the presence of ev-scale sterile neutrinos. *Journal of High Energy Physics*, 2018(8):1–35, 2018.

[212] C. Kraus et al. Limit on sterile neutrino contribution from the mainz neutrino mass experiment. *The European Physical Journal C*, 73(2):2323, 2013.

[213] J. Abdurashitov et al. First measurements in search for kev sterile neutrino in tritium beta-decay in the troitsk nu-mass experiment. *JETP Letters*, 105:753–757, 2017.

[214] S. Carbajal and A. Gago. Indirect search of heavy neutral leptons using the dune near detector. *Frontiers in Physics*, 12:1398070, 2024.

[215] D. Gorbunov and M. Shaposhnikov. How to find neutral leptons of the νMSM? *JHEP*, 10:015, 2007. [Erratum: JHEP 11, 101 (2013)].

[216] A. Atre et al. The Search for Heavy Majorana Neutrinos. *JHEP*, 05:030, 2009.

[217] A. Das and N. Okada. Inverse seesaw neutrino signatures at the LHC and ILC. *Phys. Rev. D*, 88:113001, 2013.

[218] F. F. Deppisch et al. Neutrinos and Collider Physics. *New J. Phys.*, 17(7):075019, 2015.

[219] Y. Cai et al. Lepton Number Violation: Seesaw Models and Their Collider Tests. *Front. in Phys.*, 6:40, 2018.

[220] A. Das et al. Probing right handed neutrinos at the LHeC and lepton colliders using fat jet signatures. *Phys. Rev. D*, 99(5):055030, 2019.

[221] K. Bondarenko et al. Phenomenology of GeV-scale Heavy Neutral Leptons. *JHEP*, 11:032, 2018.

[222] P. Ballett et al. Heavy Neutral Leptons from low-scale seesaws at the DUNE Near Detector. *JHEP*, 03:111, 2020.

[223] P. Coloma et al. GeV-scale neutrinos: interactions with mesons and DUNE sensitivity. *Eur. Phys. J. C*, 81(1):78, 2021.

[224] A. M. Abdullahi et al. The present and future status of heavy neutral leptons. *J. Phys. G*, 50(2):020501, 2023.

[225] S. Weinberg. Baryon and Lepton Nonconserving Processes. *Phys. Rev. Lett.*, 43:1566–1570, 1979.

[226] K. S. Babu and C. N. Leung. Classification of effective neutrino mass operators. *Nucl. Phys. B*, 619:667–689, 2001.

[227] A. de Gouvea and J. Jenkins. A Survey of Lepton Number Violation Via Effective Operators. *Phys. Rev. D*, 77:013008, 2008.

[228] J. Gargalionis and R. R. Volkas. Exploding operators for Majorana neutrino masses and beyond. *JHEP*, 01:074, 2021.

[229] K. Fridell et al. Radiative neutrino masses from dim-7 SMEFT: a simplified multi-scale approach. *JHEP*, 09:050, 2025.

[230] P. D. Bolton et al. Constraining the SMEFT Extended with Sterile Neutrinos at FCC-ee. 2 2025.

[231] A. Abada et al. FCC-ee: The Lepton Collider: Future Circular Collider Conceptual Design Report Volume 2. *Eur. Phys. J. ST*, 228(2):261–623, 2019.

[232] F. del Aguila et al. Heavy Majorana Neutrinos in the Effective Lagrangian Description: Application to Hadron Colliders. *Phys. Lett. B*, 670:399–402, 2009.

[233] L. Duarte et al. Not-that-heavy Majorana neutrino signals at the LHC. *J. Phys. G*, 45(2):025001, 2018.

[234] A. Caputo et al. The seesaw portal in testable models of neutrino masses. *JHEP*, 06:112, 2017.

[235] G. Magill et al. Dipole Portal to Heavy Neutral Leptons. *Phys. Rev. D*, 98(11):115015, 2018.

[236] J. Alcaide et al. Probes of the Standard Model effective field theory extended with a right-handed neutrino. *JHEP*, 08:031, 2019.

[237] J. M. Butterworth et al. Higgs phenomenology as a probe of sterile neutrinos. *Phys. Rev. D*, 100(11):115019, 2019.

[238] A. Biekötter et al. The effective field theory of low scale see-saw at colliders. *Eur. Phys. J. C*, 80(8):743, 2020.

[239] D. Barducci et al. The see-saw portal at future Higgs Factories. *JHEP*, 03:117, 2021.

[240] J. De Vries et al. Long-lived Sterile Neutrinos at the LHC in Effective Field Theory. *JHEP*, 03:148, 2021.

[241] G. Cottin et al. Heavy neutral leptons in effective field theory and the high-luminosity LHC. *JHEP*, 09:039, 2021.

[242] R. Beltrán et al. Long-lived heavy neutral leptons at the LHC: four-fermion single-N_R operators. *JHEP*, 01:044, 2022.

[243] R. Beltrán et al. Long-lived heavy neutral leptons from mesons in effective field theory. *JHEP*, 01:015, 2023.

[244] M. Mitra et al. Reexamining right-handed neutrino EFTs up to dimension six. *Phys. Rev. D*, 106(11):113008, 2022.

[245] D. Barducci and E. Bertuzzo. The see-saw portal at future Higgs factories: the role of dimension six operators. *JHEP*, 06:077, 2022.

[246] F. Delgado et al. Assessment of the dimension-5 seesaw portal and impact of exotic Higgs decays on non-pointing photon searches. *JHEP*, 09:079, 2022.

[247] L. Duarte et al. Bounding the Dimension-5 Seesaw Portal with non-pointing photon searches. *JHEP*, 04:133, 2024.

[248] G. Zapata et al. Sensitivity prospects for lepton-trijet signals in the νSMEFT at the LHeC. *Eur. Phys. J. C*, 84(3):326, 2024.

[249] D. Barducci et al. Probing the dipole portal to heavy neutral leptons via meson decays at the high-luminosity LHC. *Phys. Rev. D*, 108(11):115009, 2023.

[250] E. Fernández-Martínez et al. Effective portals to heavy neutral leptons. *JHEP*, 09:001, 2023.

[251] R. Beltrán et al. Probing heavy neutrino magnetic moments at the LHC using long-lived particle searches. *JHEP*, 07:153, 2024.

[252] E. J. Chun et al. Collider imprints of a right handed neutrino magnetic moment operator. *Phys. Rev. D*, 109(11):115002, 2024.

[253] A. Biswas et al. Phenomenology of Dirac neutrino EFTs up to dimension six. *Phys. Rev. D*, 112(5):055023, 2025.

[254] M. Mitra et al. Probing right-handed neutrinos via trilepton signals at the HL-LHC. *Phys. Rev. D*, 111(1):015005, 2025.

[255] R. Beltrán et al. Heavy neutral leptons and top quarks in effective field theory. *JHEP*, 05:238, 2025.

[256] L. Duarte et al. Future collider sensitivities to νSMEFT interactions. *J. Phys. G*, 52(6):065001, 2025.

[257] S. Pascoli et al. Heavy neutrinos with dynamic jet vetoes: multilepton searches at $\sqrt{s} = 14$, 27, and 100 TeV. *JHEP*, 06:049, 2019.

[258] A. Abada et al. FCC Physics Opportunities: Future Circular Collider Conceptual Design Report Volume 1. *Eur. Phys. J. C*, 79(6):474, 2019.

[259] F. F. Deppisch et al. Relaxing limits from Big Bang Nucleosynthesis on Heavy Neutral Leptons with axion-like particles. *JCAP*, 02:054, 2025.

[260] D. Liventsev et al. Search for heavy neutrinos at belle. *Physical Review D—Particles, Fields, Gravitation, and Cosmology*, 87(7):071102, 2013.

[261] J. Dorenbosch et al. A search for decays of heavy neutrinos in the mass range 0.5–2.8 gev. *Physics Letters B*, 166(4):473–478, 1986.

[262] P. Vilain et al. Search for heavy isosinglet neutrinos. *Physics Letters B*, 343(1-4):453–458, 1995.

[263] O. Adriani et al. Search for isosinglet neutral heavy leptons in z0 decays. *Physics Letters B*, 295(3-4):371–382, 1992.

[264] P. Achard et al. Search for heavy isosinglet neutrino in e+ e- annihilation at lep. *Physics Letters B*, 517(1-2):67–74, 2001.

[265] D. collaboration. Search for neutral heavy leptons produced in z decays. *Zeitschrift für Physik C Particles and Fields*, 74:57–71, 1997.

[266] A. Das et al. Constraining sterile neutrinos from precision higgs data. *Physical Review D*, 95(11):115013, 2017.

[267] M. Blennow et al. Non-unitarity, sterile neutrinos, and non-standard neutrino interactions. *Journal of High Energy Physics*, 2017(4):1–26, 2017.

[268] F. Del Aguila et al. Effects of new leptons in electroweak precision data. *Physical Review D—Particles, Fields, Gravitation, and Cosmology*, 78(1):013010, 2008.

[269] J. de Blas. Electroweak limits on physics beyond the standard model. In *EPJ Web of Conferences*, volume 60, pp. 19008. EDP Sciences, 2013.

[270] S. Antusch and O. Fischer. Non-unitarity of the leptonic mixing matrix: Present bounds and future sensitivities. *Journal of High Energy Physics*, 2014(10):1–30, 2014.

[271] G. Aad et al. Search for Heavy Neutral Leptons in Decays of W Bosons Using a Dilepton Displaced Vertex in s=13 TeV pp Collisions with the ATLAS Detector. *Phys. Rev. Lett.*, 131(6):061803, 2023.

[272] A. Abada et al. Sterile neutrinos facing kaon physics experiments. *Physical Review D*, 95(7):075023, 2017.

[273] Z. Liu et al. Probing dark matter particles at CEPC. *JHEP*, 06:009, 2019.

[274] M. Antonello. IDEA: A detector concept for future leptonic colliders. *Nuovo Cim. C*, 43(2-3):27, 2020.

[275] A. Blondel et al. Searches for long-lived particles at the future FCC-ee. *Front. in Phys.*, 10:967881, 2022.

[276] S. Ajmal et al. Searching for type I seesaw mechanism in a two heavy neutral leptons scenario at FCC-ee. *JHEP*, 05:054, 2025.

[277] J. Abdallah et al. Photon events with missing energy in e+ e- collisions at s**(1/2) = 130-GeV to 209-GeV. *Eur. Phys. J. C*, 38:395–411, 2005.

[278] J. Abdallah et al. Search for one large extra dimension with the DELPHI detector at LEP. *Eur. Phys. J. C*, 60:17–23, 2009.

[279] E. Fernandez-Martinez et al. Global constraints on heavy neutrino mixing. *JHEP*, 08:033, 2016.

[280] A. Hayrapetyan et al. Review of searches for vector-like quarks, vector-like leptons, and heavy neutral leptons in proton–proton collisions at $\sqrt{s}$=13 TeV at the CMS experiment. *Phys. Rept.*, 1115:570–677, 2025.

[281] D. Liventsev et al. Search for heavy neutrinos at Belle. *Phys. Rev. D*, 87(7):071102, 2013. [Erratum: Phys.Rev.D 95, 099903 (2017)].

[282] F. Bergsma et al. A Search for Decays of Heavy Neutrinos in the Mass Range 0.5-GeV to 2.8-GeV. *Phys. Lett. B*, 166:473–478, 1986.

[283] P. Vilain et al. Search for heavy isosinglet neutrinos. *Phys. Lett. B*, 343:453–458, 1995.

[284] R. Barouki et al. Blast from the past II: Constraints on heavy neutral leptons from the BEBC WA66 beam dump experiment. *SciPost Phys.*, 13:118, 2022.

[285] K. Abe et al. Search for heavy neutrinos with the T2K near detector ND280. *Phys. Rev. D*, 100(5):052006, 2019.

[286] E. Cortina Gil et al. Search for heavy neutral lepton production in K+ decays to positrons. *Phys. Lett. B*, 807:135599, 2020.

[287] B. Aubert et al. A Search for Invisible Decays of the Upsilon(1S). *Phys. Rev. Lett.*, 103:251801, 2009.

[288] A. Freitas. Higher-order electroweak corrections to the partial widths and branching ratios of the Z boson. *JHEP*, 04:070, 2014.

[289] S. Mohanty. Search for a light sterile neutrino with KATRIN. *PoS*, EPS-HEP2023:164, 2024.

[290] M. Tanabashi et al. Review of particle physics. *Phys. Rev. D*, 98:030001, Aug 2018.

[291] W. C. Haxton. ATOMIC EFFECTS AND HEAVY NEUTRINO EMISSION IN BETA DECAY. *Phys. Rev. Lett.*, 55:807–809, 1985.

[292] A. Denner et al. Feynman rules for fermion number violating interactions. *Nucl. Phys. B*, 387:467–481, 1992.

[293] S. G. Gorishnii et al. The $O(\alpha_s^3)$-corrections to $\sigma_{tot}(e^+e^- \to hadrons)$ and $\Gamma(\tau^- \to \nu_\tau + hadrons)$ in QCD. *Phys. Lett. B*, 259:144–150, 1991.

[294] J. L. Feng et al. Simulating heavy neutral leptons with general couplings at collider and fixed target experiments. *Phys. Rev. D*, 110(3):035029, 2024.